Modelling the effect of acoustic waves on the thermodynamics and kinetics of crystal nucleation from a solution

Seyyed Reza Haqshenas

A dissertation submitted in partial fulfillment

of the requirements for the degree of

Doctor of Philosophy

of

University College London.

Department of Mechanical Engineering

University College London

April 26, 2017

I, Seyyed Reza Haqshenas, confirm that the work presented in this thesis is my own. Where information has been derived from other sources, I confirm that this has been indicated in the work.

Abstract

A phase transformation in a metastable solution can be affected when it is subjected to high-intensity acoustic waves. Despite the extensive experimental evidence, the nature of this phenomenon has been little studied theoretically. This work aims to tackle this issue and develop the theoretical basis for investigating the *thermodynamics* and *kinetics* of crystallisation induced by an acoustic field.

In the first part of thesis, we investigated the effect of acoustic waves on the *thermodynamics* of crystallisation by the aid of the Gibbs droplet model in a generic format. We have developed a new model based on non-equimolecular clusters which can overcome some of the shortcomings of the conventional form of the classical nucleation theory (CNT) in describing the thermodynamics of small clusters. The model is validated by comparing the predicted kinetics of water droplet formation from the gas phase against experimental data. Our results demonstrate a close agreement with experimental data, better than predictions by CNT.

In the second part, we studied the *kinetics* of phase transformation in an acoustic field. We developed a master equation based on a hybrid Szilard-Fokker Planck model, which accounts for mass transportation due to acoustic waves. This model is employed to determine the kinetics of nucleation and the early stage of growth of clusters including the Ostwald ripening phenomenon in an isothermal sonocrystallisation process and is solved numerically for different scenarios in a system with and without mass transportation. Our results show that the effect of pressure on the kinetics of nucleation is cluster size-dependent in contrast to CNT. Furthermore, we calculated mass transportation for different excitations modelled as plane waves propagating in a semi-infinite medium which tends to be rather noticeable only in the case of shock waves. The derivations are generic and can be used with any acoustic source and waveform.

Dedicated to my dear parents

Acknowledgements

I would like to extend my sincere thanks and gratitude to my supervisors Professor Nader Saffari and Professor Ian John Ford who have continuously supported me throughout this research. I am very grateful for their inspiring discussions, thoughtful advices, invaluable guidance and friendship.

I am thankful to my friends and colleagues at the UCL Ultrasonics Group, including Dr. Pierre Gélat, Dr. Christopher Wright, Dr. Ki Joo Pahk, Mats De Andrade, and Antonio Gómez, for their encouragement, feedbacks and support. I am especially very grateful to Pierre for proofreading the thesis, in spite of his busy schedule.

I wish to thank the Sonocrystallisation Group in the department of chemical engineering at UCL, including Professor Asterios Gavriilidis, Dr. Luca Mazzei, Dr. Rashid Jamshidi, Damiano Rossi and Luigi Gargiulo for their collaboration and help for conducting sonocrystallisation experiments.

I acknowledge the Engineering and Physical Sciences Research Council for funding this work (grant number EP/I031480/1). I also acknowledge the use of the UCL Legion High Performance Computing Facility (Legion@UCL), and associated support services.

Finally, I would like to express my sincerest gratitude and acknowledgments to my dear family. I am indebted to them for their unlimited love, endless support and persistent encouragements throughout my endeavours.

Contents

1 Introduction **30**

1.1 Overview 30

1.2 Background 31

1.2.1 Phase transition in a solution 31

1.2.2 Effects associated with acoustic waves propagating in a liquid medium 32

1.3 Experimental assessment of sonocrystallisation 34

1.4 Modelling approaches 43

1.5 Aims and objectives 49

1.5.1 Problem statement 49

1.5.2 Research objectives and contributions 49

1.6 Thesis structure 50

2 Thermodynamics of cluster formation I: Silent condition **52**

2.1 Model of cluster formation 53

2.2 Dividing surface 58

2.3 The new cluster model 60

2.3.1 The new surface 60

2.3.2 Number of surface molecules 62

2.3.3 Cluster size and volume 67

2.4 Work of cluster formation 69

2.4.1 Critical cluster 72

2.4.2 Non-critical cluster 75

2.5 Nucleus size 83
2.6 $\Delta\mu$ in crystallisation from a solution 84
2.7 Summary 85

3 Thermodynamics of cluster formation II: With acoustic waves 87
3.1 Work of cluster formation 88
3.1.1 Non-critical cluster 88
3.1.2 Critical cluster 90
3.2 Nucleus size 91
3.3 Incompressible solution and isothermal condition 92
3.4 Summary 104

4 Kinetics of cluster formation I: Mass conserved system 106
4.1 Master equations for nucleation 108
4.1.1 Hybrid model 112
4.2 Nucleation rate 113
4.2.1 Quasi-stationary and stationary nucleation rate 114
4.3 Transition frequencies 123
4.3.1 Monomer attachment frequency 123
4.3.2 Monomer detachment frequency 125
4.4 Non-dimensionalisation 130
4.5 Summary 132

5 Kinetics of cluster formation II: Non-mass conserved system 135
5.1 Conservation of mass in a mixture 136
5.1.1 Simplified conservation of mass equation 139
5.2 Hybrid model with mass transportation 142
5.3 Nucleation rate 145
5.4 Non-dimensionalisation 146
5.5 Summary 150

6 Validation of the new cluster model using water droplet nucleation data 153

6.1 Water droplet nucleation 153

6.2 Simulation results 155

6.3 Summary 160

7 Simulation of thermodynamics and kinetics of cluster formation in an acoustic field 161

7.1 Acoustic wave propagation 162

7.1.1 Numerical implementation 163

7.2 Mass conserved system 168

7.2.1 Numerical implementation 168

7.2.2 Simulation results 171

7.3 Non-mass conserved system 181

7.3.1 Numerical implementation 181

7.3.2 Simulation results 183

7.4 Simulations at different λ 199

7.5 Summary 207

8 Conclusions 210

8.1 Contributions to the field 210

8.2 Further work 214

Appendices 217

A Material properties 217

B Second-order derivative of the grand potential of the system 219

C Fokker-Planck equation with mass transportation 221

D Number of excess molecules 223

E Discrete form of monomer detachment frequency 225

Bibliography **228**

List of Figures

2.1 Density fluctuation in the old phase described by the cluster and DFT approaches. The vertical dashed lines show the abrupt change in the spatial density at an arbitrary location of the dividing surface. Refer to the text for details. 54

2.2 Cluster formation in a system with constant volume, temperature and chemical potential. Refer to the text for details. 55

2.3 (a) Size of the new phase (n_n), and (b) the interface phase (n_σ) at different location of the DS obtained by solving Equation (2.27). 66

2.4 Ratio of $\rho_{n,\text{eff}}$ to ρ_n for different locations of the DS. The dot-dashed line represents this ratio for the EDS cluster ($\lambda = 0$). . . 68

2.5 Work of cluster formation obtained by both new models, i.e. Equation (2.57) presented as new model 1 and Equation (2.60) shown as new model 2 for $\lambda = 0.35$, and the conventional form of CNT at the supersaturation ratio $r = 15$. . . 80

2.6 Work of cluster formation obtained by both new models, i.e. Equation (2.57) and Equation (2.60) for $\lambda = 0.35$, and the conventional form of CNT at the supersaturation ratio $r = 50$. 80

2.7 Excess Helmholtz free energy $F_{\sigma,1}$ for clusters defined by the new surface with different λ at the supersaturation ratio $r = 15$. 81

2.8 Excess Helmholtz free energy $F_{\sigma,2}$ for clusters defined by the new surface with different λ at the supersaturation ratio $r = 15$. 81

2.9 Effective surface tension obtained by calculating Equation (2.63) using $F_{\sigma,1}$ for clusters defined by the new surface with different λ at the supersaturation ratio $r = 15$. 82

2.10 Effective surface tension obtained by calculating Equation (2.63) using $F_{\sigma,2}$ for clusters defined by the new surface with different λ at the supersaturation ratio $r = 15$. 82

2.11 Size of the critical cluster at different supersaturation ratios. Clusters are defined by the new surface with $\lambda = 0.35$. 84

3.1 Work of cluster formation for clusters defined by different values of λ with $r_0 = 15$ and a) $\Delta p = 10$ MPa, and b)$\Delta p = 100$ MPa. Pressure change is static. 94

3.2 Numerical differentiation of the nucleation work with respect to static pressure variation (isothermal), see the LHS of Equation (3.19). 96

3.3 Excess size of the critical cluster in the system exposed to isothermal static pressure rise, see the RHS of Equation (3.19). . . 96

3.4 Contour plot of the nucleation work at different supersaturation ratios and static pressure magnitudes. The DS coincides with the EDS. 97

3.5 Contour plot of the nucleation work at different supersaturation ratios and static pressure magnitudes. The DS is placed within the EDS with $\lambda = 0.35$. 97

3.6 Isobaric nucleation work at different supersaturation ratios. The labels on curves refer to the pressure magnitude in MPa, the DS is positioned at $\lambda = 0$. 97

3.7 See the caption of Figure 3.6. Here the DS is positioned at $\lambda = 0.35$. 98

3.8 Isobaric nucleation work at different supersaturation ratios ($1 \leq r_0 < 50$). The DS is positioned at $\lambda = 0.35$. 98

3.9 Work of cluster formation for two different supersaturation ratios and pressure magnitudes. The DS is positioned at $\lambda = 0.35$. 100

3.10 Nucleation work calculated for the EDS and non-EDS ($\lambda = 0.35$) clusters at different supersaturation ratios over one cycle of excitation. The second axis on the RHS illustrates Δp for p_m = 100 MPa and f = 100 kHz. The time axis is non-dimensionalised with respect to the driving frequency, i.e. $\tau = tf$. The magnified area at the top shows the nucleation work at the peak positive pressure instant. 103

3.11 The same as Figure 3.10 but with $p_m = 10$ MPa. 103

4.1 Transitions between system macrostates and the snapshots of molecular clusters. Macrostates are identified by the number of molecules in the system creating the density fluctuations. Following the cluster modelling methodology, they are represented by the size of emerged clusters. Growth and decay processes take place according to transition probabilities per unit time f_n and g_n, respectively. 109

4.2 Schematic representation of the hybrid model. See the text for details. 113

4.3 z^2, solid curves, and z_0^2, dashed curves, at different pressure magnitudes and at two different supersaturation ratios of r_0 = 15 and r_0 = 30. The non-EDS cluster model with λ = 0.35 is considered here. 117

4.4 Likewise Figure 4.3 but for the EDS clusters. The small variations at high pressure values are due to numerical calculations. 117

4.5 $k_p(t)$ over non-dimensionalised time (one period of excitation) with parameters p_m = 10 MPa, f = 100 kHz at r_0 = 15 and $r_0 = 30$. Clusters are defined by $\lambda = 0.35$. 121

4.6 $k_p(t)$ calculated for EDS over non-dimensionalised time (one period of excitation) with parameters p_m = 10 MPa, f = 100 kHz at r_0 = 15 and r_0 = 30. 121

4.7 Similar to Figure 4.5 but with parameters p_m = 50 MPa, f = 100 kHz at r_0 = 15 and r_0 = 30. Clusters are defined by $\lambda = 0.35$. 122

4.8 Similar to Figure 4.5 but with parameters p_m = 100 MPa, f = 100 kHz at r_0 = 15 and r_0 = 30. 122

4.9 The RHS of Equation (4.30) calculated with p_m = 1 MPa, f = 100 kHz at r_0 = 15 and r_0 = 30 for non-EDS clusters with $\lambda = 0.35$ over (a) an oscillation period, (b) magnified about time interval $0 < \tau < 0.2$. 126

4.10 Likewise Figure 4.9 with p_m = 50 MPa, f = 100 kHz at r_0 = 15 and r_0 = 30 for non-EDS clusters with $\lambda = 0.35$. 127

4.11 Likewise Figure 4.9 with p_m = 100 MPa, f = 1 MHz at r_0 = 15 and r_0 = 30 for non-EDS clusters with $\lambda = 0.35$. 127

6.1 Effective surface tension (γ_{eff}) at different λ calculated by Equation (2.63) at T = 300 K. ▲: Statistical mechanical simulations (Lau et al., 2015b) at the cluster size of $n = 3, 6, 12, 24, 48, 76, 96$. Solid black curve shows the best fit to statistical mechanical simulations. 155

6.2 Logarithmic concentration (logarithm in base 10 in all figures) of supercritical clusters at two different λ values over time. Vertical lines labelled $\tau_{n,0}$ and $\tau_{n,1}$ indicate the beginning of the nucleation stage in models with $\lambda = 0$ and $\lambda = 0.37$, respectively. The unlabelled vertical line indicates the end of nucleation and monomer-driven growth of supercritical clusters in the case of $\lambda = 0$ while nucleation is still ongoing in the case of $\lambda = 0.37$. This is due to a faster nucleation rate for $\lambda = 0$ which leads to quicker depletion of the imposed supersaturation of monomers. 157

6.3 Supersaturation ratio at two different λ values over time. See the caption of Figure 6.2 for details. 157

6.4 Logarithm of the nucleation rate versus the supersaturation ratio at T = 300 K. The nucleation rate calculated by our new model using λ values determined from statistical mechanical calculation of Lau et al. (Lau et al., 2015b) at the data points of Brus 2008 and 2009 (solid line with ◆ and dashed line with ▶, respectively). The experimental results of Brus et al. 2008 and 2009 (Brus et al., 2008, 2009) are also shown (solid line with • and dashed line with ■, respectively). The nucleation rate determined by the BD model at the data points of Brus 2008 and 2009 (▲ and ▼, respectively). 158

6.5 λ calculated from the experimental nucleation rate (Wölk and Strey, 2001) for water nucleation at different temperatures. The error bars show the range in λ at a specific temperature as a function of the supersaturation ratio. The lower and upper limits correspond to the smallest and largest experimental supersaturation ratios at a specific temperature, respectively. 159

7.1 Plane wave field across space up to $1.5x_s$ at $\tau_w = 2\pi$ with f = 1 MHz and p_m = 10 MPa. 165

7.2 Plane wave field across space up to $1.5x_s$ at $\tau_w = 2\pi$ with f = 1 MHz and p_m = 50 MPa. 166

7.3 Plane waveform across space up to $1.5x_s$ over one period with f = 1 MHz and p_m = 50 MPa. 166

7.4 (a) Relative intensity across space, (b) temperature variation across space for p_m = 50 MPa and f – 1 MHz. 167

7.5 Stationary nucleation rate at different supersaturation ratios determined by the BD model. 172

7.6 Concentration of supercritical clusters at different pressure magnitudes over time with $\lambda = 0.35$. Vertical lines labelled $\tau_{n,100}$ to $\tau_{n,1}$ indicate the beginning of the nucleation stage for different static pressures of old phase. Static pressure decreases from the black curve (100 MPa) at the top to the red curve at the bottom (1 MPa). 172

7.7 Supersaturation ratio at different pressure magnitudes over time with $\lambda = 0.35$. 174

7.8 Concentration of supercritical clusters (solid line) and mean size of supercritical clusters (dashed line) at the static pressure of 100 MPa and with $\lambda = 0.35$. Around $\log(\tau) = -0.7$ the concentration of supercritical clusters becomes a maximum and starts to decline whereas the mean size of supercritical clusters increases and plateaus shortly after. 174

7.9 Concentration of supercritical clusters (solid line) and mean size of supercritical clusters (dashed line) at the static pressure of 1 MPa and with $\lambda = 0.35$. Around $\log(\tau) = 8.8$ the supersaturation ratio approaches unity, the concentration of supercritical clusters becomes a maximum and starts to decline. The mean size of supercritical clusters drops too but a ripening process could not be identified. 174

7.10 Logarithmic CSD, i.e. the contour plot of logarithmic size-weighted cluster size distribution ($\log(nZ)$), over time at the static pressure 1 MPa with $\lambda = 0.35$. The black dashed line shows the time-dependent size of the critical cluster. 175

7.11 The same as Figure 7.10 but at the static pressure of 50 MPa. 175

7.12 The same as Figure 7.10 but at the static pressure of 100 MPa. 176

7.13 CSD at the end of the nucleation stage ($r \approx 1$) at two static pressures of 100 MPa, the left vertical axis, and 50 MPa, the right vertical axis. Refer to the text for details. 176

7.14 Supersaturation ratio over time at different excitation frequencies and pressure magnitude of p_m = 50 MPa with λ = 0.35. 178

7.15 Nucleation work over time at different excitation frequencies and pressure magnitude of p_m = 50 MPa with λ = 0.35. The legend is the same as that of Figure 7.14. 178

7.16 (a) Concentration of supercritical clusters over time where the old phase is exposed to pressure fluctuation with p_m = 50 MPa at different frequencies. The legend is the same as that of Figure 7.14. (b) magnified towards the end of simulation with f = 0 MHz (when $r \cong 1$). We can see that at f = 0, 20, 100 kHz, Z_s reaches its maximum value at $\log(\tau)$ = 0.9, 1.4, 1.5, respectively. The Ostwald ripening process follows. In contrast, at higher frequencies the nucleation stage is still ongoing at this time. . . 179

7.17 Logarithmic CSD over time where the solution is exposed to an acoustic wave with excitation parameters of f = 100 kHz and p_m = 50 MPa with λ = 0.35. 180

7.18 The same as Figure 7.17 but with excitation parameters of f = 2 MHz and p_m = 50 MPa. 180

7.19 Change in the concentration of monomers across a wavelength centered about $0.5x_s$ over one period in a travelling wave field with p_m = 50 MPa, f = 1 MHz. 185

7.20 Four snapshots of contours shown in Figure 7.19. 185

7.21 Change in the concentration of monomers across a wavelength centered about $0.5x_s$ over one period in a travelling wave field with p_m = 50 MPa, f = 100 kHz. 186

7.22 Four snapshots of contours shown in Figure 7.21. 186

7.23 Change in the concentration of monomers across a wavelength centered about $0.5x_s$ over one period in a travelling wave field with p_m = 10 MPa, f = 1 MHz. 187

7.24 Four snapshots of contours shown in Figure 7.23. 187

7.25 The same as Figure 7.23 but for a standing wave field with p_m = 50 MPa, f = 1 MHz. 187

7.26 Four snapshots of contours shown in Figure 7.25. 188

7.27 Change in the concentration of monomers across a wavelength centered about $2x_s$ over one period in a travelling wave field with p_m = 50 MPa, f = 1 MHz. (b) magnified around $2x_s$. 188

7.28 (a) Snapshots of the contour plot shown in Figure 7.27 in initial few time steps. (b) Zoomed in around $2x_s$. 191

7.29 Snapshots of (a) dimensionless mass flux due to the pressure gradient, (b) dimensionless mass flux due to the concentration gradient, and (c) dimensionless pressure diffusion term, around $2x_s$ at the first three time instances. 192

7.30 Change in the concentration of monomers across four wavelengths and over ten excitations in a travelling wave field with p_m = 50 MPa, f = 1 MHz. 194

7.31 Change in the concentration of monomers in a pre-shock zone for a solute species with relatively large molecules, R_0 = 10 nm. Simulation is performed across a wavelength centered about $0.5x_s$ and over one period in a travelling wave field with p_m = 50 MPa, f = 1 MHz. 194

7.32 Change in the concentration of monomers in the post-shock distance for a solute species with relatively large molecules, R_0 = 10 nm. Simulation is performed across a wavelength centered about $2x_s$ and over one period in a travelling wave field with p_m = 50 MPa, f = 1 MHz 194

7.33 Concentration of monomers (equivalent to the supersaturation ratio) across a wave length over time. 196

7.34 Concentration of monomers over time at some locations, see Figure 7.33. 196

7.35 Concentration of supercritical clusters over time at different locations. Vertical dashed lines indicate the beginning of the nucleation stage at different locations. A similar colour code as the curves is used for these vertical lines. 198

7.36 Nucleation work over time at different locations. 198

7.37 Concentration of supercritical clusters across space at the end of the first cycle of sonication. 198

7.38 CSD in $\overline{x}$ = 1.99. Vertical dashed line shows the size of the critical cluster. 199

7.39 CSD in $\overline{x}$ = 2.02. Vertical dashed line shows the size of the critical cluster. 199

7.40 Supersaturation ratio over time at different values of λ and the static pressure of p_m = 1 MPa. 200

7.41 Supersaturation ratio over time at different values of λ and the static pressure of p_m = 100 MPa.The legend is the same as that of Figure 7.40. 200

7.42 CSD at the end of the nucleation stage ($\log(\tau)$ = 2) at a static pressure of 50 MPa and at different λ values. 200

7.43 n_n' at different λ values for a range of cluster sizes. 202

7.44 (a) Detachment frequency, Equation (4.40), for a supercritical cluster of size n = 70 over time. Parameters of acoustic wave are f = 2 MHz and p_m = 50 MPa at a pre-shock location. (b) As in (a) but evaluated for a supercritical cluster of size $n = 10^{4.5}$. . . 202

7.45 (a) Supersaturation ratio over time when the old phase is exposed to an acoustic wave, the same acoustic wave parameters as in Figure 7.44, with different λ values. (b) magnified about $\log(\tau)$ = 0.25. 203

7.46 Effective supersaturation ratio calculated for a monomer over time at two locations; just before the shock $\overline{x} = 1.99$ (the black solid curve) and just after the shock $\overline{x} = 2.01$ (the blue dashed curve). 204

7.47 Likewise Figure 7.46 but for a cluster of size $n = 1000$. 204

7.48 Excess free energy of a cluster of size $n = 10$ over time at two locations; just before the shock $\overline{x} = 1.99$ (the black solid curve) and just after the shock $\overline{x} = 2.01$ (the blue dashed curve). $F_{\sigma,1}$ is calculated by Equation (3.25). 206

7.49 Likewise Figure 7.48 but for a cluster of size $n = 1000$ 206

7.50 Excess free energy of a cluster of size $n = 10$ across space at different time instants. 206

7.51 The ratio of the excess free energy for the non-EDS cluster with $\lambda = 0.35$ to the excess free energy of the EDS cluster of the same size ($F_{\sigma,cl}$), calculated at $\overline{x} = 1.99$. Curves present readings at different time instants shown in the legend. The dotted curve in magenta colour is the ratio of the contribution of the surface tension term and the cyan solid curve is $F_{\sigma,r}$ given by Equation (2.61) with a constant supersaturation ratio, see the text for details. 207

List of Tables

7.1 Non-dimensionalisation constants calculated using equations presented in Section 5.4. 184

A.1 Solution properties at $T = 293$ K 217

A.2 Water properties I 218

A.3 Water properties II (at $T = 293$ K) 218

Symbols

Alphanumeric

A_σ interfacial surface area, m^2.

C_0 number concentration of nucleation sites, m^{-3}.

C_1 molar concentration of the species 1 (solvent), mole m^{-3}.

C_2 molar concentration of the species 2 (solute), mole m^{-3}.

C_e solubility at the reference state, m^{-3}.

C_h heat capacity,J kg^{-1} K^{-1}.

C_m molar concentration of the solution, mole m^{-3}.

C_p specific heat at constant pressure,J K^{-1}.

c_0 speed of sound, ms^{-1}.

c local speed of sound, ms^{-1}.

D diffusivity of a monomer in the old phase, m^2 s^{-1}.

F Helmholtz free energy of the old phase, J.

F_σ Helmholtz free energy of the interface phase, J.

f_n attachment frequency of monomers to n-size clusters, s^{-1}.

f frequency of an acoustic wave, s^{-1}.

g_n detachment frequency of monomers from n-size clusters, s^{-1}.

I intensity of acoustic waves, W m^{-2}.

J_0 kinetic prefactor in the stationary nucleation rate, s^{-1} m^{-3}.

J_n forward flux of a cluster size n along the size axis, s^{-1} m^{-3}.

J_{qs} quasi-stationary nucleation rate, s^{-1} m^{-3}.

J_s stationary nucleation rate, s^{-1} m^{-3}.

$\mathbf{j_2}$ molecular flux of the species 2 (solute) in an open system, kg s^{-1} m^{-2}.

K_n inward flux of n-size clusters from the bath to the system, s^{-1} m^{-3}.

k_B the Boltzmann constant, m^2 kg s^{-2} K^{-1}.

k_f coefficient in the volume diffusion equation resembling the collision kernel of a monomer with an n-mer in the Smoluchowski coagulation equation, m^3 s^{-1}.

k_ρ relative variation in density due to a phase transformation, DL.

k_w wavenumber, rad m^{-1}.

L_n outward flux of n-size clusters from the system to the bath, s^{-1} m^{-3}.

M_1 molar weight of the species 1 (solvent) in the solution, kg $mole^{-1}$.

M_2 molar weight of the species 2 (solute) in the solution, kg $mole^{-1}$.

M_a acoustic Mach number, DL.

M_m total molar weight of the solution, kg $mole^{-1}$.

m mass of a cluster, kg.

m_0 mass of a monomer in the new phase, kg.

$\mathcal{N}_\mathcal{A}$ Avogadro's number, $mole^{-1}$.

N_d maximum size of a cluster modeled by the discrete Szilard equation in the hybrid model, DL.

N total number of monomers in the old phase, DL.

n_Σ number of molecules in the system, DL.

n_e number of molecules in the EDS cluster, DL.

n_n number of molecules in the new phase or the size of the new phase, DL.

n_σ number of molecules in the interface phase or the size of the interface phase, DL.

n number of molecules in a cluster or the size of a cluster, DL.

P_i probability of adopting the macrostate i, DL.

p_a acoustic pressure in the old phase, Pa.

p_m amplitude of an acoustic wave, Pa.

p_n pressure of the new phase inside a cluster, Pa.

p_σ pressure of the interface phase, Pa.

p pressure of the old phase, Pa.

R_0 radius of a molecule in the new phase, considered to be a sphere, m.

R_n radius of a cluster defined by an arbitrary dividing surface, m.

$\mathbf{r}$ position vector relative to the origin of a system of coordinates, m.

r_0 supersaturation ratio (mole ratio) at the reference state, DL.

r time dependent supersaturation ratio (mole ratio), DL.

S_Σ entropy of the system, J K^{-1}.

S_n entropy of the new phase, J K^{-1}.

S_σ entropy of the interface phase, J K^{-1}.

S entropy of the old phase, J K^{-1}.

s_n specific entropy of the new phase, J K^{-1}.

s_σ specific entropy of the interface phase, J K^{-1}.

s specific entropy of the old phase, J K^{-1}.

T temperature, K.

t time, s.

U_Σ energy of the system, J.

U_n energy of the new phase, J.

U_σ energy of the interface phase, J.

U energy of the old phase, J.

u particle velocity due to a plane wave in Cartesian coordinate system, m s^{-1}.

$\mathbf{u}$ velocity vector in Cartesian coordinate system, m s^{-1}.

V_n volume of the new phase, m^3.

V_σ volume of the interface phase, m^3.

V_Σ volume of the entire system, m^3.

w total work done on a system to create a cluster of size n.

x_e composition (mole fraction) of the old phase at equilibrium, DL.

x composition (mole fraction) of the old phase, DL, or distance from the acoustic source, m.

x_s shock distance from the acoustic source, m.

Z_n the number density (concentration) of n-size clusters, m^{-3}.

z the Zeldovich factor, DL.

Greek letters

α_f frequency dependent sound absorption, Neper m^{-1}.

β coefficient of nonlinearity, DL.

δ_0 sound diffusivity, m^2s^{-1}.

δ separation distance of an arbitrary surface from the EDS, m.

δ_t Tolman length, m.

η_B bulk viscosity, Pa s.

η dynamic (shear) viscosity, Pa s.

Γ Goldberg number, DL.

γ_s specific heat ratio, DL.

γ_{eff} effective surface tension of the classical cluster, J m^{-2}.

γ_∞ surface tension of a planar surface, J m^{-2}.

γ size dependent surface tension, J m^{-2}.

κ	thermal conductivity, $\mathrm{Wm^{-1}K^{-1}}$.
ξ	retarded distance, m.
λ_a	acoustic wavelength, m.
λ	dimensionless quantity which distinguishes an arbitrary dividing surface from the EDS, DL.
μ_n	chemical potential of the new phase, J.
μ_σ	chemical potential of the interface phase, J.
μ	chemical potential of the old phase, J.
ν_n	specific volume of the new phase, $\mathrm{m^3}$.
ν	specific volume of the old phase, $\mathrm{m^3}$.
Ω_Σ	thermodynamic grand potential of the system, J.
Ω_σ	thermodynamic grand potential of the interface phase, J.
Ω	thermodynamic grand potential of the old phase, J.
ω	angular frequency of the sound source, rad $\mathrm{s^{-1}}$.
ρ_1	mass density of the species 1 (solvent) in the solution (per unit volume of the solution), kg $\mathrm{m^{-3}}$.
ρ_2	mass density of the species 2 (solute) in the solution (per unit volume of the solution), kg $\mathrm{m^{-3}}$.
ρ_m	mass density of the solution, kg $\mathrm{m^{-3}}$.
ρ_n	molecular number density of the new phase, $\mathrm{m^{-3}}$.
ρ	molecular number density of the old phase (solute), $\mathrm{m^{-3}}$.
Σ	system of molecules before and after a phase transformation.
$\mathcal{T}\left(i \to j; t\right)$	transition probability from the macrostate i to j at time t, DL.
τ_w	non-dimensionalised retarded time w.r.t to the wave speed, DL.
τ_n	nucleation time lag, s.
τ	non-dimensionalised time, DL.

Operators

Δn_{exc} excess number of molecules in a cluster of volume V_n compared with the same volume of the old phase, DL.

Δs_{exc} excess entropy gained by the system through cluster formation, J K^{-1}.

$\Delta\overline{Z_1}$ difference in the concentration of monomers due to mass transportation normalised by its initial concentration, DL.

$\Delta\mu$ difference in the chemical potentials of the old and new phases, J.

$\Delta\Omega$ difference between the grand potentials of the system before and after a phase transformation, J.

Superscripts

e equimolar surface.

$''$ second derivative with respect to the cluster size n.

$'$ state of the system before cluster formation; first derivative with respect to the cluster size n.

∞ infinitely dilute solution.

$*$ critical cluster.

t surface of tension.

Acronyms

BD Becker-Döring.

CNT classical nucleation theory.

CSD cluster size distribution.

DFT density functional theory.

DL dimensionless quantity.

DS dividing surface.

EDS equimolar dividing surface.

FPE Fokker-Planck equation.

GDE general dynamic equation.

HIFU high intensity focused ultrasound.

HON homogeneous nucleation.

LHS left hand side.

MD molecular dynamics.

MZW metastable zone width.

ODE ordinary differential equation.

PDE partial differential equation.

RHS right hand side.

US ultrasound waves.

List of refereed journal papers

(i) **S. R. Haqshenas**, I. J. Ford and N. Saffari, "Modelling the effect of acoustic waves on nucleation", The Journal of Chemical Physics, 145, 024315 (2016); doi:10.1063.

(ii) **S. R. Haqshenas** and N. Saffari, "Multi-resolution analysis of passive cavitation detector signals", Journal of Physics: Conference Series, 581, 1 (2015). doi:10.1088.

(iii) (In press) C. J. Wright, **S. R. Haqshenas**, J. Rothwell and N. Saffari, "Unmyelinated peripheral nerves can be stimulated in vitro using pulsed ultrasound," Ultrasound in Medicine & Biology (2017).

(iv) (in preparation for The Journal of Chemical Physics) **S. R. Haqshenas**, I. J. Ford and N. Saffari, "Modelling the effect of acoustic waves on the thermodynamics and kinetics of phase transformation: including mass transportation".

(v) (in preparation for The Journal of the Acoustical Society of America) M. O. de Andrade, **S. R. Haqshenas**, K. J. Pahk and N. Saffari, "Bubble nucleation in therapeutic ultrasound".

Chapter 1

Introduction

1.1 Overview

Acoustic waves can promote a process of phase transition in a liquid phase. In the case of a solid new phase, the process is called sonocrystallisation. The particles produced by sonocrystallisation feature: i) a smaller mean size, ii) a narrower cluster size distribution (CSD), and iii) a more uniform shape, comparing to particles made by conventional modes of crystallisation in the absence of acoustic waves (Ruecroft et al., 2005). These appealing characteristics have boosted the application of sonocrystallisation for production and purification of solid particles in various industries, in particular, pharmaceutical, food, and fine chemicals sectors.

The first papers about the physical, chemical and biological effects of high frequency acoustic waves were published in 1927 (Richards and Loomis, 1927; Wood and Loomis, 1927). They are followed by numerous publications from the former Soviet Union researchers in the post World War II era (Kapustin, 1963). Sonocrystallisation in solutions has been extensively investigated experimentally since then, though the nature of this phenomenon has been little studied theoretically. This work attempts to tackle this issue and develop the theoretical basis for investigating the thermodynamics and kinetics of crystallisation induced by an acoustic field in a solution. Our overall aims are two fold: i) develop a model that can describe the thermodynamics of phase transition

for small clusters; such a model is deemed important as the size of the critical cluster reduces as the intensity of the acoustic field increases, and ii) identify and model the effects of acoustic waves on the aggregative and non-aggregative mechanisms of the kinetics of sonocrystallisation.

In this chapter, we will outline background information on crystallisation in a solution, and effects of acoustic waves propagating in a liquid medium. We will provide a brief review of experimental sonocrystallisation literature and of the existing theoretical models. Finally, the problem investigated in this thesis will be stated and specific objectives will be defined.

1.2 Background

1.2.1 Phase transition in a solution

A supersaturated binary solution is a metastable phase made of a single component solute species dissolved in a solvent. The solution tends to transform from the metastable to the stable state because of the necessity to attain a lower level of energy. This is the thermodynamic driving force for initiating the nucleation process (Kashchiev, 2000) which is the first stage of a phase transition. Nucleation is the formation of nanoscopic nuclei which are in equilibrium with the old phase and is followed by the growth stage where nuclei grow and reach a macroscopic size. Nuclei are formed through random collision of solute molecules which creates an agglomerate of molecules, also known as a cluster. Clusters may evolve or decay depending on the balance between the energy they have gained because of the formation of a favourable stable phase and the surface tension. This energy balance determines the work of cluster formation. To predict the evolution of clusters, we need to determine the work and kinetics of cluster formation together over time.

Nucleation in a supersaturated solution does not occur spontaneously up to a certain level of supersaturation. The solubility curve indicates the equilibrium supersaturation value as a function of temperature. The width of this metastable zone between the solubility curve and the curve fitted through the

supersaturation points at which nucleation experimentally takes place is called the metastable zone width (MZW) (Mullin, 1972). A smaller MZW facilitates nucleation and provides the advantages of crystallisation at lower supersaturation levels, e.g. slow and controlled crystal growth which affect the final crystal size and shape (Mullin, 1972).

The thermodynamic state of the old phase influences the nucleation work and kinetics, hence the size distribution and morphology of final crystals in a polymorphic crystallisation. If the old phase is exposed to an external field, e.g. electric, magnetic, or acoustic field, nucleation is facilitated and crystal properties are modified (Kapustin, 1963; Conrad, 2000; Munir et al., 2006; Revalor et al., 2010). Electric and magnetic fields are usually used in the process of solidification of metals and alloys, polymers and ionic solutions. However, the acoustic field has been used in a wider range of applications, e.g. ; metallurgy, crystallisation of proteins, polymers, organic and inorganic salts (Atamanenko et al., 2010; Kitayama et al., 2013; Suslick and Price, 1999; Sander et al., 2014; Ruecroft et al., 2005). To model nucleation in a sonocrystallisation process, we, therefore, need to identify the effects associated with propagation of acoustic waves in a medium and quantify their links with the physics (both thermodynamics and kinetics) of phase transformation.

1.2.2 Effects associated with acoustic waves propagating in a liquid medium

Acoustic waves are defined by the vibrations of fluid particles about their normal configuration which lead to the transmission of mass and energy in the fluid through consecutive compression and rarefaction cycles (Kinsler et al., 1999). The rarefaction pressure swing of the wave can nucleate bubbles or induce a liquid-gas transition (Neppiras and Noltingk, 1951; Blander and Katz, 1975; Akulichev, 1982; Baidakov et al., 1981), called acoustic cavitation.

The two types of acoustic cavitation which occur are broadly demarcated into two categories: inertial and stable cavitation. Inertial cavitation is the event when tiny cavities or dissolved gases in the liquid grow rapidly due to

the rarefaction created by the acoustic waves and collapse violently in the compression cycle of the waves. This collapse generates enormous shock waves travelling at a speed of about 4000 m s^{-1} and with a magnitude of up to 1 GPa as well as a temperature rise at the centre of the bubble of about 5000 K (Flint and Suslick, 1991; Suslick and Flannigan, 2008). This can also lead to a significant temperature variation at a rate of 10^{10} K s^{-1} (Flint and Suslick, 1991; Suslick and Flannigan, 2008). All these effects happen locally and over a very short period of time, i.e. spatially and temporally on scales of the volume of a bubble and nano-seconds respectively (Akhatov et al., 2001; Ohl et al., 1999). In the case of an asymmetric collapse, e.g. due to an oscillation and implosion of a bubble in the vicinity of a solid surface, a jet of fluid, at speeds greater than 100 m s^{-1}, is generated (Suslick and Price, 1999).

In the case of stable cavitation,the created bubbles periodically oscillate in the acoustic field and irradiate pressure waves to the surrounding medium. These bubbles may grow and implode, or dissolve into the fluid depending on the boundary conditions and acoustic excitation. The total pressure amplitude around these bubbles is of the order of that of the driving acoustic field, hence considerably weaker relative to which occurs in inertial cavitation (Leighton, 1997). We should note that occurrence of acoustic cavitation in a solution depends on several parameters, namely: the dissolved gas content of the solution, the driving pressure magnitude and frequency. Degassing a solution and using a high driving frequency, e.g. greater than 3 MHz for water, (Neppiras and Noltingk, 1951) may in fact inhibit acoustic cavitation (Leighton, 1997).

During propagation of acoustic waves in the fluid, acoustic energy may be partially converted into random thermal energy through different mechanisms, e.g. including viscous losses and/or relaxational losses, and temperature may vary depending on the propagation distance or time of interest (Kinsler et al., 1999). Further, acoustic waves may distort due to the nonlinearity in the equation of state of the fluid and shock waves can be formed. The acoustic absorption coefficient depends on the frequency of acoustic waves and may

become important in liquids with high viscosity and/or in the (post-)shock region where waves are already distorted and where higher harmonics appear.

The temperature, flow and pressure fields at each spatial location are comprised of the direct field from the acoustic source and the indirect field generated by acoustic cavitation when this phenomenon occurs. The latter is a localised effect which is limited to locations in the vicinity of bubbles. This effect can however be substantial if inertial cavitation occurs. These variable temperature, flow and pressure fields imply that a phase transition in an acoustic field is unsteady and the use of conventional equations which bear the assumption of a stationary process is not justified in general. This motivates the need to treat sonocrystallisation as an unsteady process which shapes our vision in this work for modelling sonocrystallisation.

1.3 Experimental assessment of sonocrystallisation

Experimental studies of sonocrystallisation are extensive and the majority of them report the observed effects of sonication with different excitation parameters on crystallisation in various solutions. However, few of these works were designed to test hypotheses or perform a causality analysis. We will provide a brief review of experimental works here with a focus on the latter category. A review of theoretical works will be presented in the subsequent section.

The very first works that examined sonochemistry and phase transformation processes, date back to 1927 by Richards, Loomis, and Wood (Richards and Loomis, 1927; Wood and Loomis, 1927; Tuulmets et al., 2014), where effects of a standing wave field on different chemical reactions as well as crystallisation in a supersaturated solution were investigated. They reported that supersaturated solutions of crystalline solids and supercooled liquids are little affected by the sound field; however crystals are modified.

Attention to the field of sonocrystallisation surged during the 1950s and the 1960s and several researchers investigated the effects of ultrasound on cry-

stallisation and developed several hypotheses about the interaction between sound waves and crystallisation. One of the earliest reviews of such investigations was published by Kapustin in 1963 (Kapustin, 1963) and Hem in 1967 (Hem, 1967) summarising achievements until then. These papers present the following potential mechanisms involved in sonocrystallisation

- agitation and streaming in the solution: the acoustically induced flow can result in a more uniform temperature distribution throughout the bulk of the solution, and consequently result in finer particles and a narrower particle size distribution.

- dispersion of crystals: this hypothesis expresses that waves or cavitation break up supernuclei (large stable clusters) and spread them in the bulk of the solution by streaming and produce crystallisation sites. This can boost the nucleation rate significantly.

- super cooling, shock waves and possible jetting after the implosion of cavitating bubbles: supercooling leads to an enhanced supersaturation ratio. The other two effects can promote crystallisation via the preceding mechanisms.

- the surface of bubbles: the interface of gas/vapour bubbles with the liquid may work as sites for heterogeneous nucleation of crystals.

Although the phenomena caused by acoustic cavitation are usually hypothesised as the main mechanisms governing sonocrystallisation, it was experimentally shown (Mazhul, 1963; Yu et al., 2012) that in a field that is weak enough to inhibit cavitation or in a degassed medium where cavitation is not observed, the nucleation rate is still increased and crystallisation is enhanced. Likewise, Ward et al. (Ward et al., 2015) reported an increase in the nucleation rate in the supersaturated aqueous potassium chloride (KCl) solution subject to evanescent waves induced by laser and in the absence of cavitation. They placed a micro-droplet of the supersaturated solution on the surface of

a Dove prism and shone a laser to the prism to create evanescent waves at the interface of the glass and the droplet. They reported a similar average number of nucleation events relative to laser induced nucleation in bulk, but with a laser power reduced by a factor of three.

These results imply that the wave field itself and potentially its associated effects such as streaming, may enhance the crystallisation process in the absence of cavitation. Therefore, the effects of acoustic waves, either directly or indirectly through cavitation, can be divided into variation in pressure, temperature, and flow field. We will explore literature for each effect individually.

Static pressure can be more readily controlled experimentally, therefore reviewing crystallisation and solidification in supersaturated solutions and supercooled liquids under static pressure can be insightful. This has been studied and presented in several works in different disciplines, e.g. (Larson and Garside, 1986; Lorber et al., 1996; Groß and Jaenicke, 1993; Munir et al., 2006). In a nutshell, they showed that pressure can stimulate or inhibit nucleation, depending on the properties of the old and new phases, by influencing the difference in the chemical potentials of these phases and consequently the nucleation work.

In a very interesting work about the phase transition of supercooled water and aqueous solutions to ice using observations from clouds containing ice, it was shown that pressure has a similar effect on homogeneous nucleation of ice as the addition of solutes to supercooled water (Koop et al., 2000). For instance, adding 4 mol of NaCl per kg of water reduces the melting and freezing temperatures to almost similar values as applying 0.14 GPa pressure to pure water. The authors explained this observation as follows: in either mentioned situation, the effective activity of water molecules is similar and that is the decisive factor. So for any combination of the solute concentration and pressure magnitude that yields an equivalent effective activity, one should expect to achieve a similar nucleation work. They also claim that for a given volume of the test setup, the nucleation rate (hence the kinetics of nucleation) is a

function of Δa_w only, where $\Delta a_w = a_{w,eff}(T) - a_{w,l}(T)$ is the difference between the effective activity of water and its activity in a solution in equilibrium with ice at temperature T under zero pressure.

Several studies have shown that wave propagation in melts and supercooled liquids causes periodic phase transformation (Kapustin, 1963; Arakelyan, 1987; Chavanne et al., 2001). One of the most precise sets of experiments were conducted by Caupin and Balibar's group using supercooled liquid helium exposed to a high intensity focused ultrasound field. In one set of experiments, they irradiated ultrasound at 1 MHz from a focused hemispherical transducer onto the surface of a glass placed on the hemisphere plane (Chavanne et al., 2001). The reflection of the laser from the glass-helium interface was measured to detect formation of the solid phase. Heterogeneous nucleation of the solid helium was observed to happen over the compression cycle followed by a decay and finally melting during the rarefaction cycle. They did not report whether cavitation occurred prior to nucleation of crystals or not but they mentioned that cavitation was observed around the focus of the transducer.

A similar trend was experimentally observed in solidification of supercooled liquids (Hunt and Jackson, 1966), where the authors demonstrated that nucleation occurs after the collapse of a cavity rather than through or after the expansion phase. The large positive pressure generated by the collapse of a cavity lowers the freezing temperature of the liquid and results in nucleation. In their experiments, cavities were produced in absence of acoustic waves, made through the release of entrapped gas by impact in the U-shaped tubes.

In another set of experiments by the Caupin and Balibar team, the glass piece was removed and a similar hemispherical focused transducer was attached to a vessel, and was driven by a burst of 6 pulses at 1 MHz and at 140 kHz (Werner et al., 2004; Ishiguro et al., 2007; Balibar and Caupin, 2006). They observed cavitation in the supercooled liquid helium through rarefaction cycle. The pressure magnitudes when cavitation took place were in agreement with theoretical cavitation thresholds. However, nucleation of clusters could not be

detected even at pressure magnitudes greater than the thresholds for crystal nucleation obtained by CNT. To explain this observation, they suggested that CNT is too simple to capture the entire physics of such an involved process, the fact that CNT does not account for a change in the surface tension with pressure was specifically mentioned.

The problem of crystallisation in ^{4}He induced by acoustic waves has also been investigated by other groups. Abe et al. (Abe et al., 2005) and Kimura et al. (Kimura et al., 2004) conducted experiments using planar transducers at the higher driving frequency of 9 MHz compared with that employed in Caupin's experiments. Nucleation was detected using imaging of the test vessel, of about one centimetre in size, at a rate of 1000 fps which is less precise for detecting the onset of nucleation compared to the laser-based system of Caupin's group, and is quite slow relative to the driving frequency. Their results showed that at temperature, i.e. $T < 400$ mK, nucleation is temperature independent and can take place at the melting pressure if the acoustic intensity exceeds a specific threshold. The threshold was almost constant within this temperature range and exponentially increased with temperature for $400 < T < 600$ mK. The authors could not observe nucleation at higher temperatures with the maximum driving pressure the transducer could generate, and no theoretical explanation was provided for this.

To rigorously investigate nucleation induced by acoustic waves in a supersaturated solution, Soare et al. (Soare et al., 2011) conducted nucleation experiments in supersaturated $(NH_4)_2SO_4$ and $KMnO_4$ solutions. Nucleation is triggered by controlled laser induced cavitation (a nano-second laser source). The justification for use of laser induced cavitation was based on the fact that effects associated with acoustic cavitation are usually considered as the main contributors to nucleation in a sonocrystallisation process. Although the type of bubble, cavitation and sequence of events in the acoustic cavitation and laser induced cavitation are different, this work allows deducing very interesting and useful information about nucleation in a dynamic pressure field. They

demonstrated that crystals are nucleated in a ring around the laser focus, where the bubble is created and collapses. Temporally, their observations are as follows: i) cavitation is taking place over 200 μs, ii) disturbances in light emission were recorded after 30 – 50 μs, and iii) visible crystals identified at about 1 s. Therefore, they concluded that crystallisation tends to take place almost at the same time as cavitation due to initial evaporation of the solution by laser (we should note that in the case of acoustic cavitation, this high initial temperature is not present). Also, the thermal effects in the liquid due to the collapse of the bubble do not play an important role, mainly because of the large thermal heat capacity of surrounding water. Furthermore, temperature transients increase solubility and relieve supersaturation which is the driving force of nucleation. A similar reasoning about temperature effects was mentioned in the classic work by Richards and Loomis (Richards and Loomis, 1927). Considering ultrasonically induced nucleation, they suggest that an explanation in terms of the pressure transient or shock waves generated by collapse should be sought.

One should note that at the focus of the laser, a pressure wave is launched by the laser plasma which is sometimes referred to as the primary shock. A vapour bubble is subsequently formed, the collapse of which creates a secondary shock (Akhatov et al., 2001; Andreev et al., 2006). Given that crystals are formed over a similar time scale as the bubble, see (Soare et al., 2011), we can theorise that the primary compression shock tends to play an important role in initiating nucleation. This was overlooked in the discussion by Soare et al.. A similar argument was put forward in laser induced ice formation in supercooled water by Lindinger et al. (Lindinger et al., 2007). They reported homogeneous ice nucleation in supercooled water was mediated by the optical breakdown induced by a focused Nd:YAG laser pulse. They reported that the primary pressure wave generated by the breakdown plasma expansion, and the secondary pressure waves emitted by the collapse of the laser induced bubble are the potential mechanisms initiating nucleation. This two-step mechanism

was also suggested for crystallisation in a supersaturated solution irradiated by a femtosecond laser shot (Yoshikawa et al., 2006; Nakamura et al., 2007).

In an eminent work, Ohsaka and Trinh attempted to answer whether the positive or negative pressure phase of the shock will trigger nucleation. A single bubble was deployed in supercooled water using a needle syringe and excited by an acoustic source. The bubble was observed to oscillate stably for a few cycles after which it either collapsed or ejected away from its original location. In the cases that the bubble oscillated and shattered at its location, the ice nuclei were formed at the bubble's spot after its disappearance. They estimated the maximum undercooling in water for the positive and negative pressure pulses and showed that enough undercooling could only be achieved by the positive pressure phase.

Nalajala et al. (Nalajala and Moholkar, 2011) measured CSD in a solution which was subjected to the mechanical agitation (stirring) and the same solution was exposed to an ultrasonic field with a frequency of 20 kHz. The mean and variance of the CSD in the sonocrystallisation experiment compared to the stirring experiment were lower and higher, respectively. They concluded that the nucleation rate is higher in the sonocrystallisation experiment but the growth rate is lower relative to the stirring experiment. Comparing these two experiments and given that pressure and shock waves were only present in sonocrystallisation but noting that stirring provides uniform convective flow only, they concluded that shock waves promote nucleation and enhance the nucleation rate, and streaming mainly influences the growth of crystals in a similar fashion to stirring.

Guo et al. (Guo et al., 2006a,b) investigated the hypothesis relating the enhancement of the nucleation rate to the improved mass transfer in the solution due to sonication. They surmised that the diffusivity of solute molecules in the solution is a function of energy injected into the solution through ultrasound irradiation. They attempted to obtain diffusivity by fitting the theoretical predictions of the induction time exploiting CNT to the experimental

values. The main limitation of this work is that several quantities can be affected by ultrasound, of which only one parameter was considered.

With regards to the effect of temperature on sonocrystallisation, it is known that solubility increases with temperature which leads to reducing supersaturation hence the driving force of nucleation. Based on this observation, many works reasoned that temperature variation due to absorption of acoustic waves or transient events such as the collapse of bubbles cannot be the driving mechanism of nucleation (Richards and Loomis, 1927; Hunt and Jackson, 1966; Lindinger et al., 2007; Soare et al., 2011). The large temperature rises associated with inertial cavitation reported in the literature refer to the maximum temperature inside the bubble at its centre. This high temperature significantly plummets over time and across space, and with the concentration of non-condensable gas inside the bubble, e.g. see (Akhatov et al., 2001).

We have reviewed the effect of acoustic waves, shock waves, flow and temperature on crystallisation. The reported experiments were carried out with transducers running at different frequencies in the range of 20 kHz $< f <$ 9 MHz. The frequency of acoustic waves influences wave propagation, absorption and hence temperature variation and even acoustic cavitation. In addition to the works reviewed so far, we will further investigate the effect of the frequency of sound waves on crystallisation here.

Experiments performed on a supersaturated solution of adipic acid at three different excitation frequencies of $204, 355.5$ and 610 kHz showed that the MZW and CSD narrowed down compared to the silent condition, i.e. no ultrasound irradiation, and became the narrowest at the driving frequency of 355.5 kHz (Wohlgemuth et al., 2010). No explanation was provided for these observations, though. Likewise, an experiment conducted on the anti-solvent sonocrystallisation of glycine at excitation frequencies of 20 kHz and 1.6 MHz showed that sonocrystallisation at the higher frequency favoured crystal growth rather than crystal nucleation. The authors drew this conclusion based on the observation that the mean size of crystals was larger than in the 20 kHz

sonication case and within the range of the silent condition while the CSD was narrower than in both cases (Nii and Takayanagi, 2014). A similar observation was also reported by Wohlgemuth et al. (Wohlgemuth et al., 2010). They observed that at the frequency of 610 kHz the mean value of the CSD is almost equal to that one in the silent condition. However, the CSD narrows the most compared to cases with other driving frequencies.

To summarise, the attributes of sonocrystallisation are as follows: i) low induction time, i.e. the time that crystals appear, ii) fast nucleation rate, iii) narrow MZW [1], and iv) CSD with lower variance and typically lower mean. These effects are correlated and are influenced by the parameters of acoustic waves, and the properties of the solution. The former includes frequency, amplitude, and sonication protocol. The latter is comprised of temperature, cooling rate, and the supersaturation ratio. In order to control the entire process, it is required to study the interaction between the physics of acoustic waves (together with their associated effects) and the physics of crystallisation.

In the beginning of this section, we represented the potential mechanisms of how acoustic waves may influence crystallisation in a liquid from Hem's review paper published in 1967 (Hem, 1967). Review papers published half a century later, similar hypotheses are still discussed, suggesting the little insightful progress, especially theoretically, has been made (Castillo-Peinado and Luque de Castro, 2016; Sander et al., 2014; Ruecroft et al., 2005; Ratsimba et al., 1999). Nonetheless, new applications have been developed, e.g. sonocrystallisation in a continuous flow and micro/milli channels/vessels which reveal novel applications of sonocrystallisation.

Clearly, the interaction between acoustic waves and crystallisation in a supersaturated solution is very complex. Several effects rendered by acoustic

[1]Reducing MZW can allow the formation of crystals of different shapes in the case of polymorphic substances, e.g. see Gracin et al. (Gracin et al., 2005), which is practically difficult to produce in the silent condition. This is because some morphologies only appear when nucleation takes place at a very low supersaturation level which can be achieved in sonocrystallisation

waves contribute to both nucleation and growth stages of crystallisation. Correlation between these effects and the output of crystallisation process have been primarily studied experimentally. A well-developed theoretical model that can explain the interaction between these two physical phenomena is still absent. The related theoretical and numerical works are reviewed in the following section.

1.4 Modelling approaches

As we discussed in the former section, acoustic waves create fluctuations in the temperature, pressure and flow fields (both directly and indirectly through cavitation) in the old phase. We will review works attempting to incorporate these effects into the thermodynamics and kinetics of phase transition in a supersaturated solution. Our intention is to focus only on works which employ classical thermodynamics to investigate the phase transition in a variable pressure or temperature field.

Within the scope of our work, the Gibbs droplet model is extensively used to determine the thermodynamics of phase transformation. This model is thoroughly explained in Chapter 2, but for the ease of the reader and to facilitate our current discussion, it will be briefly outlined here. The Gibbs model considers that a mechanical work is required to make the old phase metastable and initiate nucleation of the new phase. The new phase is characterised as a cluster of molecules with a density that differs from the old phase. This work becomes maximum in the case of a critical cluster, which is the cluster in an unstable thermodynamic equilibrium with the old phase, and is given by

$$W = -n\Delta\mu + W_\sigma = -(p_n - p)\, V_n + W_\sigma,$$

where $\Delta\mu$ is the difference between the chemical potentials of the old and new phases, p_n is pressure of the new phase with volume V_n and size n, p is pressure of the old phase and W_σ is the interfacial excess energy needed to create the new phase with the surface area A_n. The first and second terms on the right

hand side (RHS) are usually referred to as volume work, and surface work, respectively. The work of the formation of the critical cluster (W) is called the nucleation work. If we write the surface work as $W_\sigma = A_n\gamma_\infty$, where γ_∞ is the equilibrium planar surface tension, this equation turns into the conventional form of CNT.

The stationary nucleation rate is proportional to the nucleation work as follows

$$J \propto \exp(\frac{-W}{k_B T}),$$

where k_B is the Boltzmann constant.

The nucleation rate is sensitive to changes in temperature, pressure, and impurities in the old phase (Oxtoby, 1992). The correlation between variation in pressure of the old phase and nucleation has been first studied in the problem of droplet formation from a gas phase in the presence of inert carrier gases, see for example (Ford, 1992; Oxtoby and Laaksonen, 1995; Kashchiev, 1996; Luijten and van Dongen, 1999; Luijten et al., 1999; Wedekind et al., 2008). Ford used a statistical mechanical approach to model the effect of a carrier gas on the phase equilibrium between the old (vapour) and the new (droplet) phases. The other works are, however, based on classical thermodynamics.

The majority of theoretical works were originally accomplished by the former Soviet Union scientists mainly focusing on crystallisation in metals and were published in Russian. Akulichev and Bulanov (Akulichev and Bulanov, 1983) investigated the effect of a standing sound field on the size of nuclei in melts, and a supersaturated solution. They used a perturbation method to calculate hydrodynamic equations and the nucleation kinetics. Consequently, the variable size of nuclei was estimated at variable pressure and temperature. They modelled the effect of the acoustic field on the kinetics of crystallisation through variation in solubility due to temperature and pressure fluctuation, i.e. $\frac{\partial Z}{\partial T}dT + \frac{\partial Z}{\partial p}dp$ where Z is the equilibrium supersaturation. They showed that nuclei undergo periodic melting/dissolution and solidifica-

tion/crystallisation.

In a work concerned more about the effects of sound fields on crystallisation from a thermodynamic point of view, Arakelyan (Arakelyan, 1987) considered that acoustic waves influence $\Delta\mu$ through changing the supersaturation ratio by two mechanisms: i) changing the solubility due to temperature fluctuation resulting from the absorption of sound energy, i.e. $\Delta Z_T = -\frac{\partial Z}{\partial T}\Delta T$ where ΔT is temperature variation due to acoustic waves (likewise Akulichev and Bulanov (Akulichev and Bulanov, 1983)), and ii) change in solubility due to the second order pressure effects (if we use a second order equation of state and accounting for nonlinear density variation in a pressure field), i.e. ΔZ_p. Therefore one gets $\Delta\mu \propto \Delta Z_s + \Delta Z_T + \Delta Z_p$ where ΔZ_s is the supersaturation ratio. For the range of excitation parameters they were interested in, i.e. high driving frequency (10 to 90 MHz) and low pressure amplitude, the temperature effect on crystallisation was more pronounced than the pressure effect, i.e. $\Delta Z_T \gg \Delta Z_p$.

Kashchiev and Van Rosmalen (Kashchiev and Van Rosmalen, 1995) proposed a variation of CNT estimating the pressure dependent nucleation rate of a condensed phase in a solution. They showed that when pressure in a solution changes from p_0 to p, the nucleation work varies by $(p - p_0)(1 - \rho/\rho_n)V_n$ where ρ and ρ_n are the number density of the old and new phases, respectively. One should note that this model only considers the effect of pressure on the volume work but not the surface work (W_σ). Caupin et al. (Balibar and Caupin, 2006) consider this shortcoming as a possible reason for the failure of CNT in explaining experimental results.

In spite of this, the Kashchiev and Van Rosmalen model was used to estimate the effects of shock waves on nucleation (Virone et al., 2006). Virone et al. estimated the magnitude of pressure at the centre of an inertially collapsing bubble excited by ultrasound waves at the frequency of 20 kHz and substituted in this model to theoretically estimate the nucleation rate in the presence of strong shock waves emitted from bubble implosion. Since the

magnitude of pressure was so high, they obtained an extremely high rate of nucleation. This agrees with experimental observations that crystals are formed almost instantly in a sonocrystallisation process. However, nucleation induced by shock waves is an unsteady process and the use of modified CNT (with the above-mentioned relationship) to estimate the nucleation rate is questionable.

Calculations based on the Kashchiev and Van Rosmalen model for a solution with the condensed new phase show that the size of the critical cluster will decrease with increasing pressure magnitude. This is in agreement with the experimental observation of the CSDs with smaller mean values. Nevertheless, it does not provide any information about the effect of pressure on the variance of the CSD.

This model and these analyses based on it for crystallisation in a supersaturated solution are challenged by another set of works (Harzali et al., 2011; Dodds et al., 2007). These works present sonocrystallisation experiments using a specific solution with $\rho/\rho_n \approx 1$, i.e. the aqueous solution of $ZnSO_4$. Thus, the mentioned model predicts a negligible effect of pressure on the nucleation work, and hence on the nucleation rate. In contrast, substantial effects were observed experimentally. To explain these observations, they suggested *the segregation hypothesis* which is described as follows: the forced convective-diffusion stimulated by oscillation and collapse of bubbles segregate heavier molecules (e.g. solute) from lighter molecules (e.g. solvent) and creates high concentration zones where nucleation is highly promoted (Louisnard et al., 2007). The envisaged mechanism for improving nucleation is enhancement in transition frequencies of molecules to clusters in these high concentration zones. They claim that the thermodynamic effects of acoustic waves are negligible and can be overlooked.

In contrast to this hypothesis, there exists experimental evidence, e.g. (Mazhul, 1963; Yu et al., 2012), that the direct acoustic field in the absence of cavitation can enhance nucleation. As this hypothesis will be scrutinised in the coming chapters, the thorough review of this work will not be

undertaken here.

Regarding nucleation under non-isothermal conditions, Kashchiev (Kashchiev, 1982) and Oxtoby and Kashchiev (Oxtoby and Kashchiev, 1994) developed a model based on the generic form of the Gibbs model to calculate the nucleation work and the size of nuclei in a non-isothermal phase transformation process. Ford (Ford, 1996) derived a relationship for the temperature dependence of the nucleation work (including both volume and surface works) and the nuclei size based on the thermodynamics of small systems developed by Hill (Hill, 1962). This work which led to the second nucleation theorem was further elaborated and exploited to analyse several experimental results (Ford, 1996, 1997, 2001; Kashchiev, 2006). Ford in derived the second nucleation theorem using the generic Gibbs model and demonstrated its generality beyond the Gibbs model (Ford, 2001). Through these derivations, Ford also derived the pressure dependence of the nucleation work in a generic format.

Ford's results showed that the Gibbs model in its generic format can provide a surprisingly good estimate of the thermodynamic properties of small nanoscopic clusters, and of the pressure and temperature dependence of the nucleation work, when compared with the results obtained by the thermodynamics of small systems (Hill, 1962; Ford, 1996). Hill's method uses statistical mechanics to determine the thermodynamic properties of small systems including clusters and colloidal particles. The key concept in Hill's approach is that the differential and integral forms of some intensive thermodynamic quantities are different in the limit of small systems. However, this difference vanishes in the limit of large (macroscopic) systems and therefore Hill's thermodynamics converges to the ordinary thermodynamics. The detailed discussion of Hill's thermodynamics is beyond the scope of the work in this thesis and the reader is referred to (Hill, 1962) or for a simpler representation (Ford, 1996).

Saclier et al. (Saclier et al., 2010), and Cogné et al. (Cogné et al., 2015, 2016) studied the influence of pressure and temperature oscillations around a collapsing bubble stimulated by ultrasonic waves, on the nucleation work and

the rate of ice formation. Instead of using the second nucleation theorem, they incorporated the effects of variable pressure and temperature into CNT as follows: i) the classical Clausius-Clapeyron equation was used to determine the pressure dependent melting enthalpy, ii) a set of empirical equations was used to interpolate melting temperature at different pressure magnitudes, and iii) likewise, the temperature and pressure dependence of density and surface tension were accounted for using empirical equations. This method is material dependent as it uses empirical relationships and suffers from the shortcomings of CNT; namely the premise of stationary kinetics for a physically unsteady system.

The problem of non-stationary nucleation in a system with time varying temperature was studied by solving the Becker-Döring (BD) master equation (Koek and Chvoj, 1983; Kožíšek, 1990). They showed that both the nucleation rate and the concentration of supercritical clusters are higher/lower compared to the quasi-stationary values for different heating/cooling rates.

The cluster dynamics in either discrete (e.g. the BD model) or continuous format (e.g. the Fokker-Planck equation (FPE)) has been successfully used to determine the kinetics of nucleation in time variable and unsteady situations (Kashchiev, 1969b; Kozísek and Demo, 1993; Kožíšek et al., 2004; Holten and van Dongen, 2009; van Putten and Kalikmanov, 2009). The cluster dynamics is determined by means of aggregative and non-aggregative mechanisms (Kashchiev, 2000). Aggregative mechanisms include nucleation, growth, and ageing, that give rise to the flux of the cluster concentration along the size axis. The non-aggregative mechanism accounts for change in the concentration of clusters driven by mass flux along the space parameter axis. These two fluxes together determine the cluster distribution over time.

An alternative approach for modelling the kinetics of nucleation and growth, is to employ a population balance equation; e.g. the general dynamic equation (GDE) (Holten and van Dongen, 2009; Vetter et al., 2013). The main differences between the GDE and the cluster dynamics are as follows: (Holten

and van Dongen, 2009; van Putten and Kalikmanov, 2009; Vetter et al., 2013) i) the GDE does not provide any information about the kinetics of subcritical clusters, ii) it uses a deterministic growth model and hence the stochastic effects are ignored, and iii) it does not account for phenomena like the Ostwald ripening. Nonetheless, the GDE has been modified to address some of these shortcomings.

Comparing the GDE with the cluster dynamics, i.e. the BD model or the FPE, the latter shows the advantage of correctly describing nucleation and growth simultaneously. Cluster dynamics is regarded to provide a rigorous description of the kinetics of a system with nucleation (Kožíšek et al., 2004; Chesnokov and Krasnoperov, 2007).

1.5 Aims and objectives

1.5.1 Problem statement

Crystallisation in a supersaturated solution exposed to an acoustic field is a complex problem at the interface of several disciplines. Sonocrystallisation is an inherently non-stationary process with time variable thermodynamic states. Depending on the excitation parameters and solution properties, various effects have been experimentally observed. However, the interaction between a sound field and the phase transition in a solution has been little studied theoretically. This lack of theoretical knowledge has hindered the controllability of sonocrystallisation and hence releasing its considerable potentials for industrial applications.

1.5.2 Research objectives and contributions

This work aims to achieve a deeper insight into the interaction between an acoustic field and the crystallisation process. The main objectives are to understand the physics of the process and identify the mechanisms through which sonication influences crystallisation. We set our aims as follows: i) to develop a model that can describe the thermodynamics of phase transition for small clusters. The preceding discussion proved this to be important as the size of

the critical cluster reduces with an increase in the intensity of the acoustic field, and ii) to identify and model the effects of acoustic waves on the aggregative and non-aggregative mechanisms of the kinetics of sonocrystallisation.

The preceding discussion revealed that the generic form of the Gibbs droplet model and cluster dynamics can successfully determine the thermodynamics and kinetics of nucleation and growth of (even nanoscopic) clusters in a non-stationary system. Consequently, the following objectives are defined

(i) develop a cluster model based on the Gibbs droplet model to adequately predict the properties of a cluster in the limit of small clusters,

(ii) identify and determine the effects of fluctuation in temperature, pressure and supersaturation ratio on the thermodynamics of cluster formation for both critical and non-critical clusters,

(iii) determine the kinetics of cluster formation, using cluster dynamics equation, for the developed cluster model in a mass conserved system,

(iv) consider a non-mass conserved system and incorporate the effect of mass transportation into the thermodynamics, i.e. nucleation with variable supersaturation ratio, and the kinetics of cluster formation,

(v) validate the developments qualitatively and quantitatively, where possible, against available experimental data.

1.6 Thesis structure

In this chapter, we presented an overview of the sonocrystallisation process, reviews of the experimental and theoretical achievements in this field, the statement of the problem to be investigated, and the research objectives. The thesis is divided into three parts, namely: thermodynamics of nucleation, kinetics of nucleation, and simulation results. In Chapter 2 we will discuss the Gibbs droplet model and develop a new cluster model. The work of cluster formation will be determined for critical and non-critical clusters. We will

compute the effect of fluctuation in the thermodynamic state of the old phase on the work of clustering in Chapter 3. These two chapters will construct the *thermodynamics of nucleation* part of the thesis. We will then proceed to Chapter 4, which describes the kinetics of nucleation in a mass-conserved system using the thermodynamic model constructed in the first two chapters. This chapter will be followed by studying the kinetics of cluster formation in a non-mass conserved system by incorporating the effect of mass transportation in a sound field into the kinetics equation, presented in Chapter 5. Chapters 4 and 5 will make the second part of the thesis; *kinetics of nucleation*. Validation of the developed cluster model against experimental water nucleation data will be presented in Chapter 6. Finally, we will discuss the numerical simulation results of sonocrystallisation in a generic aqueous solution in Chapter 7 and attempt to explain qualitatively some experimental trends. Finally, Chapter 8 will present the conclusions from this thesis work followed by a discussion of areas for future work.

Chapter 2

Thermodynamics of cluster formation I: Silent condition

In this chapter, we will study the thermodynamics of phase transformation based on the Gibbs droplet model with an arbitrary dividing surface. We will take this model to determine: i) the work of cluster formation for both critical and non-critical clusters, and ii) the size of critical clusters, see Sections 2.4 and 2.5.

The Gibbs droplet model is usually simplified by considering the equimolar dividing surface (EDS) or the surface of tension with the capillarity approximation which results in a conventional form of CNT. The EDS clusters are identified by zeroing the surface concentration. The capillarity approximation assumes that the surface tension of an n-size cluster is equal to the planar surface tension. This approximation has contributed to the inability of CNT in explaining some experimental results (Ford, 1997). It has been shown that by choosing a size-dependent surface tension model, a better agreement with some experiments can be achieved. Nevertheless, these equations are useful for larger clusters but are expected to break down for small clusters. We will show in the next chapter that this issue becomes more significant in the case of sonocrystallisation as the critical cluster size typically decreases as the pressure magnitude increases. Therefore, we opt not to employ the EDS or the surface of tension in this work. Instead, we have developed a new model by defining a

new dividing surface (DS) and estimating its associated size and surface tension in Section 2.3. Finally, we will look at some properties of clusters defined by this new DS.

2.1 Model of cluster formation

Mechanical work is required to convert the homogeneous old phase into a metastable state and start the formation of a new phase. The new phase is a density fluctuation which appears within the old phase and makes the entire system heterogeneous. Based on classical thermodynamics, the coexistence between two distinct phases, separated by a flat surface, happens if the chemical potential and pressure of the two phases are equal. Under this condition, the new phase is in an unstable equilibrium with the old phase. The free energy required to create such a density fluctuation is called the nucleation work. The new phase can then grow spontaneously and form a stable particle when it randomly absorbs molecules. Therefore, it is of crucial importance in the physics of phase transformation to determine the nucleation work.

To this purpose, it is required to describe the density fluctuation in the old phase, and to determine its growth over time. The two main approaches to describe this density variation within the old phase are the cluster method and the density functional theory (DFT) (Kashchiev, 2000). The former approach was established by Volmer 1926 (Volmer and Weber, 1926) and Gibbs 1928 (Gibbs, 1928). Whilst it remains the cornerstone of nucleation theories and CNT, it suffers from some shortcomings which will be further discussed in the following. However, the DFT is more recent (Cahn and Hilliard, 1959) and overcomes the inconsistencies associated with the cluster representation of the density fluctuation. Nevertheless, the implementation of the DFT method requires the knowledge of interaction potentials between molecules and subsequently the molecular model of the system ought to be known. As we aim to stay within the realm of continuum mechanics and thermodynamics, the cluster formalism and the Gibbs droplet model will be used to analyse the

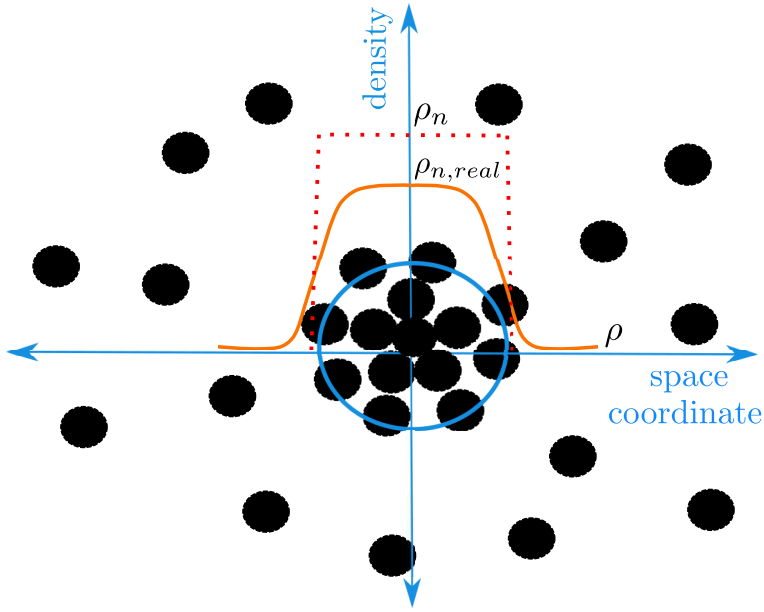

Figure 2.1: Density fluctuation in the old phase described by the cluster and DFT approaches. The vertical dashed lines show the abrupt change in the spatial density at an arbitrary location of the dividing surface. Refer to the text for details.

nucleation process. Albeit, we will employ the Gibbs model in its generic form and develop an improved model of nucleation.

Gibbs used a zero volume arbitrary dividing surface to split the heterogeneous system into two homogeneous subsystems of the old and new phases. Hereafter, a Gibbs geometrical dividing surface will be referred to as DS. The chemical potential of the macroscopic subsystem including the old phase is equal to the chemical potential of the original state of the system prior to the formation of the density fluctuation. We will show that this also leads to equal pressures. The nanoscopic subsystem of the new phase is assumed to possess a uniform pressure and density with the physicochemical properties of the bulk new phase. This nanoscopic subsystem identified by the DS is called a cluster. It should be noted that representing the density fluctuation by a cluster of molecules is hypothetical and differs from the real physical density fluctuation. Moreover, assigning the bulk density to a cluster of molecules is arguable, in particular, for small clusters. In spite of this, the simplicity of the cluster formalism and its overall success in explaining some experimental

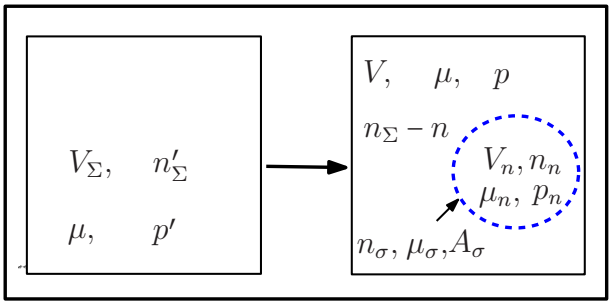

Figure 2.2: Cluster formation in a system with constant volume, temperature and chemical potential. Refer to the text for details.

observations have led to its widespread use and made it a basis for further developments in this field.

The DS is a smart mathematical notion which Gibbs introduced to derive a general and exact formulation of the thermodynamics of phase transformation. Nevertheless, the Gibbs method is unable to give a realistic and physical representation of the spatial density fluctuation, see Fig. 2.1.

Thermodynamically, we model the DS as an interface phase between the new phase inside the cluster surface and the old phase surrounding the DS. Therefore, the system includes three phases after cluster formation, namely the core of the cluster taking the new phase, the old phase surrounding the new phase and the interface phase. The properties of the old phase are displayed below with no suffix whereas the suffices n and σ label the new and interface phases, respectively.

We consider the whole system, represented by Σ, as a volume element coupled to a heat and particle bath. The phase change takes place within this system. The choice of heat and particle bath essentially means that temperature and volume of the system remain constant and the old phase in the system has the same chemical potential as that of the bath. This set of constraints is usually experimentally favoured and will be adopted in the following analysis. Figure 2.2 shows the system in two different states: the initial state in the absence of a cluster, denoted by the prime superscript; and after formation of a cluster where three phases are present. The energy of the system at the

initial state reads (Guggenheim, 1985; Abraham, 1974)

$$U'_\Sigma = TS'_\Sigma - p'V_\Sigma + \mu n'_\Sigma, \tag{2.1}$$

where S'_Σ, p', and n'_Σ are entropy, pressure and the size of the old phase at the initial state, respectively. T, V_Σ, and μ are the temperature, volume, and chemical potential of the system, respectively. These quantities remain constant as we assumed that the system is coupled to a heat and particle bath. At the final state where the system consists of three phases; energy, volume, entropy and size, i.e. number of molecules, are extensive properties of the system and thus we have (Guggenheim, 1985; Abraham, 1974)

$$\begin{aligned} U_\Sigma &= U + U_n + U_\sigma \\ S_\Sigma &= S + S_n + S_\sigma \\ V_\Sigma &= V + V_n + V_\sigma. \end{aligned} \tag{2.2}$$

Likewise, the number of molecules in the old phase after cluster formation is equal to $n_\Sigma - n_n - n_\sigma = n_\Sigma - n$ where n is the total size of the cluster, i.e. $n = n_n + n_\sigma$, see Fig. 2.2. The energy of the old and new phases is obtained using equations similar to Eq. (2.1) but evaluated at their corresponding properties. However, the energy of the interface phase will include an additional term accounting for the excess energy required to balance the interfacial tension of the dividing surface and reads (Guggenheim, 1985)

$$U_\sigma = TS_\sigma - p_\sigma V_\sigma + \mu_\sigma n_\sigma + \Omega_\sigma, \tag{2.3}$$

where Ω_σ is the grand potential associated with the interface phase. Thus, adding up the energy of all subsystems gives (Guggenheim, 1985; Abraham, 1974)

$$\begin{aligned} U_\Sigma &= U + U_n + U_\sigma = TS - pV + \mu\left(n_\Sigma - n_n - n_\sigma\right) \\ &\quad + TS_n - p_nV_n + \mu_n n_n + TS_\sigma + \mu_\sigma n_\sigma - p_\sigma V_\sigma + \Omega_\sigma, \end{aligned} \tag{2.4}$$

Ω_σ is also represented by $A_\sigma\gamma$ where A_σ is the interfacial surface area and γ is the specific surface energy which has been referred to with different terms, e.g. the interfacial tension by Guggenheim (Guggenheim, 1985) or the superficial intensive parameter by Abraham (Abraham, 1974) or surface tension by Gibbs (Gibbs, 1928). In this work, we will use the term surface tension to address the parameter γ although this term somewhat lacks generality, as we will discuss further below. Regardless of the terminology, the surface tension is defined to make the free energy of the interface phase independent of the location of the dividing surface (Ford, 1996). It is hence a function of the cluster size, temperature and chemical potential of the interface phase.

In Eq. (2.4), we modelled the interface phase as a layer with volume V_σ; however, this term vanishes in the case of a Gibbs DS. Moreover, we can plausibly postulate that the composition of the old phase stays constant during the phase transformation(Abraham, 1974; Kashchiev, 2000). Writing the Gibbs-Duhem relation for the old phase yields

$$-\nu dp + d\mu = 0 \quad \xrightarrow{\mu=const.} \quad \nu dp = 0 \quad \Longrightarrow \quad p = p', \tag{2.5}$$

where ν is the specific volume of the old phase. Therefore, pressure of the old phase remains unchanged through the phase transformation process.

Utilising the cluster model and the fundamental thermodynamics equations 2.1-2.5, the thermodynamics of the phase change can be studied. We will continue this chapter by studying different dividing surfaces and will propose a new cluster model. Subsequently, we will determine the work of cluster

formation for different types of clusters.

2.2 Dividing surface

The interface phase separates the new and old phases and divides up a heterogeneous system into two homogeneous subsystems with different physical properties. In van der Waals treatment of an interface phase, the surface layer is assumed to be a layer with well-defined volume, material content and thermodynamic properties (Guggenheim, 1985). Using Eq. (2.3), the Helmholtz free energy of a single species interface phase reads

$$F_\sigma = U_\sigma - TS_\sigma = -p_\sigma V_\sigma + n_\sigma \mu_\sigma + \Omega_\sigma. \tag{2.6}$$

Defining the boundary of an interface layer and subsequently identifying its physical properties are challenging. Gibbs introduced a geometrical surface with $V_\sigma = 0$ and allowed n_σ to take negative values as well, to account for this simplification in the calculation of Helmholtz free energy of the interface phase. Thus, the Helmholtz free energy of an interface phase defined by a Gibbs surface is given by

$$F_\sigma = n_\sigma \mu_\sigma + \Omega_\sigma. \tag{2.7}$$

In the Gibbs model, the free energy of the surface, i.e. given by Eq. (2.7), is independent of the location of the DS (Ford, 1996) but surface tension γ changes accordingly. In the simplest scenario, the DS can be positioned such that $n_\sigma = 0$. This particular surface is called the EDS and has the Helmholtz free energy of $F_\sigma = \Omega_\sigma = A_\sigma \gamma$ (Kashchiev, 2000). This is a common choice of the DS which together with the capillarity approximation form the conventional format of CNT. The correct value of the interfacial Helmholtz free energy can be obtained if the size, temperature and chemical potential dependence of γ is known.

Gibbs introduced and used a specific DS called the surface of tension (Gibbs, 1928). Assuming a spherical cluster with a zero volume interface

layer, and therefore no rigidity, the surface of tension is placed at a location that satisfies the mechanical equilibrium condition between the two phases surrounding it, given by the Laplace equation

$$p_n - p = \frac{2\gamma^t}{R_n^t}. \tag{2.8}$$

Here γ^t is the surface tension of the surface of tension, and R_n^t is the radius of the cluster defined by the surface of tension. Gibbs used this DS and derived the exact equation for the nucleation work.

The main difficulties associated with the EDS and the surface of tension pertain to the unknown size dependency of the surface tension. In practice, the capillarity approximation is usually exercised, which assumes $\gamma(n) = \gamma_\infty$ where γ_∞ is the planar surface tension between two phases in equilibrium and is therefore constant. The choice of EDS and the capillarity assumption which is often made in the conventional form of CNT trades the accurate calculation of the interfacial Helmholtz free energy with simplicity in implementation. This approximation is limited to the equilibrium condition and rather large clusters but deviates from the real free energy of the interface for small clusters of few molecules or the non-equilibrium condition as demonstrated by the DFT and molecular dynamics (MD) simulations (Lau et al., 2015b; Talanquer and Oxtoby, 1995). Gibbs developed an equation to estimate the size-dependent surface tension (Gibbs, 1928) which was taken and further expanded by Tolman (Tolman, 1949). The formula of Tolman reads

$$\gamma^t(n) = \frac{\gamma_\infty}{1 + \dfrac{2\delta_t}{R_n^t}}, \tag{2.9}$$

where δ_t is the unknown Tolman length, i.e. the distance between the surface of tension and the EDS. Several methods have been developed to determine the Tolman length (Samsonov et al., 2003; Kashchiev, 2003b) and improvements on Tolman's formula were also suggested using higher order polynomial functions (Helfrich, 1973; Holten et al., 2005). The MD or DFT simulations are usually

required to determine an appropriate Tolman length. Nevertheless, the Tolman equation is useful for larger clusters but is expected to break down for small clusters.

Recently Kashchiev introduced a new DS called the conservative surface, which is characterised by the size-independent surface tension $\frac{\partial\gamma(n)}{\partial n} = 0$ (Kashchiev, 2003a). This condition leads to $\gamma(n) = \gamma_\infty$ for all clusters defined by this DS. An approximate formula for finding the location of this conservative DS was suggested in that study, despite its justification being criticised by others (Schmelzer and Baidakov, 2004). However, the idea of identifying a DS which is characterised by the size-independent surface tension is appealing, as it removes some complexity in calculation of the thermodynamics and kinetics of cluster formations. In this thesis, this concept will be employed for the specification of clusters and will be further explained in the following section.

2.3 The new cluster model

2.3.1 The new surface

Now, we specify the dividing surface and associated surface tension which will be used in this work. A suitable DS is a surface which can more precisely approximate the excess free energy. An accurate estimation of the excess free energy of the surface requires the knowledge of the size of the interface phase n_σ and the size-dependent surface tension $\gamma(n)$, see F_σ in Eq. (2.7). The former is zero for the EDS but ought to be determined for any non-EDS surface. This will be addressed in Section 2.3.2.

As we have discussed before, finding $\gamma(n)$ requires a suitable model of the size-dependent surface tension, e.g. the Tolman equation or other polynomial expansion models. In the case of the sonocrystallisation process, a model which is valid for very small clusters is needed: we will show that the critical cluster size (for a condensed new phase with $\Delta n_{exc} > 0$) decreases as the pressure magnitude increases. Therefore, we opt not to employ the EDS or the surface of tension in this work. Instead, we considered a new dividing surface which is

identified as follows: 1) this surface has the size-independent surface tension of γ_∞, and 2) the surface is positioned such that we obtain a reference excess free surface energy. The former condition leads to $\gamma(n) = \gamma_\infty$ and consequently $\Omega_\sigma = A_\sigma \gamma_\infty$ for a spherical cluster. We denote this surface as the new surface in this work.

The mathematical definition of the new surface is similar to that of the conservative surface of Kashchiev, i.e. $\frac{\partial \gamma(n)}{\partial n} = 0$. However, the method for finding the location of the DS is different. We will evaluate the effective surface tension for the new surface and compare the results with statistical mechanics simulations or the effective surface tension retrieved from experimental data to determine the position of the surface (the equations will be presented in Section 2.4.2). This ensures that an accurate approximation of the excess free energy of the cluster is achieved. Kashchiev, however, proposes a linear interpolation between the size of critical clusters at spinodal and at the present state of the system. This formula therefore generates exact values for critical clusters at two extremes but not necessarily for other non-critical clusters. This approximation has been shown to fail in some circumstances (Schmelzer and Baidakov, 2004) and therefore was avoided here.

All the former cluster models share the concept of defining a cluster only by its volume. To the best of our knowledge, no model is available or used in the literature to determine n_σ for an arbitrary DS. However, in order to determine thermodynamics of the interface phase in non-EDS clusters, we need to have a suitable approximation of n_σ depending on the type of the DS in place. This becomes more important when we study clusters of few molecules as the notion of the condensed core with bulk properties does not hold for such clusters (Ford, 2001; Kalikmanov, 2012). We developed a new model to determine n_σ for any arbitrary DS which is presented in the next section.

2.3.2 Number of surface molecules

At the final state of the system which contains a new cluster within the old phase, we can write (Guggenheim, 1985)

$$n_\Sigma = \rho_n V_n + \rho V + n_\sigma = \rho_n V_n + \rho(V_\Sigma - V_n) + n_\sigma, \tag{2.10}$$

where ρ_n and ρ are the molecular number density of the new and old phases, respectively, see Fig. 2.2. This equation can be re-arranged to give

$$n_\Sigma - \rho V_\Sigma = (\rho_n - \rho)V_n + n_\sigma, \tag{2.11}$$

where the left hand side (LHS) is invariant with respect to the choice of the dividing surface. If we choose the EDS, we will have by definition $n_\sigma = 0$ and therefore LHS $= (\rho_n - \rho)V_n^e$ where V_n^e is the volume of a cluster defined using the EDS. Given the LHS is invariant with the choice of the surface, the equation for an arbitrary surface becomes LHS $= (\rho_n - \rho)V_n^e = (\rho_n - \rho)V_n + n_\sigma$ which yields

$$n_\sigma = (\rho_n - \rho)(V_n^e - V_n), \tag{2.12}$$

and substituting $V_n = n_n\nu_n = \frac{n_n}{\rho_n}$ and $V_n^e = n_e\nu_n = \frac{n_e}{\rho_n}$ where n_e is the size of an EDS-defined cluster and V_n is the specific volume of a molecule in the new phase, this equation simplifies to

$$n_\sigma = (1 - \frac{\rho}{\rho_n})(n_e - n_n) = k_\rho(n_e - n_n), \tag{2.13}$$

where $k_\rho = 1 - \frac{\rho}{\rho_n}$. This is a generic equation and is valid for any shape of cluster. We can write

$$k_\rho n_e = k_\rho n_n + n_\sigma = \Delta n_{exc}, \tag{2.14}$$

where Δn_{exc} is the excess number of molecules in the cluster of volume V_n comparing to the same volume of old phase. This quantity is independent of

the choice of dividing surface. In the case of a condensed new phase we have $k_\rho > 0$ and consequently $\Delta n_{exc} > 0$. However, when the new phase is less dense than the old phase, e.g. bubble formation, k_ρ and Δn_{exc} become negative.

Now, explicit equations that completely specify a cluster of a given size for any arbitrary DS must be obtained. To this end, Eq. (2.12) for a spherical cluster reads

$$\begin{aligned} n_\sigma &= (\rho_n - \rho)(V_n^e - V_n) = \frac{4\pi}{3}(\rho_n - \rho)(R_n^{e\,3} - R_n^3) \\ &= \frac{4\pi}{3}(\rho_n - \rho)(R_n^e - R_n)(R_n^{e\,2} + R_n R_n^e + R_n^2), \end{aligned} \tag{2.15}$$

where R_n^e is the radius of a cluster defined by the EDS. Considering $\delta = R_n^e - R_n$ which is the radial separation between the EDS and the arbitrary surface, it follows

$$\begin{aligned} n_\sigma &= \frac{4\pi}{3}(\rho_n - \rho)\delta(R_n^{e\,2} + R_n^{e\,2} - R_n^e\delta + R_n^{e\,2} + \delta^2 - 2R_n^e\delta) \\ &= \frac{4\pi}{3}\delta(\rho_n - \rho)(3R_n^{e\,2} - 3R_n^e\delta + \delta^2). \end{aligned} \tag{2.16}$$

Substituting $R_n^e = \left(\frac{3\nu_n}{4\pi}\right)^{1/3} n_e^{1/3} = R_0 n_e^{1/3}$, where $R_0 = \left(\frac{3\nu_n}{4\pi}\right)^{1/3}$ is the radius of a molecule [1] in the new phase, in the above equation yields

$$n_\sigma = 4\pi R_0^2\delta(\rho_n - \rho)\left(n_e^{2/3} - \frac{\delta}{R_0}n_e^{1/3} + \frac{\delta^2}{3R_0^2}\right) = k_\sigma\left(n_e^\beta - \frac{\delta}{R_0}n_e^{1-\beta} + \frac{\delta^2}{3R_0^2}\right), \tag{2.17}$$

where $k_\sigma = 4\pi R_0^2\delta(\rho_n - \rho)$ and $\beta = 2/3$. Given that $R_0 = \left(\frac{3\nu_n}{4\pi}\right)^{1/3}$ and $\rho_n\nu_n = 1$, we can write k_σ as follows $k_\sigma = k_\rho 3\lambda$ where $\lambda = \frac{\delta}{R_0}$ is a dimensionless quantity that distinguishes an arbitrary dividing surface from the EDS.

[1] a molecule is considered to be a sphere with radius R_0 obtained from the effective molecular volume using the equation shown above.

Considering a cubic cluster of length l_e, we have $V_n^e = l_e^3 = n_e \nu_n$. Inserting this into Eq. (2.12) and after some algebra we arrive at

$$n_\sigma = k_\sigma \left(n_e^\beta - \frac{\lambda}{S_f} n_e^{1-\beta} + \frac{\lambda^2}{3S_f^2} \right), \tag{2.18}$$

where $k_\sigma = \frac{1}{S_f} k_\rho 3\lambda$, and $S_f = \left(\frac{4\pi}{3}\right)^{1/3}$ is the shape factor and $\beta = 2/3$. Therefore we can use the formula in the form of Eq. (2.18) for both spherical and cubic clusters with shape factors of $S_f = 1$ and $S_f = \left(\frac{4\pi}{3}\right)^{1/3}$, respectively.

Having determined the number of excess molecules and utilising Eq. (2.14), the number of molecules in the new phase is obtained by

$$n_n = n_e - \frac{n_\sigma}{k_\rho} = n_e - \frac{3\lambda}{S_f} \left(n_e^\beta - \frac{\lambda}{S_f} n_e^{1-\beta} + \frac{\lambda^2}{3S_f^2} \right). \tag{2.19}$$

Therefore, in general we can write

$$n_\sigma(n_e) = k_\rho \mathcal{F}(n_e), \tag{2.20}$$

$$n_n(n_e) = n_e - \mathcal{F}(n_e), \tag{2.21}$$

where

$$\mathcal{F}(n_e) = \frac{3\lambda}{S_f} \left(n_e^\beta - \frac{\lambda}{S_f} n_e^{1-\beta} + \frac{\lambda^2}{3S_f^2} \right). \tag{2.22}$$

If $\lambda \ll 1$, i.e. $\delta \ll R_0$, the number of molecules in the interface and new phase can be approximated by the second order error ($\mathcal{O}(\lambda^2)$) as follows

$$n_\sigma(n_e) = k_\rho \frac{3\lambda}{S_f} n_e^\beta + \mathcal{O}(\lambda^2), \tag{2.23}$$

$$n_n(n_e) = n_e - \frac{3\lambda}{S_f} n_e^\beta + \mathcal{O}(\lambda^2). \tag{2.24}$$

These equations give n_n and n_σ as a function of n_e which is the size of an EDS-defined cluster. We are, however, interested in determining these quantities

and the size of a cluster as a function of either the core size or the number of molecules in the interface. In this regard, we start with Eq. (2.19) and solve it for n_e while employing $\beta = 2/3$ as follows

$$n_n = n_e - \frac{3\lambda}{S_f}\left(n_e^{2/3} - \frac{\lambda}{S_f}n_e^{1/3} + \frac{\lambda^2}{3S_f^2}\right) = \left(n_e^{1/3} - \frac{\lambda}{S_f}\right)^3, \tag{2.25}$$

which gives

$$n_e = \left(n_n^{1/3} + \frac{\lambda}{S_f}\right)^3, \tag{2.26}$$

by substituting this relationship in Eq. (2.18), we obtain n_σ and the cluster size in the following format

$$\begin{aligned} n_\sigma(n_n) &= k_\rho \mathcal{G}(n_n), \\ n(n_n) &= n_n + n_\sigma(n_n) = n_n + k_\rho \mathcal{G}(n_n), \end{aligned} \tag{2.27}$$

where

$$\mathcal{G}(n_n) = \frac{3\lambda}{S_f}\left(n_n^{2/3} + \frac{\lambda}{S_f}n_n^{1/3} + \frac{\lambda^2}{3S_f^2}\right). \tag{2.28}$$

Henceforth, we assume the cluster is spherical and therefore $S_f = 1$. Depending on the density of the new and old phases and the location of the dividing surface, n_σ can become positive or negative. For the case of a condensed new phase, i.e. $k_\rho > 0$, if the dividing surface is placed beyond the EDS; this gives $\lambda < 0$ and subsequently $\mathcal{G}(n_n) < 0$. On the other hand, if the arbitrary dividing surface is enclosed in the EDS, we have $\lambda > 0, \mathcal{G}(n_n) > 0$.

Finally, this model satisfies the following conditions

$$\lim_{n\to\infty} \frac{n_\sigma}{n} = 0 \qquad , \qquad \lim_{n\to\infty} \frac{n_n}{n} = 1. \tag{2.29}$$

These conditions imply that for large clusters the number of molecules in the core becomes dominant and the EDS becomes acceptable for defining the boundary of a cluster. However, for a small cluster for which a core with bulk properties does not exist, the contribution of interface phase takes on an important role which can be modelled through interface terms with non-zero n_σ (or λ in our model).

If the arbitrary surface is selected such that it coincides with the surface of tension, then $R_n = R_n^t$ and in the limits of $R_n^t \to \infty$ the separation length converges to the Tolman length $\delta \to \delta_t$ and subsequently $\lambda \to \lambda_t = \frac{\delta_t}{R_0}$.

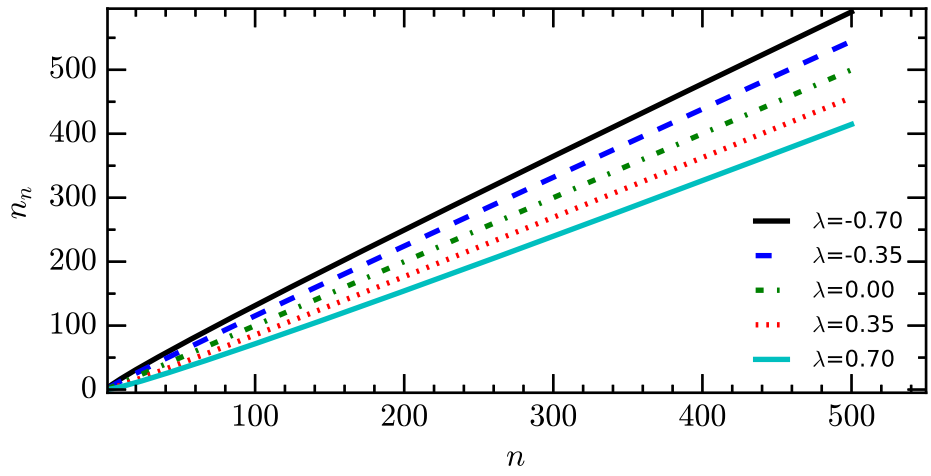

(a)

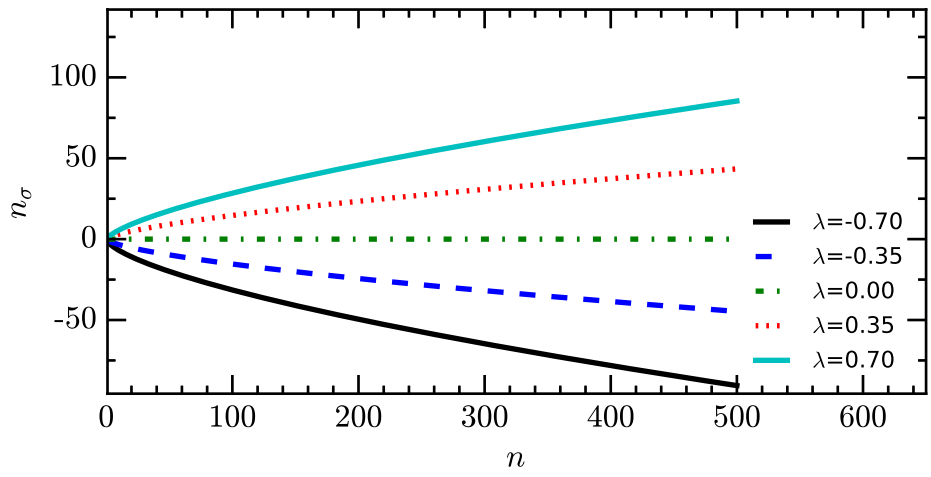

(b)

Figure 2.3: (a) Size of the new phase (n_n), and (b) the interface phase (n_σ) at different location of the DS obtained by solving Eq. (2.27).

Figure 2.3 shows the size of the new and interface phases for different values of λ. The value of $k_\rho = 0.66$ was used for these calculations. The material properties used for simulations presented in this chapter are listed in Table A.1 in Appendix A and all simulations are carried out at $T = 293$ K.

Since k_ρ is positive a DS within the EDS (which gives a positive λ) results in positive n_σ whereas placing the DS beyond the EDS gives negative values for the interface phase size. Furthermore, we can see that the larger the cluster size n, the larger the new phase size n_n compared to the interface size n_σ which in limit fulfills the relationships shown in Eq. (2.29).

In summary, the equations required to estimate the size of the new and interface phases for any arbitrary DS were derived in this section. Now, we can use this model to completely define a cluster of given size identified by any arbitrary DS and calculate the thermodynamics of phase transformation from a metastable old phase.

2.3.3 Cluster size and volume

The Gibbs geometrical surface is characterised by $V_\sigma = 0$ while allowing n_σ to take a negative value. This results in $V_c = V_n = n_n \nu_n$, where V_c is the cluster volume, and the cluster size $n = n_n + n_\sigma$. Therefore, the mass of the cluster becomes $m = n m_0$, where m_0 is the mass of a monomer in the new phase. Since different number of molecules are used to determine the mass and volume of the cluster, n and n_n respectively, the effective density of the cluster will be different from the bulk density of the new phase. The effective density is obtained by

$$\begin{aligned} \rho_{c,\text{eff}} &= \frac{m}{V_c} = \frac{n m_0}{n_n \nu_n} = \frac{n}{n_n}\frac{m_0}{\nu_n} = \left(1 + \frac{n_\sigma}{n_n}\right) m_0 \rho_n \\ &= \left(1 + \frac{n_\sigma}{n_n}\right) \rho_c, \end{aligned} \tag{2.30}$$

where ρ_c is the bulk mass density of the new phase. We surmised that the physiochemical properties of the new phase, i.e. ν_n and m_0, are equal to their

corresponding bulk values. Likewise, the effective number density of the cluster reads

$$\rho_{n,\text{eff}} = \frac{n}{V_c} = \frac{n}{n_n \nu_n} = \frac{n}{n_n}\rho_n = \left(1 + \frac{n_\sigma}{n_n}\right)\rho_n. \tag{2.31}$$

Depending on the sign of n_σ, the effective density of a cluster can be higher or lower than the bulk density of the new phase. This is more noticeable for small clusters since for large clusters we have $\lim_{n\to\infty} \frac{n_\sigma}{n_n} = 0$, see Eq. (2.29). When the new phase is denser than the old phase, i.e. k_ρ is positive, a positive λ gives a positive n_σ and vice versa, see Section 2.3.2 and Fig. 2.3. Therefore, a positive λ for a denser new phase results in clusters with higher effective density than the bulk new phase density.

Figure 2.4 shows the ratio of the effective to the bulk density for different positions of the DS. We can see that the density of the EDS clusters are size-independent, in contrast to the simulation results of statistical mechanics (Lau et al., 2015a; Factorovich et al., 2014; Angélil et al., 2014, 2015; Malijevsky and Jackson, 2012). However, the non-EDS clusters show a size-dependent trend which is in qualitative agreement with statistical mechanics simulations. Moreover, this figure shows that at a positive λ, the smaller the clusters, the higher their density. As is shown in the inset of this figure, we can infer that

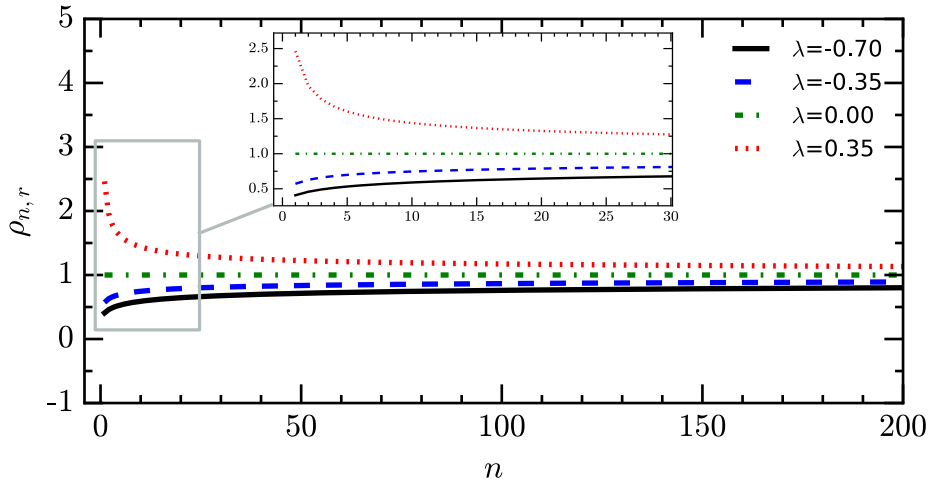

Figure 2.4: Ratio of $\rho_{n,\text{eff}}$ to ρ_n for different locations of the DS. The dot-dashed line represents this ratio for the EDS cluster ($\lambda = 0$).

n_σ is larger than n_n for small clusters when λ is positive. Therefore, in small clusters of a condensed phase, the majority of molecules may accumulate on the interface than inside the volume of the new phase. This deduction is in general agreement with the simulation results of statistical mechanics manifesting an inhomogeneous small water droplet (with $n = 9$) with a denser interface (Factorovich et al., 2014). This demonstrates that the non-EDS cluster may provide a representation of the agglomerate which is in a better agreement with the simulation results obtained by means of statistical mechanics. The dividing surface is the unphysical element of the Gibbs model. Therefore, the validity of calculating the density of a cluster and making comparison with statistical mechanics results may seem questionable. We should remark that the objective of this comparison in the preceding discussion was only to illustrate that non-EDS clusters can represent the new phase more realistically compared with EDS-defined clusters, despite the mentioned feature of the Gibbs model.

2.4 Work of cluster formation

The reversible work of creating a cluster is equal to the change in the thermodynamic potential of the system at its initial and final states (Abraham, 1974). For the system shown in Fig. 2.2 and considering the imposed constraints of constant V_Σ, T, and μ, the grand potential $\Omega = U - TS - \mu n = F - \mu n$ is the suitable thermodynamic potential (Reiss, 1965; Ford, 2001; Vehkamaki, 2006) and therefore the work of formation is written $\Delta\Omega = \Omega_\Sigma - \Omega'_\Sigma$. Here F is the Helmholtz free energy . For the initial state of the system, by using Eqs. (2.1) and (2.5) we can write

$$\Omega'_\Sigma = U'_\Sigma - TS'_\Sigma - \mu n'_\Sigma = -pV_\Sigma. \tag{2.32}$$

Similarly by using Eqs. (2.2) and (2.4) with a Gibbs DS, the grand potential in the final state becomes

$$\Omega_\Sigma = U_\Sigma - TS_\Sigma - \mu n_\Sigma = -pV + \mu(-n_n - n_\sigma) - p_n V_n + \mu_n n_n + \mu_\sigma n_\sigma + \Omega_\sigma. \quad (2.33)$$

The work of cluster formation is obtained by subtracting the last two equations as follows

$$\Delta\Omega = -pV + \mu(-n_n - n_\sigma) - p_n V_n + \mu_n n_n + \mu_\sigma n_\sigma + \Omega_\sigma + pV_\Sigma, \quad (2.34)$$

which simplifies to

$$\Delta\Omega = (p - p_n)V_n + n_n(\mu_n - \mu) + n_\sigma(\mu_\sigma - \mu) + \Omega_\sigma. \quad (2.35)$$

It should be noted that μ and μ_n are evaluated at temperature T and at pressures p and p_n, respectively. The chemical potential of the new phase at the pressure of the old phase can be determined by writing the Gibbs-Duhem relation for the new phase:

$$V_n dp_n = n_n d\mu_n, \quad (2.36)$$

and integrating this equation gives $\int_{p_n}^{p} V_n dp_n = n_n(\mu_n(p) - \mu_n(p_n))$ which rearranges to

$$n_n\mu_n(p_n) = n_n\mu_n(p) - \int_{p_n}^{p} V_n dp_n. \quad (2.37)$$

Substituting this into Eq. (2.35) yields

$$\begin{aligned}\Delta\Omega &= -n_n\Delta\mu(p,T,x) - n_\sigma\left(\mu-\mu_\sigma\right) + \left(p-p_n\right)V_n \\ &\quad - \int_{p_n}^{p} V_n dp_n + \Omega_\sigma,\end{aligned} \tag{2.38}$$

where $\Delta\mu(p,T,x)$ is difference in the chemical potentials of the old and new phases at temperature T, pressure p and composition x of the old phase and is given by

$$\Delta\mu(p,T,x) \;=\; \mu(p,T,x) \;-\; \mu_n(p,T). \tag{2.39}$$

For the sake of brevity of notation, independent variables, i.e. p, T, x, will not be displayed unless required. Nevertheless, we shall note that they may vary over time in the system and in time and space in the bath. Henceforth, μ_n is always evaluated at pressure p_n except in $\Delta\mu$ as shown in Eq. (2.39). In the case of a condensed new phase, the cluster can be considered practically incompressible. Thus, the work of formation of a condensed cluster becomes

$$\Delta\Omega \;=\; -n_n\Delta\mu \;-\; n_\sigma\left(\mu-\mu_\sigma\right) \;+\; \Omega_\sigma, \tag{2.40}$$

where substituting Ω_σ with $A_\sigma\gamma$ gives

$$\Delta\Omega \;=\; -n_n\Delta\mu \;-\; n_\sigma\left(\mu-\mu_\sigma\right) \;+\; A_\sigma\gamma. \tag{2.41}$$

Equations 2.40 and 2.41 are generic and valid for a condensed cluster of any size identified by any DS. To be able to use these equations, n_σ and μ_σ should also be determined for a generic dividing surface. A model to determine the former was explained in Section 2.3.2. The latter is discussed in the following sections for two different types of clusters, the critical clusters and non-critical clusters.

2.4.1 Critical cluster

The system at the final state contains three phases all of which are at the same temperature T but at different pressures. The system is in complete equilibrium if any infinitesimal change in it is reversible (Guggenheim, 1985). To derive the equilibrium conditions, or "features" as Reiss remarks, (Reiss, 1965) we need to estimate the increment in the grand potential of the system arising from an infinitesimal variation in the system variables

$$\begin{aligned} d\Omega_\Sigma \;=\; & -pdV \;-\; Vdp \;-\; d\mu\,(n_n + n_\sigma) \;-\; \mu\,(dn_n + dn_\sigma) \;-\; p_n dV_n \\ & -\; V_n dp_n \;+\; \mu_n dn_n \;+\; n_n d\mu_n \;+\; \mu_\sigma dn_\sigma \;+\; n_\sigma d\mu_\sigma \\ & +\; A_\sigma d\gamma \;+\; \gamma dA_\sigma. \end{aligned} \tag{2.42}$$

By virtue of Eq. (2.36), a similar Gibbs-Duhem relation for the old phase, and the Gibbs-Duhem relation of $n_\sigma d\mu_\sigma = -A_\sigma d\gamma$ together with the fact that $dV_\Sigma = dV + dV_n = 0$ and $d\mu = 0$ (thus $dp = 0$),[2] Eq. (2.42) simplifies to

$$d\Omega_\Sigma \;=\; \left[(p \;-\; p_n)\,dV_n \;+\; \gamma dA_\sigma\right] \;+\; (\mu_\sigma - \mu)\,dn_\sigma \;+\; (\mu_n - \mu)\,dn_n. \tag{2.43}$$

The first term, enclosed by a square bracket is equal to the total work w done on the system and the last two terms account for the openness of each phase within the system (Guggenheim, 1985; Reiss, 1965). The imposed isothermal change is natural if (Guggenheim, 1985)

$$d\Omega_\Sigma \;<\; w, \tag{2.44}$$

and reversible if $d\Omega_\Sigma = w$. From Eqs. (2.43) and (2.44), we obtain

[2] μ, T and V_Σ are the constrained variables of the system in the bath and are constant.

$$(\mu_\sigma - \mu)\, dn_\sigma \;+\; (\mu_n - \mu)\, dn_n < 0, \tag{2.45}$$

to have a natural isothermal change taking place in the system. Likewise, for the reversible change in the system we have equality instead of inequality: $(\mu_\sigma - \mu)\, dn_\sigma \;+\; (\mu_n - \mu)\, dn_n = 0$. Here n_σ and n_n are independent variables, [3] hence this equation yields

$$\mu \;=\; \mu_n(p_n) \;=\; \mu_\sigma, \tag{2.46}$$

for the reversible change happening in the system. This indicates the system and all the phases within it are in complete equilibrium if all the phases have the same chemical potential values.

A cluster which is in thermodynamic equilibrium with the old phase is called the critical cluster or nucleus. We will use an asterisk to denote the properties of such a cluster.

The generalized Laplace equation for the critical cluster reads $p_n^* - p = \frac{d\Omega_\sigma^*}{dV_n^*}$ (Guggenheim, 1985; Kashchiev, 2000). Substituting this equation and the former relations derived for the equilibrium state into Eq. (2.40) gives the work of formation of the critical cluster as follows

$$\begin{aligned} \Delta\Omega^* &= -n_n^*\Delta\mu + \Omega_\sigma^* = -(p_n^* - p)V_n^* + \Omega_\sigma^* \\ &= -\frac{d\Omega_\sigma^*}{dV_n^*}V_n^* + \Omega_\sigma^* = -n_n^*\frac{d\Omega_\sigma^*}{dn_n^*} + \Omega_\sigma^*, \end{aligned} \tag{2.47}$$

given that $n^* = n_n^* + {n_\sigma}^*$, this equation may be reformulated as

$$\Delta\Omega^* = -n^*\Delta\mu + n_\sigma^*\Delta\mu + \Omega_\sigma^*. \tag{2.48}$$

The last two terms in the above equation essentially represent the excess Helmholtz free energy of the interface phase of the critical cluster size n^*,

[3] for our cluster model they in fact translate to λ and n_n, see(Section 2.3.2.

i.e. $F_\sigma^* = {n_\sigma}^* \Delta\mu + \Omega_\sigma^*$. The work of formation of a critical cluster is called the nucleation work and can be determined by any of the formulas in Eqs. (2.47) and (2.48).

The grand potential of the interface phase can be written as a function of n_σ (Kalikmanov, 2012) or the area of the cluster, basically a function of n_n. In any case, we can plausibly consider $\Omega_\sigma = \Omega_\sigma(n_n)$. Therefore, the Taylor series expansion of Ω_σ about n reads

$$\Omega_\sigma(n_n) = \Omega_\sigma(n) - n_\sigma \left.\frac{d\Omega_\sigma}{dn_n}\right|_n + \frac{{n_\sigma}^2}{2}\left.\frac{d^2\Omega_\sigma}{dn_n^2}\right|_n - \frac{{n_\sigma}^3}{6}\left.\frac{d^3\Omega_\sigma}{dn_n^3}\right|_n + \mathcal{O}({n_\sigma}^4). \tag{2.49}$$

Evaluating this equation at the critical cluster and inserting the results in the last formula of Eq. (2.47) gives

$$\Delta\Omega^* = \Omega_\sigma(n^*) - \left(n_n^* \left.\frac{d\Omega_\sigma}{dn_n}\right|_{n_n^*} + {n_\sigma}^* \left.\frac{d\Omega_\sigma}{dn_n}\right|_{n^*}\right) + \frac{{n_\sigma}^{*2}}{2}\left.\frac{d^2\Omega_\sigma}{d{n_n}^2}\right|_{n^*} - \frac{{n_\sigma}^{*3}}{6}\left.\frac{d^3\Omega_\sigma}{d{n_n}^3}\right|_{n^*} + \mathcal{O}({n_\sigma}^4). \tag{2.50}$$

If a cluster is defined by the EDS, see Section 2.2 for details, and the capillarity approximation is imposed, the above equation simplifies to the nucleation work given by the conventional form of CNT, i.e. $\Delta\Omega^* = A_\sigma^*\gamma_\infty/3 = a_0 {n^*}^{2/3}\gamma_\infty/3$. This equation indicates that the work required to create a critical cluster mainly depends on the grand potential of the surface phase and its derivatives with respect to the cluster size. Henceforth, the choice of an appropriate DS with known size-dependency of its corresponding grand potential is necessary in order to achieve an accurate estimate of the nucleation work. This equation highlights the usually overlooked significance of choosing an appropriate DS.

The equilibrium state of a thermodynamic system may be *stable* or *metastable* (Guggenheim, 1985). In the nucleation theory literature, the metastable

state is usually referred to as unstable equilibrium (Ford, 1996, 2001; Vehkamaki, 2006; Schmelzer et al., 2005). The equilibrium state is stable/unstable, if the grand potential becomes a minimum/maximum at the equilibrium. Following Guggenheim (Guggenheim, 1985) for the phase stability, the first derivative is zero at an extremum and the sign of the second derivative with respect to independent variables indicates the type of the extremum, i.e. negative at a maximum or positive at a minimum. Using Eq. (2.42), the second order derivative of the grand potential with respect to the volume of a critical cluster reads

$$\left.\frac{d^2\Omega_\Sigma}{dV_n^2}\right|_{T,\mu} = \gamma\frac{d^2A_\sigma}{dV_n^2}. \tag{2.51}$$

Considering a spherical cluster, we can write $\frac{dA_\sigma}{dV} = \frac{dA_\sigma}{dR}\cdot\frac{1}{dV/dR} = 2/R$ and therefore $\frac{d^2A_\sigma}{dV_n^2} = -R^{-4}/2\pi$, which is a negative number. Thus, the RHS of the last line of the above equation will be negative. This implies that the equilibrium is unstable and consequently the critical cluster is in unstable equilibrium with the old phase. This agrees with the fact that $\Delta\Omega > 0$ hence the work required for cluster formation becomes a maximum for a critical cluster. Thus, if a perturbation is introduced into the system, the state of the critical cluster will change. For example, the absorption of monomers due to random impingements will lead to the spontaneous growth of the critical cluster whereas the depletion of monomers from the critical cluster will lead to the dissolution of the nucleus.

2.4.2 Non-critical cluster

The equality of the chemical potentials of all phases is a necessary condition for a cluster in equilibrium with the old phase, as shown in Eq. (2.46). However, this condition may not hold for a non-critical cluster, i.e. a non-equilibrium cluster, which makes it a complicated situation to analyse. For a non-critical cluster we assume $\mu_\sigma \approx \mu_n(p_n)$. This assumption is justified if the diffusive

exchange of molecules from the interface phase to the new phase is faster than the diffusion of molecules towards the interface from the old phase (Vehkamaki, 2006). By virtue of Eq. (2.37) evaluated for a condensed new phase and of this approximation, we obtain $\mu - \mu_\sigma \approx \Delta\mu - \nu_n(p_n - p)$ and subsequently Eq. (2.40) transforms to

$$\Delta\Omega = -n\Delta\mu + n_\sigma\nu_n(p_n - p) + \Omega_\sigma. \tag{2.52}$$

We now need to determine the quantity $p_n - p$ for a non-critical cluster. This is not a trivial problem and needs knowledge from statistical or molecular models. Nevertheless, the following two methods have previously been used to estimate this quantity using continuum thermodynamics (Vehkamaki, 2006).

In the first method, we evaluate Eq. (2.37) at pressure of the critical cluster p_n^* for an incompressible cluster which gives

$$\mu_n(p_n) = \mu_n(p_n^*) + \nu_n\left(p_n - p_n^*\right). \tag{2.53}$$

As shown in Eq. (2.46), the equilibrium condition for a critical cluster yields $\mu_n(p_n^*) = \mu(p)$. Substituting this relationship in Eq. (2.53) and using Eq. (2.37) and $\rho_n = \nu_n^{-1}$ gives

$$p_n - p = \rho_n\Delta\mu + (p_n - p_n^*). \tag{2.54}$$

The last term in the above equation is the difference between the inner pressure of a non-critical cluster and a critical cluster for the same pressure of the old phase p. Inserting this into Eq. (2.52) yields

$$\Delta\Omega = -n\Delta\mu + n_\sigma\left(\Delta\mu + \nu_n\left(p_n - p_n^*\right)\right) + \Omega_\sigma. \tag{2.55}$$

p_n for $9 < n < 960$ was calculated for the case of water droplet formation by (Factorovich et al., 2014) using statistical mechanics simulation at different temperatures: $278\ \mathrm{K}, 298\ \mathrm{K}, 318\ \mathrm{K}$. As shown there, the pressure difference $p_n - p_n^*$ is within the range of few bars maximum. Given that ν_n is of the

order of a fraction of nm^3, we can approximate the second term in the above equation by $n_\sigma \Delta\mu$ as $\nu_n(p_n - p_n^*)$ is relatively small compared to $\Delta\mu$. Therefore this equation simplifies to

$$\Delta\Omega = -n\Delta\mu + n_\sigma\Delta\mu + \Omega_\sigma = -n_n\Delta\mu + \Omega_\sigma, \tag{2.56}$$

which can also be written as

$$\Delta\Omega = -n\Delta\mu + F_{\sigma,1}, \tag{2.57}$$

where $F_{\sigma,1} = n_\sigma\Delta\mu + \Omega_\sigma$. Making comparison between Eqs. (2.56) and (2.40) reveals that this approximation essentially sets $\mu - \mu_\sigma$ to zero. This condition is a result of mathematically cancelling the pressure term against the supersaturation term in the former equations whilst not enforcing the physical equilibrium conditions. Evaluating this equation for the critical cluster n^* yields Eq. (2.48) as anticipated. This reveals that the work of formation of a non-critical cluster can be reasonably approximated by the equation that determines the work of formation of a critical cluster.

In the second method, the pressure difference between the inside and outside of a cluster is approximated using the generalised Laplace equation $p_n - p = \frac{d\Omega_\sigma}{dV_n}$ (Vehkamaki, 2006). This method basically assumes that the Laplace equation can be extended to sub-critical and supercritical clusters despite the fact that it was derived for the critical cluster. Employing this approximation transforms Eq. (2.52) to

$$\Delta\Omega = -n\Delta\mu + n_\sigma\nu_n\frac{d\Omega_\sigma}{dV_n} + \Omega_\sigma, \tag{2.58}$$

and given $\frac{d\Omega_\sigma}{dV_n} = \frac{d\Omega_\sigma}{dn_n}.\frac{dn_n}{dV_n} = \frac{d\Omega_\sigma}{dn_n}.\frac{1}{\nu_n}$ it follows that

$$\Delta\Omega = -n\Delta\mu + n_\sigma\frac{d\Omega_\sigma}{dn_n} + \Omega_\sigma = -n\Delta\mu + F_{\sigma,2}, \tag{2.59}$$

where $F_{\sigma,2} = n_\sigma\frac{d\Omega_\sigma}{dn_n} + \Omega_\sigma$. This equation simplifies to the following relationship

by using Eq. (2.49)

$$\begin{aligned}\Delta\Omega &= -n\Delta\mu + \Omega_\sigma(n) + n_\sigma\left(\frac{d\Omega_\sigma}{dn_n} - \left.\frac{d\Omega_\sigma}{dn_n}\right|_n\right) \\ &\quad + \frac{{n_\sigma}^2}{2}\left.\frac{d^2\Omega_\sigma}{dn_n^2}\right|_n - \frac{{n_\sigma}^3}{6}\left.\frac{d^3\Omega_\sigma}{dn_n^3}\right|_n + \mathcal{O}(n_\sigma^4). \end{aligned} \tag{2.60}$$

The work of formation of a non-critical cluster varies depending on the way it is being identified. To elaborate on this effect, we keep the cluster size n constant and compare the work of formation of a classical cluster (identified with the EDS and the capillarity approximation) with a non-EDS cluster of the same size. The identical cluster size implies equivalent "bulk" work (i.e. $-n\Delta\mu$, it should be noted that this is different from volume work as volume depends on n_n not n), whereas the excess free energy is different. The ratio of excess free energies is determined by

$$F_{\sigma,r} = \frac{F_{\sigma,1}}{F_{\sigma,cl}} = \frac{n_\sigma\Delta\mu + \Omega_\sigma}{\Omega_{\sigma,cl}}. \tag{2.61}$$

For a spherical cluster, we can write $\Omega_\sigma = A_\sigma\gamma(n) = a_0\gamma(n)n_n^{2/3}$ where $a_0 = 4\pi R_0^2$ and $\Omega_{\sigma,cl} = A_{cl}\gamma_\infty = a_0\gamma_\infty n^{2/3}$, thus the above equation simplifies to

$$F_{\sigma,r} = \frac{n_\sigma\Delta\mu + a_0\gamma(n)n_n^{2/3}}{a_0\gamma_\infty n^{2/3}} = \frac{\Delta\mu}{a_0\gamma_\infty}\left(\frac{n_\sigma}{n^{2/3}}\right) + \frac{\gamma(n)}{\gamma_\infty}\left(\frac{n_n}{n}\right)^{2/3}. \tag{2.62}$$

We can use the EDS cluster to define the effective surface free energy as $F_{\sigma,\text{eff}} = \Omega_{\sigma,\text{eff}} = A_{cl}\gamma_{\text{eff}}$. Considering that the majority of simulations conducted by means of MD or other statistical mechanical approaches report results for the EDS-defined clusters, this choice also allows us to make a comparison between our γ_{eff} and excess free energy with their counterparts in these works. For an n-size cluster, the excess free energy should be independent of the DS and therefore we can set $F_{\sigma,\text{eff}} = F_{\sigma,1}$. This yields $\gamma_{\text{eff}} = F_{\sigma,1}/A_{cl}$. Employing Eqs. (2.61) and 2.62, we can write $\gamma_{\text{eff}} = \gamma_\infty F_{\sigma,r}$ which simplifies to

$$\gamma_{\text{eff}} = \frac{\Delta\mu}{a_0}\left(\frac{n_\sigma}{n^{2/3}}\right) + \gamma(n)\left(\frac{n_n}{n}\right)^{2/3}. \tag{2.63}$$

The first term accounts for temperature and concentration dependence of the effective surface tension and the second term describes the curvature dependence of the effective surface tension. The fact that concentration influences the excess free energy and consequently the effective surface tension, based on our definition, was demonstrated and formulated in different works too (Baidakov et al., 1997; Ford, 1997; Horsch et al., 2008).

We have developed two models to determine the work of cluster formation for non-critical clusters. In order to use these models, we need to determine $\Delta\mu$ and specify the dividing surface and the associated surface tension. Calculation of $\Delta\mu$ at different supersaturation ratios is explained in Section 2.6. With regard to the DS, we will use the new surface explained in Section 2.3 in this work.

Thus far, we have utilised two methods for calculating $p_n - p$ for a non-critical cluster which gave rise to two models as follows

New model 1 Equation (2.57) and use of $F_{\sigma,1}$ to determine the work of cluster formation and the excess free energy of clusters together with the new surface to specify the cluster boundary.

New model 2 Equation (2.59) and use of $F_{\sigma,2}$ to determine the work of cluster formation and the excess free energy of clusters together with the new surface to specify the cluster boundary.

Both Eqs. (2.57) and (2.59) become identical for the EDS cluster. However, evaluating Eq. (2.59) for the critical non-EDS clusters give the nucleation works which are different from those obtained from the exact Eq. (2.50). Figures 2.5 and 2.6 show the work of cluster formation at two different supersaturation ratios determined by calculating Eqs. (2.57) and (2.59) for clusters identified by the new surface with $\lambda = 0.35$. Considering the CNT curve, the cluster is defined by the EDS, and the capillarity condition is imposed.

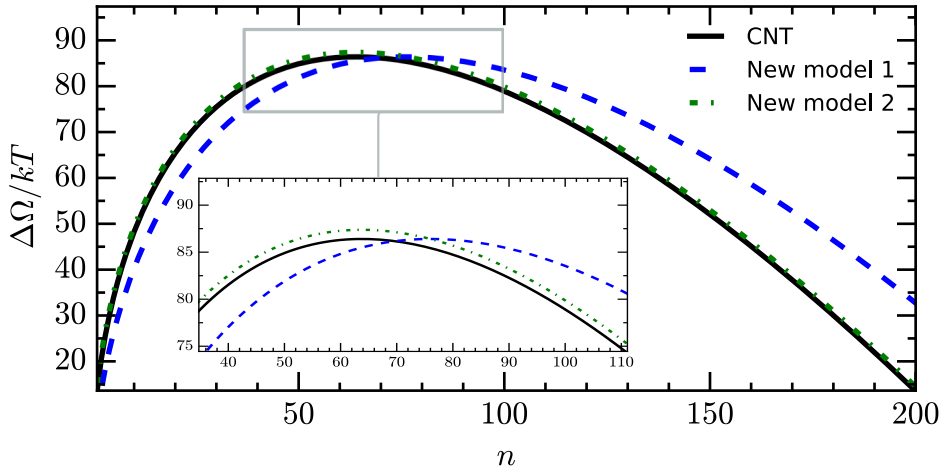

Figure 2.5: Work of cluster formation obtained by both new models, i.e. Equation (2.57) presented as new model 1 and Eq. (2.60) shown as new model 2 for $\lambda = 0.35$, and the conventional form of CNT at the supersaturation ratio $r = 15$.

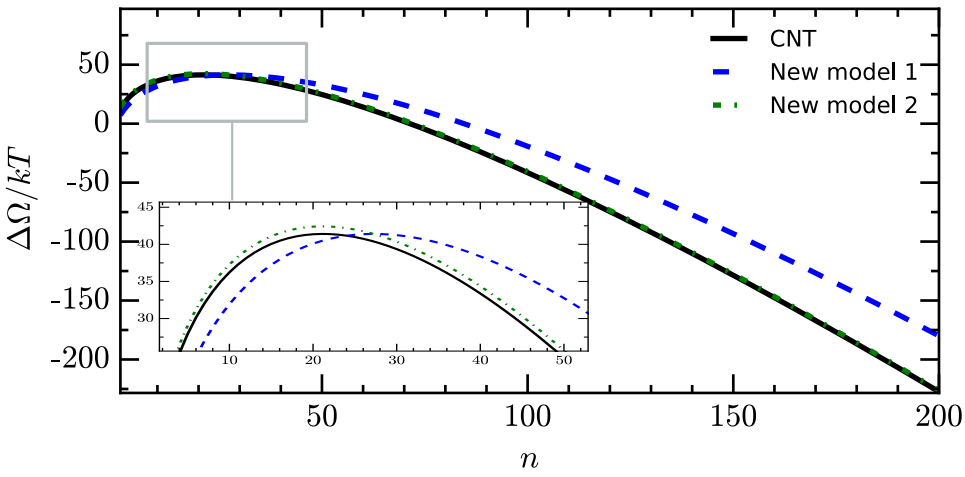

Figure 2.6: Work of cluster formation obtained by both new models, i.e. Equation (2.57) and Eq. (2.60) for $\lambda = 0.35$, and the conventional form of CNT at the supersaturation ratio $r = 50$.

These figures show i) these models predict different sizes of the critical cluster, i.e. where the cluster formation work peaks, ii) the new model 1 which refers to Eq. (2.57) and the new surface-defined clusters and CNT predicts identical height for the clustering work whereas the new model 2, i.e. Equation (2.59) and the new surface-clusters, estimates higher peak values.

The excess free energy and the effective surface tension are determined and plotted in Figs. 2.7 to 2.10. We can see that at a constant supersaturation

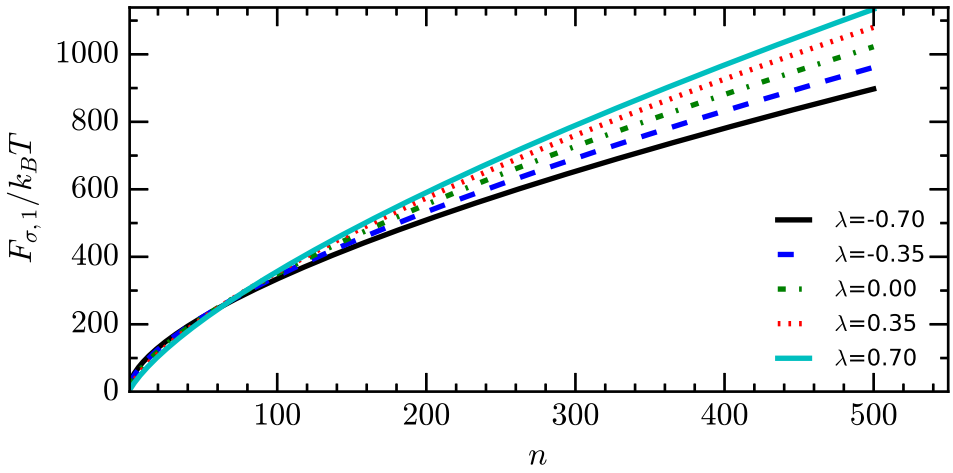

Figure 2.7: Excess Helmholtz free energy $F_{\sigma,1}$ for clusters defined by the new surface with different λ at the supersaturation ratio r = 15.

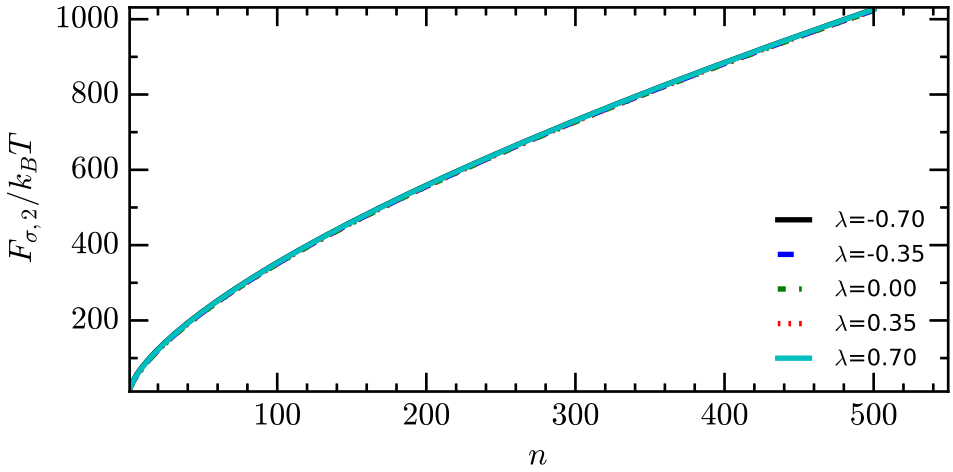

Figure 2.8: Excess Helmholtz free energy $F_{\sigma,2}$ for clusters defined by the new surface with different λ at the supersaturation ratio r = 15.

ratio, $F_{\sigma,1}$ considerably varies with a shift in the position of the DS whereas the change in $F_{\sigma,2}$ is negligible and its value is approximately equal to the excess free energy of the EDS clusters.

The effective surface tension calculated by Eq. (2.63) and shown in Fig. 2.9 varies in an increasing and decreasing fashion for positive and negative λ values, respectively, converging to the asymptote of γ_∞ in the limit of large clusters. In contrast, γ_{eff} computed by evaluating Eq. (2.61) with $F_{\sigma,2}$ is larger than γ_∞ for any position of the DS. This does not agree with the size-dependent surface tension obtained from statistical mechanics simulations (Lau et al., 2015b,a;

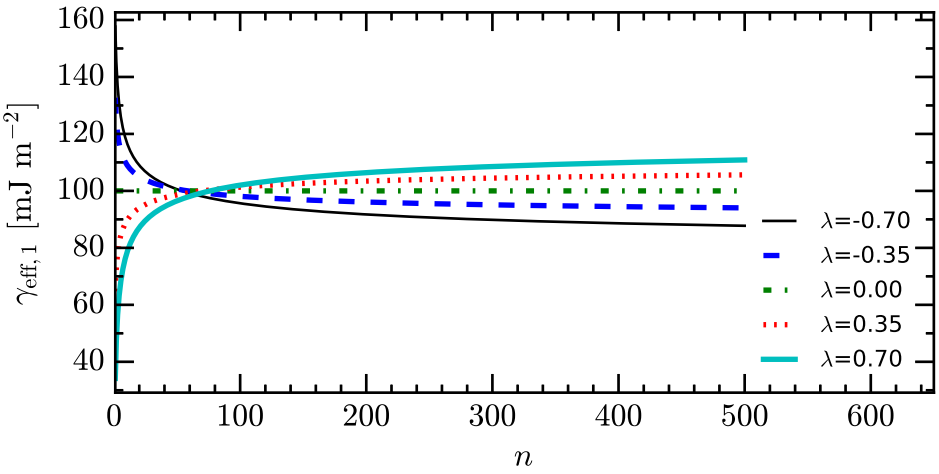

Figure 2.9: Effective surface tension obtained by calculating Eq. (2.63) using $F_{\sigma,1}$ for clusters defined by the new surface with different λ at the supersaturation ratio r = 15.

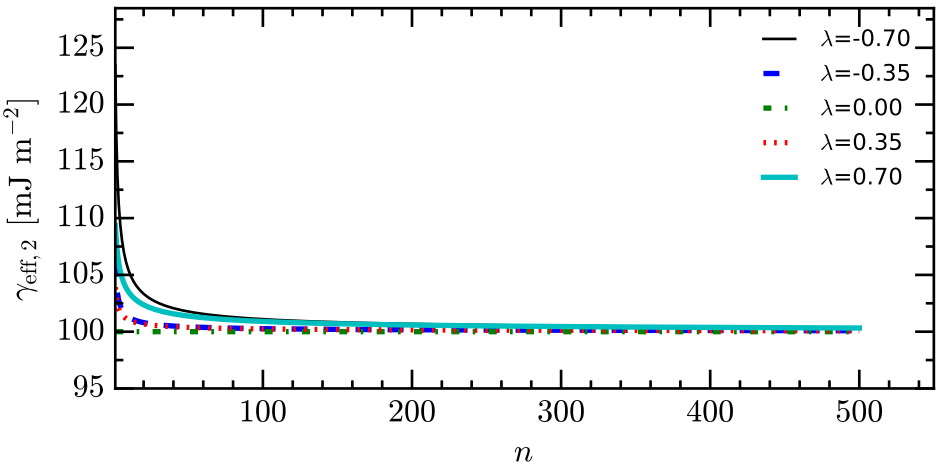

Figure 2.10: Effective surface tension obtained by calculating Eq. (2.63) using $F_{\sigma,2}$ for clusters defined by the new surface with different λ at the supersaturation ratio r = 15.

Samsonov et al., 2003; Kashchiev, 2003b). This together with Fig. 2.8 implies that $F_{\sigma,2}$ cannot suitably approximate the excess free energy of clusters. Thus, the new model 1 is favourable. In addition, this formulation can estimate cluster formation work for both critical and non-critical non-EDS clusters. Consequently, this model suits our needs better and will be utilised in this work. It should be noted that the nucleation work is a physical property of the system and is independent of the location of the dividing surface. Con-

sequently, the desired formulation has to agree with the result of the exact Eq. (2.50) for the critical cluster with non-zero n_σ.

2.5 Nucleus size

It was shown that the critical cluster (nucleus) is in unstable equilibrium with the old phase. The size of the critical cluster is then the extremum of the equilibrium equation which can be found by solving $\frac{d\Delta\Omega}{dn} = 0$ for n. Using Eq. (2.56) to model the work of cluster formation and differentiating it with respect to the cluster size n gives

$$\frac{\partial\Delta\Omega}{\partial n} = -n_n'(n_n)\Delta\mu + a_0\gamma(n)\frac{2}{3}n_n^{-1/3}n_n'(n_n) + a_0 n_n^{2/3}\gamma'(n) = 0, \quad (2.64)$$

where the prime superscript denotes the derivative with respect to the cluster size n. $\gamma(n)'$ depends on the type of the DS used to define the cluster and its corresponding model. n_n' will be non-zero if $n_n \neq 0$ which allows to simplify this relationship to

$$-\Delta\mu + a_0\gamma(n)\frac{2}{3}n_n^{-1/3} + a_0 n_n^{2/3}\frac{\gamma'(n)}{n_n'(n_n)} = 0. \quad (2.65)$$

Enforcing the capillarity approximation or using a specific DS which has a size-independent surface tension associated to it, this equation can then be solved which yields the following familiar expression

$$n_n^* = \left(\frac{2}{3}\frac{a_0\gamma_\infty}{\Delta\mu}\right)^3. \quad (2.66)$$

If the EDS is used, then this equation reduces to the equation of a nucleus size presented in the nucleation literature (Kashchiev, 2000; Vehkamaki, 2006; Schmelzer et al., 2005). $n_\sigma{}^*$ cannot be determined by this formulation. However, taking a model of the DS should allow the determination of $n_\sigma{}^*$ associated with the n_n^* as it is explained in Section 2.3. As shown in Fig. 2.11, the nucleus size linearly increases with the inverse of the difference in the chemical poten-

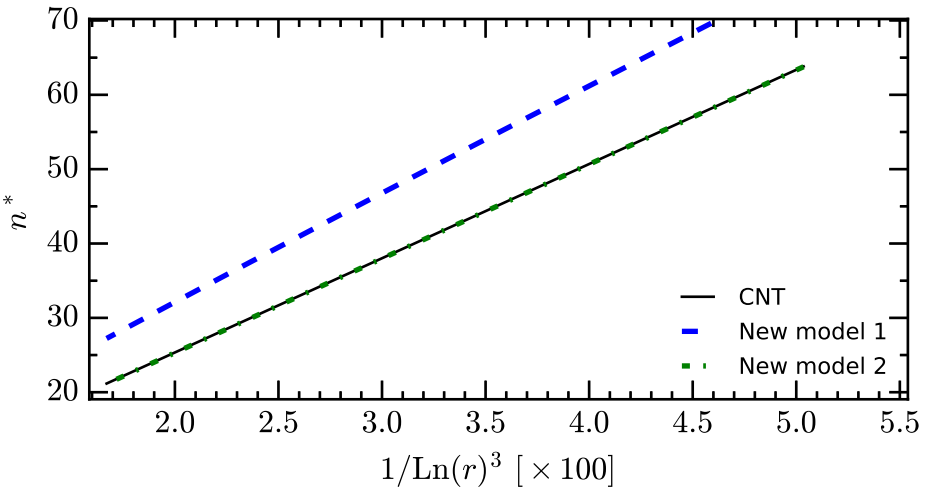

Figure 2.11: Size of the critical cluster at different supersaturation ratios. Clusters are defined by the new surface with $\lambda = 0.35$.

tial cubed, as stipulated by Eq. (2.66). Furthermore, we can see that the new model 1 estimates larger nuclei compared to CNT and to the new model 2. The results presented in Fig. 2.11 are computed as follows: i) Eq. (2.57) was solved for $1 \leq n \leq 1000$ at different supersaturation ratios, ii) the cluster size at which the work of cluster formation peaks was found as the nucleus size at the corresponding supersaturation ratio. As shown in this figure, the results are linear as predicted by Eq. (2.66).

2.6 $\Delta\mu$ in crystallisation from a solution

Physically, a solution is modelled as a mixture of two species; the one which is liquid in the pure state at a given temperature and pressure and present in the highest proportion is called the solvent and the other species is referred as the solute (Guggenheim, 1985). The solvent is treated as an inert medium for phase transition and therefore the old phase is mainly characterised by the properties of the solute species, e.g. ρ is equal to the number density of solute molecules in the solution.

The chemical potential of the old phase can be written as $\mu = k_B T \ln(a)$ where a is the activity of the solute molecules in the solution and k_B is the Boltzmann constant (Guggenheim, 1985). For an ideal and dilute solution, we

can write $a = a^{\infty} r$ where r is the supersaturation ratio (the solute mole ratio) and a^{∞} is the solute activity in the solution where the solute and condensate are in phase equilibrium (Kashchiev, 2000) (in an infinitely dilute solution). a^{∞} only depends on the nature of the solute, the solvent, pressure and temperature but not r or x. The supersaturation ratio r in a dilute solution can be approximated by the ratio of $\frac{x}{x_e}$ where x_e is the mole fraction of the solute at the phase equilibrium state.

The difference between the chemical potentials of a supersaturated solution and the solution at the equilibrium state then reads $\mu - \mu^{\infty} = k_B T \ln(\frac{a}{a^{\infty}})$, which rearranges to $\mu = \mu^{\infty} + k_B T \ln(r)$ (Guggenheim, 1985).

The activity of the new phase is approximated by the activity of the condensate in equilibrium with the solute, i.e. a^{∞}, and therefore its chemical potential becomes $\mu_n = \mu^{\infty}$. Consequently, at constant pressure and temperature we can write $\Delta\mu = k_B T \ln(r)$ (Guggenheim, 1985; Kashchiev, 2000).

2.7 Summary

We have established the thermodynamics of critical and non-critical clusters based on the Gibbs droplet model with an arbitrary dividing surface. The conservation of mass was used to determine the number of molecules in the interface phase n_σ as a function of the cluster size n, see Eq. (2.27). We have also calculated the effective surface tension of this arbitrary surface, Eq. (2.63), and demonstrated its size and chemical potential dependencies.

With the aid of these new contributions, we can model the cluster by any DS and estimate its associated surface tension. The new developments may resemble a classical model with a variable surface tension as a function of the cluster size and chemical potentials of the new and old phases.

Finally, we have defined the new surface which is characterised by the parameter λ, and the size-independent surface tension of γ_∞. This new DS facilitates numerical implementations and removes some complexity.

Now, we require to study the effect of pressure and temperature variation

on the thermodynamics of phase transition modelled by non-EDS clusters. In the next section, we will proceed to derive the required equations when the old phase is subject to such thermodynamics.

Chapter 3

Thermodynamics of cluster formation II: With acoustic waves

In Chapter 2 we developed a model for characterising a cluster and computing the work of cluster formation when the thermodynamic state of the old phase remains unchanged. This condition does not hold if the old phase is exposed to acoustic waves. Propagation of acoustic waves in the bath creates pressure fluctuation, temperature variation and mass transportation due to a spatial pressure gradient (Bird et al., 1960). The effect of the variation in pressure, temperature and composition on the work of formation of a cluster should then be quantified which is the subject of this chapter. We will begin to formulate the work of cluster formation for a generic cluster when the old phase experiences temperature and pressure perturbations. Initially, we will consider the influence of acoustic waves on non-critical clusters of fixed size. Subsequently, we will study the effect of the variation in the thermodynamic state of the old phase on the nucleation work and the size of the critical cluster. Finally, we will present a simplified form of these equations for an isothermal condition and an incompressible solution by employing the new model 1 explained in the previous chapter.

3.1 Work of cluster formation

3.1.1 Non-critical cluster

To compare with the silent condition, we are interested in evaluating the effect of acoustic waves on the work of formation of a cluster of a given size n. Consequently, we consider the invariant cluster size but variable thermodynamic parameters. The total differential of $\Delta\Omega$ is calculated by differentiating Eq. (2.41) which gives

$$\begin{aligned} d\Delta\Omega &= -(n_n + n_\sigma)d\mu - (dn_n + dn_\sigma)\mu + n_n d\mu_n + dn_n\mu_n \\ &\quad + n_\sigma d\mu_\sigma + dn_\sigma\mu_\sigma + dA_\sigma\gamma + A_\sigma d\gamma, \end{aligned} \tag{3.1}$$

and subsequently, this re-arranges to

$$\begin{aligned} d\Delta\Omega &= -(n_n + n_\sigma)d\mu + n_n d\mu_n + n_\sigma d\mu_\sigma + A_\sigma d\gamma \\ &\quad - dn_n(\mu - \mu_n) - dn_\sigma(\mu - \mu_\sigma) + dA_\sigma\gamma. \end{aligned} \tag{3.2}$$

Imposing the invariant cluster size condition gives $dn_n = dn_\sigma = dA_\sigma = 0$. Hence, the above equation simplifies to

$$d\Delta\Omega = -(n_n + n_\sigma)d\mu + n_n d\mu_n + n_\sigma d\mu_\sigma + A_\sigma d\gamma. \tag{3.3}$$

The change in the chemical potential of the old phase with respect to pressure and temperature can be estimated using a Gibbs-Duhem relation

$$d\mu = \left(\frac{\partial\mu}{\partial T}\right)_p dT + \left(\frac{\partial\mu}{\partial p}\right)_T dp = -sdT + \nu dp, \tag{3.4}$$

where s is the specific entropy of the old phase. Likewise a Gibbs-Duhem relation for the interface phase reads $d\mu_\sigma = -s_\sigma dT - \frac{A_\sigma}{n_\sigma}d\gamma$ and for the new

phase becomes $d\mu_n(p) = -s_n dT + \nu_n dp$. Substituting these equations of $d\mu, d\mu_n$ and $d\mu_\sigma$ in Eq. (3.3) then gives

$$d\Delta\Omega = -\left[-s(n_n + n_\sigma) + n_n s_n + n_\sigma s_\sigma\right] dT - \left[\nu(n_n + n_\sigma) - n_n \nu_n\right] dp, \tag{3.5}$$

which can be written as

$$d\Delta\Omega = -\Delta s_{exc} dT - \nu \Delta n_{exc} dp, \tag{3.6}$$

where $\Delta s_{exc} = -s(n_n + n_\sigma) + n_n s_n + n_\sigma s_\sigma$ is the excess entropy gained by the system through the formation of a cluster of size n and Δn_{exc} is defined in Eq. (2.14). This equation is basically independent of the method of determining the chemical potential of different phases. Thus, it holds for the new model 1 developed in Section 2.4.2 which assumes $\mu_\sigma \approx \mu$.

Integrating Eq. (3.6) gives the work required to form clusters at a temperature, pressure and composition which differ from the reference state. This is expressed as

$$\Delta\Omega(n_n, n_\sigma, p, T) = \Delta\Omega_0(n_n, n_\sigma) - \int_{T_0}^{T} \Delta s_{exc} dT - \int_{p_0}^{p} \nu \Delta n_{exc} dp, \tag{3.7}$$

where $\Delta\Omega_0(n_n, n_\sigma)$ is the work required to create an n-sized cluster while the system is at the reference thermodynamic state (T_0, p_0, x_0).

In sonocrystallisation experiments, a supersaturated solution is usually made first, and then an acoustic wave is introduced. Therefore, it is practically desirable to choose the supersaturated state in silent condition, i.e. prior to the application of the acoustic waves, as the reference state. The difference in the chemical potentials at the reference state needs then to be obtained. Using the formulation explained in Section 2.6, at constant pressure and temperature of

the reference state we can write $\Delta\mu_0 = k_B T_0 \ln(r_0)$ where $r_0 = \frac{x_0}{x_e}$ and x_e is evaluated at T_0 and p_0.

Employing the new model 1 , the work of cluster formation in the reference state is obtained by evaluating Eq. (2.57) which yields

$$\Delta\Omega_0 = -nk_B T_0 \ln(r_0) + n_\sigma k_B T_0 \ln(r_0) + a_0 \gamma_\infty n_n^{2/3}. \tag{3.8}$$

Substituting this equation into Eq. (3.7) allows us to determine the effect of perturbation in the thermodynamic state of the old phase on the work of cluster formation for non-critical clusters.

3.1.2 Critical cluster

Now, we need to determine the change in the nucleation work due to variation in the thermodynamic state of the old phase. We start with Eq. (3.1) and substitute μ_n by the following relation obtained by evaluating the Gibbs-Duhem relation of Eq. (2.37) for a condensed new phase

$$\mu_n(p) = \mu_n(p_n) - \nu_n (p_n - p), \tag{3.9}$$

which gives

$$\begin{aligned} d\Delta\Omega = & -(n_n + n_\sigma)d\mu + n_n d\mu_n + n_\sigma d\mu_\sigma + A_\sigma d\gamma \\ & - dn_n(\mu - \mu_n(p_n) + \nu_n (p_n - p)) - dn_\sigma(\mu - \mu_\sigma) + dA_\sigma \gamma. \end{aligned} \tag{3.10}$$

Applying equilibrium conditions stated in Eq. (2.46) simplifies this equation for a critical cluster as follows

$$d\Delta\Omega^* = -(n_n^* + {n_\sigma}^*)d\mu + n_n^* d\mu_n^* + {n_\sigma}^* d{\mu_\sigma}^* + A_\sigma^* d\gamma, \tag{3.11}$$

which is akin to Eq. (3.3) being evaluated at the critical cluster. Therefore, by using the same Gibbs-Duhem relations used to simplify Eq. (3.3), we arrive at

$$d\Delta\Omega^* = -\Delta s^*_{exc} dT - \nu \Delta n^*_{exc} dp, \tag{3.12}$$

where Δs^*_{exc} and Δn^*_{exc} are the excess quantities evaluated for a critical cluster. The integral form obtained by integrating this equation reads

$$\Delta\Omega^*(p,T) = \Delta\Omega^*_0 - \int_{T_0}^{T} \Delta s^*_{exc} dT - \int_{p_0}^{p} \nu \Delta n^*_{exc} dp. \tag{3.13}$$

This equation was first derived by Hill (Hill, 1962) and re-established by Ford (Ford, 2001). We should note that in the above derivations, no assumption is considered for the critical cluster at either thermodynamic states (prior and after pressure and temperature variation). Despite that this equation and Eq. (3.7), which is developed in this work, look similar, they are for two different cluster types and have developed based on different assumptions.

3.2 Nucleus size

We determined the nucleus size in the silent condition in Section 2.5. Now, we are interested in assessing the influence of the variation in the thermodynamic state of the old phase on the size of the critical cluster.

As we have mentioned before, the size of the critical cluster is the extremum of the equilibrium equation which can be found by solving $\frac{d\Delta\Omega}{dn} = 0$ for n. Thus, differentiating Eq. (3.7) with respect to n gives

$$\frac{\partial \Delta\Omega}{\partial n} = \frac{\partial \Delta\Omega_0}{\partial n} - \int_{T_0}^{T} \Delta s'_{exc} dT - \int_{p_0}^{p} \Delta n'_{exc} \nu dp, \tag{3.14}$$

where $\Delta s'_{exc} = -s + s_n n'_n(n_n) + s_\sigma n'_\sigma(n_n)$ and $\Delta n'_{exc} = 1 - \frac{\rho}{\rho_n} n'_n(n_n)$ where $n'_\sigma(n_n)$ and $n'_n(n_n)$ are the first derivative of n_σ and n_n with respect to the cluster size n and are given in Appendix D. This is a complete equation for calculation of the variation in the work required for cluster formation with respect to the size of cluster at different thermodynamic states and is valid for any cluster model. Substituting $\Delta\Omega_0$ from Eq. (3.8) yields

$$\frac{\partial \Delta\Omega}{\partial n} = -k_B T_0 \ln(r_0)(1 - n'_\sigma(n_n)) + a_0 \gamma_\infty \frac{2}{3} n_n^{-1/3} n'_n(n_n) - \int_{T_0}^{T} \Delta s'_{exc} dT - \int_{p_0}^{p} \Delta n'_{exc} \nu dp. \quad (3.15)$$

This relationship uses the new model 1 to determine the work of cluster formation at the reference state. The size of the critical cluster is the root of $\frac{\partial \Delta\Omega}{\partial n} = 0$. The generic solution for the critical cluster size in an arbitrary state depends on material properties and change in density and entropy of all phases with pressure and temperature, respectively. The solution for special cases though can be derived. The case of an isothermal process with incompressible old and new phases is considered and discussed below.

3.3 Incompressible solution and isothermal condition

The absorption of propagating acoustic waves in a medium mainly depends on the viscosity of the medium and the wavelength. Wave propagation in an aqueous medium can be considered as an isothermal process since the absorption is low, especially during a short exposure. This is further discussed in Chapter 7. In this case, the effect of a pressure perturbation on the work of formation of an n-sized cluster is determined by omitting the temperature term in Eq. (3.6) which reads

$$\left(\frac{\partial \Delta\Omega}{\partial p}\right)_T = -\nu(n_n + n_\sigma) + n_n \nu_n = -\nu \Delta n_{exc}. \quad (3.16)$$

This equation states that the pressure rise reduces the work of formation of a cluster size n if the new phase is denser than the old phase, i.e. Δn_{exc} is positive, and vice versa. Consequently, in comparison with the silent condition, the energy required to create an identical cluster is reduced over the compression interval of an acoustic wave and increased over the rarefaction cycle.

The RHS of Eq. (3.16) can be reformulated as follows

$$-\nu(n_n + n_\sigma) + n_n\nu_n \;=\; -\nu k_\rho n_n \;-\; \nu n_\sigma \;=\; -\nu k_\rho n \;-\; \nu_n n_\sigma, \tag{3.17}$$

where the n_n and n_σ terms after the first equal sign show the effect of pressure on the work of formation of the new and interface phases, respectively, which can also be re-arranged to display the effect of pressure on the "bulk" work and the excess free energy, i.e. the n and n_σ terms after the second equal sign.

Integrating Eq. (3.16) gives the integral form of the work of cluster formation which is equal to Eq. (3.7) with the temperature term eliminated. If the partial molecular density of the old and new phases are assumed pressure independent, e.g. in sonocrystallisation process where the old phase is a liquid and the new phase is a solid, the integral form of the work of cluster formation simplifies to

$$\Delta\Omega(n_n, n_\sigma, p) \;=\; \Delta\Omega_0(n_n, n_\sigma) \;-\; \Delta n_{exc}\nu\Delta p, \tag{3.18}$$

where $\Delta p = p - p_0$ is the variation in pressure. This equation is solved for different positions of the DS and static pressure magnitudes at the supersaturation ratio of $r_0 = 15$, see Fig. 3.1. The physicochemical properties of the solution are the same as those used in the previous chapter, listed in Table A.1 in Appendix A. For all the simulations presented in this thesis, we consider the room temperature and atmospheric pressure as the reference state, $T_0 = 293$ K and $p_0 = 0.1$ MPa respectively. We can see in Fig. 3.1 that the nucleation barrier and the size of the critical cluster are inversely proportional to the pressure magnitude and are functions of the position of the DS. The latter will be further discussed below.

In the case of isothermal acoustic wave propagation, the nucleation work varies with pressure as follows

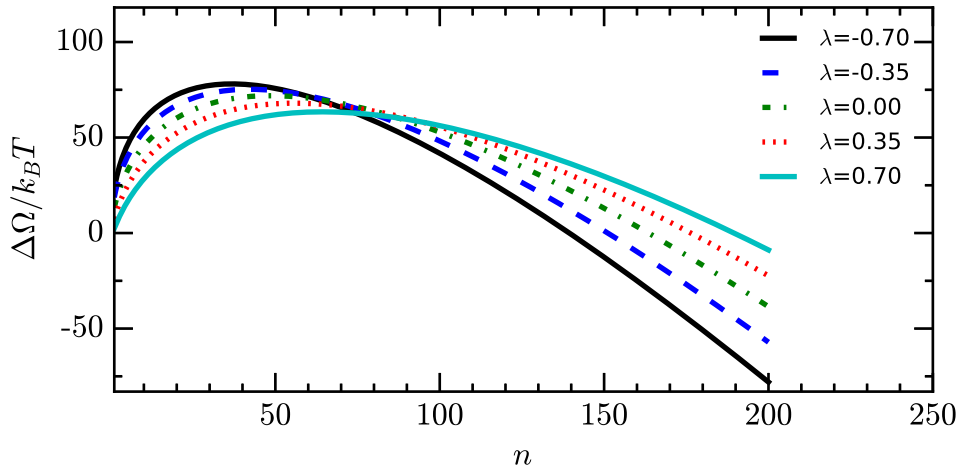

(a)

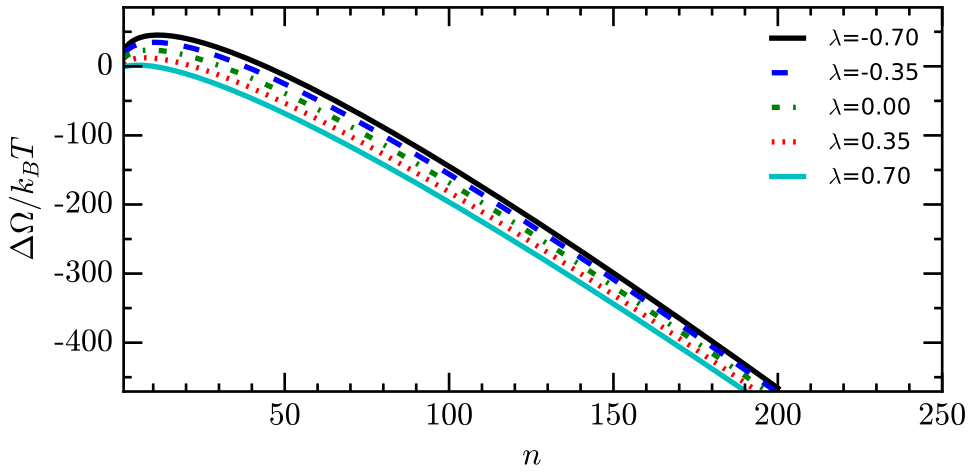

(b)

Figure 3.1: Work of cluster formation for clusters defined by different values of λ with r_0 = 15 and a) Δp = 10 MPa, and b)Δp = 100 MPa. Pressure change is static.

$$\left(\frac{\partial \Delta\Omega^*}{\partial p}\right)_T = -\nu \Delta n^*_{exc}, \tag{3.19}$$

which tells that the height of the nucleation barrier reduces with pressure elevation if the new phase is condensed. It conveys the physical implication that a change in pressure can have an effect on the nucleation rate. The consequent dependence of the nucleation rate on pressure was investigated in the context of an extension to the nucleation theorem by Luijten et al., (Luijten and van Dongen, 1999; Luijten et al., 1999) and was also discussed

in Ford (Ford, 1992). We will extensively discuss this subject in the following two chapters.

Finally, the nucleation work in an incompressible solution experiencing isothermal acoustic wave propagation becomes

$$\Delta\Omega^*(p) \;=\; \Delta\Omega_0^* \;-\; \Delta n_{exc}^* \nu \Delta p. \tag{3.20}$$

The nucleation work at the reference state determined by the new model 1 is independent of the location of the DS, e.g. see the barrier height shown in Figs. 2.5 and 2.6 for $\lambda = 0$ and $\lambda = 0.35$, respectively. Thus, the first term in Eq. (3.20) remains unchanged if the supersaturation ratio is constant. However, the second term in the RHS varies depending on the position of the DS. This is because of the variation in the surface tension with respect to the chemical potential of the old phase which has been accounted for in Eq. (3.11) (i.e. term $A_\sigma^* d\gamma$). Nonetheless, if we calculate the LHS of Eq. (3.19) and plot the results against pressure variation, we expect to obtain the excess size of the critical cluster.

Figures 3.2 and 3.3 display the results of calculations of the LHS and the RHS of Eq. (3.19) at $r_0 = 15$. The LHS was calculated by computing the numerical differentiation of the nucleation work with respect to pressure. The nucleation work at each pressure magnitude was obtained by numerically finding the maximum of Eq. (3.18) determined for $1 \leq n \leq 1000$ at each pressure. Subsequently, the RHS was obtained by calculating Eq. (2.14) for each critical cluster. We can see that these curves follow a similar trend in both figures. The trend shows the excess critical cluster size is roughly independent of the position of the DS at high pressure magnitudes. This is because the nucleus size decreases and becomes of the order of few molecules as the pressure magnitude increases.

The consensus for the effect of pressure on the nucleation work is that pressure contribution is more significant at lower supersaturation ratios; (Kashchiev and Van Rosmalen, 1995; Kashchiev, 2000) observable in Figs. 3.4

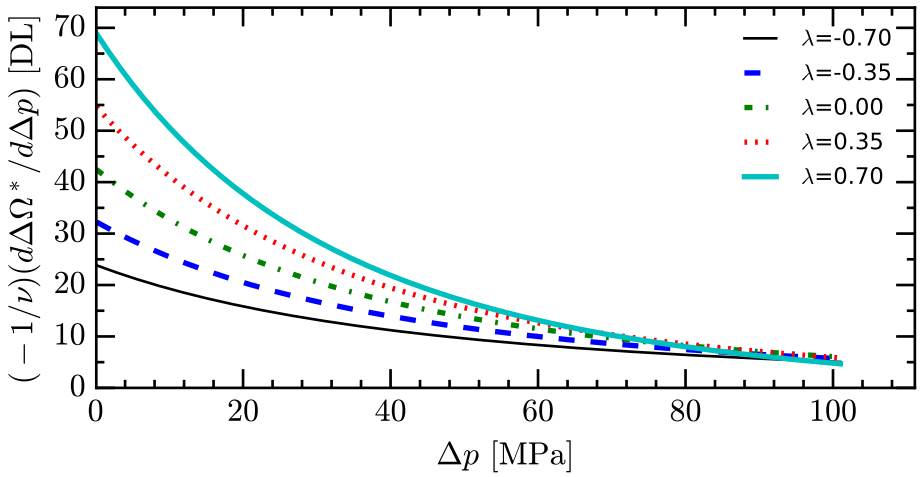

Figure 3.2: Numerical differentiation of the nucleation work with respect to static pressure variation (isothermal), see the LHS of Eq. (3.19).

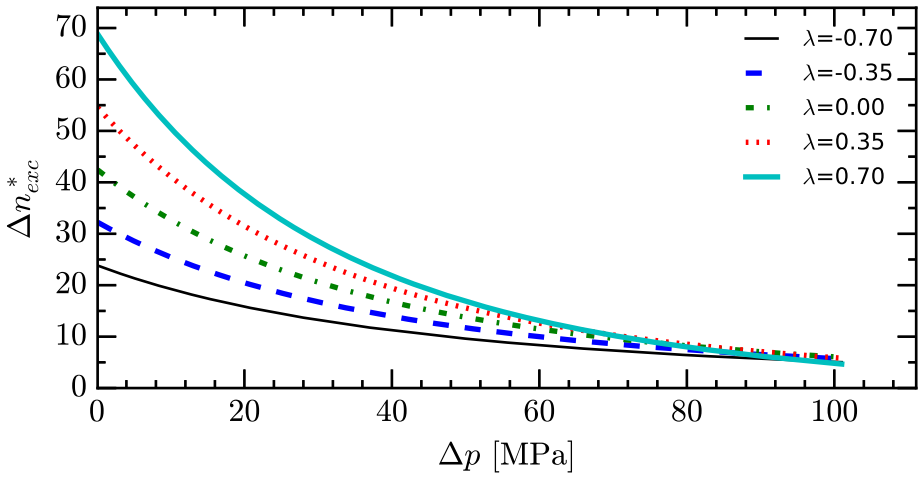

Figure 3.3: Excess size of the critical cluster in the system exposed to isothermal static pressure rise, see the RHS of Eq. (3.19).

and 3.5 for clusters defined by the EDS and λ = 0.35, respectively. For instance, in Fig. 3.4 at r_0 = 50 we see lower changes in the nucleation work with pressure rise of eight orders of magnitude than a similar situation at r_0 = 15. We can see a similar trend in Fig. 3.5 where λ = 0.35.

In addition, Figs. 3.6 and 3.7 depict the isobaric nucleation work contours showing alike behaviour projected by converging isobaric curves towards the upper end of the supersaturation ratio axis. Furthermore, the slope of the isobaric curves changes more at lower pressure magnitudes. This means that at high pressure magnitude, the nucleation work does vary a little by making

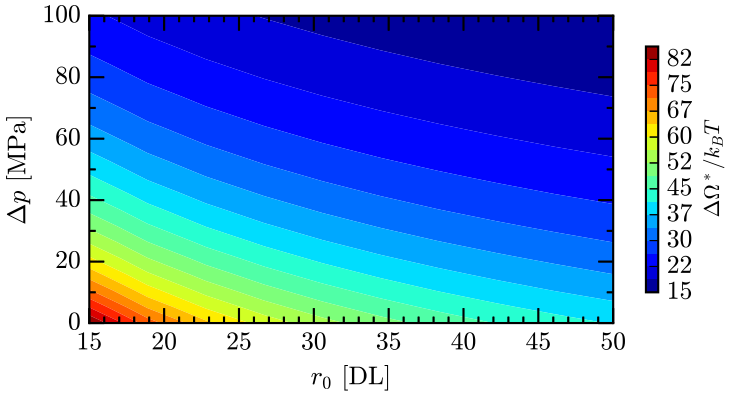

Figure 3.4: Contour plot of the nucleation work at different supersaturation ratios and static pressure magnitudes. The DS coincides with the EDS.

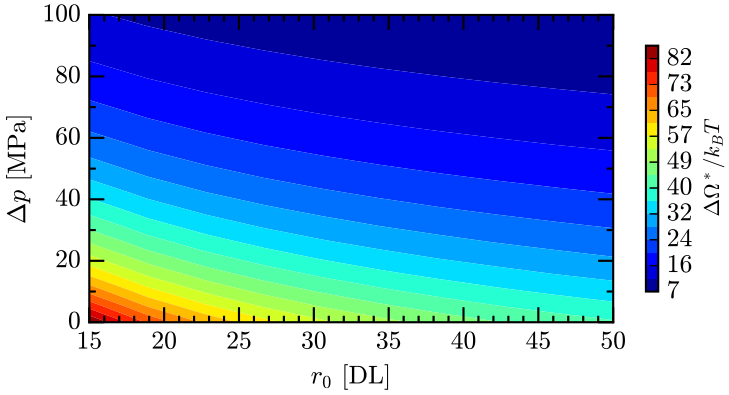

Figure 3.5: Contour plot of the nucleation work at different supersaturation ratios and static pressure magnitudes. The DS is placed within the EDS with $\lambda = 0.35$.

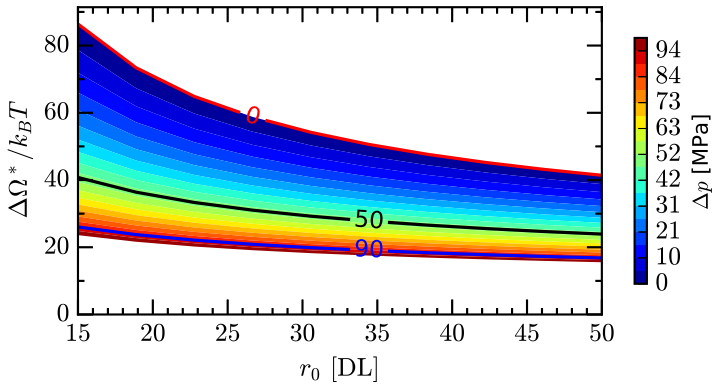

Figure 3.6: Isobaric nucleation work at different supersaturation ratios. The labels on curves refer to the pressure magnitude in MPa, the DS is positioned at $\lambda = 0$.

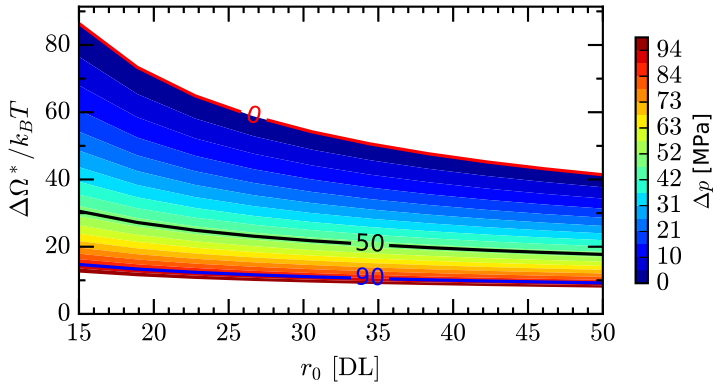

Figure 3.7: See the caption of Fig. 3.6. Here the DS is positioned at $\lambda = 0.35$.

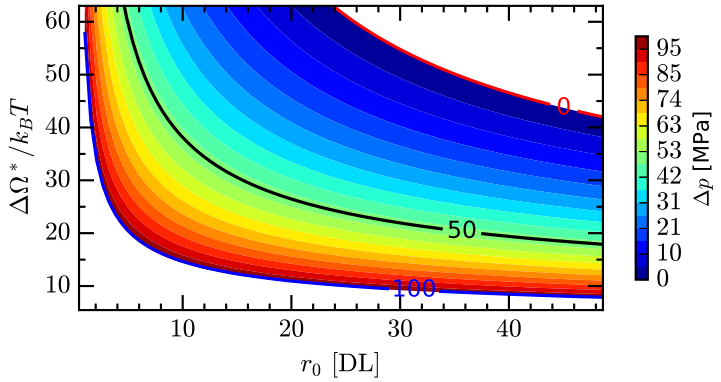

Figure 3.8: Isobaric nucleation work at different supersaturation ratios ($1 \leq r_0 < 50$). The DS is positioned at $\lambda = 0.35$.

the solution more supersaturated, e.g. see the 90 MPa flat curve. This effect leads to the following deductions: i) in theory, increasing pressure high enough (where the exact value depends on the solution properties) would allow phase transformation to happen even in very dilute solutions since the nucleation barrier can be surmounted. ii) The MZW is narrowed down which also results in crystallisation in reduced supersaturations which are widely reported in the sonocrystallisation literature (Ruecroft et al., 2005; de Castro and Priego-Capote, 2007). This finding elucidates the experimental application of sonocrystallisation in situations that the solution has to be dilute, e.g. to prevent clogging a channel or wetting a membrane. iii) The influence of the supersaturation ratio is more substantial at lower pressure magnitudes. Therefore, pressure effect becomes more notable at lower supersaturations and vice versa.

Additionally, a similar nucleation barrier can be observed for different combinations of the pressure magnitude and supersaturation ratio. For instance, Figs. 3.8 and 3.9 demonstrate that almost an equal nucleation work can be obtained when $r_0 = 1,\ \Delta p = 100$ MPa and $r_0 = 28.5,\ \Delta p = 0$ MPa. To clarify this, we can use Eq. (3.8) to reformulate Eq. (3.18) as follows

$$\begin{aligned}\Delta\Omega(n_n, n_\sigma, p) &= \Delta\Omega_0(n_n, n_\sigma) - \Delta n_{exc}\nu\Delta p \\ &= -nk_BT_0\ln(r_0) + n_\sigma k_BT_0\ln(r_0) + a_0\gamma_\infty n_n^{2/3} - \Delta n_{exc}\nu\Delta p \\ &= -n_n\left(k_BT_0\ln(r_0) + \frac{\Delta n_{exc}}{n_n}\nu\Delta p\right) + a_0\gamma_\infty n_n^{2/3}, \end{aligned} \tag{3.21}$$

which simplifies to

$$\Delta\Omega(n_n, n_\sigma, p) = -n_n k_BT_0\ln(r_{\text{eff}}(n)) + a_0\gamma_\infty n_n^{2/3}, \tag{3.22}$$

where

$$r_{\text{eff}}(n) = r_0\exp\left(\tfrac{\Delta n_{exc}\nu\Delta p}{n_n k_BT}\right), \tag{3.23}$$

presents the effective supersaturation ratio. Different combinations of the pressure magnitude and supersaturation ratio that give a similar effective supersaturation ratio will predict the same nucleation barrier. Employing Eq. (2.29) gives $\lim_{n_n\to\infty}\frac{\Delta n_{exc}\nu\Delta p}{n_n k_BT} = \frac{k_\rho\nu\Delta p}{k_BT}$. This means that in contrast to the EDS clusters and the conventional CNT, this model predicts a size-dependent pressure effect specifically for small clusters which tends to become constant for relatively large clusters. Using Eq. (3.17), the second line of Eq. (3.21) can be reformulated as

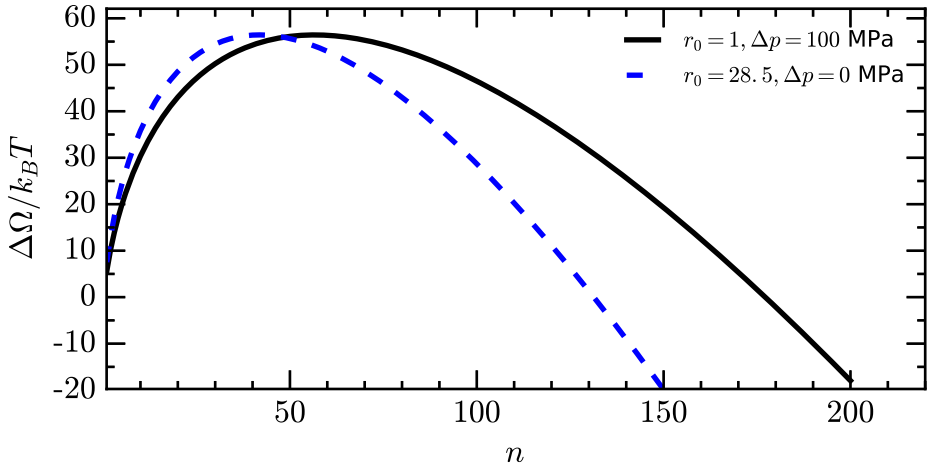

Figure 3.9: Work of cluster formation for two different supersaturation ratios and pressure magnitudes. The DS is positioned at $\lambda = 0.35$.

$$\begin{aligned}\Delta\Omega(n_n, n_\sigma, p) \quad = \quad & -n\left(k_B T_0 \ln(r_0) \; + \; k_\rho \nu \Delta p\right) \; + \\ & n_\sigma \left(k_B T_0 \ln(r_0) \; - \; \nu_n \Delta p\right) \; + \; a_0 \gamma_\infty n_n^{2/3}, \end{aligned} \tag{3.24}$$

which comparing this equation with Eq. (2.57) gives

$$F_{\sigma,1}(n_n, n_\sigma, p) \; = \; n_\sigma \left(k_B T_0 \ln(r_0) \; - \; \nu_n \Delta p\right) \; + \; a_0 \gamma_\infty n_n^{2/3}. \tag{3.25}$$

This demonstrates that the excess free energy of the non-EDS cluster is a function of the supersaturation ratio and pressure and hence it will be time dependent (besides being size dependent).

As we can see in Fig. 3.9, although the effective supersaturation ratio and the nucleation work are the same, the nuclei sizes are different. To elaborate on this, we need to determine the nucleus size.

Using Eq. (3.15) and imposing the isothermal and incompressibility conditions, we can find the nucleus size which reads

$$\frac{\partial \Delta\Omega}{\partial n} = -k_B T_0 \ln(r_0) + a_0\gamma_\infty \frac{2}{3} n_n^{-1/3} n_n'(n_n) + k_B T_0 \ln(r_0) n_\sigma'(n_n) - \Delta n_{exc}' \nu \Delta p. \quad (3.26)$$

By virtue of the relationship $n_n'(n_n) + n_\sigma'(n_n) = 1$; see Appendix D, and setting Eq. (3.26) equal to zero, we arrive at the following polynomial equation

$$-k_B T_0 \ln(r_0) + a_0\gamma_\infty \frac{2}{3} n_n^{-1/3} - \frac{1}{n_n'(n_n)} \Delta n_{exc}' \nu \Delta p = 0. \quad (3.27)$$

Expanding $n_n'(n_n)$ and after some algebra, we obtain

$$n_n \left(1 + \frac{k_B T_0 \ln(r_0)}{k_\rho \nu \Delta p}\right) - \left(\frac{2}{3}\frac{a_0\gamma_\infty}{k_\rho \nu \Delta p} - 2\lambda\right) n_n^{2/3} + \lambda^2 n_n^{1/3} = 0, \quad (3.28)$$

which changing variable $n_n = X^3$ reformats it to

$$X^3 \left(1 + \frac{k_B T_0 \ln(r_0)}{k_\rho \nu \Delta p}\right) - \left(\frac{2}{3}\frac{a_0\gamma_\infty}{k_\rho \nu \Delta p} - 2\lambda\right) X^2 + \lambda^2 X = 0. \quad (3.29)$$

This is a cubic polynomial equation which can have three distinct roots. By factoring out X, we can deduce that one root is zero (which is not acceptable in the physical sense) and obtain the following quadratic equation

$$X^2 \left(1 + \frac{k_B T_0 \ln(r_0)}{k_\rho \nu \Delta p}\right) - \left(\frac{2}{3}\frac{a_0\gamma_\infty}{k_\rho \nu \Delta p} - 2\lambda\right) X + \lambda^2 = 0. \quad (3.30)$$

We can numerically solve this equation at any time instant and obtain n_n^* and consequently n^* as pressure varies over time. If we define the cluster by the EDS, this equation simplifies and gives the analytic solution for the size of the nucleus (n_e^*) as follows

$$n_e^* = \left(\frac{2}{3} \frac{\frac{a_0 \gamma_\infty}{k_B T_0}}{\ln(r_0) + \frac{k_\rho \nu \Delta p}{k_B T_0}} \right)^3 . \tag{3.31}$$

This equation demonstrates the effect of pressure fluctuation and composition variation on the size of the EDS-defined nuclei. This equation for the EDS clusters was first derived by Kashchiev and van Rosmalen (Kashchiev and Van Rosmalen, 1995). This equation can be represented in the following format as well

$$n_e^* = \left(\frac{2}{3} \frac{a_0 \gamma_\infty}{k_B T_0 \ln(r_{\text{eff,e}})} \right)^3 . \tag{3.32}$$

where $r_{\text{eff,e}} = r_0 \exp\left(\frac{k_\rho \nu \Delta p}{k_B T}\right)$ is the effective supersaturation ratio for the EDS clusters. Unlike the non-EDS clusters, the nucleus size remains the same for the similar values of the effective supersaturation if clusters are defined by the EDS. Having determined n^*, the nucleation work is given by Eq. (2.57) for the cluster size of n^*.

Thus far we have considered the static pressure condition. In the case of a system exposed to an acoustic wave, we will show in Chapter 7 that for a system located in the pre-shock region the local pressure is given by $p = p_a + p_0$ where p_0 is the ambient pressure at the reference state and $p_a = p_m \cos(2\pi f t)$ is the acoustic pressure in the system with magnitude p_m and frequency f. The pressure difference then reads $\Delta p = p - p_0 = p_a$. As pressure magnitude oscillates during the cycle of an acoustic wave, both the nucleation work and the size of the nucleus vary. Over the compression phase of the wave, $\Delta p > 0$ hence the nucleation barrier substantially drops when $k_\rho > 0$, see Fig. 3.10, whereas during the rarefaction phase the negative pressure difference causes a significant increase in the nucleation work. Consequently, over one part of the acoustic wave, nucleation is promoted whereas over another part it is impeded. Compared to the reference state, i.e. $\Delta p = 0$, the ratio of increase or decrease is asymmetric which will lead to an unequal influence on the nucleation rate

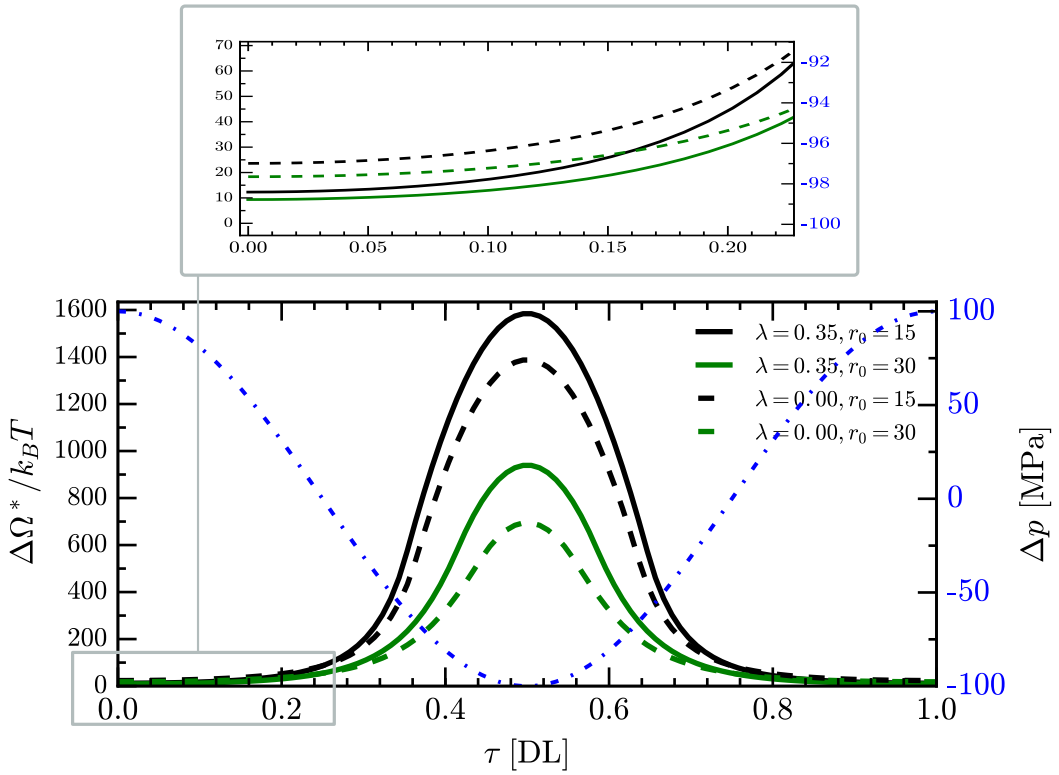

Figure 3.10: Nucleation work calculated for the EDS and non-EDS ($\lambda = 0.35$) clusters at different supersaturation ratios over one cycle of excitation. The second axis on the RHS illustrates Δp for $p_m = 100$ MPa and $f = 100$ kHz. The time axis is non-dimensionalised with respect to the driving frequency, i.e. $\tau = tf$. The magnified area at the top shows the nucleation work at the peak positive pressure instant.

which is the subject of the next two chapters.

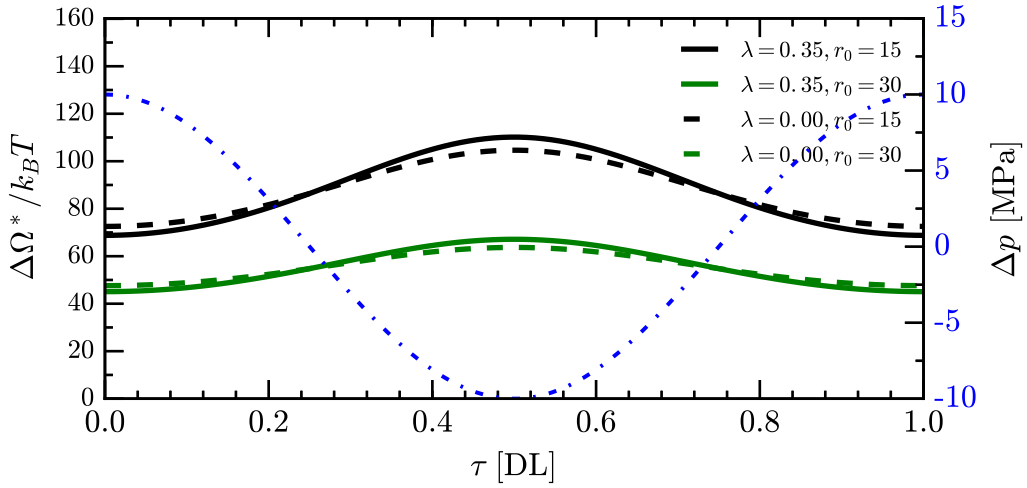

Figure 3.11: The same as Fig. 3.10 but with $p_m = 10$ MPa.

Comparing Figs. 3.10 and 3.11, we can observe that the estimates of the nucleation barrier using the EDS and non-EDS clusters are similar in values at low pressure magnitudes. However, these estimates may considerably diverge as the pressure magnitude increases. Nonetheless, the estimated nuclei sizes would be different despite the fact that the nucleation barrier height may not change noticeably at lower pressure magnitudes, see Fig. 3.1.

3.4 Summary

We have determined the effect of pressure and temperature variation on the thermodynamics of cluster formation. The work of formation of non-critical and critical clusters change under this circumstance, see Eqs. (3.7) and (3.13), as well as the size of the critical cluster. We have derived a generic equation to estimate the non-EDS nucleus size, Eq. (3.14), which simplifies to Eqs. (3.30) and (3.32) for the non-EDS cluster identified by the new surface and the EDS cluster, respectively.

Under isothermal conditions, this theory predicts that the nucleation barrier is reduced or raised with an increase in pressure if the new phase is more or less dense than the old phase, respectively. The nucleation work contour plots as a function of both the pressure magnitude and supersaturation ratio were obtained. They show an identical nucleation barrier could be surmounted with different combinations of the pressure magnitude and supersaturation ratio. This can be elucidated by defining an effective supersaturation ratio, Eq. (3.23), which includes both supersaturation ratio and pressure terms. It was shown using the non-EDS cluster model predicts a size-dependent pressure effect which is stronger for smaller clusters.

Moreover, the nucleation work and the size of nuclei vary over a period of an acoustic wave revealing that nucleation is enhanced over half a period of the acoustic wave and is impeded over the other half a period. More specifically, nucleation is promoted over the rarefaction/compression cycle and is obstructed over the compression/rarefaction cycle if k_ρ is negative/positive,

respectively. Here, we assumed the acoustic wave is a simple sinusoidal wave and the system is mass-conserved. We will extend these calculations using more complex waveforms and elaborate more on these findings in Chapter 7.

Employing the theory developed in this chapter and Chapter 2, we can determine the thermodynamics of phase transformation for a solution exposed to an acoustic field. In the next section, we will proceed to develop the kinetics of cluster growth and decay subject to such thermodynamics.

Chapter 4

Kinetics of cluster formation I: Mass conserved system

We have studied the thermodynamics of phase transition in a system exposed to pressure and temperature perturbations. The cluster model which relies on continuum thermodynamics was used to mathematically formulate this process. The subject of this chapter is to study the dynamics of this process. To this end, we will begin this chapter with explaining some definitions borrowed from statistical mechanics, namely: the microstate and the macrostate of a system.

The microstate is a conceivable microscopic configuration that an isolated system of constant energy and number of particles can adopt with a certain probability (Ford, 2013). The set of all microstates of a system forms the *phase space* of the system. A particular collection of microstates with a common specific property is called a macrostate and is characterised by a probability distribution of this collection of microstates over the phase space (Ford, 2013). The study of macrostates allows the expected state of the system to be determined without the need for a detailed investigation of the microscopic behaviour of particles. We now aim to model the evolution of these macrostates and their associated time-dependent probability distributions for the problem of phase transformation.

We employ the same model of the system and bath described in

Section 2.1, i.e. the system has a small volume and can exchange particles with the bath (environment), but we consider the density fluctuation representation instead of the cluster model temporarily. Since the volume of the system is constant, we can identify the macrostates of the system by the number of particles occupying the system. Therefore system macrostates evolve with fluctuations in the number of molecules in the system. In the case of nucleation, we assume that the system initially contains only monomers, i.e. the probability of having n-mers with $n > 1$ is negligible. Dispersion of these particles changes the particle density of the system over time; in other words, the system moves from one macrostate to another.

The evolution from the initial state to the final state can then be represented by time-dependent transition probabilities for moving between macrostates. For instance, the system may move from the macrostate i, i.e. the system encloses i particles, to the macrostate j with the transition probability of $\mathcal{T}(i \to j; t)$. If we assume that these transition probabilities are Markovian, i.e. they only depend on the macrostates i and j not on earlier history, the evolution of macrostate probabilities can then be modelled by the *master equation* as follows(Ford, 2016)

$$\frac{dP_i(t)}{dt} = \sum_{j \neq i} \left(P_j(t)\mathcal{T}(j \to i; t) - P_i(t)\mathcal{T}(i \to j; t) \right), \tag{4.1}$$

where P_i is the time-dependent probability of embracing the macrostate i. This master equation models the propagation of the probability into the phase space as the evolution of the probability of each macrostate with time. This is the fundamental equation for studying the kinetics of a dynamic process, e.g. phase transformation, without the need to delve into expressing microstates. This formulation is a discrete representation of the dynamics. Thus, we need to solve a set of ordinary differential equations (ODEs) with as many equations as the number of possible macrostates. We will continue this chapter by presenting a simplified form of this master equation, in both discrete and continuous formats, suitable for the problem of nucleation. We will then determine the

transition probabilities and investigate the effect of wave propagation on them. In this chapter we will assume that the system is closed, hence do not consider mass transfer due to wave propagation. The effect of mass transportation on the cluster dynamics is the subject of next chapter and will be discussed there.

4.1 Master equations for nucleation

Equation (4.1) is a generic master equation for estimating the propagation of probability into the phase space. We can develop a simple form of this master equation to suit modelling the kinetics of nucleation. Following the assumption that the system volume is quite small, we can plausibly postulate that single bound molecular clusters are the main microstates of the phase space. Consequently, density fluctuation and as a result the transition between macrostates take place by the attachment or depletion of single molecules. Furthermore, the concentration of monomers is very high, especially at the beginning of nucleation, which justifies this assumption and the overlooking of transition by the collision of n-mers, $n > 1$ (Ford, 2016; Kashchiev, 2000). The snapshots of the evolution of such clusters and macrostates are illustrated in Fig. 4.1. Therefore the generic master equation is simplified to

$$\frac{dP_i(t)}{dt} = \sum_{j=i-1, j\neq i}^{j=i+1} \left(P_j(t)\mathcal{T}(j \to i; t) - P_i(t)\mathcal{T}(i \to j; t)\right). \tag{4.2}$$

As in Section 2.1, density fluctuation will be represented by the cluster model and therefore macrostates are identified by the size of molecular clusters in the system.[1] Thus, P_n reads the probability of containing n-size clusters in a small system. Equation (4.2) can then be expanded as follows

$$\frac{dP_n(t)}{dt} = f_{n-1}(t)P_{n-1}(t) - g_n(t)P_n(t) - f_n(t)P_n(t) + g_{n+1}(t)P_{n+1}(t), \tag{4.3}$$

[1] in fact the shape of the cluster should be accounted for as well, because the equally-sized clusters may exist in different shapes. However, this restriction can be relaxed and usually the fixed shape of a cluster in equilibrium is used (Kashchiev, 2000).

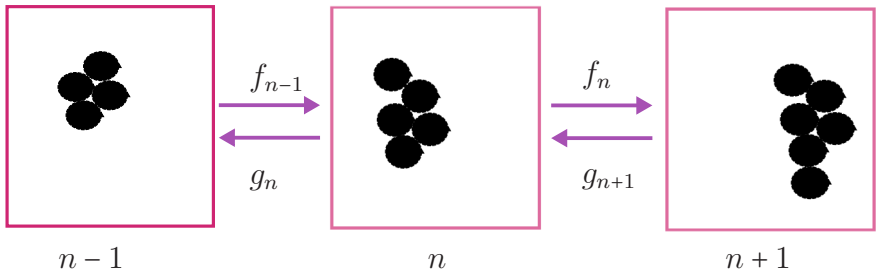

Figure 4.1: Transitions between system macrostates and the snapshots of molecular clusters. Macrostates are identified by the number of molecules in the system creating the density fluctuations. Following the cluster modelling methodology, they are represented by the size of emerged clusters. Growth and decay processes take place according to transition probabilities per unit time f_n and g_n, respectively.

where f_n and g_n are the attachment and detachment frequencies of monomers to and from an n-size cluster, respectively.

The probability P_n in a small system corresponds to the population, i.e. the number density, of n-size clusters in a large system. This is a corollary which results from applying the law of large numbers: the accumulation of many random draws from the probability distribution P_n for the small system actually corresponds to the system populations. Therefore P_n can be replaced by the number density of n-size clusters Z_n which casts a master equation in the following format

$$\frac{dZ_n(t)}{dt} = f_{n-1}(t)Z_{n-1}(t) - g_n(t)Z_n(t) - f_n(t)Z_n(t) + g_{n+1}(t)Z_{n+1}(t), \tag{4.4}$$

This master equation is known as the Szilard equation or the Becker-Döring equation and is used for modelling a birth/death process including nucleation of the new phase from the old phase. This process is illustrated in Fig. 4.1. If N is the time-dependent total number of monomers in the old phase, we will need to solve a set of N ODEs together as $n = 1, 2, \ldots, N$.

In terms of the physics of nucleation, the process is initiated due to ther-

modynamic instability or metastability. Clusters emerge and grow by the positive net flux of monomers. This gradually tends to drop the concentration of monomers (in other words the supersaturation ratio) which terminates the nucleation stage at the limit of the supersaturation ratio of unity. Thus, nucleation terminates when stable thermodynamic equilibrium is reached. With an increase in the concentration of clusters, these may aggregate and form larger clusters which then begins a new stage of the phase transition, termed as the ageing stage. A phenomenon which tends to appear under this condition is Ostwald ripening, which is a process where large clusters absorb monomers from small clusters and decay the concentration of small clusters. The Ostwald ripening regime can be modelled by modifying the above master equation for $n = 1$ as follows (Vetter et al., 2013)

$$\frac{dZ_1(t)}{dt} = -2f_1(t)Z_1(t) + 2g_2(t)Z_2(t) + \sum_{n=3}^{N} g_n(t)Z_n(t) - \sum_{n=2}^{N} f_n(t)Z_n(t), \quad (4.5)$$

Equations (4.4) and (4.5) allow determining the kinetics of nucleation, the growth governed by monomers and the Ostwald ripening processes. The forward flux of a cluster size n along the size axis, i.e. $n \rightarrow n+1$, is given by

$$J_n(t) = f_n(t)Z_n(t) - g_{n+1}(t)Z_{n+1}(t). \quad (4.6)$$

Employing this definition, the master equation shown in Eq. (4.4) transforms to

$$\frac{dZ_n(t)}{dt} = J_{n-1}(t) - J_n(t), \quad (4.7)$$

which shows that the change in the concentration of n-size clusters is governed by an aggregative mechanism and determined by the net flux along the cluster size axis. This holds true if the system is closed for mass exchange. In a system open for mass transportation the non-aggregative change in the concentration of the cluster size n is modeled by adding the following two terms: i) K_n: the

inward flux of n-size clusters to the system from the bath, and ii) L_n: the outward flux of n-size clusters from the system to the bath. Therefore, we arrive at a master equation which encounters the effects of both aggregative and non-aggregative processes on the cluster dynamics

for $n = 1$:

$$\frac{dZ_1(t)}{dt} = -2f_1(t)Z_1(t) + 2g_2(t)Z_2(t) + \sum_{n=3}^{N} g_n(t)Z_n(t) - \sum_{n=2}^{N} f_n(t)Z_n(t) + K_1(t) - L_1(t), \tag{4.8}$$

for $n \geq 2$:

$$\frac{dZ_n(t)}{dt} = f_{n-1}(t)Z_{n-1}(t) - g_n(t)Z_n(t) - f_n(t)Z_n(t) + g_{n+1}(t)Z_{n+1}(t) + K_n(t) - L_n(t). \tag{4.9}$$

The Szilard model is a discrete representation of the master equation and the N equations should be solved consecutively to determine the kinetics of the process. This is computationally expensive and hence a continuous model is favoured. The truncated second-order Taylor expansion of the discrete Szilard equation about point n produces the continuous form of the Szilard model which is known as the Fokker-Planck Equation (FPE) and reads (Kashchiev, 2000)

$$\frac{\partial Z(n,t)}{\partial t} = -\frac{\partial}{\partial n}\left(v(n,t)Z(n,t) - \frac{1}{2}\frac{\partial\left[d(n,t)Z(n,t)\right]}{\partial n}\right) + K(n,t) - L(n,t), \tag{4.10}$$

where $v(n,t)$ and $d(n,t)$ are given by

$$v(n,t) = f(n,t) - g(n,t) \tag{4.11}$$

$$d(n,t) = f(n,t) + g(n,t). \tag{4.12}$$

$v(n,t)$ is the drift velocity along the size axis, known as the growth rate, specifying the rate of deterministic incrementation of the cluster size n. $d(n,t)$ is the rate of random change of the cluster size along the size axis or the dispersion of the cluster size along the size axis.

We explained the discrete and continuous master equations for nucleation, each of which have advantages and disadvantages. To treat the shortcomings associated with either of these, we use a hybrid model in this work which is explained in the next section.

4.1.1 Hybrid model

The FPE is computationally favoured if the concentration of large clusters is desired. However, because of approximations in the derivation of the FPE, it is inaccurate at small clusters compared to the Szilard equation. Therefore a hybrid model is envisaged to take advantage of both the discrete and continuous description of the cluster dynamics (Ozkan and Ortoleva, 2000).

The cluster size axis n is divided into two sections, a discrete part $n = 1, \ldots, N_d$ and a continuous part $n = [N_d + 1, N]$ where N_d is the boundary between the discrete and the continuous sections. N_d is chosen such that the simulation results are independent of this choice and the FPE numerically converges to the result of the Szilard model, i.e. $\|Z_n - Z(n)\|^2 \approx 0$. The boundary condition of the continuity of cluster flux, see Eq. (4.6), is applied at the transition point between the discrete and the continuous models.

The hybrid model allows determination of the dynamics of cluster formation for a broad range of cluster sizes, even up to clusters of a few billion molecules. The hybrid method is schematically illustrated in Fig. 4.2.

For the benefit of the reader, all the equations constructing the hybrid

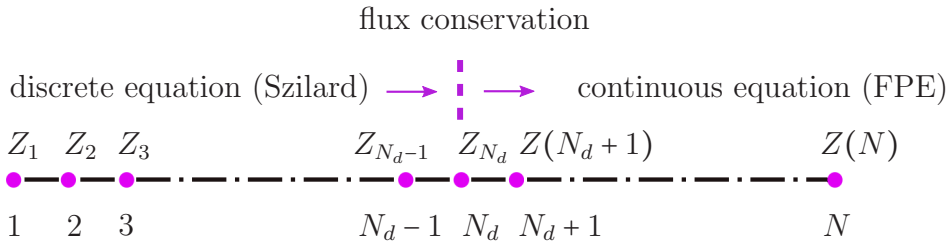

Figure 4.2: Schematic representation of the hybrid model. See the text for details.

model are reproduced below

for $n = 1$:

$$\frac{dZ_1(t)}{dt} = -2f_1(t)Z_1(t) + 2g_2(t)Z_2(t) + \sum_{n=3}^{N} g_n(t)Z_n(t) - \sum_{n=2}^{N} f_n(t)Z_n(t) + K_1(t) - L_1(t), \tag{4.13a}$$

for $1 < n \leq N_d$:

$$\frac{dZ_n(t)}{dt} = f_{n-1}(t)Z_{n-1}(t) - g_n(t)Z_n(t) - f_n(t)Z_n(t) + g_{n+1}(t)Z_{n+1}(t) + K_n(t) - L_n(t),$$

for $N_d < n \leq N$:

$$\frac{\partial Z(n,t)}{\partial t} = -\frac{\partial}{\partial n}\left(v(n,t)Z(n,t) - \frac{1}{2}\frac{\partial[d(n,t)Z(n,t)]}{\partial n}\right) + K(n,t) - L(n,t). \tag{4.13b}$$

4.2 Nucleation rate

Nucleation rate is the rate of appearance of supercritical clusters per unit volume in the system at each time instant. This is also interpreted as the rate of passage of particles over the nucleation barrier. The hybrid model gives the time variable concentration of different clusters which can be used to determine

the nucleation rate as follows

$$J(t) = \frac{d\zeta(t)}{dt}, \tag{4.14}$$

where

$$\zeta(t) = \sum_{n>n^*(t)} Z_n(t), \tag{4.15}$$

and the size of the critical cluster n^* is obtained by solving for the root of Eq. (3.15). This is the generic definition of the nucleation rate and can be used for both stationary and non-stationary phase transition when the old phase is exposed to acoustic waves. This equation requires the solution of the hybrid model over a range of cluster sizes with $N \gg n^*$. However, these calculations can be circumvented under two particular conditions: i) when the system reaches a steady state and therefore the rate at which supercritical clusters appear is constant, and ii) when the system is in equilibrium and hence the detailed microscopic balance holds. The former condition is further discussed in Section 4.2.1 and the latter is explained and used in Section 4.3 to determine the detachment frequencies.

4.2.1 Quasi-stationary and stationary nucleation rate

When the stable supercritical clusters are formed steadily, this follows $dZ_n/dt = 0$ for all cluster sizes which results in $J_1 = J_2 = \cdots = J_{n^*} = \cdots = J_{N-1} = \text{const.} = J_s$, where J_s is the stationary nucleation rate. Writing the rate equation, Eq. (4.6), and applying the stationary condition, we can approximate the stationary nucleation rate by (Kashchiev, 2000)

$$J_s = J_0 \exp\left(-\frac{\Delta\Omega^*}{k_B T}\right), \tag{4.16}$$

where J_0 is a kinetic prefactor and the height of nucleation barrier ($\Delta\Omega^*$) is determined from Eq. (2.47) or Eq. (2.48). J_0 weakly depends on thermodynamic variables controlling the nucleation process and is defined by (Kashchiev,

2000)

$$J_0 \;=\; z f_{n^*} C_0, \tag{4.17}$$

where z is the Zeldovich factor and C_0 is the concentration of nucleation sites in the old phase. For homogeneous nucleation (HON) in a condensed old phase, C_0 is approximated by the number density of molecules as each molecule can work as an active centre for cluster formation. Therefore we can write $C_0 = \frac{N}{V_\Sigma} = \frac{1}{\nu} = \rho$ (Kashchiev, 2000). The Zeldovich factor is given by

$$z \;=\; \left[\frac{-\,d^2\Delta\Omega(n)/dn^2\big|_{n=n^*}}{2\pi k_B T} \right]^{1/2}, \tag{4.18}$$

which takes the following form by using the new model 1 (Eq. (2.57) and using the new surface to define clusters)

$$z^2 \;=\; \left(\frac{2}{9} a_0 \gamma_\infty n_n^{*\,-\frac{4}{3}} n_n'^{*\,2} \;-\; \left(-\Delta\mu \;+\; \frac{2}{3} a_0 \gamma_\infty n_n^{*\,-1/3} \right) n_n''^{\,*} \right) \Big/ \left(2\pi k_B T\right). \tag{4.19}$$

where $\Delta\mu = k_B T \ln(r_0)$, and $n_n'' = \frac{d^2 n_n}{dn^2}$ and is given in Appendix D. Quantities with asterisks are evaluated at the size of the critical cluster. The second term in the numerator ($\left(-\Delta\mu \;+\; \frac{2}{3} a_0 \gamma_\infty n_n^{*\,-1/3}\right) n_n''^{\,*}$) appears only if a non-EDS cluster is used. For the conventional form of CNT, we will have $n_n'' = 0$ and hence this equation simplifies to the typical form of the Zeldovich factor, see (Kashchiev, 2000) for example.

In the physical sense, the Zeldovich factor manifests the probability that a critical cluster can transform to a supercritical cluster and hence $0 < z \leq 1$.

Perturbations in the thermodynamic state of the system lead to the variation in the nucleation work and consequently the Zeldovich factor. This effect can be modelled if we use Eq. (3.13) to calculate the cluster size derivative of the nucleation work in Eq. (4.18). By doing so, we will arrive at

$$
\begin{aligned}
z^2 &= \left(- d^2\Delta\Omega_0(n) \Big/ dn^2 \Big|_{n=n^*} + \int_{T_0}^{T} \Delta s''_{exc} dT + \int_{p_0}^{p} \Delta n''_{exc} \nu dp \right) \Big/ (2\pi k_B T) \\
&= \left(\frac{2}{9} a_0 \gamma_\infty n_n^{*-\frac{4}{3}} n_n'^{*2} - \left(-\Delta\mu + \frac{2}{3} a_0 \gamma_\infty n_n^{*-\frac{1}{3}} \right) n_n''^{*} + \int_{T_0}^{T} \Delta s''_{exc} dT \right. \\
&\quad \left. + \int_{p_0}^{p} \Delta n''_{exc} \nu dp \right) \Big/ (2\pi k_B T) \\
&= z_0^2 + \left(\int_{T_0}^{T} \Delta s''_{exc} dT + \int_{p_0}^{p} \Delta n''_{exc} \nu dp \right) \Big/ (2\pi k_B T) ,
\end{aligned}
\tag{4.20}
$$

where z_0 is the Zeldovich factor at the reference state, $\Delta s''_{exc} = s_n n_n''^{*} + s_\sigma n_\sigma''^{*}$ and $\Delta n''_{exc} = -\frac{\rho}{\rho_n} n_n''^{*}$. For an isothermal condition and an incompressible solution, this equation reads

$$
z^2 = z_0^2 - \frac{\Delta p \ \nu_n \ n_n''^{*}}{2\pi k_B T}. \tag{4.21}
$$

Computing the Zeldovich factor for the supersaturated solution using the new model 1 at different pressure magnitudes shows that the squared Zeldovich factor can be raised by one order of magnitude for an isothermal pressure increase of two orders of magnitude from the ambient pressure, see Figs. 4.3 and 4.4. Also for non-EDS clusters, z^2 deviates from z_0^2 by a very small margin only at high pressure magnitudes, see the dashed curves in Fig. 4.3. Therefore, we can safely invoke the following approximation over this pressure range $z^2(p) \approx z_0^2(p)$ and with a negligible error in the calculation of the nucleation rate, especially given the experimental precision, $z^2(p) \approx z_0^2(p_0)$. Likewise, the pressure and temperature dependence of the Zeldovich factor is usually considered to be weak and hence ignored (Kashchiev, 2000).

Under a typical stationary nucleation condition, the thermodynamic state varies slowly compared to the rate of nucleation of critical clusters. Therefore, the transition rates are considered constant and time-independent. However,

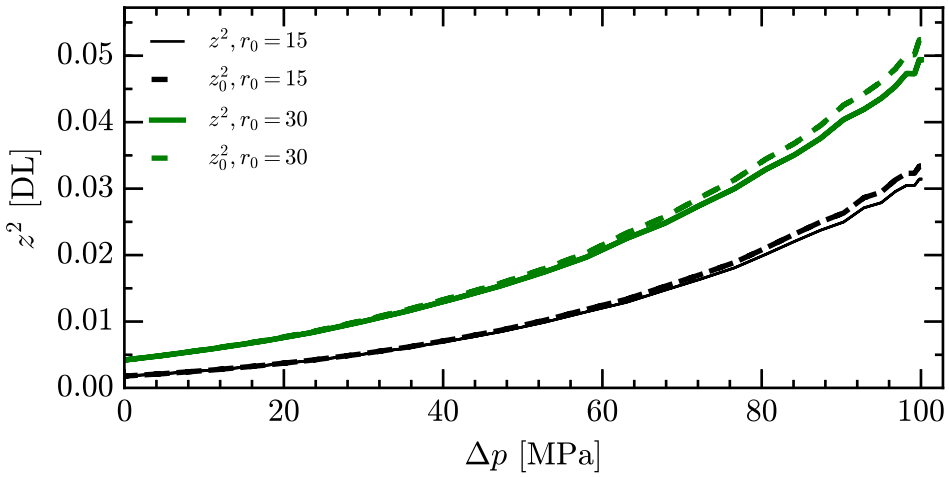

Figure 4.3: z^2, solid curves, and z_0^2, dashed curves, at different pressure magnitudes and at two different supersaturation ratios of $r_0 = 15$ and $r_0 = 30$. The non-EDS cluster model with $\lambda = 0.35$ is considered here.

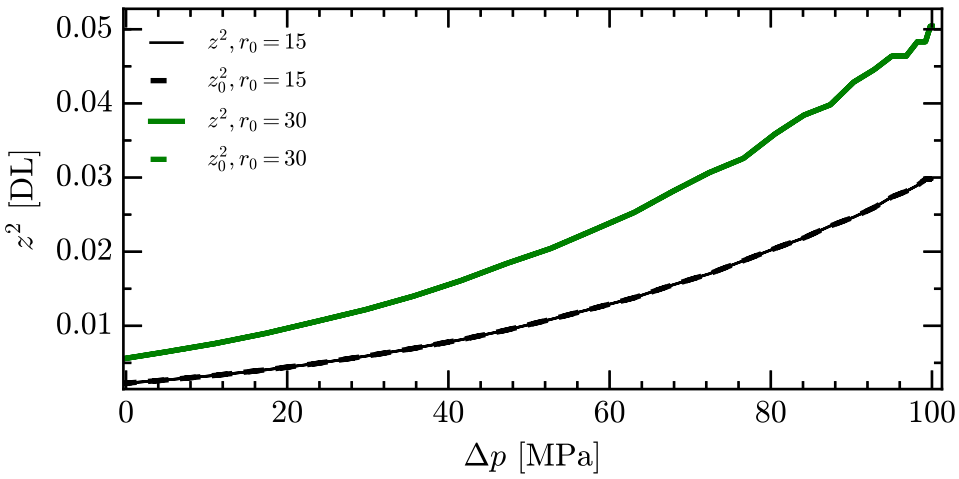

Figure 4.4: Likewise Fig. 4.3 but for the EDS clusters. The small variations at high pressure values are due to numerical calculations.

when the old phase is exposed to acoustic waves, this condition may not hold true due to perturbations in temperature, pressure and the localised supersaturation ratio. Under this condition, transition frequencies and the clusters concentration will be time varying. Nevertheless, when the following condition is satisfied, we can assume the process to be quasi-stationary and use $J_s(t)$ as a first order approximation for the quasi-stationary nucleation rate $J_{qs}(t)$ (Kashchiev, 1970, 2000).

$$\left|\frac{d}{dt}\left(\frac{\Delta\Omega^*(t)}{k_BT(t)}\right)\right| < \frac{16}{\pi^3\tau_n(t)}, \tag{4.22}$$

where τ_n is the time variable nucleation time lag, i.e. the time required to reach to the steady state nucleation at a specific thermodynamic state of the system, and is given by (Kashchiev, 1969b)

$$\tau_n(t) = \frac{4}{\pi^3 z^2(t) f_{n^*}(t)}. \tag{4.23}$$

By virtue of Eqs. (3.20) and (4.23), we can identify the condition for quasi-stationary nucleation in an incompressible old phase while experiencing isothermal wave propagation. This reads

$$\left|\frac{d}{dt}\left(\frac{\Delta\Omega_0^*(t)}{k_BT}\right) - \frac{\Delta n_{exc}^*(t)\ \nu}{k_BT}\frac{d\Delta p}{dt}\right| < 4z^2(t) f_{n^*}(t). \tag{4.24}$$

The instantaneous isothermal Zeldovich factor is obtained from Eq. (4.20) by eliminating the integral of excess entropy. Defining the nucleation work at the reference state as before, the time dependent component at the reference state would be the supersaturation ratio r_0 hence $\Delta\mu$. In a closed system, supersaturation is practically variable as the concentration of monomers gradually decays during nucleation. In addition, in the case the system is open and mass transfer occurs, the concentration of monomers and the supersaturation ratio will be variable as time progresses. n^* changes with time but as a result of variations in the thermodynamic state of the old phase. Therefore, we can write $\frac{d\Delta\Omega_0^*(t)}{dt} = \frac{d\Delta\Omega_0^*(t)}{d\Delta\mu}\frac{d\Delta\mu}{dt} = -n_n^*(t)\frac{d\Delta\mu}{dt}$, which becomes $\frac{d\Delta\Omega_0^*(t)}{dt} = -n_n^*(t)\ k_BT\ \frac{\dot{r_0}(t)}{r_0(t)}$, if we use the equation of $\Delta\mu = k_BT\ln(r_0(t))$ and assume that the equilibrium surface tension at the reference state, i.e. γ_∞, is independent of the supersaturation ratio r_0. The single overdot denotes the first derivative of a variable with respect to time. This relationship together with $\frac{d\Delta p}{dt} = \frac{d(p(t)-p_0)}{dt} = \frac{dp(t)}{dt}$, allow simplifying Eq. (4.24) to the following format

$$\left|-n_n^*(t)\frac{\dot{r_0}(t)}{r_0(t)} - \frac{\Delta n_{exc}^*(t)\ \nu}{k_BT}\dot{p}(t)\right| < 4z^2(t) f_{n^*}(t), \tag{4.25}$$

it subsequently follows that

$$\left| \dot{r_0}(t) \; + \; \frac{r_0(t)\; \Delta n^*_{exc}(t)\; \nu}{n^*_n(t)\; k_B T} \dot{p}(t) \right| < \frac{4}{n^*_n(t)} r_0(t) z^2(t) f_{n^*}(t). \tag{4.26}$$

This relationship states that if the total rate of an isothermal change in the supersaturation ratio and pressure in the system is slower than the rate with which monomers collide with a critical cluster, the process can be considered quasi-stationary and the nucleation rate can be approximated by Eq. (4.16). In the closed system, the rate of the variation in the supersaturation ratio ($\dot{r_0}(t)$) is related to the depletion of monomers and is quite slow (Kashchiev, 2000). Thus, the LHS of the above equation can be approximated by the pressure term only which gives

$$|\dot{p}(t)| < \frac{4 k_B T}{\Delta n^*_{exc}(t)\; \nu} z^2(t) f_{n^*}(t). \tag{4.27}$$

This equation allows checking the condition for quasi-stationary nucleation in a closed system exposed to isothermal wave propagation. Considering Eq. (4.27), the quasi-stationary condition holds when an isothermal perturbation of pressure at any point in the wave field happens more slowly than the weighted attachment rate of monomers to a critical cluster.

Equation (4.27) is valid for a closed system exposed to any acoustic waveform. Modelling the pressure oscillation in the system by a single frequency tone of $p_a = p_m \cos(2\pi f t)$ further simplifies this equation to

$$2\pi f \, |p_m \sin(2\pi f t)| < \frac{4 k_B T}{\Delta n^*_{exc}(t)\; \nu} z^2(t) f_{n^*}(t), \tag{4.28}$$

which rearranges to

$$f < \frac{2 k_B T}{\pi \; \Delta n^*_{exc}(t) \; \nu \; |p_m \sin(2\pi f t)|} z^2(t) f_{n^*}(t), \tag{4.29}$$

and can be reformulated as

$$f < k_p(t) f_{n^*}(t), \tag{4.30}$$

where

$$k_p = \frac{2}{\pi} \frac{k_B T}{\Delta n^*_{exc}(t)\ \nu\ p_m}\ \frac{z^2(t)}{|\sin(2\pi f t)|} = \frac{2}{\pi} \frac{1}{(\Delta n^*_{exc}(t)\ \nu\ p_m)\,/k_B T}\ \frac{z^2(t)}{|\sin(2\pi f t)|}. \tag{4.31}$$

The coefficient k_p is the instantaneous weight of the attachment frequency to the critical cluster at that time instant and conveys a physical meaning which can be inferred by using Eq. (3.19) as follows

$$k_p = \frac{2}{\pi} \frac{k_B T}{-p_m \left(\dfrac{\partial \Delta\Omega^*}{\partial p}\right)_T}\ \frac{z^2(t)}{|\sin(2\pi f t)|}. \tag{4.32}$$

The second fraction in the above equation is the inverse of the pressure induced change in the nucleation work (or the height of nucleation barrier) normalised by the thermal energy $k_B T$. Thus, if pressure substantially increases the nucleation barrier, the denominator of this term tends to become a large number which may result in a small value of k_p. This may violate the condition shown in Eq. (4.30) if the driving frequency is high enough.

As shown in Figs. 4.5 to 4.8, k_p can drop to 10^{-13} for the solution with supersaturation ratio $r_0 = 15$, at $p_m = 100$ MPa and $10^{-4.5}$ at $p_m = 10$ MPa. For this supersaturated solution, f_{n^*} is of the order of $10^8 - 10^{10}$ s^{-1} (Kashchiev, 2000). Therefore, the quasi-stationary condition will be violated at a driving frequency of the order of kHz and MHz if p_m is about 100 MPa and 10 MPa, respectively. This combination of frequency and pressure magnitude can be readily created experimentally when the acoustic field is generated by a high intensity focused ultrasound (HIFU) transducer.

Computation of the kinetics of nucleation and the nucleation rate require the transition frequencies. This is the subject of Section 4.3.

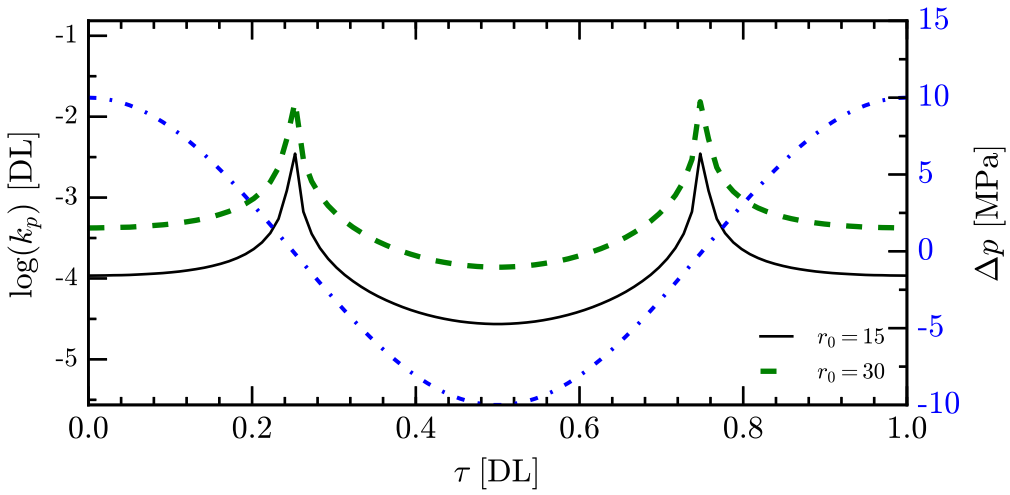

Figure 4.5: $k_p(t)$ over non-dimensionalised time (one period of excitation) with parameters p_m = 10 MPa, f = 100 kHz at r_0 = 15 and r_0 = 30. Clusters are defined by λ = 0.35.

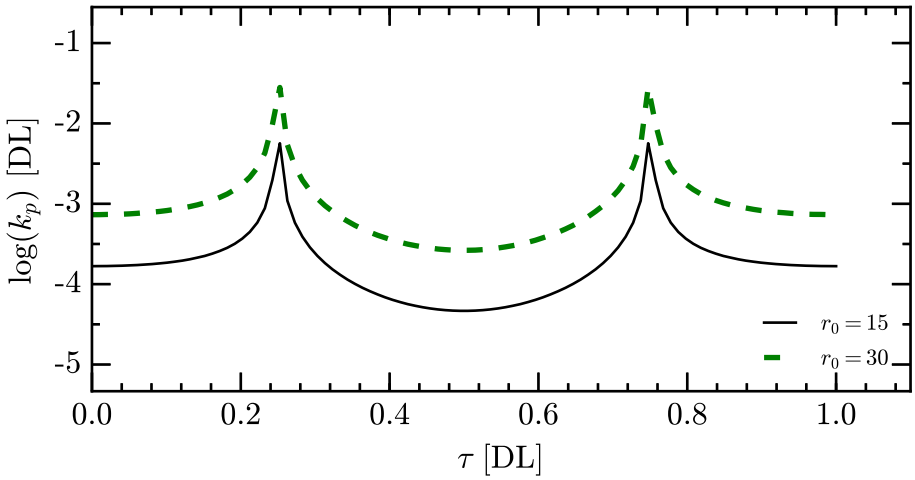

Figure 4.6: $k_p(t)$ calculated for EDS over non-dimensionalised time (one period of excitation) with parameters p_m = 10 MPa, f = 100 kHz at r_0 = 15 and r_0 = 30.

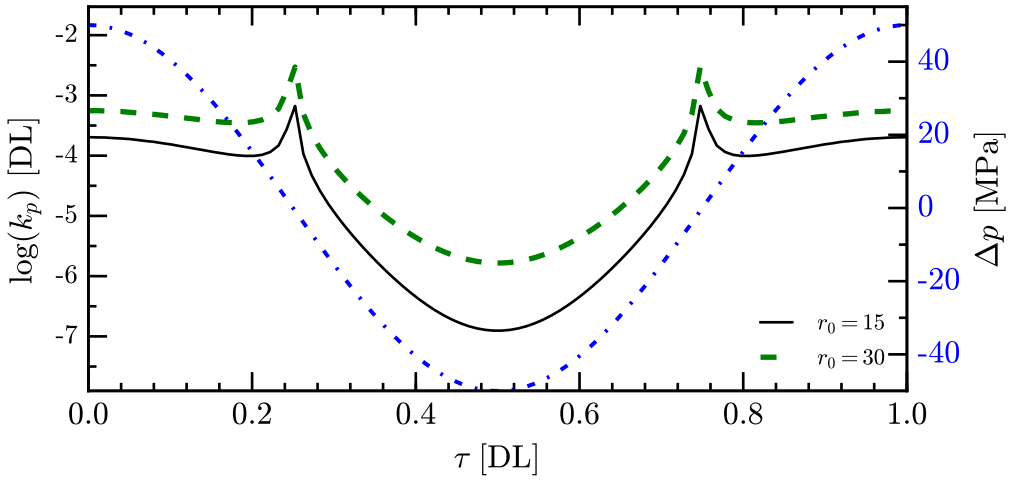

Figure 4.7: Similar to Fig. 4.5 but with parameters p_m = 50 MPa, f = 100 kHz at r_0 = 15 and r_0 = 30. Clusters are defined by λ = 0.35.

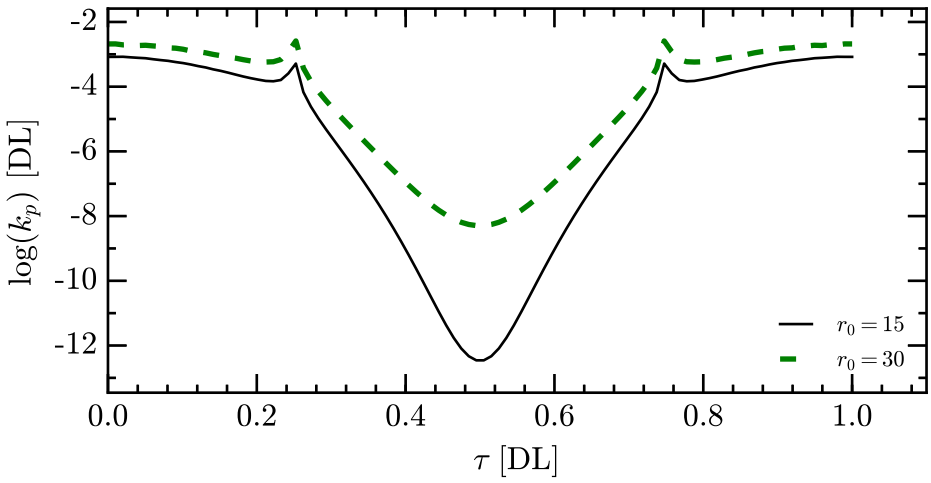

Figure 4.8: Similar to Fig. 4.5 but with parameters p_m = 100 MPa, f = 100 kHz at r_0 = 15 and r_0 = 30.

4.3 Transition frequencies

In the master equation, Eq. (4.1), the probability that the system reaches the macrostate j from the macrostate i is given by $\mathcal{T}(i \to j; t)$. In the case of nucleation, we identified macrostates by the size of clusters emerging in the old phase and assumed that the transition mechanism is the attachment and detachment of monomers to and from a cluster. Therefore we used the monomer attachment and detachment frequencies to model the dynamics of the process of cluster formation. In this section, we present equations for these transition frequencies and will study the effect of pressure and temperature perturbations on them.

4.3.1 Monomer attachment frequency

The monomer attachment to a condensed-phase cluster depends on the state of the old phase. The three main governing mechanisms of the monomer attachment in HON are (Kashchiev, 2000): i) direct impingement of molecules, ii) volume diffusion of molecules and iii) transfer of molecules through the interface of the cluster with the old phase. The direct impingement is the governing mass transport mechanism when the old phase is gaseous. In the case of homogeneous nucleation in liquid or solutions, the latter two mechanisms are mainly considered. The interface-transfer is governed by a random jump of monomers in the vicinity of a cluster over a distance comparable with the molecular diameter. Thus, the probability of the interface transfer is proportional with the concentration of monomers in immediate contact with the cluster. This quantity is unknown and usually approximated by the concentration of monomers in the bulk old phase Z_1. Nevertheless, this concentration tends to fade in dilute solutions. Volume diffusion happens by the diffusion flux of monomers towards the surface of a cluster. Therefore it depends on the surface area of the cluster, the diffusivity and the concentration of monomers in the old phase.

Given the physics of the interface transfer, the models that have been developed for this process bear many approximations, see (Kashchiev, 2000) for

example, though volume diffusion models are laid out based on solid foundations. Nevertheless, both mechanisms may take place simultaneously depending on the cluster size, e.g. for small clusters interface transfer may be dominant and once the cluster has grown enough the volume transfer becomes more important. Kashchiev showed that for $n > 8$, the attachment of monomers in solutions is expected to be controlled by volume diffusion (Kashchiev, 2000). In spite of this, the rates obtained by either of this methods are of the same order of magnitude (Kashchiev and Van Rosmalen, 2003). Consequently, we can postulate that volume diffusion is the controlling monomer attachment mechanism for all clusters if homogeneous nucleation of solids in a dilute solution exposed to acoustic waves is the matter of concern.

Volume diffusion can be modelled based on two different approaches: i) the continuum approach, i.e. modelling the conservation of condensable mass in a supersaturated solution, and ii) the atomic approach, i.e. using a random-walk model to determine the probability of collision of a monomer with a cluster and estimating the attachment frequency accordingly. Using the first approach, the attachment frequency of monomers to a spherical n-size cluster in the condensed phase is given by (Kashchiev, 2000)

$$f_n(t) = k_f(n_n)Z_1(t), \tag{4.33}$$

where

$$k_f(n_n) = 4\pi\alpha_n D R_0(1 + n_n^{-1/3})(1 + n_n^{1/3}), \tag{4.34}$$

where α_n is the sticking coefficient which is nearly unity in a dilute solution and D is the diffusivity of a monomer in the old phase. Here we assumed that both cluster and monomers are mobile and diffusing through the medium. This is implemented by using the effective diffusivity and radius for collision between a monomer and an n-size cluster, as shown by Smoluchowski (Ziff et al., 1985).

The diffusivity of a cluster was estimated based on the Stokes-Einstein

equation. k_f resembles the collision kernel of a monomer with an n-mer in the Smoluchowski coagulation equation. This notion may be employed to generalise this equation for the case of non-spherical clusters by making a modification of the collision kernel using the fractal dimension of the cluster (Ziff et al., 1985). These equations are valid for both discrete and continuous cluster size variable n.

The RHS of Eq. (4.30) is calculated using Eq. (4.33) and results are plotted for different excitation settings in Figs. 4.9 to 4.11. We can see that the quasi-stationary condition only holds for the setting of $r_0 = 15, f = 100$ kHz$, p_m =$ 1 MPa and is violated for other settings. Hence, nucleation in a dilute solution exposed to low excitation amplitude and frequency may be treated as a quasi-stationary process. However, nucleation in a high frequency/intensity sound field is a non-stationary process.

4.3.2 Monomer detachment frequency

The rate at which monomers detach from an n-size cluster depends on the characteristics of the clusters rather than properties of the bulk new phase. This rate can be estimated following the Zeldovich method which integrates the thermodynamics under equilibrium condition into the cluster dynamics. At the thermodynamic equilibrium state, a balance between the number of monomers gained and lost by two adjacent clusters on the size axis, i.e. $J_{n,eq} = 0$, should hold. The generalised form of the Zeldovich method for the case of time-variable supersaturation and a quasi-equilibrium condition, reads (Kashchiev, 1969a)

$$g_n(t) \;=\; f_{n-1}(t)\;\exp\left(\frac{\Delta\Omega_n(t) - \Delta\Omega_{n-1}(t)}{k_B T(t)}\right), \tag{4.35}$$

and this equation for the case of continuous cluster size n becomes

$$g(n,t) \;=\; f(n,t)\;\exp\left(\frac{\dfrac{\partial}{\partial n}\Delta\Omega(n,t)}{k_B T(t)}\right). \tag{4.36}$$

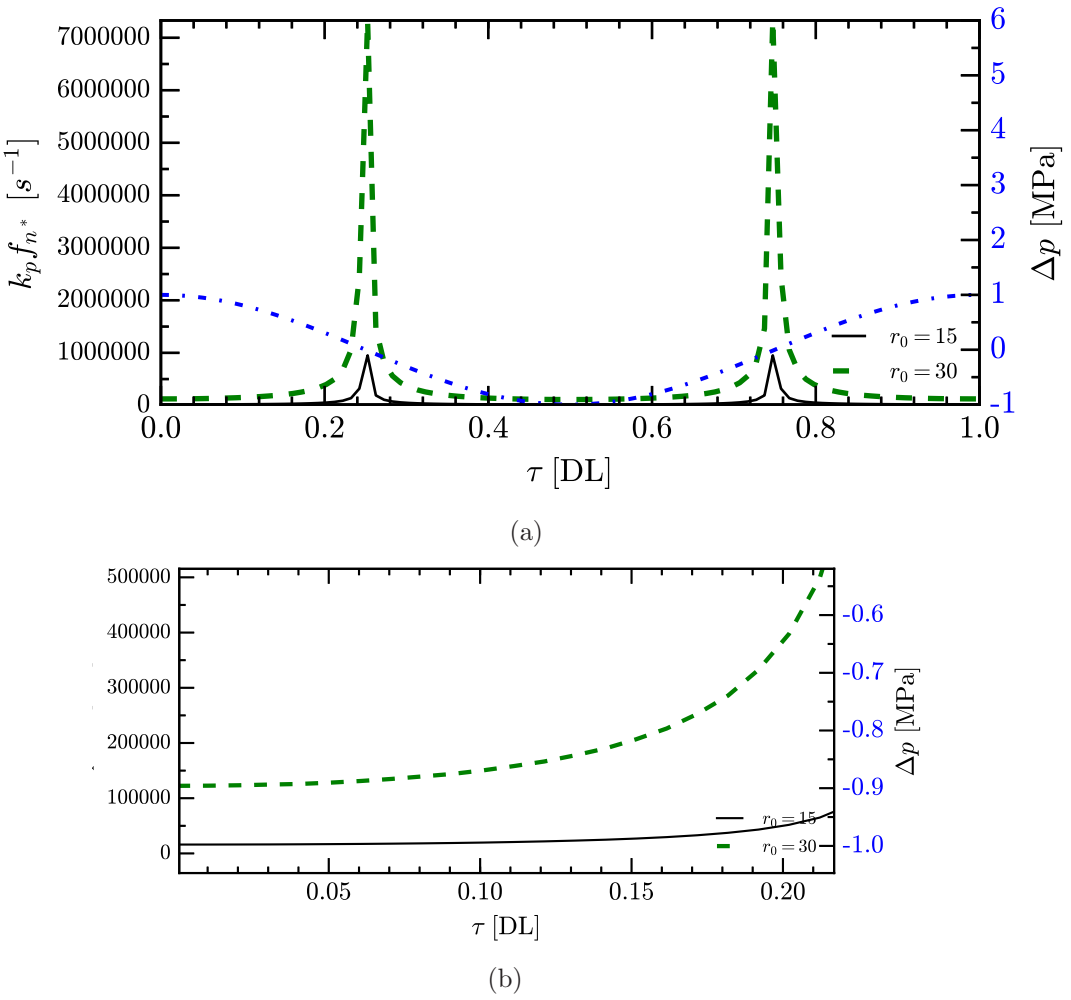

Figure 4.9: The RHS of Eq. (4.30) calculated with p_m = 1 MPa, f = 100 kHz at r_0 = 15 and r_0 = 30 for non-EDS clusters with λ = 0.35 over (a) an oscillation period, (b) magnified about time interval $0 < \tau < 0.2$.

For the sake of brevity, the time variable t will not be noted in the following equations while all parameters are considered to be time-dependent. Substituting Eq. (3.14) into above equation results in

$$\begin{aligned} g(n,p,T,x) \quad = \quad & f(n,x)\exp\left(\frac{1}{k_B T}\frac{\partial \Delta\Omega_0}{\partial n}\right) \\ & \times \exp\left(\frac{1}{k_B T}\int_T^{T_0} \Delta s'_{exc} dT\right) \\ & \times \exp\left(\frac{1}{k_B T}\int_p^{p_0} \Delta n'_{exc}\nu dp\right). \end{aligned} \tag{4.37}$$

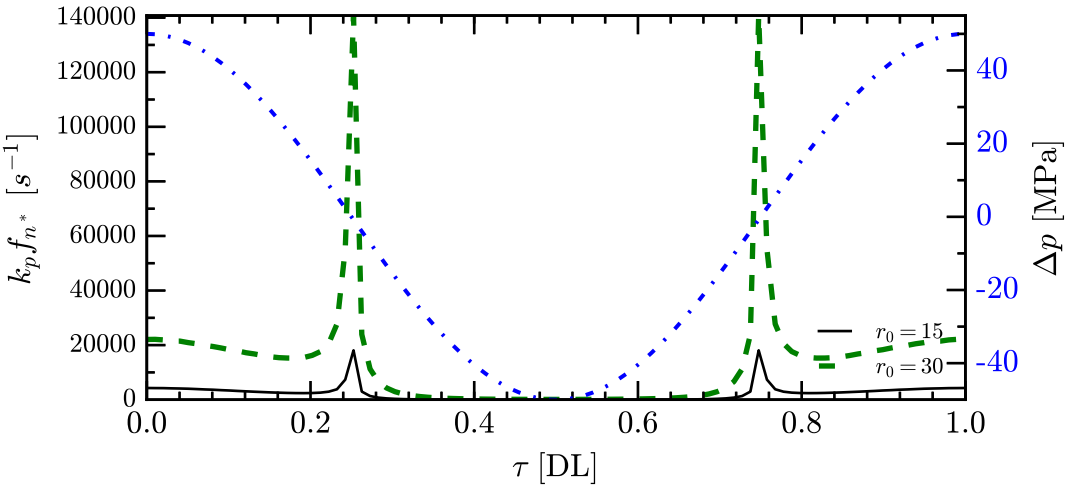

Figure 4.10: Likewise Fig. 4.9 with p_m = 50 MPa, f = 100 kHz at r_0 = 15 and r_0 = 30 for non-EDS clusters with λ = 0.35.

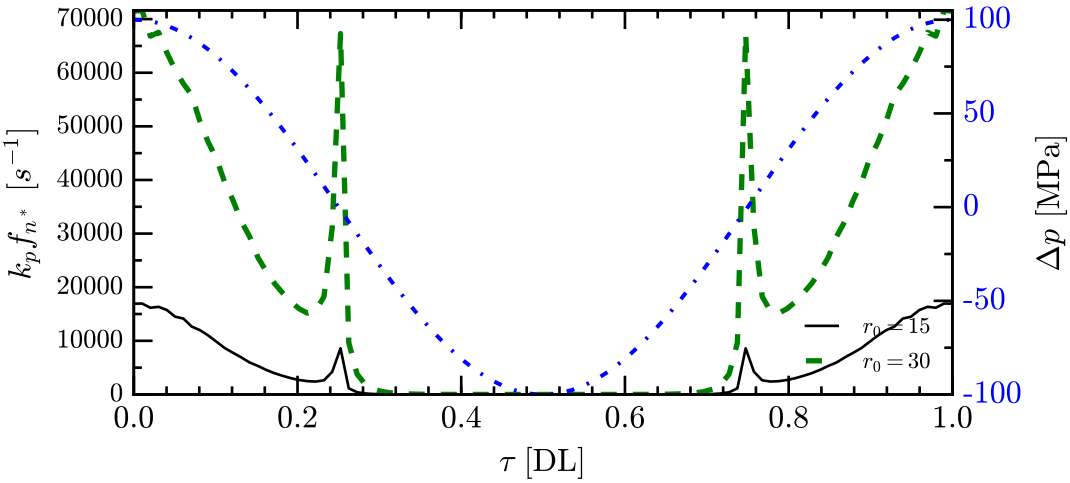

Figure 4.11: Likewise Fig. 4.9 with p_m = 100 MPa, f = 1 MHz at r_0 = 15 and r_0 = 30 for non-EDS clusters with λ = 0.35.

The minus signs before the integrals in Eq. (3.14) are removed here by reversing the integration limits. This equation manifests the effect of a change in temperature and pressure on the detachment frequency of monomers from a cluster of the size n. In our case where we are interested in investigating the effects of acoustic waves on nucleation and growth, this equation gives the full picture within the framework of the cluster dynamics by accounting for the effect of: i) pressure fluctuation, ii) temperature variation due to absorption or cavitation of a bubble, and iii) mass transportation via pressure diffusion. If

we use the same reference state as before, after some manipulations we obtain

$$
\begin{aligned}
g(n,p,T,x) \quad = \quad & f(n,x)\; r_0^{\left[\frac{T_0}{T}(n_\sigma{}'(n_n)-1)\right]} \\
& \times \exp\left(\frac{2}{3}\frac{a_0\gamma_\infty}{k_BT} n_n^{-1/3} n_n'(n_n)\right) \\
& \times \exp\left(\frac{1}{k_BT}\int_T^{T_0} \Delta s'_{exc} dT\right) \\
& \times \exp\left(\frac{1}{k_BT}\int_p^{p_0} \Delta n'_{exc}\nu dp\right). \qquad (4.38)
\end{aligned}
$$

So far, we considered the cluster size n to be a continuous variable. It is shown in Appendix E that equations derived for the detachment frequency for the case of continuous n can also be used for the case of discrete representation of the cluster formation work. Consequently Eqs. (4.37) and (4.38) can be employed in conjunction with the Szilard model, too.

4.3.2.1 Incompressible solution and isothermal condition

The nucleation work and nucleus size in an incompressible solution which is exposed to an acoustic wave were studied in Section 3.3. Here we are interested in calculating the attachment and detachment frequencies under this condition. Given the volume diffusion mechanism, the diffusivity and the concentration of monomers are the main factors affecting the attachment rate of monomers to an n-mer. The effect of pressure on diffusivity is almost negligible due to weak pressure dependence of viscosity and incompressibility of the solution. The concentration of monomers can be spatially influenced by mass transportation due to pressure diffusion. This effect is negligible at low and medium pressure magnitudes. Nevertheless, in strong acoustic fields and especially in the vicinity of an oscillating surface, e.g. near the wall of an inertially collapsing bubble, mass transportation can be significant and should be accounted for (Louisnard et al., 2007).

An acoustic wave propagating in a solution alters the thermodynamic state and consequently changes the detachment frequency, as demonstrated in

Eq. (4.38). In the case of an isothermal condition and pressure independent partial molecular density, this equation simplifies to

$$g(n,p,T,x) = f(n,x)\; r_0^{(n_\sigma{}'(n_n)-1)} \exp\left(\frac{2}{3}\frac{a_0\gamma_\infty}{k_BT} n_n^{-1/3} n_n'(n_n)\right) \times \exp\left(-\frac{\nu\Delta p}{k_BT}\Delta n'_{exc}\right). \quad (4.39)$$

Subsequently, approximating the molar concentration with the concentration of monomers, i.e. $r_0 = \frac{x_0}{x_e} = \frac{Z_1}{C_e}$ where C_e is the solubility at the reference state, we arrive at

$$g(n,p,T,x) = k_f(n_n)\; C_e r_0^{n_\sigma{}'(n_n)} \exp\left(\frac{2}{3}\frac{a_0\gamma_\infty}{k_BT} n_n^{-1/3} n_n'(n_n)\right) \times \exp\left(-\frac{\nu\Delta p}{k_BT}\Delta n'_{exc}\right). \quad (4.40)$$

The latest assumption is justified because the concentration of monomers in the system at the initial time and during nucleation is significantly greater than that of n-mers. The situation that n-size clusters, $2 \le n \le 4$, are present in the initial condition was studied before (Kozísek and Demo, 2005) and it was shown that the nucleation rate would change by less than one order of magnitude. Consequently, the considered initial condition is justified for our work.

Equation (4.40) predicts a detachment frequency which is supersaturation-dependent for very small clusters but almost supersaturation-independent in the limit of large clusters (as shown in Appendix D, in the limit of large clusters $n_\sigma{}'(n_n)$ tends to zero, i.e. $\lim_{n_n\to\infty} n'_\sigma = 0$). In the literature, the detachment frequency (also denoted by evaporation or decay rate) is usually reported to be intrinsic to the cluster, i.e. it is explicitly independent of the surrounding supersaturation (Ford, 1997; Schaaf et al., 2001; Kashchiev, 2000). However, Kashchiev (Kashchiev, 2000) states that, this holds true as long as the excess

free energy of the cluster is $\Delta\mu$-independent and the process is isothermal. Unlike the EDS-defined clusters, the excess free energy of non-EDS clusters depends on $\Delta\mu$ as is shown in Eq. (2.57) and also Eq. (3.88) in (Kashchiev, 2000).

In addition, the MD simulations of homogeneous nucleation of a supersaturated vapour phase at the triple point temperature for a Lennard-Jones fluid show a supersaturation-dependent decay rate for small clusters (Yasuoka and Matsumoto, 1998). Yasuoka and Matsumoto have shown that decay rates in the supersaturated vapour are larger than those in the vacuum for small clusters of $10 < n < 40$. In contrast, the decay rates in these two situations fairly match for larger clusters ($n > 40$). This trend of the supersaturation ratio dependence of the detachment frequency is in qualitative agreement with the theoretical predictions of Eq. (4.40). In spite of this agreement, further elaborations require access to the values of the detachment frequency calculated by statistical mechanical simulations in the limit of small clusters. Apart from the work of (Yasuoka and Matsumoto, 1998), we are not aware of such published works.

4.4 Non-dimensionalisation

We will non-dimensionalise the hybrid model for a mass conserved system to reduce the number of parameters, to estimate the relative physical significance of different terms, and to facilitate the numerical implementation of the hybrid master equations. Given the terms in Eq. (4.13) while imposing the mass conserved condition $K_n(t) = L_n(t) = 0$, we can write the following relationships for the non-dimensionalisation

$$t = t_c\ \tau, \qquad Z_n = z_c\ \overline{Z_n}, \qquad f_n = f_c\ \overline{f_n}, \qquad g_n = g_c\ \overline{g_n}. \tag{4.41}$$

Taking Eq. (4.38) into account, essentially $g_n = f_n \square$ where $\square$ is a dimensionless quantity which results in $g_c = f_c$. Substituting these relations into the

first line of Eq. (4.13) and after some manipulations we arrive at

$$\frac{d\overline{Z_1}}{d\tau} = -2f_c t_c\,\overline{f_1}(t)\overline{Z_1} + 2g_c t_c\,\overline{g_2}(t)\overline{Z_2} + g_c t_c \sum_{n=3}^{N}\overline{g_n}(t)\overline{Z_n} - f_c t_c \sum_{n=2}^{N}\overline{f_n}(t)\overline{Z_n}. \tag{4.42}$$

For simplicity, we choose the following set of non-dimensionalisation coefficients

$$f_c\; t_c = g_c\; t_c = 1, \tag{4.43}$$

where $t_c = 1/4\pi R_0 D C_e$, see Eq. (4.34). The term $1/4\pi R_0 D C_e$ is equal to the rate of impingement of the solute monomers together in an infinitely dilute solution in equilibrium and depends on the physical properties of the solution.

We also choose the equilibrium monomer concentration to non-dimensionalise the concentration of clusters, i.e. $z_c = C_e$. This technically means that $\overline{Z_1}(t) = r_0(t)$ if we use the approximation just mentioned above. Exploiting these scaling factors in Eq. (4.42) yields

$$\frac{d\overline{Z_1}}{d\tau} = -2\overline{f_1}(t)\overline{Z_1} + 2\,\overline{g_2}(t)\overline{Z_2} + \sum_{n=3}^{N}\overline{g_n}(t)\overline{Z_n} - \sum_{n=2}^{N}\overline{f_n}(t)\overline{Z_n}, \tag{4.44}$$

where using Eqs. (4.34) and (4.40) gives

$$\overline{f_n} = (1+n_n^{-1/3})(1+n_n^{1/3})\overline{Z_1}, \tag{4.45}$$

$$\overline{g_n} = (1+n_n^{-1/3})(1+n_n^{1/3}) r_0^{n_\sigma'(n_n)} \exp\left(\frac{2}{3}\frac{a_0\gamma_\infty}{k_B T} n_n^{-1/3} n_n'(n_n)\right) \times \exp\left(-\frac{\nu\Delta p}{k_B T}\Delta n_{exc}'\right). \tag{4.46}$$

Terms $\dfrac{a_0\gamma_\infty}{k_B T}$ and $\dfrac{\nu\Delta p}{k_B T}$ are dimensionless quantities referring to the relative

surface energy and relative change in chemical potential of the system because of a pressure variation, respectively.

Repeating the same procedure for other equations in the hybrid model gives the non-dimensionalised hybrid model for a mass conserved system as follows

for $n = 1$:

$$\frac{d\overline{Z_1}}{d\tau} = -2\overline{f_1}(t)\overline{Z_1} + 2\,\overline{g_2}(t)\overline{Z_2} + \sum_{n=3}^{N}\overline{g_n}(t)\overline{Z_n} - \sum_{n=2}^{N}\overline{f_n}(t)\overline{Z_n}, \quad (4.47a)$$

for $1 < n \leq N_d$:

$$\frac{d\overline{Z_n}}{d\tau} = \overline{f_{n-1}}\;\overline{Z_{n-1}} - \overline{g_n}\;\overline{Z_n} - \overline{f_n}\;\overline{Z_n} + \overline{g_{n+1}}\;\overline{Z_{n+1}}, \quad (4.47b)$$

for $N_d < n \leq N$:

$$\frac{\partial\overline{Z(n)}}{\partial\tau} = -\frac{\partial}{\partial n}\left(\overline{v(n)}\;\overline{Z(n)} - \frac{1}{2}\frac{\partial\left[\overline{d(n)}\;\overline{Z(n)}\right]}{\partial n}\right), \quad (4.47c)$$

where the dimensionless growth and dispersion rates read

$$\overline{v(n)} = \overline{f(n)} - \overline{g(n)}, \quad (4.48)$$

$$\overline{d(n)} = \overline{f(n)} + \overline{g(n)}, \quad (4.49)$$

where $\overline{f(n)}$ and $\overline{g(n)}$ are calculated by evaluating Eq. (4.45) for the continuous cluster size n.

4.5 Summary

The kinetics of nucleation in a mass conserved system was studied in this chapter. The attachment and detachment of monomers are assumed to be the

controlling mechanisms of the cluster dynamics calculated by solving a hybrid model. The hybrid model is essentially a combination of the discrete Szilard equation and the FPE which allows computation of the cluster dynamics across a broad range of cluster sizes. This model is valid for any thermodynamic state of the old phase and gives a wealth of information about the process, e.g. the CSD, the nucleation time lag, the nucleation rate.

To solve this hybrid model, equations of transition frequencies under acoustic excitation are required which were determined here. For a closed system and an incompressible old phase, variations in pressure and temperature of the old phase influence the detachment frequency of monomers whereas the attachment frequency remains intact. Equations (4.37) and (4.38) account for these effects on the monomer detachment rate from a generic cluster and a cluster identified by the new surface and new model 1 , respectively.

Solving the hybrid model is computationally expensive and time-consuming. When the kinetics of the cluster formation is a stationary or quasi-stationary process, we can determine the kinetics using explicit equations which are favoured for numerical implementation. We derived the condition for quasi-stationary phase transformation in a system exposed to acoustic waves, see Eq. (4.26) for a generic system and Eqs. (4.27) and (4.30) for a closed system. We showed that the quasi-stationary condition for crystallisation in a solution is likely to be dismissed at high pressure magnitudes and excitation frequencies, especially at a low supersaturation ratio.

Finally, we investigated the effect of pressure and temperature perturbations on the Zeldovich factor and derived Eq. (4.20) which accounts for these effects. The numerical calculations for a generic solution, under isothermal condition, demonstrate that the Zeldovich factor is fairly pressure independent and can be approximated by its value at the reference state.

In this chapter, we laid the foundations for the calculation of the phase transformation kinetics in a closed system subjected to wave propagation, hence overlooking mass transport effects of wave propagation. This phenome-

non and its effect on the cluster dynamics are the subject of the next chapter.

Chapter 5

Kinetics of cluster formation II: Non-mass conserved system

Hitherto, we have studied the thermodynamics and kinetics of phase transformation in a closed system subjected to pressure and temperature perturbations. We have shown that in a closed system, these localised perturbations influence the thermodynamics and kinetics of nucleation by changing the work of cluster formation and consequently the detachment frequency of monomers. Thus, a model based on the closed system assumption only explains the effect of wave propagation on the aggregative mechanism of cluster formation (nucleation and growth). Nevertheless, acoustic waves propagate across space and therefore pressure and temperature will vary across both space and time. These spatial gradients and their second order effects such as acoustic streaming may generate mass transportation and heat transfer. These effects produce the non-aggregative mechanism which influences the kinetics of the phase transition.

In this chapter we relax the assumption of the closed system and will include the effect of mass transportation mediated by wave propagation. The objective is to cast a kinetic model, both in discrete and continuous forms, which accounts for the effects of wave propagation on both aggregative and non-aggregative mechanisms. We will determine the net flux of clusters to the system, i.e. the term $K_n - L_n$ in Eqs. (4.8) and (4.10), resulting from wave

propagation. As it is explained in Section 2.6, the solution is modelled as a mixture of two species, namely the solute and solvent. Therefore, we will begin this chapter with the continuity equation for a mixture and we will proceed with the calculation of forced diffusion created by wave propagation. Initially in Section 5.1 we will consider only non-aggregative clusters to be present in the system. We will then combine this contribution with the previous results obtained in Section 4.1 to achieve a model which accounts for both aggregative and non-aggregative effects of acoustic waves which we will present in Section 5.2.

5.1 Conservation of mass in a mixture

This section concentrates on the non-aggregative mechanism and therefore we will ignore clustering and coalescence of clusters and assume the behaviour of clusters are independent of each other in the solution.

A schematic of the system in a bath is shown in Fig. 2.2. We now consider the same system and assume that it is a volume element fixed in space. Its position relative to the origin of a fixed system of coordinates is specified by the position vector $\mathbf{r}$. All the physical variables like density, pressure, and temperature will therefore be functions of space and time. Denoting the properties of the solution, the solvent and the solute with suffices *m, 1* and *2*, respectively, the mass density of the solution reads $\rho_m(t,\mathbf{r}) = \rho_1(t,\mathbf{r}) + \rho_2(t,\mathbf{r})$. In the previous chapters, we have used number density instead of mass density. The relationship between these densities are as follows: for instance for the old phase number density is equal to $\rho(t,\mathbf{r}) = \dfrac{\rho_2(t,\mathbf{r})\,\mathcal{N}_\mathcal{A}}{M_2}$ where M_2 is the molar weight of the solute and $\mathcal{N}_\mathcal{A}$ is the Avogadro's number.

The conservation of mass for the solution is given by (Bird et al., 1960)

$$\frac{\partial \rho_m(t,\mathbf{r})}{\partial t} = -\nabla\cdot(\rho_m(t,\mathbf{r})\ \mathbf{u}), \tag{5.1}$$

which in the case of an incompressible fluid, i.e. a solution with constant mass density, becomes

$$\nabla \cdot \mathbf{u} = 0. \tag{5.2}$$

Here $\mathbf{u}$ is the velocity vector in the Cartesian coordinate system.

The generic form of the conservation of mass for the solute species in the solution reads (Bird et al., 1960)

$$\frac{\partial \rho_2(t,\mathbf{r})}{\partial t} = -\rho_2(t,\mathbf{r})\ \nabla \cdot \mathbf{u} - \mathbf{u} \cdot \nabla \rho_2(t,\mathbf{r}) - \nabla \cdot \mathbf{j_2}, \tag{5.3}$$

where $\mathbf{j_2}$ is the molecular flux of species 2 (the solute). This equation expresses the rate of change in the total number of the solute molecules accumulated in the volume element resulting from different mass transport mechanisms: the convective flux (the first two terms on the RHS) and the molecular flux of the solute species (the last term on the RHS). Convection represents mass transportation due to the average velocity of all molecules which is the average velocity of the fluid as a whole. Diffusion is viewed as mass transportation due to the instantaneously changing stochastic velocity of individual molecules, compared to the averaged fluid velocity. For the transportation of dilute species in a mixture where the solvent dominates the momentum of the system, we can consider a reference velocity equal to the velocity of the dominant component, i.e. the solvent here, and identify a diffusive flux and a convective flux accordingly.

Considering the cluster size as a discrete variable, we can write mass density of the solute species in terms of concentration of different clusters as follows

$$\frac{\rho_2(t,\mathbf{r})\ \mathcal{N}_\mathcal{A}}{M_2} = \sum_{n=1}^{N(t)} n Z_n(t,\mathbf{r}), \tag{5.4}$$

Defining $Y_n(t,\mathbf{r}) = \frac{M_2}{\mathcal{N}_\mathcal{A}} n Z_n(t,\mathbf{r})$ as the mass density of n-size clusters in the solution, this equation reformulates to

$$\rho_2(t,\mathbf{r}) = \frac{M_2}{\mathcal{N}_\mathcal{A}} \sum_{n=1}^{N(t)} n Z_n(t,\mathbf{r}) = \sum_{n=1}^{N(t)} Y_n(t,\mathbf{r}), \tag{5.5}$$

This equation tells that the solute can be considered to be made of $N(t)$ species with mass densities of $Y_n(t),\ n = 1, \ldots, N(t)$. Z_n (or Y_n) and as a result ρ_2 change in the system because of mass transportation. Thus, hereafter we will use the superscript mt to distinguish the effect of mass transportation. Also, the notation $(t, \mathbf{r})$ will be omitted for the sake of brevity though concentrations, densities and pressure are temporally and spatially variable. The conservation of mass for the n^{th} component in the solution, which $n = 1, \ldots, N(t)$, is given by (Bird et al., 1960)

$$\frac{\partial}{\partial t} Y_n^{mt} \;=\; -\, Y_n^{mt}\,(\nabla \cdot \mathbf{u}) \;-\; \mathbf{u} \cdot \nabla Y_n^{mt} \;-\; \nabla \cdot \mathbf{j}_{[\mathbf{n}]}. \tag{5.6}$$

Here $\mathbf{j}_{[\mathbf{n}]}$ is the molecular flux of clusters of the size n. Invoking the definition of Y_n and dividing both sides by $nM_2/\mathcal{N}_{\mathcal{A}}$, we arive at the concentration form of this equation as follows

$$\frac{\partial}{\partial t} Z_n^{mt} \;=\; -\, Z_n^{mt}\ \nabla \cdot \mathbf{u} \;-\; \mathbf{u} \cdot\ \nabla Z_n^{mt} \;-\; \frac{\mathcal{N}_{\mathcal{A}}}{M_2\ n} \nabla \cdot \mathbf{j}_{[\mathbf{n}]}. \tag{5.7}$$

These formulations are subject to the following considerations; i) the solution is modelled as a binary mixture, ii) the solute species is a set of clusters with various sizes and concentrations, iii) mass transportation is a non-aggregative process, and iv) all the clusters travel with the flow velocity and the no-slip condition holds. The latter consideration is plausible given that clusters are in nanoscopic scales and the solution is dilute (Bird et al., 1960; Hirschfelder et al., 1954).

The change in the concentration of clusters due to non-aggregative mechanism is therefore given by

$$K_n(t, \mathbf{r}) \;-\; L_n(t, \mathbf{r}) \;=\; \frac{\partial}{\partial t} Z_n^{mt}(t, \mathbf{r}). \tag{5.8}$$

Replacing the RHS by Eq. (5.7) gives the discrete representation of the net mass flux in the system. The equations derived in this section are in a generic format and account for the variation in the concentration of clusters

of different sizes because of mass convection and diffusion.

Now, we need to define the molecular flux term, i.e. $\mathbf{j_2}$, used in former equations. The molecular flux of the solute species consists of four contributions, (Bird et al., 1960) namely: ordinary diffusion driven by the spatial concentration gradient of species ($\mathbf{j^x}$), pressure diffusion ($\mathbf{j^p}$) which describes the tendency for the mass flux under the influence of pressure gradient, forced diffusion ($\mathbf{j^g}$) which is a mass flux due to imposed external forces, and a thermal diffusion ($\mathbf{j^T}$) term which expresses mass diffusion because of the temperature gradient. The overall molecular flux is then equal to $\mathbf{j_2} = \mathbf{j^x} + \mathbf{j^p} + \mathbf{j^g} + \mathbf{j^T}$. The molecular flux for an ideal binary solution in the absence of external forces becomes (Bird et al., 1960)

$$\begin{aligned}\mathbf{j_2} \quad = \quad & -\frac{C_m^2}{\rho_m} M_1 M_2 \; D_{12} \nabla x_2 \; - \; \frac{C_m^2}{\rho_m \mathcal{R} T} M_2^2 M_1 \; D_{12} x_2 \left(\frac{\overline{V_2}}{M_2} \; - \; \frac{1}{\rho_m} \right) \nabla p \\ & - \; D_2^T \nabla \ln T \end{aligned} \tag{5.9}$$

where $C_m = C_1 + C_2 = \frac{\rho_m}{M_m}$ is the total molar concentration of the solution (the molar density of the solution), D_{12} and x_2 and D_2^T are the diffusivity and mole fraction and the thermal diffusion coefficient of the solute in the solution, respectively. $\overline{V_2} = \frac{M_2}{\rho_2}$ is the partial molal volume and M_m and M_1 are the molar mass of the solution and solvent, respectively. The ratio of thermal diffusivity over (mass) diffusivity is called the Soret coefficient, i.e. $S^T = \frac{D_2^T}{D_{12}}$.

A simpler form of this equation can be obtained if we impose some assumptions. Such an approximation is discussed below.

5.1.1 Simplified conservation of mass equation

As discussed in Section 4.3.2.1, we can postulate that the solute species is mainly constituted of monomers and therefore approximate the mole fraction by the number concentration ratio of monomers. Therefore, we will have $x_2 = \frac{Z_1^{mt}}{C_m \mathcal{N}_\mathcal{A}}$. Substituting these relationships into Eq. (5.9) gives

$$\mathbf{j_2} \approx \mathbf{j_{[1]}} = -\frac{M_1 M_2 D}{M_m \mathcal{N}_\mathcal{A}} \nabla Z_1^{mt} - \frac{M_1 M_2^2 D}{M_m \mathcal{N}_\mathcal{A} \mathcal{R} T} Z_1^{mt} \left(\frac{\overline{V_2}}{M_2} - \frac{1}{\rho_m} \right) \nabla p - D_2^T \nabla \ln T, \tag{5.10}$$

where D is the diffusivity of monomers used before in Section 4.3.1.

The effect of a temperature gradient on mass transport is usually considered negligible unless there is a steep temperature gradient (Bird et al., 1960). Thus, this term is negligible as far as acoustic wave propagation in the solution is concerned and can be safely neglected. In the case of inertial cavitation, a substantial temperature rise at the centre of the collapsing bubble occurs which vanishes rapidly across space from the centre of the bubble as time progresses (Storey and Szeri, 2000; Suslick and Flannigan, 2008; Shaw and Spelt, 2010). However, the temperature rise in the solution in the vicinity of the surface of the bubble is much lower and close to the temperature of the solution, rather than that of the core of the bursting bubble (Cogné et al., 2015). In contrast, the pressure gradient in the vicinity of the bursting bubble is substantially greater than the temperature gradient (Ohl et al., 1999; Storey and Szeri, 2000; Akhatov et al., 2001; Shaw and Spelt, 2010; Cogné et al., 2015). Furthermore, for an organic mixture and an aqueous solution, the absolute value of the Soret coefficient is of the order of $|S^T| \approx 0.001 - 0.01$ K^{-1} (Platten, 2006). Consequently, the contribution of the thermal diffusion term to mass transportation tends to be much smaller than that of the concentration and pressure terms and can therefore be ignored. The above equation then transforms into

$$\mathbf{j_2} = -\frac{M_2 D}{\mathcal{N}_\mathcal{A}} \left(\frac{M_1}{M_m} \nabla Z_1^{mt} + \frac{M_1}{M_m} \frac{k_j^p}{T} Z_1^{mt} \nabla p \right), \tag{5.11}$$

where $k_j^p = \frac{M_2}{\mathcal{R}} \left(\frac{\overline{V_2}}{M_2} - \frac{1}{\rho_m} \right)$. In general, the densities and consequently k_j^p are time and space dependent which makes the above equation nonlinear.

Considering that the solution is dilute, we can write $M_m \approx M_1$ and $\rho_m \approx \rho_1$, hence the above equation becomes

$$\mathbf{j_2} = -\frac{M_2 D}{\mathcal{N}_\mathcal{A}}\left(\nabla Z_1^{mt} + \frac{k_j^p}{T} Z_1^{mt} \nabla p\right). \tag{5.12}$$

Equations developed thus far in this section are based on the assumption that the solute species is present mainly in the form of monomers with a population considerably greater than n-mers. This literally transforms mass transportation into monomer transportation which yields

$$\begin{aligned} K_1 - L_1 &= \frac{\partial}{\partial t} Z_1^{mt}, \\ K_n - L_n &= 0, \qquad\qquad n \geq 2. \end{aligned} \tag{5.13}$$

Likewise, in the theory of thin film condensation, the system is usually assumed open by including the arrival and evaporation of monomers in the kinetics model of the cluster formation (Zinsmeister, 1968, 1969; ZinkeAllmang et al., 1992; Venables et al., 1984; Nieminen and Kaski, 1989; Ratsch and Venables, 2003).

The net rate of monomer transportation is obtained by combining Eqs. (5.12) and (5.7) which reads

$$\frac{\partial}{\partial t} Z_1^{mt} = -Z_1^{mt} \nabla \cdot \mathbf{u} - \mathbf{u} \cdot \nabla Z_1^{mt} - \frac{\mathcal{N}_\mathcal{A}}{M_2} \nabla \cdot \mathbf{j_2}, \tag{5.14}$$

leading to

$$\begin{aligned} \frac{\partial}{\partial t} Z_1^{mt} = &- Z_1^{mt} \nabla \cdot \mathbf{u} - \mathbf{u} \cdot \nabla Z_1^{mt} \\ &+ D \nabla \cdot \left(\nabla Z_1^{mt} + \frac{k_j^p}{T} Z_1^{mt} \nabla p\right). \end{aligned} \tag{5.15}$$

Eventually, if we consider the solution is incompressible, utilising Eq. (5.2) further simplifies this equation to the following format

$$\frac{\partial}{\partial t} Z_1^{mt} \;=\; -\;\mathbf{u}\cdot\;\nabla Z_1^{mt} \;+\; D\;\nabla\cdot\left(\nabla Z_1^{mt} \;+\; \frac{k_j^p}{T}\;Z_1^{mt}\;\nabla p\right). \tag{5.16}$$

The assumption of incompressibility for wave propagation in an aqueous solution holds true for a vast range of excitation pressures and frequencies (Hamilton and Blackstock, 1998). However, this condition may fail when the pressure perturbation is generated from a violent inertial cavitation or at a strong shock front with associated acoustic Mach number of unity or higher (Prosperetti, 1975; Hamilton and Blackstock, 1998). Equation (5.16) is highly nonlinear. In favour of simplification in the mathematical implementation, following (Louisnard et al., 2007), in the limit of a dilute and incompressible solution we can consider making an additional approximation where k_j^p is constant and only depends on the solution properties.

5.2 Hybrid model with mass transportation

Variation in the concentration of n-size clusters because of mass transportation to a non-mass conserved system can be estimated from Eq. (5.7) for the discrete representations of cluster size. Substituting this relationship for the term $K_n \;-\; L_n$, see Eq. (5.8), we will arrive at the Szilard equation which accounts for the cluster formation as a result of association and dissociation of monomers in a non-mass conserved system. The Szilard equation then reads

$$\begin{aligned}\frac{\partial}{\partial t} Z_n \;=\;& f_{n-1}(t)Z_{n-1} \;-\; g_n(t)Z_n \;-\; f_n(t)Z_n \;+\; g_{n+1}(t)Z_{n+1} \\ & -\,Z_n\;\nabla\cdot\mathbf{u} \;-\; \mathbf{u}\cdot\;\nabla Z_n \;-\; \frac{\mathcal{N}_{\mathcal{A}}}{M_2\;n}\nabla\cdot\mathbf{j}_{[\mathrm{n}]},\end{aligned} \tag{5.17}$$

The continuous format of this equation (the FPE with mass transportation) was derived in Appendix C,and reads

$$\frac{\partial}{\partial t}Z(n) = -\frac{\partial}{\partial n}\left(v(n)Z(n) - \frac{1}{2}\frac{\partial[d(n,t)Z(n)]}{\partial n}\right) - Z(n)\,\nabla\cdot\mathbf{u} - \mathbf{u}\cdot\nabla Z(n) - \frac{\mathcal{N}_A}{M_2\,n}\,(\nabla\cdot\mathbf{j}_{[n]}). \quad (5.18)$$

The terms on the RHS are divided into two main categories: the first four terms on the RHS which represent the aggregative change in the cluster concentration, and the last three terms on the RHS indicating the non-aggregative change in the cluster concentration governed by the convective and diffusive transportation of clusters.

When we consider that the solute species is mainly made of monomers and therefore utilise Eq. (5.13) and the relationships developed in the former section, we can construct the following hybrid model

for $n = 1$:

$$\frac{\partial}{\partial t}Z_1 = -2f_1(t)Z_1 + 2g_2(t)Z_2 + \sum_{n=3}^{N} g_n(t)Z_n - \sum_{n=2}^{N} f_n(t)Z_n - Z_1\,\nabla\cdot\mathbf{u} - \mathbf{u}\cdot\nabla Z_1 - \frac{\mathcal{N}_A}{M_2}\nabla\cdot\mathbf{j_2}, \quad (5.19a)$$

for $1 < n \le N_d$:

$$\frac{\partial}{\partial t}Z_n = f_{n-1}(t)Z_{n-1} - g_n(t)Z_n - f_n(t)Z_n + g_{n+1}(t)Z_{n+1}, \quad (5.19b)$$

for $N_d < n \le N$:

$$\frac{\partial}{\partial t}Z(n) = -\frac{\partial}{\partial n}\left(v(n,t)Z(n) - \frac{1}{2}\frac{\partial[d(n,t)Z(n)]}{\partial n}\right), \quad (5.19c)$$

where the molecular flux $\mathbf{j_2}$ is given in Eq. (5.10).

From the perspective of thermodynamics and fluid mechanics, the follo-

wing assumptions are made in this hybrid model; i) cluster formation is governed by the association and depletion of monomers, ii) monomers have the same convective velocity as that of the flow and the no-slip condition holds, and iii) the solution is a continuum body and encompasses different species. Since none of these assumptions restricts the temporal application of these equations, this hybrid model should be valid for describing the cluster dynamics during transient processes, e.g. under a rapid pressure fluctuation or shock waves.

This model tells that the concentration of clusters is a function of three variables, which are the cluster size n, time t, and space $\mathbf{r}$. The concentration change over time is determined by two fluxes, they are the flux along the size axis n representing the aggregative process, see Eq. (4.7), and the mass flux along the space axis $\mathbf{r}$ modelling the contribution of the non-aggregative mechanism, Eq. (5.8). In a mass-conserved system, the latter flux disappears and the flux of clusters over the size axis (aggregative mechanism) will be the only driving mechanism of the cluster dynamics. The significant point here is that these two mechanisms are coupled because attachment and detachment frequencies are functions of the concentration of monomers, see Eqs. (4.33) and (4.38) for details. This implies that these fluxes cannot be solved for independently. Nonetheless, the question that arises here is whether or not these two fluxes occur at comparable rates? If not, it would be physically reasonable to overlook the slower process in favour of further simplifications. This is further discussed in Chapter 7.

In the special case of an incompressible solution, the first line of this hybrid model can be further simplified by taking Eq. (5.16) into account which reads

$$\begin{aligned}\frac{\partial}{\partial t}Z_1 \;=\; &-2f_1(t)Z_1 \;+\; 2g_2(t)Z_2 \;+\; \textstyle\sum_{n=3}^{N} g_n(t)Z_n \;-\; \sum_{n=2}^{N} f_n(t)Z_n \\ &-\; \mathbf{u}\cdot\,\nabla Z_1 \;+\; D\,\nabla\cdot\left(\nabla Z_1 \;+\; \frac{k_j^p}{T}\,Z_1\,\nabla p\right). \qquad (5.20)\end{aligned}$$

Finally, ignoring the Ostwald ripening process, this equation can be even further simplified to

$$\frac{\partial}{\partial t} Z_1 = - f_1(t) Z_1 + g_2(t) Z_2 - \mathbf{u} \cdot \nabla Z_1 + D \nabla \cdot \left(\nabla Z_1 + \frac{k_j^p}{T} Z_1 \nabla p \right). \quad (5.21)$$

In summary, Eqs. (5.19a), (5.20), and (5.21) allow the determination of the concentration of monomers in a non-mass conserved system for the following situations, respectively; i) accounting for the Ostwald ripening process, the compressibility of the solution and all mechanisms contributing to mass transportation, ii) accounting for the Ostwald ripening process but not the Soret effect and the compressibility of the solution, furthermore, the solution is assumed to be dilute, iii) overlooking the Ostwald ripening process, the Soret effect, and the compressibility of the solution which is assumed to be dilute. Each of these situations can be taken to study the kinetics of the cluster formation in a non-mass conserved system under sonication when the underlying assumptions hold. For instance, the Ostwald ripening takes place towards the end of nucleation where the concentration of large clusters is considerably high and the supersaturation ratio is depleted significantly. Therefore, Eq. (5.21) should be adequately precise to model the effect of acoustic waves, in particular, shock waves or transient pressure oscillations emitted from a collapsing bubble, on the kinetics of nucleation.

5.3 Nucleation rate

In Section 4.2 we presented the generic equation for determining the nucleation rate, see Eq. (4.14). This equation is valid for nucleation in both mass-conserved and non-mass conserved systems. Solving the hybrid model described in Eq. (5.19), the concentration of clusters across the size axis will be obtained which allows computation of the nucleation rate via Eq. (4.14).

Equation (4.16) gives the stationary nucleation rate in a closed system which can also be utilised to obtain the first order approximation of the quasi-

stationary nucleation rate if the quasi-stationary condition, Eq. (4.22), is satisfied. The stationary nucleation rate equation holds for a non-mass conserved system as long as supercritical clusters do not appear or vanish through mass transportation (Kashchiev, 2000). This condition will be achieved in our hybrid model since we considered the mobility and transportation of monomers only. In the case of isothermal wave propagation, Eq. (4.22) simplifies to Eq. (4.26) which is restated here

$$\left| \dot{r_0}(t) \; + \; \frac{r_0(t) \; \Delta n^*_{exc}(t) \; \nu}{n^*_n(t) \; k_B T} \dot{p}(t) \right| < \frac{4}{\pi n^*_n(t)} r_0(t) z^2(t) f_{n^*}(t). \tag{5.22}$$

We should bear in mind that the supersaturation ratio, the pressure oscillation and all other variables in this equation are a function of time and of the position vector $\mathbf{r}$. Here $\dot{r_0}(t)$ includes the effects of both mass transportation and the cluster formation. Taking the approximation of $r_0(t) = \frac{Z_1}{C_e}$ used in Section 4.3.2.1, term $\dot{r_0}(t)$ is then equal to the LHS of the first line of Eq. (5.19). As we mentioned before, this equation is a set of coupled ODEs and a partial differential equation (PDE) and therefore $\dot{r_0}(t)$ cannot be explicitly solved. Thus, we will numerically solve the hybrid model and use the generic equation Eq. (4.16) to compute the nucleation rate.

5.4 Non-dimensionalisation

We will non-dimensionalise the hybrid model for an incompressible solution here. Since we assumed that only monomers transport through a non-mass conserved system, only the Szilard equation for monomers would be different from other equations in the hybrid model for a closed system presented in Chapter 4. We will use the following relationships for the non-dimensionalisation

$$t = t_c\ \tau, \qquad Z_n = z_c\ \overline{Z_n}, \qquad f_n = f_c\ \overline{f_n}, \qquad g_n = g_c\ \overline{g_n},$$
$$\mathbf{u} = u_c\ \overline{\mathbf{u}}, \qquad p = p_c\ \overline{p}, \qquad \nabla = \frac{1}{l_c}\ \bar{\nabla}, \qquad \nabla^2 = \frac{1}{l_c^2}\ \bar{\nabla}^2. \tag{5.23}$$

Expanding the last term in Eq. (5.20) and substituting the above relationships gives

$$\begin{aligned}\frac{z_c}{t_c}\frac{\partial}{\partial\tau}\overline{Z_1} \quad = \quad & -\ 2f_c z_c\ \overline{f_1}(t)\overline{Z_1}\ +\ 2g_c z_c\ \overline{g_2}(t)\overline{Z_2}\ +\ g_c z_c\ \sum_{n=3}^{N}\overline{g_n}(t)\overline{Z_n} \\ & -\ f_c z_c\ \sum_{n=2}^{N}\overline{f_n}(t)\overline{Z_n}\ -\ \frac{z_c u_c}{l_c}\ \overline{\mathbf{u}}\cdot\ \bar{\nabla}\overline{Z_1}\ +\ \frac{z_c D}{l_c^2}\bar{\nabla}^2\overline{Z_1} \\ & +\ \frac{z_c D p_c\ k_j^p}{l_c^2 T}\ \bar{\nabla}\overline{Z_1}\cdot\bar{\nabla}\overline{p}\ +\ \frac{z_c D p_c\ k_j^p}{l_c^2 T}\ \overline{Z_1}\bar{\nabla}^2 p,\end{aligned} \tag{5.24}$$

which simplifies to

$$\begin{aligned}\frac{\partial}{\partial\tau}\overline{Z_1} \quad = \quad & -\ 2f_c t_c\ \overline{f_1}(t)\overline{Z_1}\ +\ 2g_c t_c\ \overline{g_2}(t)\overline{Z_2}\ +\ g_c t_c\ \sum_{n=3}^{N}\overline{g_n}(t)\overline{Z_n} \\ & -\ f_c t_c\ \sum_{n=2}^{N}\overline{f_n}(t)\overline{Z_n}\ -\ \frac{t_c u_c}{l_c}\ \overline{\mathbf{u}}\cdot\ \bar{\nabla}\overline{Z_1}\ +\ \frac{t_c D}{l_c^2}\bar{\nabla}^2\overline{Z_1} \\ & +\ \frac{t_c D p_c\ k_j^p}{l_c^2 T}\ \bar{\nabla}\overline{Z_1}\cdot\bar{\nabla}\overline{p}\ +\ \frac{t_c D p_c\ k_j^p}{l_c^2 T}\ \overline{Z_1}\bar{\nabla}^2 p.\end{aligned} \tag{5.25}$$

The non-dimensionalisation coefficients are not unique and different choices can be made. We set the coefficients as follows

$$l_c = \Lambda, \qquad u_c = u_m = \frac{p_m}{\rho_0 c_0}, \qquad t_c = \frac{l_c}{u_c}, \qquad p_c = p_m, \qquad f_c = g_c = \frac{1}{t_c}, \tag{5.26}$$

where Λ is the mass diffusion length at the acoustic wave period of $1/f$ given by $\Lambda = \sqrt{2\frac{D}{f}}$, u_m is the magnitude of particle velocity in an acoustic field with the pressure amplitude p_m. c_0 and ρ_0 are the wave speed and mass density of

the solution at the reference temperature T_0. Unlike Section 4.4, here u_c and l_c are exploited to determine t_c through the relationship $\frac{t_c u_c}{l_c} = 1$. We also denote the dimensionless quantity $p_c k_j^p / T$ by $\overline{\beta}$ which depends only on the mixture properties at the given temperature T and the scaling factor p_c.

As we discussed in Section 5.1, the convective mass transportation and pressure diffusion are driven by wave propagation in the fluid. The distance that a wave travels over a wave period is called the wavelength and is usually taken as the characteristic length of wave propagation. Diffusion happens by the microscopic stochastic molecular motion. The mean square displacement of particles from the starting position over a wave period is taken as a characteristic length of this process, i.e. Λ. Therefore, we can define the quantity $\varepsilon = \frac{\Lambda}{\lambda_a}$ to represent the ratio of these two length scales. This quantity is relatively small for a typical aqueous solution and acoustic wave parameters. When $\varepsilon \to 1$, the wave length will be comparable to the diffusion length. For example, for a typical aqueous solution with $10^{-10} < D < 10^{-6}$ m^2 s^{-1}, a very high frequency, i.e. of the order of 10^6 MHz, is required which gives a wavelength of the same order of the mean free path [1] which tends to violate the continuum hypothesis for wave propagation and mass transportation. In this work, we will restrict ourselves to continuum mechanics hence parameters will be chosen accordingly.

We define the dimensionless Péclet number by $Pe = \frac{l_c^2}{D t_c} = \frac{l_c u_c}{D} = \frac{\Lambda u_m}{D} = \frac{u_m}{\sqrt{Df/2}}$. We may define the mean diffusive particle velocity as $\frac{\Lambda}{1/f} = \sqrt{2Df}$. Therefore Péclet number represents the ratio of the maximum particle velocity because of wave propagation to the mean diffusive particle velocity. The higher the Péclet number, the stronger the effect of pressure diffusion relative to ordinary diffusion. Using the definition of ε, this Péclet number can be written as $Pe = \varepsilon \frac{\lambda_a u_m}{D}$ where the fraction constructs another Péclet number as follows: $Pe_\lambda = \frac{\lambda_a u_c}{D} = \frac{\lambda_a u_m}{D} = \frac{\lambda_a^2 / D}{\lambda_a / u_m}$. Pe_λ can be inferred as the ratio of the mean time required for a monomer to random walk a length

[1] the molecular mean path in water at room temperature and atmospheric pressure is roughly 2.5Å = 0.25 nm.

of λ_a (ordinary diffusion) to the time to travel λ_a with the maximum velocity it could gain through wave propagation. Therefore, a high Pe_λ means convection and pressure diffusion become dominant over ordinary diffusion through a wave period. In other words, the time scale of pressure diffusion is smaller than the time scale of ordinary diffusion. We can deduce that in the case of shock, ordinary diffusion can be ignored in favour of pressure diffusion and convection.

Exploiting this set of non-dimensionalisation coefficients yields the non-dimensionalised form of Eq. (5.20) and other equations in the hybrid model which read

for $n = 1$:

$$\begin{aligned}\frac{\partial}{\partial\tau}\overline{Z_1} \;=\; &-\; 2\overline{f_1}(t)\overline{Z_1} \;+\; 2\overline{g_2}(t)\overline{Z_2} \;+\; \sum_{n=3}^{N}\overline{g_n}(t)\overline{Z_n} \\ &-\; \sum_{n=2}^{N}\overline{f_n}(t)\overline{Z_n} \;-\; \overline{\mathbf{u}}\cdot\;\bar{\nabla}\overline{Z_1} \;+\; \frac{1}{Pe}\bar{\nabla}^2\overline{Z_1} \\ &+\; \frac{\overline{\beta}}{Pe}\;\bar{\nabla}\overline{Z_1}\cdot\bar{\nabla}\overline{p} \;+\; \frac{\overline{\beta}}{Pe}\;\overline{Z_1}\bar{\nabla}^2\overline{p},\end{aligned} \tag{5.27a}$$

for $1 < n \leq N_d$:

$$\frac{\partial}{\partial\tau}\overline{Z_n} \;=\; \overline{f_{n-1}}\;\overline{Z_{n-1}} \;-\; \overline{g_n}\;\overline{Z_n} \;-\; \overline{f_n}\;\overline{Z_n} \;+\; \overline{g_{n+1}}\;\overline{Z_{n+1}}, \tag{5.27b}$$

for $N_d < n \leq N$:

$$\frac{\partial}{\partial\tau}\overline{Z(n)} \;=\; -\,\frac{\partial}{\partial n}\left(\overline{v(n)}\;\overline{Z(n)} \;-\; \frac{1}{2}\frac{\partial\left[\overline{d(n)}\;\overline{Z(n)}\right]}{\partial n}\right). \tag{5.27c}$$

Here, the dimensionless attachment and detachment frequencies are different from those obtained in Eq. (4.45) and are calculated by

$$\overline{f_n} = \frac{t_c}{t_{m,m}}(1+n_n^{-1/3})(1+n_n^{1/3})\overline{Z_1}, \tag{5.28}$$

$$\overline{g_n} = \frac{t_c}{t_{m,m}}(1+n_n^{-1/3})(1+n_n^{1/3})r_0^{n_{\sigma'}(n_n)}\exp\left(\frac{2}{3}\frac{a_0\gamma_\infty}{k_BT}n_n^{-1/3}n_n'(n_n)\right) \times \exp\left(-\frac{\nu\Delta p}{k_BT}\Delta n_{exc}'\right). \tag{5.29}$$

The quantity $t_{m,m} = 1/4\pi R_0 D C_e$ has the unit of time and can be interpreted as the mean monomer collision time in the solution. In the FPE in the hybrid model, the dimensionless growth and dispersion rates are obtained by calculating Eq. (4.48) with transition frequencies given by the above equation.

Finally, the non-dimensionalised form of Eq. (5.16) which only accounts for the transportation of monomers due to acoustic waves (when the phase transition is ignored) reads

$$\frac{\partial}{\partial\tau}\overline{Z_1} = -\,\overline{\mathbf{u}}\cdot\,\bar{\nabla}\overline{Z_1} + \frac{1}{Pe}\bar{\nabla}^2\overline{Z_1} + \frac{\overline{\beta}}{Pe}\,\bar{\nabla}\overline{Z_1}\cdot\bar{\nabla}\overline{p} + \frac{\overline{\beta}}{Pe}\,\overline{Z_1}\bar{\nabla}^2\overline{p}. \tag{5.30}$$

We will numerically solve this equation and the whole hybrid model for different boundary conditions in Chapter 7, where the non-dimensionalisation of boundary conditions will also be explained.

5.5 Summary

In this chapter, we formulated the evolution of cluster concentration over time in a non-mass conserved system. The Szilard and Fokker-Planck equations were extended by including mass transfer in an acoustic wave field. The relationships for mass transfer due to ordinary diffusion, thermal diffusion (the Soret effect), and pressure diffusion were presented, see Eqs. (**??**), (5.7) and (5.10).

We derived a set of equations for a hybrid model describing the cluster dynamics in a dilute solution assuming only monomers transport through the

system, Eq. (5.19). Moreover, the different variations of this equation for incompressible solutions with and without the Ostwald ripening process were derived and presented in Eqs. (5.20) and (5.21), respectively. These equations were non-dimensionalised and the relative importance of their different terms were also studied.

This chapter concluded the second part of the thesis. Here, a brief summary of the achievements made so far will be presented. In Chapters 2 and 3 we studied the thermodynamics of phase transition in a system under the following circumstances, respectively: i) the silent condition, and ii) with pressure and temperature perturbations. Subsequently, the kinetics of the cluster formation in a mass-conserved system was investigated in Chapter 4. In the present chapter, we progressed to develop the kinetics of cluster formation in a non-mass conserved system. The contributions in the last four chapters portray the influence of wave propagation on the thermodynamics and kinetics of cluster formation. The major feature which distinguishes these contributions from other works is that the coupled effects of dynamic pressure on both thermodynamics and kinetics of phase transformation are accounted for. These effects are ascribed to the following governing mechanisms i) altering the height of the nucleation barrier, and the clustering work for non-critical clusters, ii) changing attachment and detachment frequencies, and iii) changing the spatial population of monomers resulting from the convective mass transport and forced diffusion.

The kinetics of nucleation in an acoustic field could be easily non-stationary within the range of the pressure magnitude and frequency achievable in practice, see Section 4.2. Therefore, the full set of the kinetic equations should be solved numerically to determine the nucleation rate.

We will proceed with the validation of the cluster model developed in Chapter 2 against the experimental data of water droplet nucleation. This will be followed by evaluating the effect of acoustic waves on crystallisation in an aqueous solution in Chapter 5. These results will elucidate some of the

possible mechanisms in a sonocrystallisation process.

Chapter 6

Validation of the new cluster model using water droplet nucleation data

In this chapter, we will present the validation of the new model 1 by applying it to the test case of water droplet nucleation from the gas phase. Homogeneous nucleation of water droplets in vapour is very well understood and has been extensively studied both experimentally and theoretically. Thus, the model of water was chosen for validation of the developed model.

6.1 Water droplet nucleation

The excess free energies of water droplets of different sizes have recently been calculated by means of a statistical mechanical approach at a temperature of T = 300 K (Samsonov et al., 2003; Lau et al., 2015b). Wilhelmsen (Wilhelmsen et al., 2015) showed that calculations using the TIP4P/2005 molecular model can successfully estimate the surface energy in agreement with experiments. Thus, we will use the calculations of Lau et al. (Lau et al., 2015b), which are based on this molecular model to validate our nucleation model. We will follow the ensuing procedure

(i) λ is deduced by comparing the effective surface tension determined by our model, Eq. (2.63), with those obtained from statistical mechanics,

(ii) the nucleation rate is determined using this value of λ and compared with experimental data at $T = 300$ K obtained by Brus et al. (Brus et al., 2008, 2009).

This specific temperature is selected based on the availability of MD simulations and experimental data. Moreover, we selected the experimental results by Brus et al. (Brus et al., 2008, 2009) for the following reasons: they used the thermal diffusion cloud chamber for the measurement of the nucleation rates. This allows water droplet nucleation experiments to be conducted at high temperatures, where the required physical properties are known and MD simulations available (Wyslouzil and Wölk, 2016).

In order to calculate the kinetics of water droplet nucleation by solving the hybrid model, an expression for attachment frequency in the gaseous old phase is required. Considering that for the gaseous old phase, clusters are much smaller than the mean free path in the gas phase, the attachment rate should correspond to a particle flux modelled by the kinetic theory of gases. Consequently, the attachment frequency reads (Kashchiev, 2000; Vehkamaki, 2006)

$$f_n(t) = k_{f,g}(n_n) Z_1(t), \tag{6.1}$$

where

$$k_{f,g}(n_n) = \alpha_n a_0 \sqrt{\frac{k_B T}{2\pi m_0}} (1 + \tfrac{1}{n})^{1/2} (1 + n_n^{1/3})^2. \tag{6.2}$$

With respect to the discussion presented in Section 2.3.3, the mass of an n-size cluster is given by $m_n = n m_0$, where m_0 is the mass of a monomer in the new phase. However, the radius of a cluster is defined by n_n. Subsequently, if we use $k_{f,g}(n_n)$ instead of $k_f(n_n)$ given in Eq. (4.34), all the previous equations are applicable and can be used for this exercise. The non-dimensionalisation coefficient of time changes to $k_t = a_0 \sqrt{\frac{k_B T}{2\pi m_0}} \frac{p_{ve}}{k_B T}$ where p_{ve} is the equilibrium vapour pressure. At $T = 300$ K, we have $k_t = 5.9 \times 10^7$ s^{-1}.

6.2 Simulation results

Figure 6.1 shows the effective surface tension at different values of λ calculated at the experimental supersaturation ratio r = 3.77 at T = 300 K. We can see for small clusters of n = 3 and 6 molecules, the best fit is achieved at λ = 0.45 whereas for larger clusters (n > 12) the curve with λ = 0.37 happens to give the best agreement with the statistical mechanic results. This may suggest that λ is cluster size-dependent, similarly to the Tolman length (Talanquer and Oxtoby, 1995; Lu and Jiang, 2005; Granasy, 1998) for the surface of tension as the dividing surface. Nevertheless, since with λ = 0.37 we achieve an acceptable approximation of the size-dependent surface tension over a wide range of cluster sizes, we take this value for our calculations at this condition. The validity of this choice will be evaluated by comparing the calculated kinetics of nucleation with experiments.

The same procedure was repeated for all experimental supersaturation ratios at T = 300 K reported by Brus et al. (Brus et al., 2008, 2009). We observed a similar trend showing λ is larger for small clusters (n < 12) and decreases for larger clusters (n > 12). Likewise, in the case of the surface of tension as the dividing surface, a similar dependency of the Tolman length

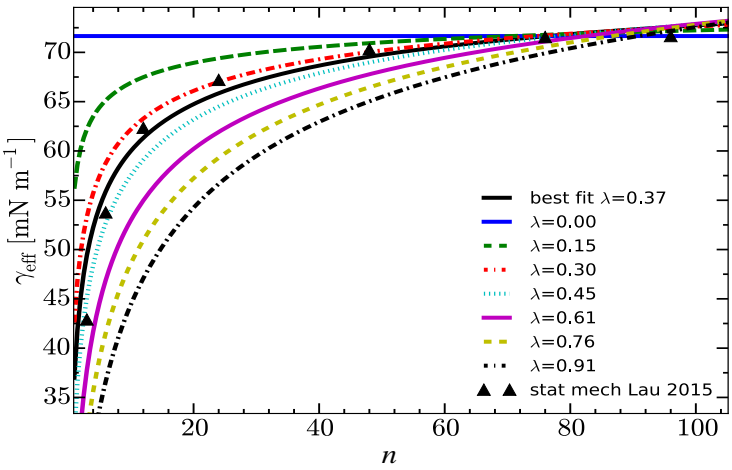

Figure 6.1: Effective surface tension (γ_{eff}) at different λ calculated by Eq. (2.63) at T = 300 K. ▲: Statistical mechanical simulations (Lau et al., 2015b) at the cluster size of $n = 3, 6, 12, 24, 48, 76, 96$. Solid black curve shows the best fit to statistical mechanical simulations.

on the droplet sizes, i.e. an inverse relationship with the droplet size, and the supersaturation ratio at a constant temperature were also reported (Lu and Jiang, 2005; Granasy, 1998).

Having determined the parameter λ for a range of supersaturation ratios at temperature T = 300 K, the hybrid model is then numerically solved and the nucleation rate is calculated. The physicochemical properties of vapour and water are given in Table A.2 in Appendix A.

Figures 6.2 and 6.3 depict the variation in the concentration of supercritical clusters ($\zeta(\tau)$) and the supersaturation ratio over time, respectively, for two cases; i) classical clusters which are defined by the EDS (λ = 0), and ii) the new surface with the DS positioned at λ = 0.37. The equilibrium monomer concentration of $C_e = p_{ve}/k_B T$ is used to determine the concentrations $Z(n)$ in the supersaturated state. The nucleation time is identified by the appearance of the first ten supercritical clusters, i.e. $\log(Z_s) \geq 1$. It is about $\tau_{n,0}$ = 1 and $\tau_{n,1}$ = 7 for these EDS and non-EDS cases, respectively, and is indicated by vertical dashed-dotted lines, see Fig. 6.2. We can see in Fig. 6.3 that around τ = 0.001 the supersaturation ratio slightly drops and reaches a plateau where the nucleation stage begins. This drop is due to the rapid formation of subcritical clusters. The intervals between the beginning of the plateau at τ = 0.01 and τ = 0.1 for the EDS and non-EDS cases, respectively, and the nucleation times indicate the time required to nucleate ten supercritical clusters. Basically, the supersaturation ratio curves shown in Fig. 6.3 can be divided into three parts: i) the relaxation part where subcritical clusters and the first ten supercritical clusters are created, ii) the part corresponds to nucleation and growth stage where the supersaturation ratio plateaus and sharply drops to unity, i.e. $r \approx 1$ at the end of this stage. The onset of this stage is indicated by a vertical dashed-dotted line in Fig. 6.2, and iii) the growth and Ostwald ripening part where starts when the concentration of the supercritical clusters decreases while the mean size of supercritical clusters increases. This usually takes place after the nucleation stage and when $r \approx 1$. The latter stage was not

studied for water droplet nucleation but thoroughly investigated in the next chapter for a sonocrystallisation process.

The system is closed and therefore the total mass is constant. As a result, the condensation depletes the monomer supersaturation and terminates the nucleation and monomer-driven growth stages around $\tau = 10^9$ for the classical cluster case. At this moment, the concentration of monomers drops drastically ($r \approx 1$). In contrast, the new model 1 with $\lambda = 0.37$ predicts a longer

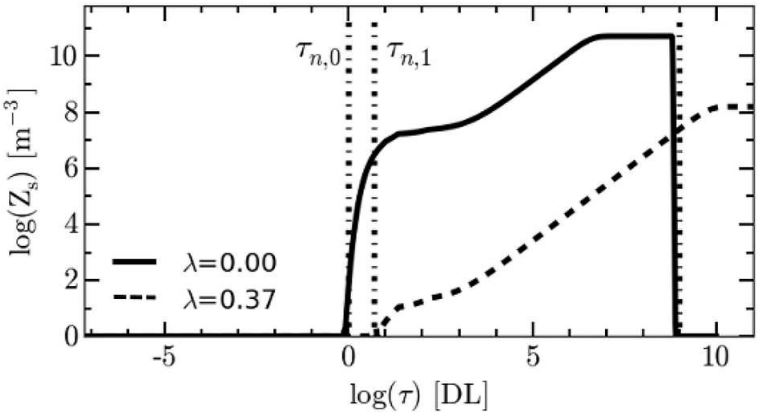

Figure 6.2: Logarithmic concentration (logarithm in base 10 in all figures) of supercritical clusters at two different λ values over time. Vertical lines labelled $\tau_{n,0}$ and $\tau_{n,1}$ indicate the beginning of the nucleation stage in models with $\lambda = 0$ and $\lambda = 0.37$, respectively. The unlabelled vertical line indicates the end of nucleation and monomer-driven growth of supercritical clusters in the case of $\lambda = 0$ while nucleation is still ongoing in the case of $\lambda = 0.37$. This is due to a faster nucleation rate for $\lambda = 0$ which leads to quicker depletion of the imposed supersaturation of monomers.

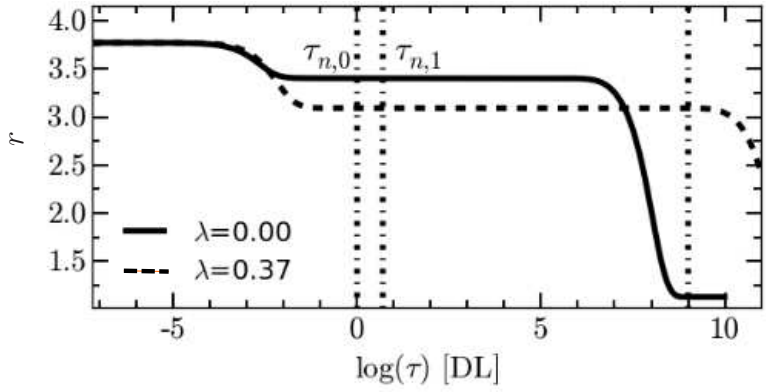

Figure 6.3: Supersaturation ratio at two different λ values over time. See the caption of Fig. 6.2 for details.

nucleation stage. This implies that this model estimates a lower nucleation rate than CNT. The sharp fall marked by the vertical line at the right hand side is due to the way we define $\zeta(\tau)$, see above, and does not hold physically. Since the supersaturation ratio drops to almost unity, the critical cluster size mathematically tends to infinity and therefore all the previously made clusters become subcritical which brings about this abrupt drop of $\zeta(\tau)$.

Repeating these calculations for all experimental supersaturation ratios, we determine the stationary nucleation rates for all these conditions. These results together with the experimental nucleation rate and values obtained using the BD model are plotted in Fig. 6.4. The procedure mentioned in the beginning of this section was repeated to obtain the value of λ at each supersaturation ratio. They are $\lambda = 0.29, 0.32, 0.35$ at $r = 3.39, 3.52, 3.61$, respectively.

The main difference between our model and BD is the non-EDS definition of clusters used in our model which results in a more accurate estimate

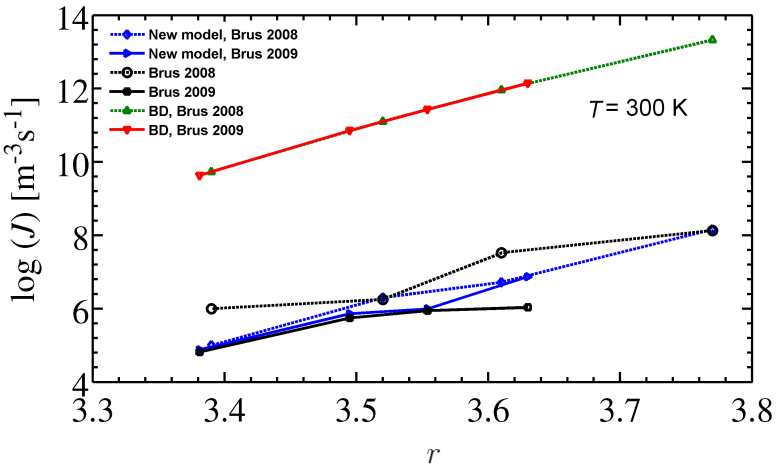

Figure 6.4: Logarithm of the nucleation rate versus the supersaturation ratio at $T = 300$ K. The nucleation rate calculated by our new model using λ values determined from statistical mechanical calculation of Lau et al. (Lau et al., 2015b) at the data points of Brus 2008 and 2009 (solid line with ◆ and dashed line with ▶, respectively). The experimental results of Brus et al. 2008 and 2009 (Brus et al., 2008, 2009) are also shown (solid line with ● and dashed line with ■, respectively). The nucleation rate determined by the BD model at the data points of Brus 2008 and 2009 (▲ and ▼, respectively).

of the excess energy. This also leads to a different critical cluster size and consequently a different nucleation rate. Additionally, the hybrid model determines the kinetics of nucleation for a stationary as well as a time variable non-stationary system. This is important because in practice the supersaturation imposed on the system is always time variable.

The agreement between the predicted nucleation rate and experimental values are very good. Although the dividing surface we used to define clusters has the property of size-independent surface tension, the effective surface tension of this surface is size, temperature and supersaturation dependent, see Eq. (2.63). This is attributed to the fact that in our model, a cluster of size n can take on different combinations of n_n and n_σ due to the arbitrary placement of the DS contrary to a cluster defined by the EDS or the surface of tension. Therefore we are able to reproduce γ_{eff} by choosing the location of the dividing surface appropriately, see Fig. 6.1.

It seems that this important characteristic addresses some of the shortcomings of CNT, at least for water at T = 300 K. Since this model does not account for non-idealities in the gas phase and the compressibility of the liquid phase, the close agreement between our numerical results and experimental va-

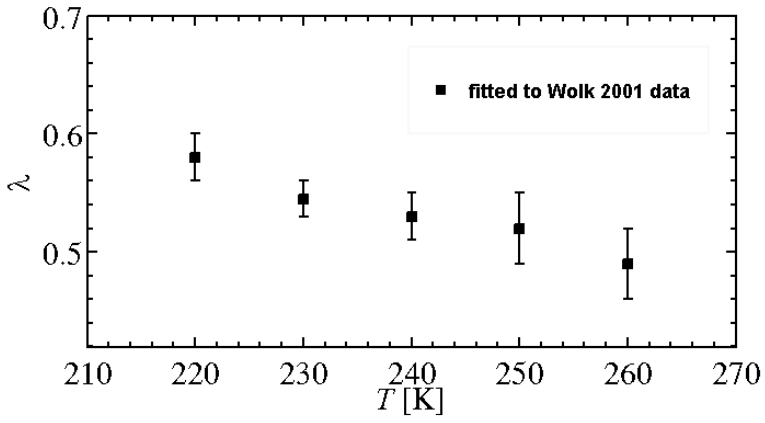

Figure 6.5: λ calculated from the experimental nucleation rate (Wölk and Strey, 2001) for water nucleation at different temperatures. The error bars show the range in λ at a specific temperature as a function of the supersaturation ratio. The lower and upper limits correspond to the smallest and largest experimental supersaturation ratios at a specific temperature, respectively.

lues should be considered carefully.

The lack of molecular simulation results at other temperatures does not allow us at this stage to extend these calculations to lower temperatures. Nevertheless, we deduced the values of λ from experimental data obtained by Wölk et al.,(Wölk and Strey, 2001) shown in Fig. 6.5. We can see the gradual descent of λ with temperature rise. A similar trend was also observed and reported for the Tolman length (Talanquer and Oxtoby, 1995; Holten et al., 2005).

6.3 Summary

In this section, we demonstrated that using a specific non-EDS dividing surface together with the Gibbs droplet model in a generic format can better predict the properties of clusters and the kinetics of nucleation compared to CNT. These results validate the new nucleation model, i.e. the new model 1 , developed and presented in Chapter 2. This also supports our intention to study the effect of pressure fluctuations on the nucleation process by means of a more generic model than CNT. These results are elaborated in Chapter 7.

Chapter 7

Simulation of thermodynamics and kinetics of cluster formation in an acoustic field

We have established the required equations to determine the kinetics of nucleation while accounting for the effect of fluctuations in the thermodynamic state of the old phase. In Chapter 6 we examined the new cluster and nucleation models by applying them to the test case of water droplet nucleation from vapour. Having validated the model and its numerical implementation, we will evaluate the effect of acoustic waves on crystallisation in an aqueous solution in this chapter.

Acoustic waves can be generated from different sources. Therefore, different pressure fields may be produced in the bath. The equations developed in this work are not restricted to a specific pressure field and are generic in this sense. When the system is mass conserved, we just need to know the thermodynamic state of the system temporally. However, in a non-mass conserved system, the fluid dynamics must be calculated to determine mass transportation in the system. The system's characteristics influence the fluid dynamics, hence a similar acoustic source tends to produce different effects on a phase transition in different systems.

The majority of experimental works do not define all the necessary para-

meters of both the acoustic field and crystallisation. Thus, a direct comparison with sonocrystallisation data seems impractical. In addition, acoustic cavitation usually takes place prior to or concurrently with crystallisation, which is often not characterised in experiments. Therefore, our objective in this chapter is to evaluate our new model in a simple acoustic field and conduct a qualitative comparison against experimental observations. Simulations will be conducted in both mass conserved and non-mass conserved systems. We will consider various scenarios of pressure oscillation in each system.

Furthermore, we will study the effect of the position of the DS (the parameter λ) on the kinetics of nucleation under isothermal pressure perturbations in Section 7.4.

In all the simulations, the reference state is considered to be at room temperature and atmospheric pressure, $T_0 = 293$ K and $p_0 = 0.1$ MPa respectively. The isothermal simulations are also conducted at T_0. The physicochemical properties of the solution, the new phase, and water at the reference state are listed in Tables A.1 to A.3 in Appendix A.

7.1 Acoustic wave propagation

The equations derived in this work are not limited to a specific source type and are generic in this sense. For the sake of simplicity, we consider finite amplitude plane acoustic waves emitted from an infinite plate oscillating harmonically in the direction normal to the plate. The radiated waves propagate through a semi-infinite dissipative and nonlinear medium. We will consider up to the second order approximation in the equation of state for density terms. Due to the nonlinearity of the medium, the wave can distort and form a shock wave. The simplest second order wave equation which describes the combined effects of dissipation and nonlinearity on the propagation of plane waves is the Burgers' equation (Hamilton and Blackstock, 1998). The Burgers' equation can be formulated in the following format (Mitome, 1989)

$$\frac{\partial v}{\partial t} + v\frac{\partial v}{\partial \xi} = \frac{\delta_0}{2}\frac{\partial^2 v}{\partial \xi^2}, \tag{7.1a}$$

$$v = u + c - c_0, \tag{7.1b}$$

$$\xi = x - c_0 t, \tag{7.1c}$$

$$\delta_0 = \frac{\eta}{\rho_1}\left(\frac{4}{3} + \frac{\eta_B}{\eta} + \frac{(\gamma_s - 1)\kappa}{\eta C_p}\right), \tag{7.1d}$$

where u is the particle velocity, c is the local wave speed, c_0 is the wave speed in the initial undisturbed condition, x is the distance from the source, ξ is the retarded distance (spatial propagation delay), δ_0 is the sound diffusivity, η is the dynamic (shear) viscosity, η_B is the bulk viscosity, γ_s is the specific heat ratio, κ is the thermal conductivity and C_p is the specific heat at constant pressure. With respect to the dilute solution assumption, we postulate that the hydrodynamic properties of the wave medium are similar to those of the solvent. This is a legitimate assumption within the range of the driving frequencies which will be used in this work, i.e. $f \leq 2$ MHz.

The Burgers' equation is widely used to calculate the progressive plane wave field in a lossy and nonlinear medium within the limitation of the weak shock theory. The condition for the weak shock is met if $M_a \ll 1$ where $M_a = u_0/c_0$ is the acoustic Mach number. We will solve the Burgers' equation in the next section and check this condition for the range of parameters used in this work.

7.1.1 Numerical implementation

Several methods have been developed to solve the Burgers' equation analytically and numerically in either the frequency domain or the time domain. Here, we will use Mitome's exact solution (Mitome, 1989) which allows determining pressure in the pre- and post-shock regions in the time domain. The final expression for the numerical computation of the wave field reads (Mitome, 1989)

$$p(\tau_w, \overline{x}) \;=\; p_m \;\frac{2}{\Gamma}\frac{\partial}{\partial \tau_w}\log\int_{-\infty}^{\infty}\exp\left[\frac{-\Gamma}{2}\left(\frac{(\tau_w \;-\; \tau_w')^2}{2\overline{x}} \;+\; \cos(\tau_w') \;+\; 1\right)\right]d\tau_w', \tag{7.2a}$$

$$\tau_w \;=\; -\,\omega\frac{\xi}{c_0} \;=\; \omega\left(t - \frac{x}{c_0}\right), \tag{7.2b}$$

$$\overline{x} \;=\; \frac{x}{x_s}, \qquad x_s \;=\; \frac{c_0}{\beta\omega M_a} \;=\; \frac{c_0^2}{\beta\omega u_m}, \tag{7.2c}$$

$$\Gamma \;=\; \frac{2\beta p_m}{\delta_0 \rho_1 \omega}. \tag{7.2d}$$

Here, τ_w is the retarded time (temporal propagation delay), x_s is the lossless shock distance, β is the coefficient of nonlinearity and Γ is the Goldberg number which indicates the importance of the nonlinearity relative to the dissipation. Furthermore, as mentioned above, the source is considered to be an oscillating plate with an angular frequency of $\omega = 2\pi f$ and a velocity magnitude of u_m. This results in the boundary condition of $p(t,0) = p_m \sin(\omega t)$ where $p_m/u_m = \rho_1 c_0$. The latter depicts the linear acoustic impedance relationship, which holds in the case of plane waves emitted by an unbounded piston (oscillator). The derivation of Eq. (7.2) is omitted here for the sake of brevity,and the reader is referred to the cited paper for more details.

The difficulties involved in the numerical implementation of Eq. (7.2) are twofold. First, the infinite bounds of the integral are difficult to handle by numerical schemes. Second, the absolute value of the argument of the exponential term can become very large resulting in an ill-conditioned situation. For instance, for a sound source oscillating at $f = 1$ MHz with $p_m = 50$ MPa and emitting acoustic waves in water at $T = 293$ K, the Goldberg number is roughly 15000 which produces a factor of $\exp(-15000) \;\simeq\; 3.9\text{E}-6515$. The fact that the integrand is small except near τ_w can be used to cope with the first difficulty. We set the integral bounds to the range in which the exponential has a value larger than a sufficiently small value. Therefore, the upper and lower limits are set to $\tau_w + \psi$ and $\tau_w - \psi$, respectively. Mitome (Mitome,

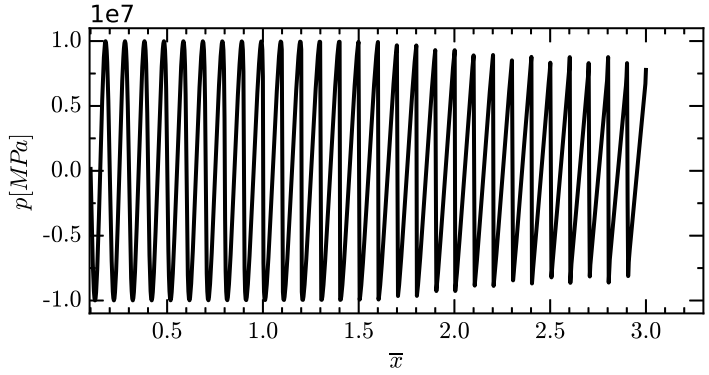

Figure 7.1: Plane wave field across space up to $1.5x_s$ at $\tau_w = 2\pi$ with $f = 1$ MHz and $p_m = 10$ MPa.

1989) suggested a ψ equal to $\sqrt{-\frac{4\overline{x}\log\upsilon}{\Gamma}}$ where υ is an infinitesimal number. Depending on the Goldberg number an appropriate υ is required. Our analysis showed that for the range of Goldberg number encountered in the context of this thesis, a constant $\psi = 10$ specifies a broad enough range to include the variation of the exponential term. To deal with the second problem, the *mpmath* library was used (Johansson, 2013). This library provides high precision floating-point arithmetic. We used a multi-interval quadrature integration scheme which splits the integration range $[\tau_w - \psi, \tau_w + \psi]$ to 40 intervals and the precision is set to 100 floating points.

As we demonstrated in Chapter 3, a relatively strong pressure field is required to considerably influence the thermodynamics of phase transition. Thus, we calculate the pressure field created by a source with $p_m = 10$ MPa and $p_m = 50$ MPa. Figures 7.1 and 7.2 show the wave propagating across space at the end of an excitation period for the driving condition $f = 1$ MHz, $p_m = 10$ MPa and $f = 1$ MHz, $p_m = 50$ MPa, respectively. We can see (more visible in Fig. 7.2) in the pre-shock region, the wave field can be safely approximated by a harmonic travelling wave as the distortion is negligible. However, around the shock formation distance (henceforth, shock distance) the waveform distorts and gradually develops into an N-shaped waveform (henceforth, N-wave) in the far field. The shock distance is inversely proportional to the pressure magnitude, see Eq. (7.2c). Hence, as shown in Fig. 7.2, the waveform distorts

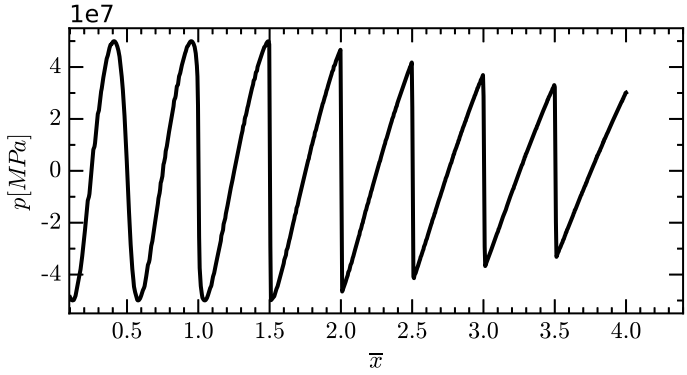

Figure 7.2: Plane wave field across space up to $1.5x_s$ at $\tau_w = 2\pi$ with $f = 1$ MHz and $p_m = 50$ MPa.

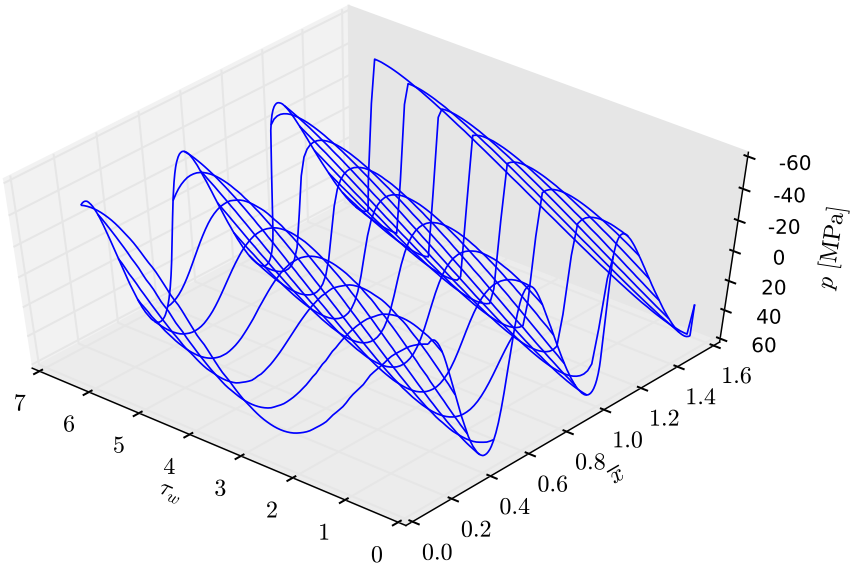

Figure 7.3: Plane waveform across space up to $1.5x_s$ over one period with $f = 1$ MHz and $p_m = 50$ MPa.

and turns into an N-wave over a shorter distance when $p_m = 50$ MPa and the driving frequency is unchanged. Increasing the pressure magnitude by a factor of five reduces the ratio of the shock distance to the wavelength by a fifth, from 10 to 2. Nevertheless, as long as $\overline{x} \ll x_s$, the harmonic travelling wave equation is sufficient to accurately represent the acoustic field, see Fig. 7.3. The acoustic Mach numbers for waves shown in Fig. 7.1 and 7.2 are $M_a = 0.004$ and $M_a = 0.02$, respectively, which satisfy the weak shock condition.

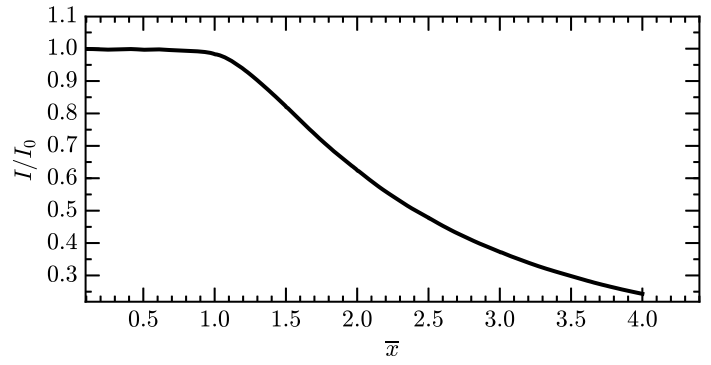

(a)

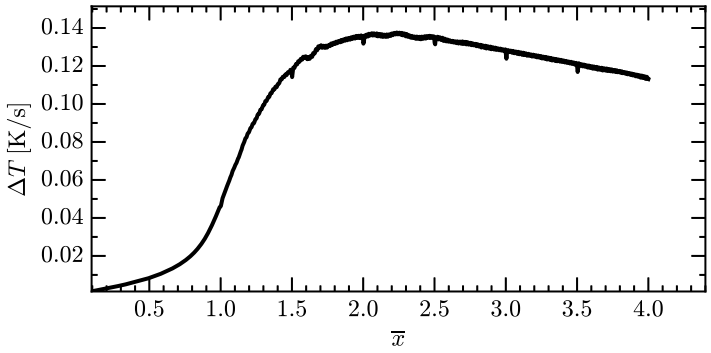

(b)

Figure 7.4: (a) Relative intensity across space, (b) temperature variation across space for $p_m = 50$ MPa and $f - 1$ MHz.

The temperature in the fluid while only accounting for the absorption of a plane wave energy is given by (Hamilton and Blackstock, 1998)

$$\frac{dT}{dt} = -\frac{1}{\rho_1 C_h}\frac{dI}{dx} = \frac{2\alpha_f I}{\rho_1 C_h}, \tag{7.3}$$

where I is the intensity of acoustic waves at the desired location, α_f is the frequency dependent absorption coefficient and C_h is the heat capacity of the fluid. α_f is obtained by the binomial expansion of the characteristic wave number (Hamilton and Blackstock, 1998)

$$\alpha_f = \frac{\delta_0}{2c_0^3}\omega^2, \tag{7.4}$$

Intensity is the time average of the energy flux pu which for a plane wave simplifies to $I = \langle p^2 \rangle / \rho_1 c_0$. The relative intensity with respect to $I_0 = p_m^2 / \rho_1 c_0$

is almost unity in the pre-shock zone but drops for $\overline{x} > 1$, see Fig. 7.4. This results in negligible temperature variation in the pre-shock region. Therefore, the isothermal assumption made in Section 3.3 is verified if i) the system is located in the pre-shock zone, or ii) the acoustic irradiation is short or pulsed for systems in $x > x_s$. Simulation parameters will be chosen such that the isothermal condition holds for the results presented in this chapter.

7.2 Mass conserved system

We derived and non-dimensionalised the governing equations for the kinetics of cluster formation in a mass conserved system in Section 4.4. In this section, we will solve these equations numerically and present the results. Different scenarios are considered to investigate the effects of the pressure magnitude, frequency and waveform on the kinetics of clustering in a closed system. Employing these equations under isothermal condition, we can study nucleation, the early stage of growth and also the Ostwald ripening regime in a system undergoing pressure variation.

7.2.1 Numerical implementation

We consider a single closed system in the bath with a time varying supersaturation ratio. Also, it is postulated that only monomers are present in the system and bath initially. The presence of n-size clusters, $2 \leq n \leq 4$, at the initial condition may change the nucleation rate by less than one order of magnitude (Kozísek and Demo, 2005). Consequently, the considered initial condition is adequate for our work.

With regards to the numerical computation, Eq. (4.47) is taken and the following procedure is applied

(i) the FPE in the hybrid model is discretised exploiting the CC70 algorithm developed by Chang and Cooper (Chang and Cooper, 1970). This algorithm is specifically designed for solving the FPE. The CC70 algorithm converts the FPE from a PDE to a set of ODEs using a special weighted finite difference scheme. This algorithm ensures that the conservation

of the total number of particles in the system and the non-negativity of $\overline{Z(n)}$ hold.

(ii) this set of ODEs obtained from the discretisation of the FPE together with the ODEs of the Szilard equations are combined and solved using the VODE solver (Brown et al., 1989). VODE is an adaptive variable ODE solver developed to deal with stiff ODEs with time-dependent coefficients (Brown et al., 1989).

The boundary conditions are defined as follows: i) equal concentration and flux condition at the boundary between discrete and continuous sections of the model, i.e. at N_d, and ii) zero flux condition at the end of the size axis, i.e. N. To present these boundary conditions mathematically, we will need the discretised form of the FPE. For ease of the reader, the dimensionless FPE is reproduced here

$$\frac{\partial \overline{Z(n)}}{\partial \tau} = -\frac{\partial}{\partial n}\left(\overline{v(n)}\ \overline{Z(n)} - \frac{1}{2}\frac{\partial\left[\overline{d(n)}\ \overline{Z(n)}\right]}{\partial n}\right) = \frac{\partial J(n)}{\partial n}, \tag{7.5}$$

where $J(n)$ is the flux in the continuous size domain and is equal to the negative of the terms in the bracket. Exploiting the central finite difference method, we can write

$$\frac{d\overline{Z}_m}{d\tau} = \frac{J_{m+1/2} - J_{m-1/2}}{\Delta n_{m-1,m+1}}, \tag{7.6}$$

where

$$\Delta n_{m-1,m+1} = \frac{n_{m+1} - n_{m-1}}{2}. \tag{7.7}$$

Therefore, the boundary condition at the matching point, where $m = N_d$, reads

$$\begin{aligned} Z_{N_d} &= Z(N_d), \\ J_{N_d} &= \frac{J_{N_d-1/2}}{\Delta n_{N_d-1,N_d+1}} \quad \Longrightarrow \quad f_{N_d} Z_{N_d} - g_{N_d+1} Z_{N_d+1} = \frac{J_{N_d-1/2}}{\Delta n_{N_d-1,N_d+1}}. \end{aligned} \tag{7.8}$$

And the boundary condition at the final point on the cluster size axis reads

$$\frac{J_{N+1/2}}{\Delta n_{N-1,N+1}} = 0, \tag{7.9}$$

thus, evaluating Eq. (7.6) at $m = N$ simplifies to

$$\frac{d\overline{Z}_N}{d\tau} = -\frac{J_{N-1/2}}{\Delta n_{N-1,N+1}}, \tag{7.10}$$

The expansion and computation of $J_{m\mp1/2}$ based on the CC70 algorithm is skipped here and the reader is referred to (Chang and Cooper, 1970) for detailed information. Finally, the mesh grid on the cluster size axis must be generated. Since a gradual and smooth increase from a relatively small N_d to a large N with a minimum number of nodes is desired, a power law expression suggested in other works (Vetter et al., 2013; Rempel, 2008) will be taken here

$$n_{m+1} = n_m + (1 + a)^m. \tag{7.11}$$

where a controls the mesh refinement. Depending on the value of N_d and the total number of molecules N, the number of nodes and subsequently the simulation time vary. For simulations reported here, we set $a = 0.001$ and N changes from 500 to 8000 based on the expected size of crystals which may appear during the simulation time interval and N_d is usually set to 500. This produces a relatively fine mesh with a large set of ODEs which is usually required when pressure fluctuates considerably. Otherwise, for simulations where the numerical computation was stable with a coarser mesh, e.g. at lower pressure magnitudes, we used the combination of $a = 0.01$, $N = 2500$ to reduce

the simulation time. The numerical scheme was coded in Python and the implementation was validated against the published results of Vetter et al. and Rempel et al. (Vetter et al., 2013; Rempel, 2008) with the identical set of parameters.

7.2.2 Simulation results

Here, we report simulations performed using different sets of parameters. We will start with varying the magnitude of pressure statically. This will be followed by a harmonic pressure excitation modelled using the Burgers' equation, described in Section 7.1. Whilst Burgers' equation is a one-dimensional model, we will demonstrate that simulation results can explain some experimental trends reported in the literature. The driving acoustic pressure magnitude and frequency were varied from 1 MPa to 50 MPa and 20 kHz to 2 MHz, respectively. This range of acoustic parameters pertains to the experimental amplitude and frequency of ultrasonic waves generated by different types of transducers, e.g. planar and high intensity focused, used in sonocrystallisation experiments.

The non-dimensionalisation constants are $f_c = g_c = t_c^{-1} = 2.9 \times 10^5$ s^{-1} and $z_c = C_e = 10^{23}$ m^{-3} s^{-1}. Unless otherwise stated, all the following simulations were conducted with $\lambda = 0.35$ which is an average value of λ formerly obtained for water droplet formation at $T = 300$ K. This choice is improvised assuming the surface energy of clusters in a dilute aqueous solution shows a similar size dependence as water droplets at the same temperature. Nevertheless, we will investigate the effect of different values of λ in Section 7.4.

7.2.2.1 Static pressure

The effect of the pressure magnitude on the nucleation barrier at different supersaturation ratios was discussed in Chapter 3. Here, we will investigate the effect of the magnitude of the static pressure on the kinetics of crystallisation. Initially we will determine the stationary nucleation rate at the ambient pressure with different supersaturation ratios, see Fig. 7.5. Setting the nucleation rate threshold at 10^6 m^{-3}s^{-1},(Kashchiev and Van Rosmalen, 2003) gives

a minimum of r_0 = 24 for nucleation to take place practically. Following the discussion in Chapter 4, we set the initial supersaturation ratio r_0 = 30 for all the simulations presented in this chapter. This tentatively allows observing the effect of pressure fluctuations on crystallisation with relatively modest pressure magnitudes obtainable experimentally.

Figure 7.6 shows the concentration of supercritical clusters over time at different pressure magnitudes of 1, 10, 50 and 100 MPa. Vertical dashed lines illustrate the nucleation time lag at different pressure magnitudes. Similar to the water droplet formation, the nucleation time lag is defined as the time required for the first ten supercritical clusters to appear. We can see that in

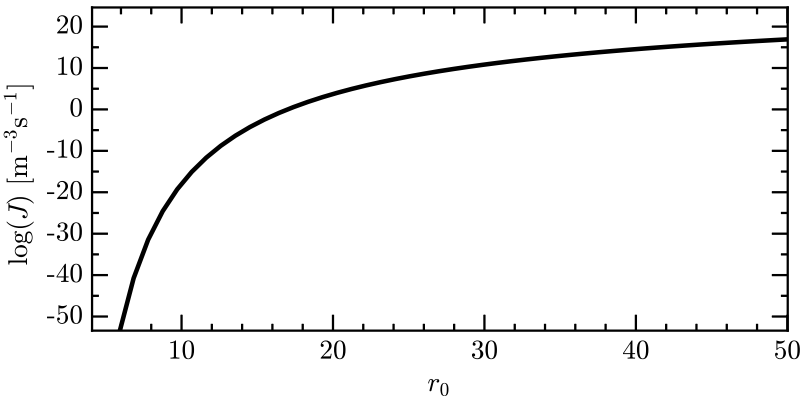

Figure 7.5: Stationary nucleation rate at different supersaturation ratios determined by the BD model.

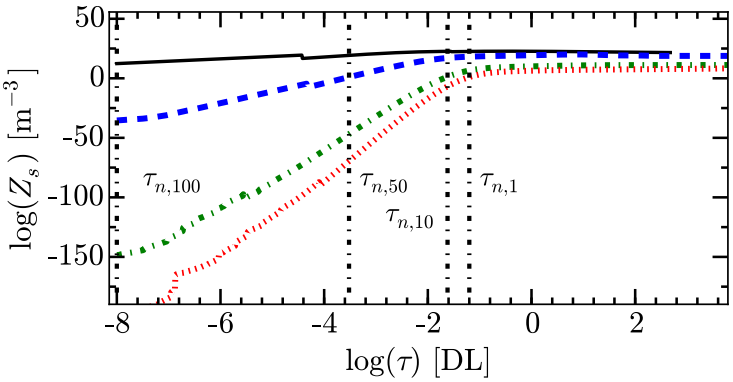

Figure 7.6: Concentration of supercritical clusters at different pressure magnitudes over time with λ = 0.35. Vertical lines labelled $\tau_{n,100}$ to $\tau_{n,1}$ indicate the beginning of the nucleation stage for different static pressures of old phase. Static pressure decreases from the black curve (100 MPa) at the top to the red curve at the bottom (1 MPa).

the case of positive k_ρ, τ_n has an inverse relationship with the pressure magnitude. For example, the nucleation time lag reduces by more than six orders of magnitude as the pressure magnitude increases only by one order from 10 MPa to 100 MPa ($\tau_{n,100} \approx 10^{-8}$ which gives $t_{n,100} \approx 30$ fs). A similar trend between the pressure magnitude and the experimental lifetime of superheated xenon, oxygen and argon liquids was reported in the literature too (Baidakov et al., 1981; Baidakov and Kaverin, 2009). They reported an inverse relationship between the driving voltage, i.e. proportional to the pressure magnitude p_m, and the lifetime for these superheated liquids. The lifetime of the superheated liquid is conceptually equivalent to the nucleation time τ_n determined in this work (Kashchiev, 2000; Baidakov, 2007). Thus, the simulation results qualitatively agree with the reported experimental observations. However, in that case, the new phase is gaseous and less dense, thus Δn_{exc} is negative and a negative Δp is required to lower the nucleation barrier and reduce the lifetime, see Eq. (3.19).

The supersaturation ratio over time is depicted in Fig. 7.7. An increase in the pressure magnitude amplifies the depletion rate of monomers in a closed system. This fast nucleation rate leads to supercritical clusters with smaller sizes. Analysing Fig. 7.8, we can see that the Ostwald ripening regime at the highest pressure (100 MPa) starts at roughly $\log(\tau) = -0.7$ when the concentration of supercritical clusters reaches its maximum and declines afterward. The average size of supercritical clusters, however, increases after this instance which is due to the absorption of depleted monomers from smaller clusters by larger clusters. The Ostwald ripening, however, could not be observed when the pressure magnitude is equal to 1 MPa, see Fig. 7.9. In this case, the concentration and the average size of supercritical clusters increase and sharply drop together. In Figs. 7.8 and 7.9, the concentration of supercritical clusters are not smooth because of the discretised nature of the numerical method employed for solving the kinetics of cluster formation.

The contour plots in Figs. 7.10-7.12 show the size-weighted cluster size

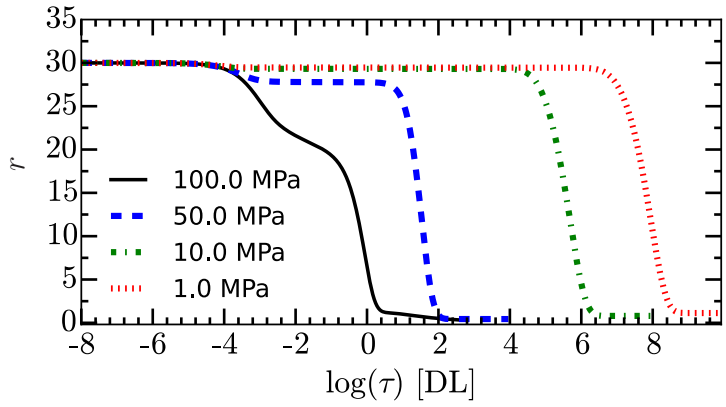

Figure 7.7: Supersaturation ratio at different pressure magnitudes over time with $\lambda = 0.35$.

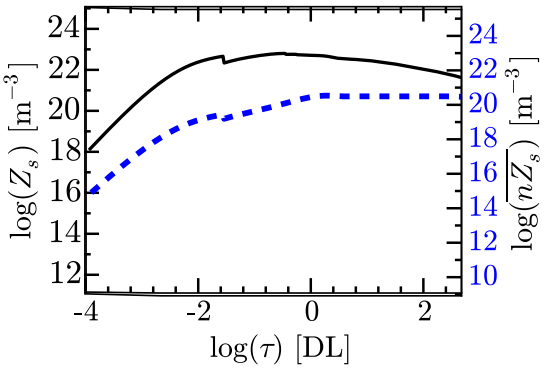

Figure 7.8: Concentration of supercritical clusters (solid line) and mean size of supercritical clusters (dashed line) at the static pressure of 100 MPa and with $\lambda = 0.35$. Around $\log(\tau) = -0.7$ the concentration of supercritical clusters becomes a maximum and starts to decline whereas the mean size of supercritical clusters increases and plateaus shortly after.

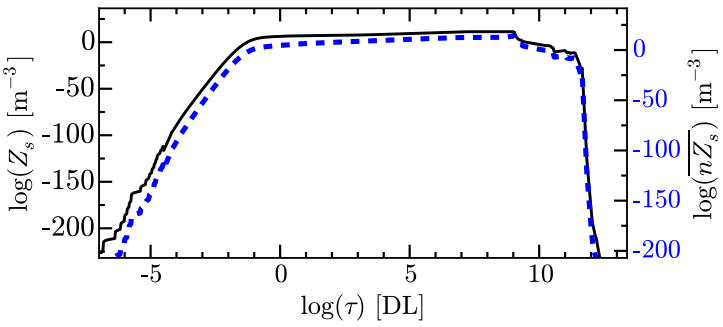

Figure 7.9: Concentration of supercritical clusters (solid line) and mean size of supercritical clusters (dashed line) at the static pressure of 1 MPa and with $\lambda = 0.35$. Around $\log(\tau) = 8.8$ the supersaturation ratio approaches unity, the concentration of supercritical clusters becomes a maximum and starts to decline. The mean size of supercritical clusters drops too but a ripening process could not be identified.

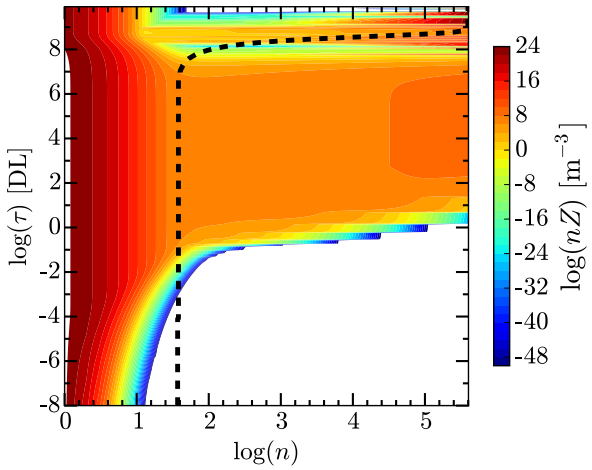

Figure 7.10: Logarithmic CSD, i.e. the contour plot of logarithmic size-weighted cluster size distribution ($\log(nZ)$), over time at the static pressure 1 MPa with $\lambda = 0.35$. The black dashed line shows the time-dependent size of the critical cluster.

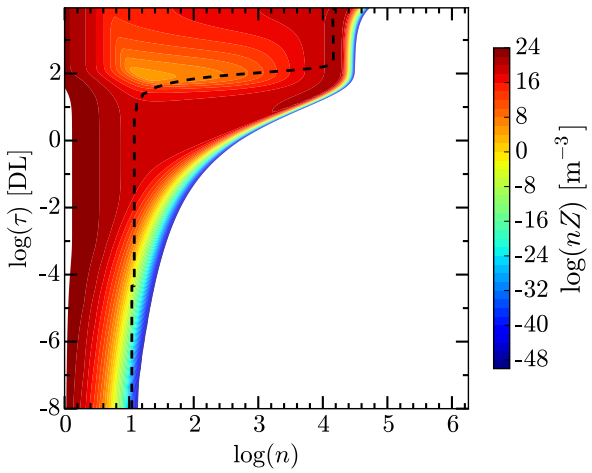

Figure 7.11: The same as Fig. 7.10 but at the static pressure of 50 MPa.

distribution at three different static pressures. The time-dependent size of the critical cluster is overlaid on each plot. We can obviously see that the size of critical clusters follows the same trend as the supersaturation ratio over time. The initial critical cluster sizes are $40, 16$ and 4 at pressure magnitudes of 1 MPa, 50 MPa and 100 MPa, respectively. Furthermore, these plots illustrate that the size of critical clusters and the mean size of supercritical clusters inversely correlate with the pressure magnitude (when $k_\rho > 0$). Reading the concentration of clusters at the end of the nucleation period, from

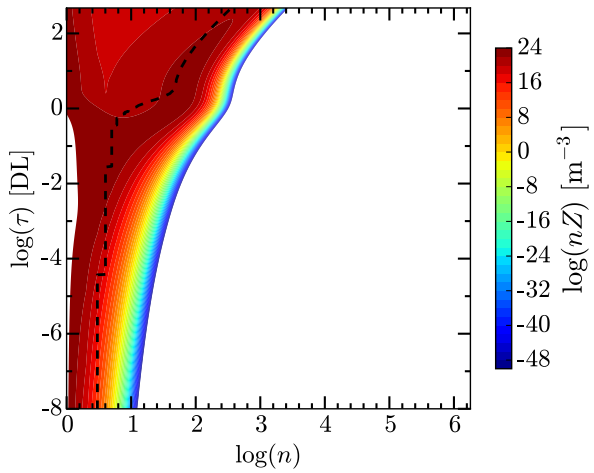

Figure 7.12: The same as Fig. 7.10 but at the static pressure of 100 MPa.

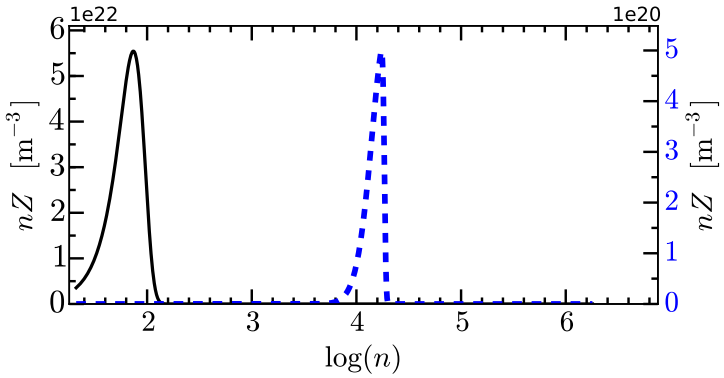

Figure 7.13: CSD at the end of the nucleation stage ($r \approx 1$) at two static pressures of 100 MPa, the left vertical axis, and 50 MPa, the right vertical axis. Refer to the text for details.

this contour, we obtain the CSD under these conditions, depicted in Fig. 7.13. This figure shows that the mean of the CSD becomes smaller as the pressure magnitude increases. This is attributed to a short nucleation period due to a fast nucleation rate which causes a significant reduction in the time difference between the birth time of different stable supercritical clusters. Furthermore, the distribution becomes broader at the higher pressure magnitudes which is due to the enhancement of the ripening process with the pressure rises (when $k_\rho > 0$).

Using the preceding discussion of the CSD plots, a more detailed analysis of the results presented in Fig. 7.7 can be carried out. Following the analysis presented in Section 6.1, the curves of the supersaturation ratio corresponding

to pressure magnitudes of 1 MPa – 50 MPa in Fig. 7.7 can be divided into three parts: i) the relaxation part where subcritical clusters and the first ten supercritical clusters are created, ii) the part corresponds to nucleation and growth stage where the supersaturation ratio plateaus and sharply drops to unity, i.e. $r \approx 1$, at the end of this stage. The onset of this part is indicated by a vertical dashed-dotted line in Fig. 7.6. Nucleation is dominated during the plateau segment whereas growth becomes significant when the plateau turns into an abrupt drop of the supersaturation ratio. This is identified by the significant increase in the mean size of supercritical clusters observable in CSD plots shown in Figs. 7.10 and 7.11. iii) the growth and the Ostwald ripening part where starts when the concentration of the supercritical clusters decreases while the mean size of supercritical clusters increases. The Ostwald ripening usually takes place after the nucleation stage when large supercritical clusters are formed (during which $r \approx 1$).

At the pressure of 100 MPa (the black curve in Fig. 7.7), the boundaries between the nucleation and growth and the Ostwald ripening zones are unclear. Analysing Fig. 7.12 at the time interval of $-4 < \log(\tau) < -0.7$, we can observe the concomitant occurrence of nucleation and growth. It can be seen in Fig. 7.7 that at the time instant $\log(\tau) = -0.7$ (when the Ostwald ripening begins), the supersaturation ratio is well above unity and therefore nucleation, growth and the Ostwald ripening are taking place simultaneously.

This analysis implies that very high pressure magnitude can lead to fast nucleation rate and a smaller mean size of the supercritical clusters but with a broader distribution as the Ostwald ripening starts at an early stage. The mean of the CSD determined at the end of nucleation and shown in Fig. 7.13 confirms this deduction.

7.2.2.2 Harmonic excitation

As shown in Section 7.1, we can approximate the pressure oscillation by a harmonic mono-frequency wave where $x \ll x_s$. Now, we consider a situation in which this condition is fulfilled. Hence, the local pressure is modelled by

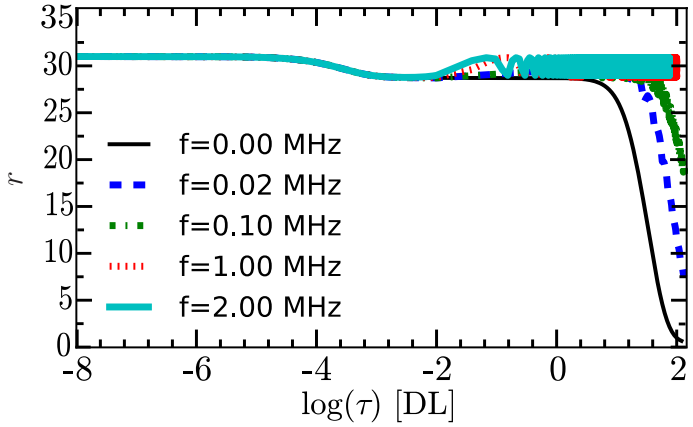

Figure 7.14: Supersaturation ratio over time at different excitation frequencies and pressure magnitude of p_m = 50 MPa with λ = 0.35.

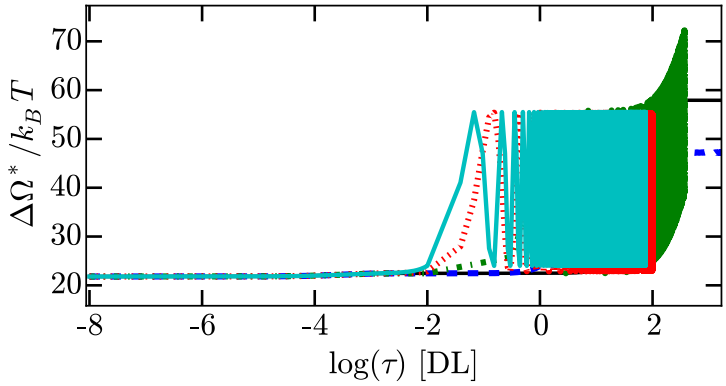

Figure 7.15: Nucleation work over time at different excitation frequencies and pressure magnitude of p_m = 50 MPa with λ = 0.35. The legend is the same as that of Figure 7.14.

$p = p_a + p_0$ where p_0 is the ambient pressure at the reference state and $p_a = p_m \cos(2\pi f t)$ is the acoustic pressure in the system with magnitude p_m and frequency f. In the next section, we will also consider a case where $x > x_s$. Furthermore, we will only account for the direct acoustic field and exclude the emitted pressure from the potential acoustic cavitation which may occur at a setting of the acoustic field.

Given the results of the static pressure condition, the thermodynamics and kinetics of phase transition are influenced more considerably at high pressure magnitudes. Therefore, in this section, we set p_m = 50 MPa and conduct simulations of nucleation in the same aqueous solution exposed to an acoustic wave with frequencies of 0.02, 0.1, 1 and 2 MHz. The quasi-stationary condi-

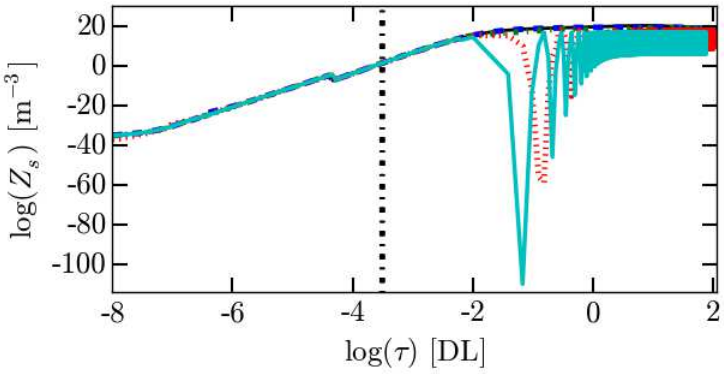

(a)

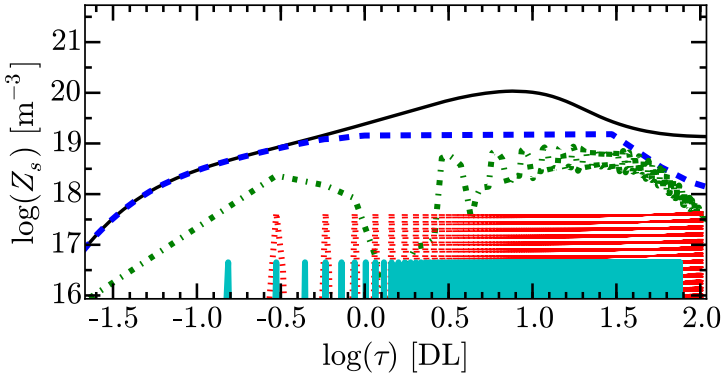

(b)

Figure 7.16: (a) Concentration of supercritical clusters over time where the old phase is exposed to pressure fluctuation with p_m = 50 MPa at different frequencies. The legend is the same as that of Figure 7.14. (b) magnified towards the end of simulation with f = 0 MHz (when $r \cong 1$). We can see that at f = 0, 20, 100 kHz, Z_s reaches its maximum value at $\log(\tau)$ = 0.9, 1.4, 1.5, respectively. The Ostwald ripening process follows. In contrast, at higher frequencies the nucleation stage is still ongoing at this time.

tion does not hold for these excitation settings, see Fig. 4.10, hence Eq. (4.14) is used to determine the nucleation rate.

Compared with the static pressure condition, the pressure oscillation leads to a smaller effective pressure magnitude which lowers the effective nucleation rate. This point is observed in Fig. 7.14 where the nucleation stage ends at $\log(\tau) = 0.8, 1.4, 1.8$ at driving frequencies of $0, 0.02$ and 0.1 MHz, respectively, whereas it is still ongoing for higher frequency oscillations. The main reason for this behaviour is the variation in the nucleation work due to pressure oscillations, see Fig. 7.15, and subsequently the detachment frequency.

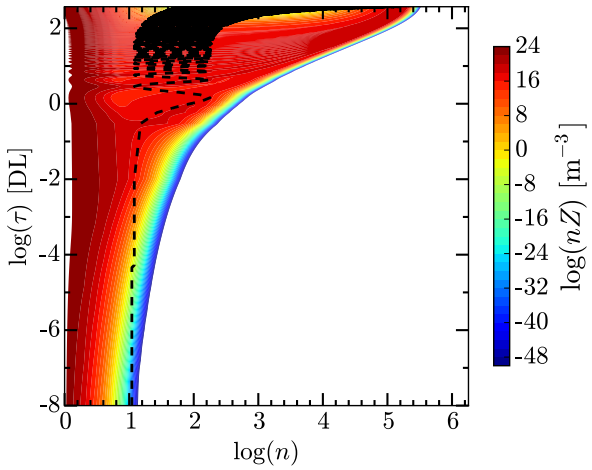

Figure 7.17: Logarithmic CSD over time where the solution is exposed to an acoustic wave with excitation parameters of f = 100 kHz and p_m = 50 MPa with λ = 0.35.

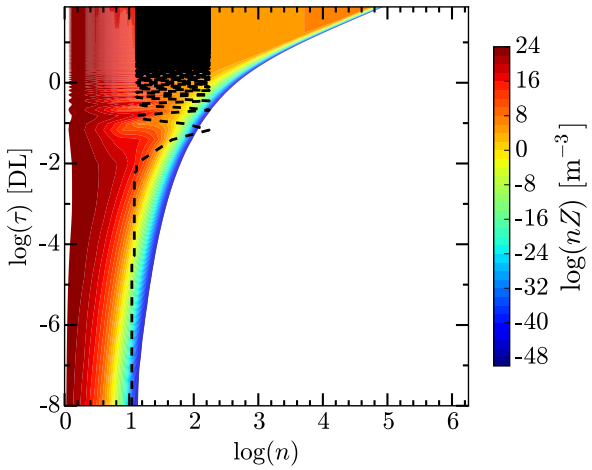

Figure 7.18: The same as Fig. 7.17 but with excitation parameters of f = 2 MHz and p_m = 50 MPa.

Equation (3.16) shows that in an isothermal process, pressure can impede or facilitate nucleation depending on the sign of $\Delta n_{exc} \Delta p$. When Δn_{exc} is positive (i.e. the formation of a condensed phase), an isothermal increase in the reference pressure reduces the nucleation work and consequently the depletion rate, Eq. (4.40), which gives a higher nucleation rate and vice versa. This also influences the concentration of supercritical clusters, shown in Fig. 7.16, such that Z_s reduces as the frequency increases.

CSD contour plots for two frequencies are shown in Fig. 7.17 and 7.18.

Comparing them with the CSD at the static pressure of p_m = 50 MPa, we observe that: i) supercritical clusters are larger in size, i.e. the concentration is non-zero for $\log(n) > 4.8$, and ii) the concentration of supercritical clusters is reduced due to pressure oscillations. In other words, acoustic waves cause a reduction in the magnitude of the CSD at the end of nucleation and shift the mean of the CSD to a larger value as the frequency increases. The latter trend was reported in the precipitation of manganese carbonate in an acoustic field (Jordens et al., 2015). We should be very cautious in using this experimental data as cavitation is likely to occur in their experiments. However, cavitation was not monitored and quantified in their work. If we only consider the trends reported at the lowest driving power, i.e. 4 W L^{-1}, as the driving frequency increases from 94 kHz to 1.1 MHz, the mean value of the crystal size grows from roughly 4 μm to 13 μm. The likelihood of cavitation reduces at higher frequencies especially at lower driving power. Hence, the qualitative comparison becomes justifiable as cavitation was not accounted for in our simulations.

7.3 Non-mass conserved system

Here, we will study mass transportation created by acoustic waves and its impact on crystallisation in the system. In the first part of this section, we will investigate mass transportation alone, without a phase transformation, for different excitations by solving Eq. (5.30). We will then solve the coupled problem of sonocrystallisation in a non-mass conserved system for the situation where mass transportation is more considerable.

7.3.1 Numerical implementation

The first line of the hybrid model in a non-mass conserved system is a PDE with derivatives with respect to the space parameter. The central finite difference method is exploited to discretise the mass transportation terms along the spatial axis x in this equation. Therefore, a set of ODEs must be solved to achieve the spatial distribution of monomers. At each spatial node, the coupled hybrid model Eq. (5.25) must be solved to compute the cluster dynamics. We

use the same numerical approach outlined in Section 7.2.1 for discretisation of the FPE along the cluster size axis. Likewise, similar boundary conditions are applied for solving the FPE. Here, cluster dynamics is both spatial- and time-dependent.

Equation (5.30) in a one dimensional acoustic field simplifies to

$$\frac{\partial}{\partial \tau}\overline{Z_1} = -\overline{u}\frac{\partial \overline{Z_1}}{\partial \overline{x_d}} + \frac{1}{Pe}\frac{\partial^2 \overline{Z_1}}{\partial \overline{x_d}^2} + \frac{\overline{\beta}}{Pe}\frac{\partial \overline{Z_1}}{\partial \overline{x_d}}\frac{\partial \overline{p}}{\partial \overline{x_d}} + \frac{\overline{\beta}}{Pe}\overline{Z_1}\frac{\partial^2 \overline{p}}{\partial \overline{x_d}^2}. \tag{7.12}$$

Here $\overline{x_d}$ refers to the dimensionless location using the non-dimensionalisation coefficient stated in Section 5.4 instead of the shock distance used to solve Burgers' equation.

Writing the central finite difference for derivatives reads

$$\left.\frac{\partial \overline{Z_1}}{\partial \overline{x_d}}\right|_m = \frac{\overline{Z_1}\big|_{m+1/2} - \overline{Z_1}\big|_{m-1/2}}{\Delta \overline{x}_{dm-1,m+1}} = \frac{\overline{Z_1}\big|_{m+1} - \overline{Z_1}\big|_{m-1}}{2\Delta \overline{x}_{dm-1,m+1}}, \tag{7.13a}$$

$$\left.\frac{\partial \overline{p}}{\partial \overline{x_d}}\right|_m = \frac{\overline{p}\big|_{m+1/2} - \overline{p}\big|_{m-1/2}}{\Delta \overline{x}_{dm-1,m+1}} = \frac{\overline{p}\big|_{m+1} - \overline{p}\big|_{m-1}}{2\Delta \overline{x}_{dm-1,m+1}}, \tag{7.13b}$$

$$\left.\frac{\partial^2 \overline{Z_1}}{\partial \overline{x_d}^2}\right|_m = \frac{\left(\overline{Z_1}\big|_{m+1} - \overline{Z_1}\big|_m\right)\Delta \overline{x}_{dm-1,m} - \left(\overline{Z_1}\big|_m - \overline{Z_1}\big|_{m-1}\right)\Delta \overline{x}_{dm,m+1}}{\Delta \overline{x}_{dm-1,m}\Delta \overline{x}_{dm-1,m+1}\Delta \overline{x}_{dm,m+1}}, \tag{7.13c}$$

$$\left.\frac{\partial^2 \overline{p}}{\partial \overline{x_d}^2}\right|_m = \frac{\left(\overline{p}\big|_{m+1} - \overline{p}\big|_m\right)\Delta \overline{x}_{dm-1,m} - \left(\overline{p}\big|_m - \overline{p}\big|_{m-1}\right)\Delta \overline{x}_{dm,m+1}}{\Delta \overline{x}_{dm-1,m}\Delta \overline{x}_{dm-1,m+1}\Delta \overline{x}_{dm,m+1}}, \tag{7.13d}$$

where

$$\Delta \overline{x}_{di,j} = \frac{\overline{x}_{dj} - \overline{x}_{di}}{j-i}. \tag{7.14}$$

Substituting these relations into Eq. (7.12) converts this PDE to a set of ODEs across the spatial mesh grid. We employed the same VODE solver as before for integrating over time and solving ODEs. The spatial axis is discretised using a uniform grid with 500 nodes which results in $\Delta \overline{x}_{dm-1,m+1} = \Delta \overline{x}_{dm,m+1} = \Delta \overline{x}_{dm-1,m} = \Delta \overline{x}_d$. Finally, discretising Eq. (7.12) by a central finite

difference method and using a uniform spatial grid result in

$$\left.\frac{d\overline{Z_1}}{d\tau}\right|_m = \mathcal{A}\overline{Z_1}\big|_{m-1} + \mathcal{B}\overline{Z_1}\big|_m + \mathcal{C}\overline{Z_1}\big|_{m+1}, \tag{7.15a}$$

$$\mathcal{A} = \frac{\overline{u}\big|_m}{2\Delta\overline{x_d}} + \frac{1}{Pe\Delta\overline{x_d}^2} - \frac{\overline{\beta}}{4Pe\Delta\overline{x_d}^2}\left(\overline{p}\big|_{m+1} - \overline{p}\big|_{m-1}\right), \tag{7.15b}$$

$$\mathcal{B} = \frac{\overline{\beta}}{Pe\Delta\overline{x_d}^2}\left(\overline{p}\big|_{m+1} - 2\overline{p}\big|_m + \overline{p}\big|_{m-1}\right) - \frac{2}{Pe\Delta\overline{x_d}^2}, \tag{7.15c}$$

$$\mathcal{C} = -\frac{\overline{u}\big|_m}{2\Delta\overline{x_d}} + \frac{1}{Pe\Delta\overline{x_d}^2} + \frac{\overline{\beta}}{4Pe\Delta\overline{x_d}^2}\left(\overline{p}\big|_{m+1} - \overline{p}\big|_{m-1}\right). \tag{7.15d}$$

Regarding boundary conditions, different scenarios can be considered. Here we are interested in a generic situation to investigate mass transportation due to one-dimensional plane wave propagation in the bulk of the solution, so we will choose a simple von Neumann type boundary condition of $\left.\frac{\partial\overline{Z_1}}{\partial\overline{x_d}}\right|_0 = 0$. This implies a situation where no ordinary diffusive flux takes place in the boundary. From the acoustical point of view, we assume that the boundary and the surrounding medium have identical characteristic acoustic impedances resulting in a transmission coefficient of unity.

Casting a similar relationship for the boundary condition at $m = end\ point$ will make the mass transfer model solvable. For simplicity, the length of the bath in which crystallisation occurs, is set to be equal to one wavelength, e.g. it is about 1500 μm at $f = 1$ MHz. Nonetheless, we will present the results obtained in a bath with the length of multiple wavelength.

7.3.2 Simulation results

We will initially present the simulation results of the transportation of monomers in an acoustic field with different pressure amplitudes and frequencies. We will then proceed to determine the kinetics of crystallisation over time and across space for a case where mass transportation is more substantial. The acoustic pressure amplitude is chosen to be 10 MPa and 50 MPa. Simulations with $p_m = 50$ MPa were conducted in two different frequencies of 100 kHz

Table 7.1: Non-dimensionalisation constants calculated using equations presented in Section 5.4.

	t_c [ns]	l_c [nm]	v_c [m s^{-1}]	p_c [MPa]	Pe [DL]	$\overline{\beta}$ [DL]
$p_m = 10$ MPa, $f = 1$ MHz	6.6	44.7	6.75	10	302	−0.12
$p_m = 50$ MPa, $f = 1$ MHz	1.32	44.7	33.74	50	1509	−0.61
$p_m = 50$ MPa, $f = 100$ kHz	4.18	141.4	33.74	50	4773	−0.61

and 1 MHz. This range of acoustic parameters is selected on the basis of the discussion outlined in Section 7.2.

The non-dimensionalisation constants depend on the excitation parameters and are shown in Table 7.1. The density of the solute species in an aqueous solution typically falls in the range of $1000 < \rho_{mass,2} < 2500$ kg m^{-3}. We choose $\rho_{mass,2} = 2000$ kg m^{-3} and employ the following equation to estimate the molar mass for the solute species, i.e. $M_2 = {}^4\!/\!_3\pi R_0^3 \mathcal{N}_\mathcal{A} \rho_{mass,2} = \mathcal{N}_\mathcal{A} \nu_n \rho_{mass,2}$.

Finally, for all results presented here we considered the von Neumann boundary condition mentioned above and a spatially uniform initial concentration.

As shown in Section 7.1, pressure oscillations can be approximated by a harmonic lossless mono-frequency wave where $x < x_s$. First, we consider a situation which fulfills this condition and hence the local pressure is modelled by $p = p_a + p_0$ where $p_a = p_m \sin(\omega t - k_w x)$ and k_w is the wavenumber.

The variation in the supersaturation ratio in the acoustic field is determined by defining the quantity $\Delta\overline{Z_1}$ as follows

$$\Delta\overline{Z_1} = \frac{\overline{Z_1}}{r_0} - 1, \tag{7.16}$$

subsequently, we can write $r(x,t) = \overline{Z_1} = r_0\left(1 + \Delta\overline{Z_1}\right)$ where $r(x,t)$ is the spatially and temporally variable supersaturation ratio.

Figure 7.19 shows the contour plot of the variation in the concentration of monomers across one wavelength in the pre-shock region over one period of oscillation. Although the pressure magnitude is relatively large, it has a negligible effect on the spatial distribution of monomers. This result is expected as

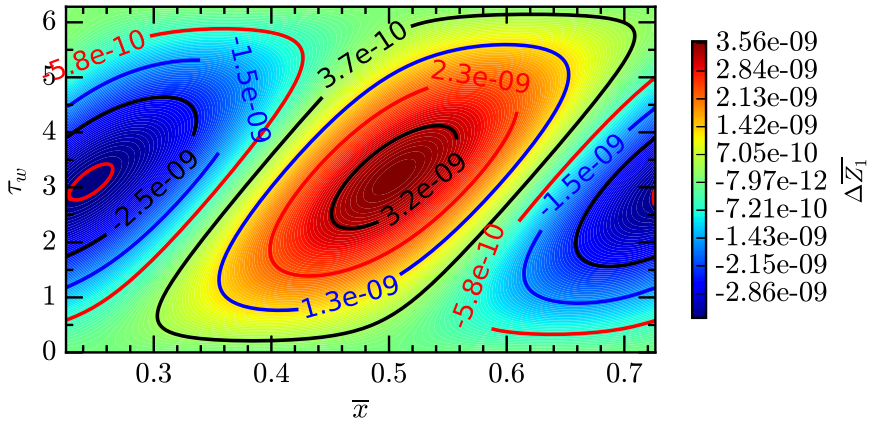

Figure 7.19: Change in the concentration of monomers across a wavelength centered about $0.5x_s$ over one period in a travelling wave field with $p_m = 50$ MPa, $f = 1$ MHz.

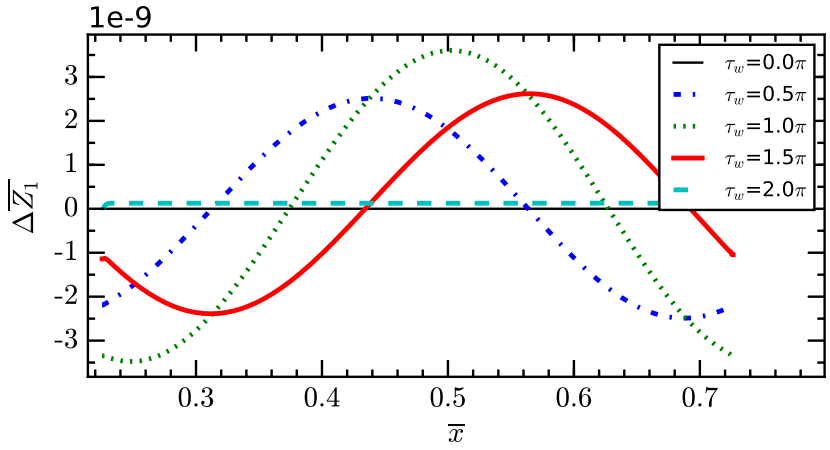

Figure 7.20: Four snapshots of contours shown in Fig. 7.19.

the pressure diffusion is typically a slow process and may become noticeable only over a large time scale or in the presence of a significant pressure gradient. At $\tau_w = 0$ the peak positive pressure is located at $\overline{x} = 0.48$ which corresponds to the concentration hot spot (the location where the concentration is maximum). The heavier species moves towards the high pressure region and consequently the hot spot smears as the acoustic wave travels. This can be seen in Fig. 7.20 that the peak in the concentration translates less than $0.2\overline{x} \approx 0.4\lambda_a$ during a period of oscillation. For a harmonic wave, the gradient and Laplacian of the pressure field is proportional to k_w and k_w^2, respectively. This implies that a stronger/weaker effect on the concentration is anticipated at higher/lower

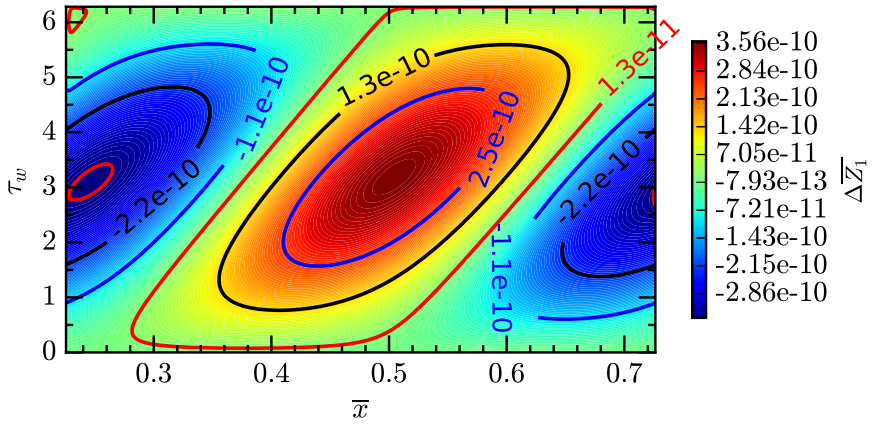

Figure 7.21: Change in the concentration of monomers across a wavelength centered about $0.5x_s$ over one period in a travelling wave field with p_m = 50 MPa, f = 100 kHz.

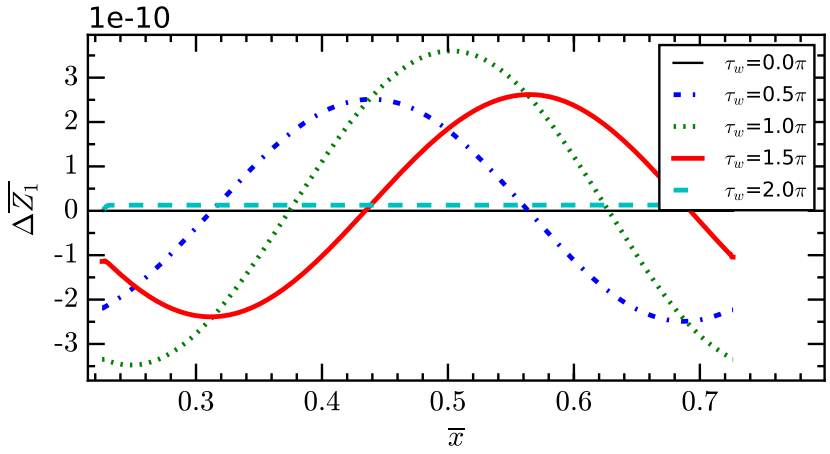

Figure 7.22: Four snapshots of contours shown in Fig. 7.21.

excitation frequencies. Figures 7.21 and 7.22 illustrate that $\Delta\overline{Z_1}$ drops by one order of magnitude if the driving frequency reduces to 100 kHz. However, the pressure source terms in the convection-diffusion mass transportation equation are linearly proportional to the pressure magnitude. Consequently, $\Delta\overline{Z_1}$ is linearly proportional to the pressure magnitude. As such, $\Delta\overline{Z_1}$ reduces by almost a factor of 0.2 when the excitation magnitude decreases to p_m = 10 MPa, exhibited in Figs. 7.23 and 7.24.

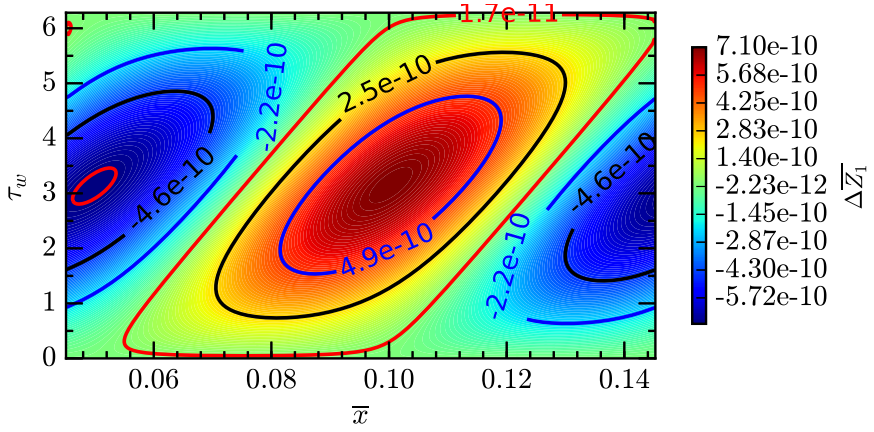

Figure 7.23: Change in the concentration of monomers across a wavelength centered about $0.5x_s$ over one period in a travelling wave field with p_m = 10 MPa, f = 1 MHz.

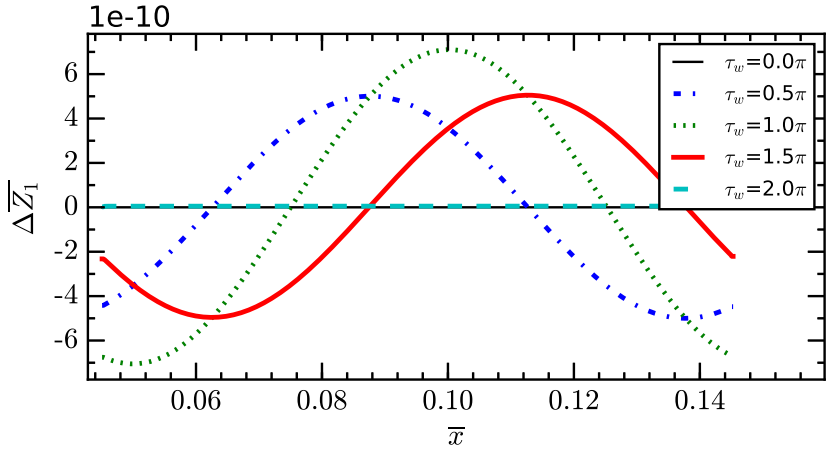

Figure 7.24: Four snapshots of contours shown in Fig. 7.23.

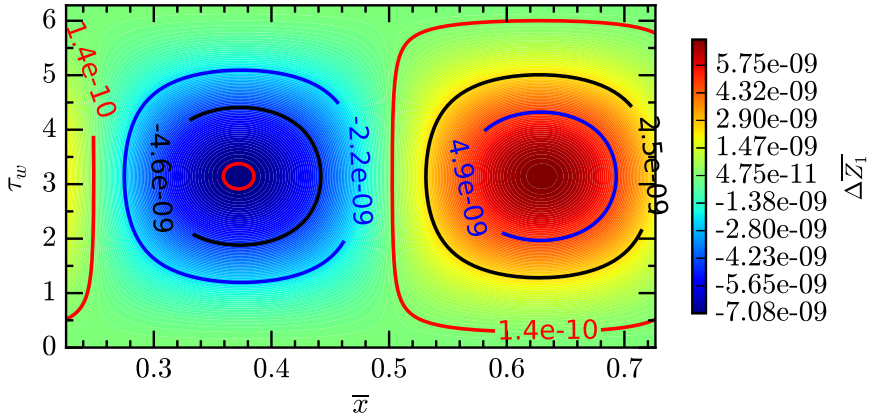

Figure 7.25: The same as Fig. 7.23 but for a standing wave field with p_m = 50 MPa, f = 1 MHz.

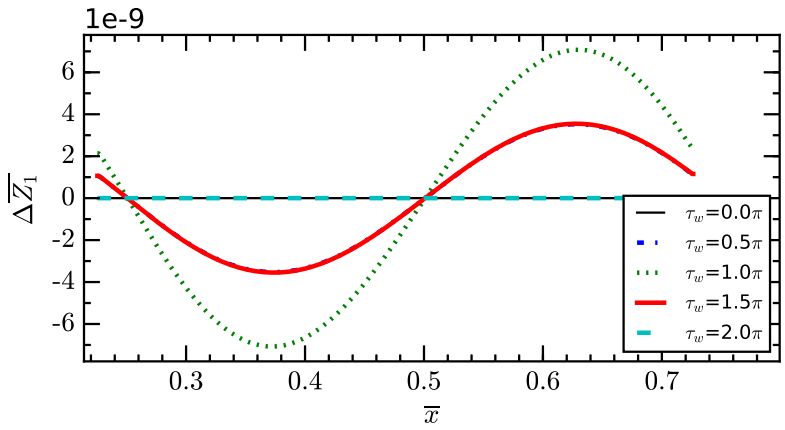

Figure 7.26: Four snapshots of contours shown in Fig. 7.25.

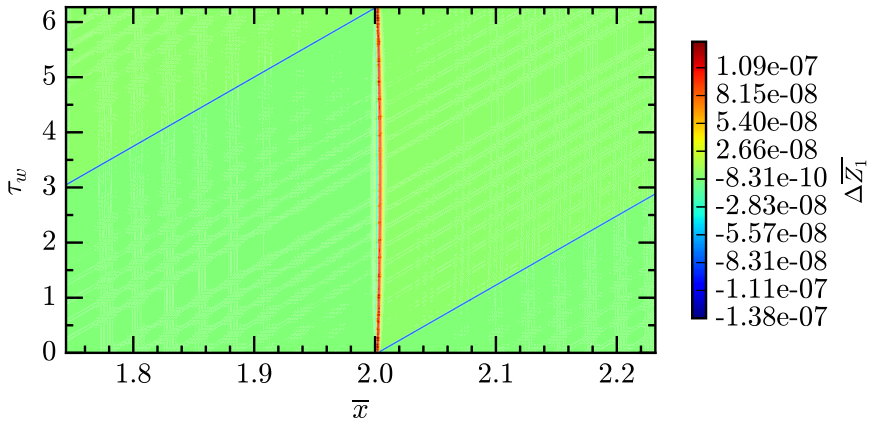

(a)

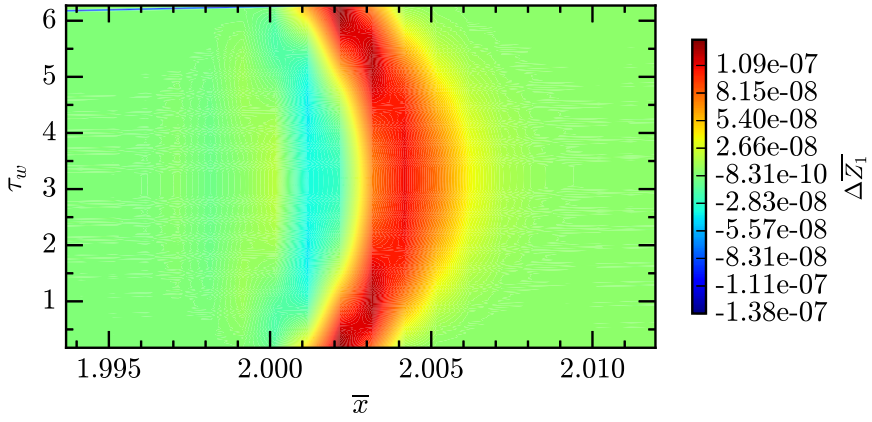

(b)

Figure 7.27: Change in the concentration of monomers across a wavelength centered about $2x_s$ over one period in a travelling wave field with $p_m = 50$ MPa, $f = 1$ MHz. (b) magnified around $2x_s$.

Thus far, we have investigated mass transportation by travelling acoustic waves in the pre-shock region. Now, we consider the situation where a standing wave field is constructed in the bath. Figures 7.25 and 7.26 depict the variation in the concentration in a lossless standing wave field in the pre-shock region modelled by $p_a = 2p_m \sin(\omega t)\sin(k_w x)$ (Kinsler et al., 1999) with $p_m = 50$ MPa and $f = 1$ MHz. Compared to the travelling wave condition, we can see that the solute species moves towards pressure antinodes and occupies a smaller area. The concentration of monomers is almost two times more than the concentration in the counterpart travelling wave situation. This corresponds to the stronger pressure amplitude in the standing wave field, i.e. $2p_m$, compared with the travelling wave situation.

Now, a case of travelling waves in the post-shock region will be studied. The source is driven by a tone of $p_m = 50$ MPa and $f = 1$ MHz. We will consider a shock in $x = 2x_s$ at $\tau_w = 0$. In this region, a full N-wave is present and a sharp pressure gradient takes place in the shock location at each time instant. This creates a narrow high concentration zone right after the shock with a peak of about two orders of magnitude larger than the same wave in the pre-shock zone, see Fig. 7.27. This increase is followed immediately by a reduction in $\Delta\overline{Z_1}$. As time progresses and the shock translates to the adjacent point in space, the concentration rises but it is about two orders of magnitude smaller than the peak and hence less identifiable in the plot. This can be better observed in Fig. 7.28 which illustrates $\Delta\overline{Z_1}$ in the few initial time steps. In particular, we can see in Fig. 7.28(b) that $\Delta\overline{Z_1}$ settles about 4×10^{-9} which is of the same order of magnitude of its peak in the pre-shock region, see Fig. 7.21.

To elaborate on this observation, the mass flux due to the concentration gradient $j_{2,Z}$ and pressure field $j_{2,p}$ are calculated in the first three time steps and plotted in Fig. 7.29. $j_{2,Z}$ and $j_{2,p}$ are the first and second terms in the total mass flux equation (Eq. (5.12)), respectively. The non-dimensionalised form of Eq. (5.12) reads

$$\overline{j_2} = \frac{\partial \overline{Z_1}}{\partial \overline{x_d}} + \overline{\beta}\ \overline{Z_1}\ \frac{\partial \overline{p}}{\partial \overline{x_d}}. \tag{7.17}$$

The forced mass transportation in this acoustic field is substantially larger (by seven orders of magnitude) than mass transportation by the ordinary diffusion. Thus, the effect of the ordinary diffusion is negligible and the concentration of the solute species is mainly proportional to the gradient of $j_{2,p}$ shown in Fig. 7.29(c). This can also be deduced from high $Pe = 1509$ for this driving condition.

The positive segment of the gradient of $j_{2,p}$ leads to an increase in the concentration whereas the negative part reduces the concentration. In the next time step, the positive segment reaches to the point which has just undergone rarefaction and therefore cannot reach the peak produced at the initial shock location. A similar narrow variation in the density of medium was also reported for the propagation of weak and strong shock waves in a gaseous medium (Yano and Inoue, 1996; Yano, 1996). They showed if the sonication carries on for a long time, these narrow high concentration points will disperse. A similar trend is observed here when we run the simulation over a longer time. This is presented in Fig. 7.30 which shows $\Delta\overline{Z_1}$ across a space of about four wavelength long and over ten cycles, i.e. 20π, with $p_m = 50$ MPa and $f = 1$ MHz. This figure clearly shows that the effect of an acoustic field on transportation of a typical solute species in a typical aqueous solution (with properties listed in Table A.1) tends to be negligible. Nevertheless, this effect may become noticeable only in the post-shock region and over a large time scale.

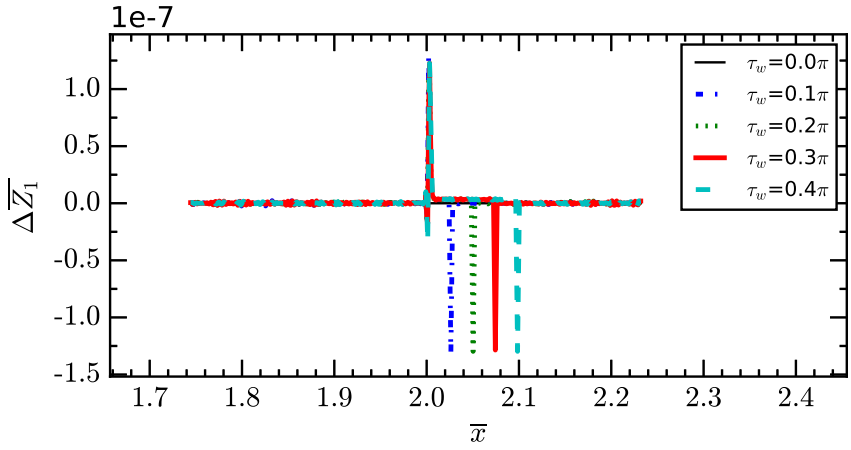

(a)

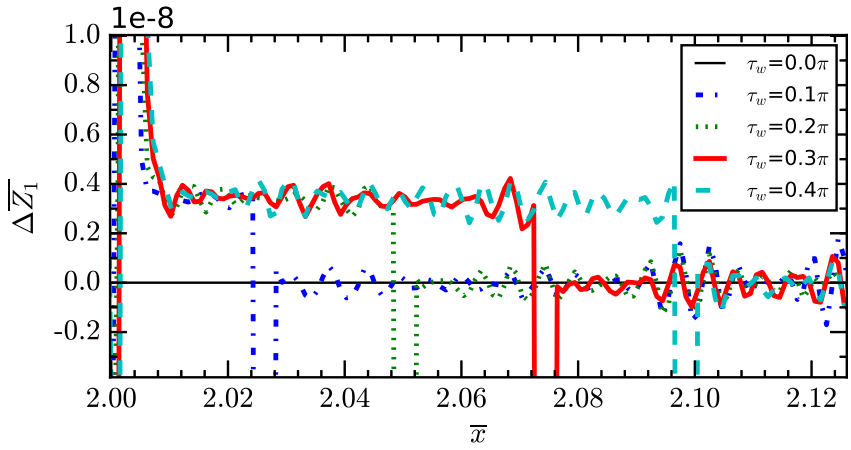

(b)

Figure 7.28: (a) Snapshots of the contour plot shown in Fig. 7.27 in initial few time steps. (b) Zoomed in around $2x_s$.

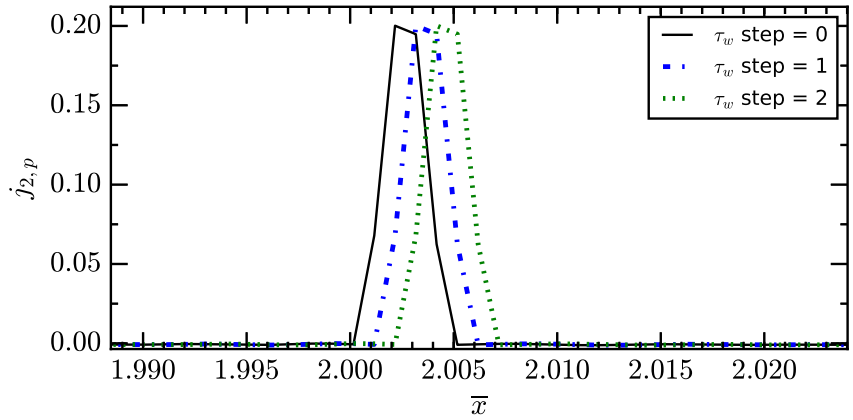

(a)

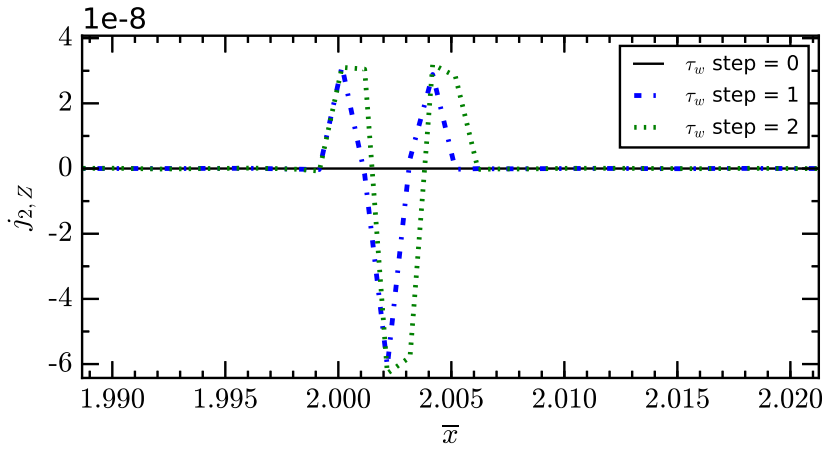

(b)

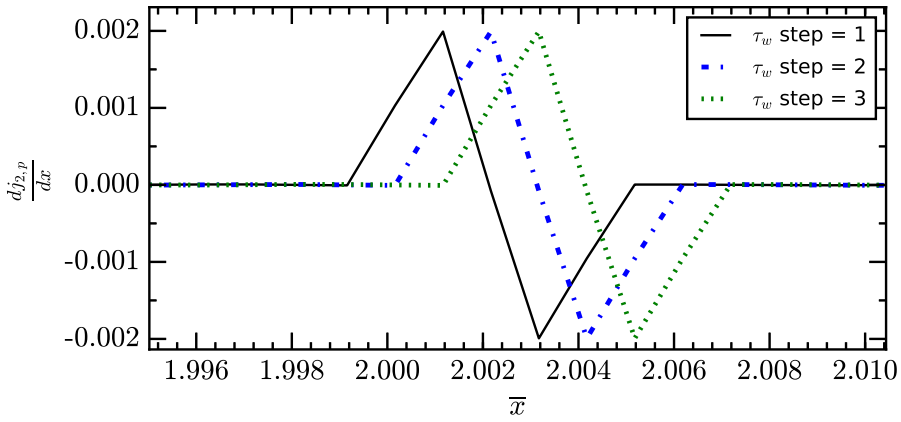

(c)

Figure 7.29: Snapshots of (a) dimensionless mass flux due to the pressure gradient, (b) dimensionless mass flux due to the concentration gradient, and (c) dimensionless pressure diffusion term, around $2x_s$ at the first three time instances.

If the solute species is made of heavier molecules, a more significant $\Delta\overline{Z_1}$ is expected for a given driving pressure (Vrentas and Vrentas, 2016; Bird et al., 1960; Louisnard et al., 2007). Invoking Eq. (7.12), we can see that the pressure gradient is weighted by $\frac{\overline{\beta}}{Pe}$ which depends on the solute density and the molecular weight. The latter can take larger values than the former and its influence on the weight coefficient is perhaps more severe. To evaluate this effect, we will keep the density constant, i.e. $\rho_{mass,2} = 2000$ kg m^{-3}, and choose a relatively large molecular radius of $R_0 = 10$ nm (this is nearly 44 and 80000 times larger in the molecular radius and volume than the ones taken so far). This results in $\nu_n = 4000$ nm^3, $M_2 = \mathcal{N}_{\mathcal{A}}\nu_n\rho_{mass,2} = 5045$ kg mol^{-1}, and $D = 2\times10^{-11}$ m^2 s^{-1} [1]. For the acoustic excitation with $p_m = 50$ MPa and $f = 1$ MHz, we will arrive at $\overline{\beta} = -51801$ and $Pe = 10316$. Consulting the data listed in Table 7.1 for the same driving condition, we can see that $\overline{\beta}$ and Péclet number are increased by 5 and roughly 1 orders of magnitude, respectively, producing a rise in $\frac{\overline{\beta}}{Pe}$ by almost 5 orders of magnitude. Figures 7.31 and 7.32 depict $\Delta\overline{Z_1}$ computed for the solute made of this large molecule in the pre- and post-shock regions. We can observe an enhancement in $\Delta\overline{Z_1}$ of the order of nearly 3 in both locations. As before, very high Péclet number confirms that the ordinary diffusion can be overlooked in comparison with the acoustically induced mass transportation.

Now, we need to estimate the effect of variation in the concentration and hence the supersaturation ratio on the thermodynamics of the phase transition. Following our discussion in Section 2.6 and employing Eq. (7.16), the contribution of the variable supersaturation ratio to the dimensionless work of the formation of the EDS cluster, i.e. $\Delta\Omega/k_BT$, reads

$$\frac{\Delta\mu}{k_BT} = \ln(r) = \ln(r_0(1+\Delta\overline{Z_1})) = \ln(r_0) + \ln(1+\Delta\overline{Z_1}), \qquad (7.18)$$

As shown above, $\Delta\overline{Z_1}$ oscillates around zero and is a relatively small number.

[1] calculated from the Stokes-Einestein equation: $D = \frac{k_BT}{6\pi\eta R_0}$

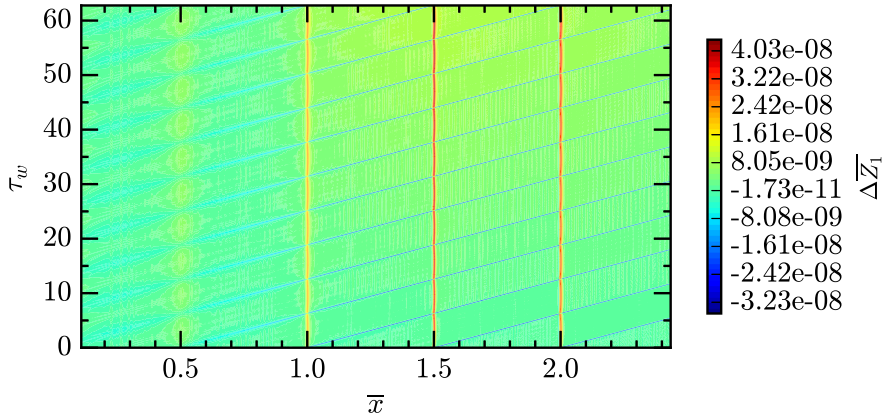

Figure 7.30: Change in the concentration of monomers across four wavelengths and over ten excitations in a travelling wave field with p_m = 50 MPa, f = 1 MHz.

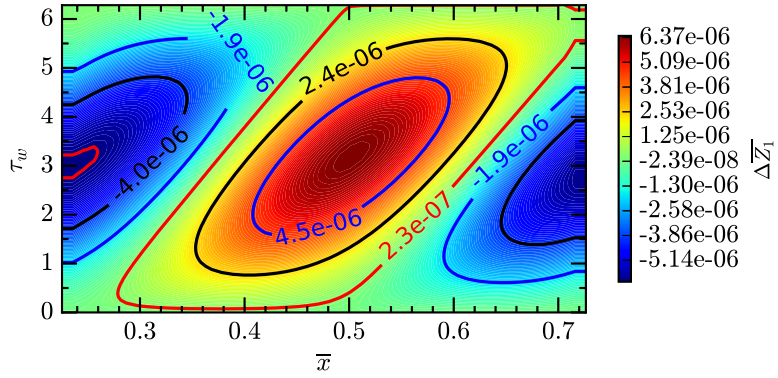

Figure 7.31: Change in the concentration of monomers in a pre-shock zone for a solute species with relatively large molecules, R_0 = 10 nm. Simulation is performed across a wavelength centered about $0.5x_s$ and over one period in a travelling wave field with p_m = 50 MPa, f = 1 MHz.

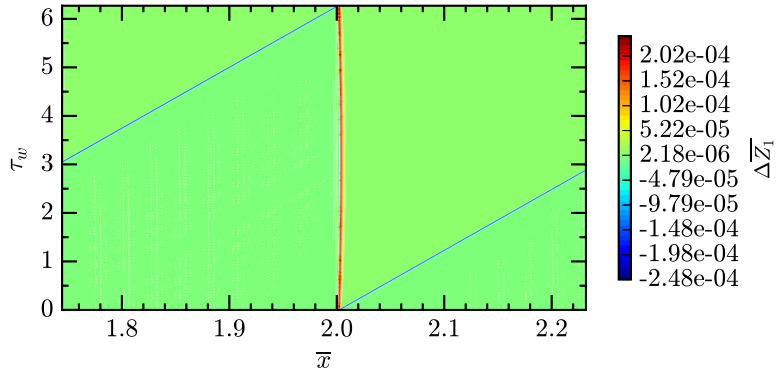

Figure 7.32: Change in the concentration of monomers in the post-shock distance for a solute species with relatively large molecules, R_0 = 10 nm. Simulation is performed across a wavelength centered about $2x_s$ and over one period in a travelling wave field with p_m = 50 MPa, f = 1 MHz

Thus, the Taylor series expansion of the second term around zero gives the following first order approximation

$$\frac{\Delta\mu}{k_BT} \approx \ln(r_0) + \Delta\overline{Z_1} + \mathcal{O}(\Delta\overline{Z_1}^2). \tag{7.19}$$

For example, around the shock region, setting $r_0 = 30$ which was used in the previous simulations gives $\Delta\mu/k_BT = 3.40 \pm 10^{-7}$. In the same situation, the contribution of pressure to the dimensionless work of cluster formation for the same cluster is about $\Delta\nu\Delta p/k_BT = {}^{5\times10^{-21}}\!/_{4\times10^{-21}} \approx 1.24$. Considering the acoustic field and the bath used in the simulations, the effect of mass transportation on $\Delta\mu$ and consequently the work of cluster formation is of $\mathcal{O}(10^{-7})$ and is therefore tentatively negligible, especially in comparison with the pressure effect which is of $\mathcal{O}(1)$.

On the kinetics of cluster formation, the attachment and detachment frequencies are proportional to r and $r^{n_\sigma{}'(n_n)}$, respectively, see Eq. (4.45). Given that variation in r is little, we anticipate an infinitesimal contribution to transition frequencies. For the EDS cluster $n_\sigma{}'(n_n) = 0$ and the detachment frequency is predicted to be independent of the supersaturation ratio.

To thoroughly investigate this matter, we will solve the complete hybrid model in a non-mass conserved system for the driving condition in which mass transportation is more noticeable. Preceding results showed that this happens at the post-shock region around $\overline{x} = 1.99$. Since at this location absorption is the highest, a long excitation tends to violate the isothermal assumption. Thus, we will solve the cluster dynamics over a shorter time interval than before, i.e. one wave period. This time is too short for very large clusters to be nucleated, so we can set the largest cluster size to a smaller value to reduce the number of ODEs and facilitate the numerical calculations. Here $N = 1000$ with $N_d = 250$ and $a = 0.01$ are chosen which gives the largest cluster size of almost 9000 molecules.

The time-dependent supersaturation ratio in a non-mass conserved system in the post-shock region is shown as a contour plot in Fig. 7.33, and in some

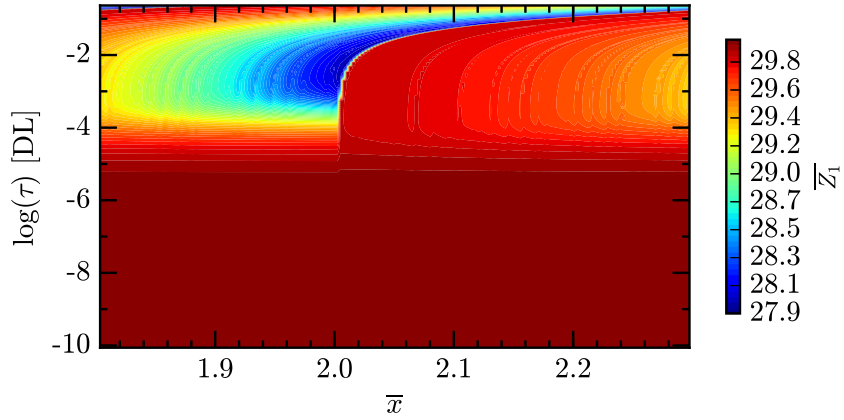

Figure 7.33: Concentration of monomers (equivalent to the supersaturation ratio) across a wave length over time.

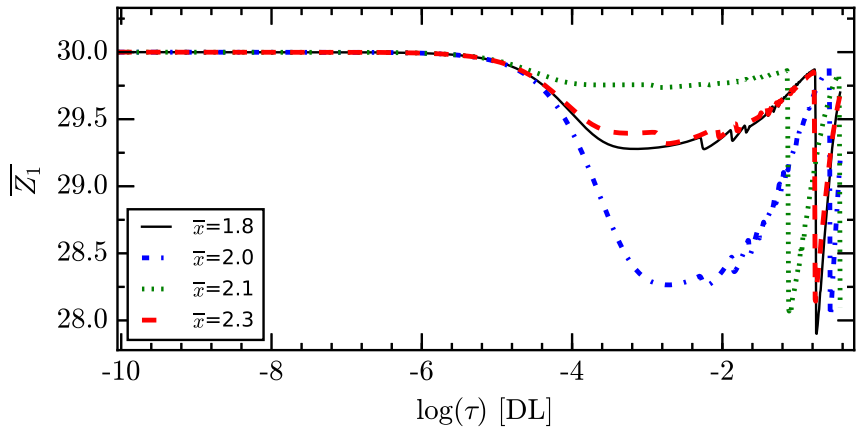

Figure 7.34: Concentration of monomers over time at some locations, see Fig. 7.33.

spatial points in Fig. 7.34. The non-dimensionallisation coefficients shown in Section 5.4 are used for numerical calculations, however, results are presented on the same time axis used in Section 7.2 (i.e. τ is the time scaled by the coefficient of the attachment frequency). This allows comparison of these results with those presented in Section 7.2.

At locations where initially the pressure amplitude is positive, i.e. points in the rear of the initial location of the shock $\overline{x} < 2.1$, nucleation is enhanced which results in a greater reduction of the supersaturation ratio than those locations beyond the shock location. As time progresses, the shock travels in the positive direction of x axis and therefore pressure behind the shock drops. Consequently, the effect of pressure on nucleation in those locations is initially constructive which gradually weakens and becomes repressive when

the rarefaction cycle begins.

In the same locations, the concentration of supercritical clusters over time is computed and depicted in Fig. 7.35. The nucleation time lags (τ_n) are calculated and shown by the vertical dashed lines. One can see that across a wavelength, they vary by about two orders of magnitude. Given that the time constant is $t_c = f_c^{-1} = 3.48$ μs, τ_n changes in the range of nano to micro seconds. This implies that nuclei are created over different time intervals across the wave field and hence they will grow to different sizes over the same time. The rate of nucleation is proportional to the inverse of the exponential of the nucleation work which is the lowest just before the shock and the highest just after the shock, see Fig. 7.36. This can also be observed in Fig. 7.35 that the concentration of supercritical clusters is initially the highest just before the shock (the blue dashed-dotted curve) and remains the highest at the end of the sonication period, see Fig. 7.37.

Figures 7.38 and 7.39 show CSDs right before and after the initial location of the shock. The vertical dashed lines display the time-dependent size of the critical clusters (n^*). Since the simulation time is equal to only one sonication period, these plots only depict the concentration of clusters just in the beginning of nucleation hence the growth stage and the Ostwald ripening regime are not simulated. Considering Eq. (3.30) for a non-EDS cluster and Eq. (3.32) for the EDS cluster, together with Eq. (7.19), the dependence of n^* on mass transportation and the pressure amplitude are given by $\overline{\Delta Z_1}$ (of first order accuracy) and $\frac{k_\rho \nu \Delta p}{k_B T}$, respectively. Taking the distribution of $\overline{\Delta Z_1}$ into account and given that the smallest size of n^* in both spots are equal, we may deduce that the effect of mass transportation on the size of nuclei is negligible compared to the pressure effect (the former is of $\mathcal{O}(10^{-7})$ whereas the latter is of $\mathcal{O}(1)$ with the value of 1.24). Consequently, we may extend this conclusion and correlate the spatial variation of the CSD to mainly the pressure field.

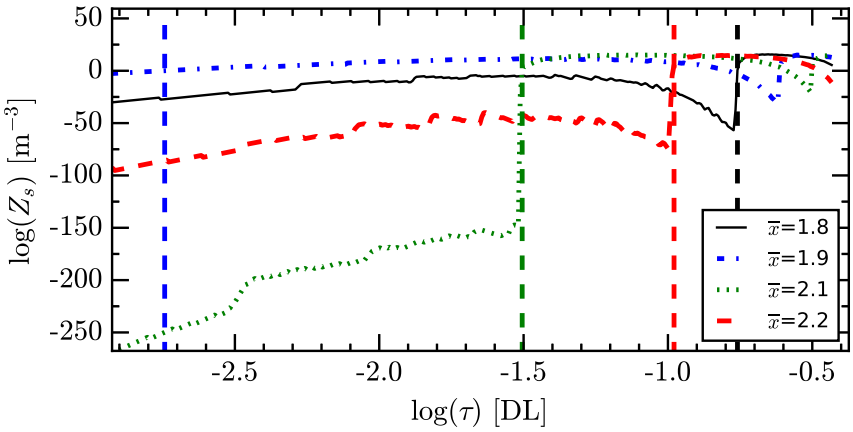

Figure 7.35: Concentration of supercritical clusters over time at different locations. Vertical dashed lines indicate the beginning of the nucleation stage at different locations. A similar colour code as the curves is used for these vertical lines.

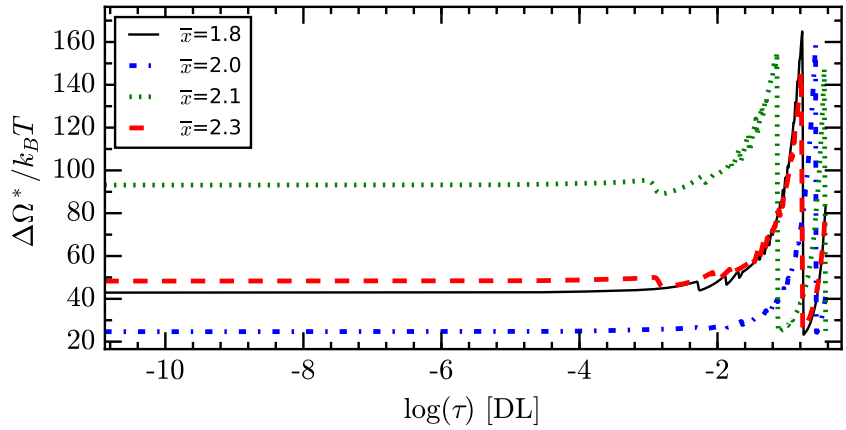

Figure 7.36: Nucleation work over time at different locations.

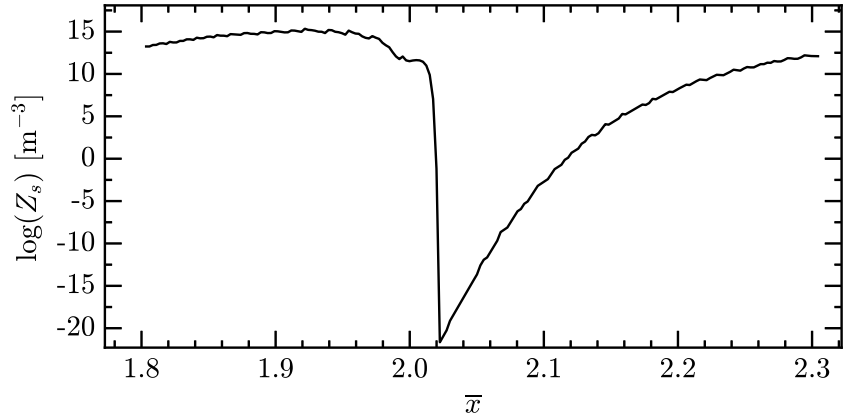

Figure 7.37: Concentration of supercritical clusters across space at the end of the first cycle of sonication.

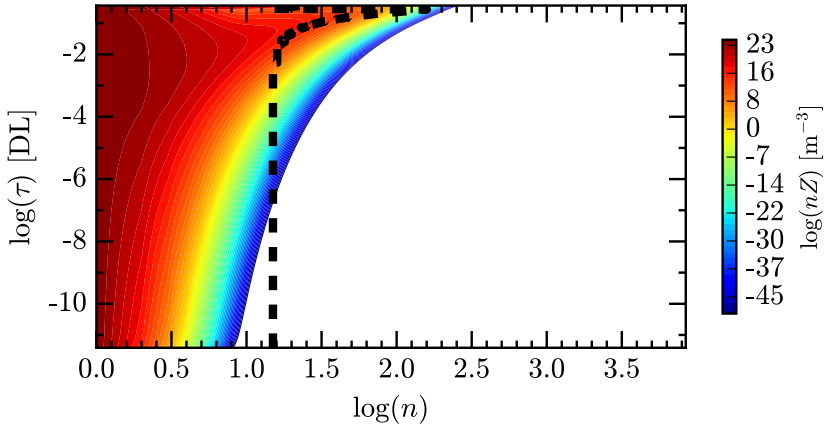

Figure 7.38: CSD in $\overline{x}$ = 1.99. Vertical dashed line shows the size of the critical cluster.

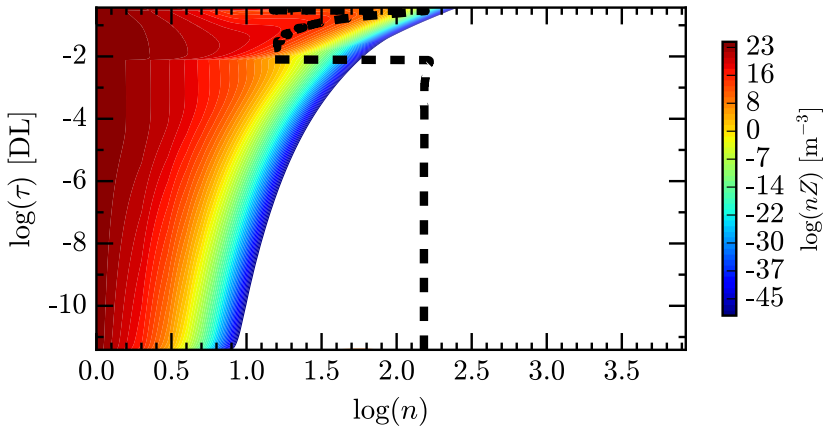

Figure 7.39: CSD in $\overline{x}$ = 2.02. Vertical dashed line shows the size of the critical cluster.

7.4 Simulations at different λ

In Chapter 6 we demonstrated by choosing a suitable λ value, we could correctly predict the water droplet nucleation rate. To study the effect of an acoustic wave on crystal nucleation, we employed the new surface with size-independent λ = 0.35. Here, we perform a sensitivity analysis of the parameter λ including the case of λ = 0 (representing the EDS cluster) on the kinetics of clustering. The clustering work and thermodynamics at different λ values were presented and discussed in Chapters 2 and 3.

Figures 7.40 and 7.41 show variation in the supersaturation ratio over time at two different pressure magnitudes and different λ values. Given $k_\rho > 0$, a negative λ basically implies that the dividing surface is placed beyond the

EDS.

The supersaturation ratio over time at different λ and pressure magnitudes is depicted in Figs. 7.40 and 7.41. At a small static pressure magnitude, the

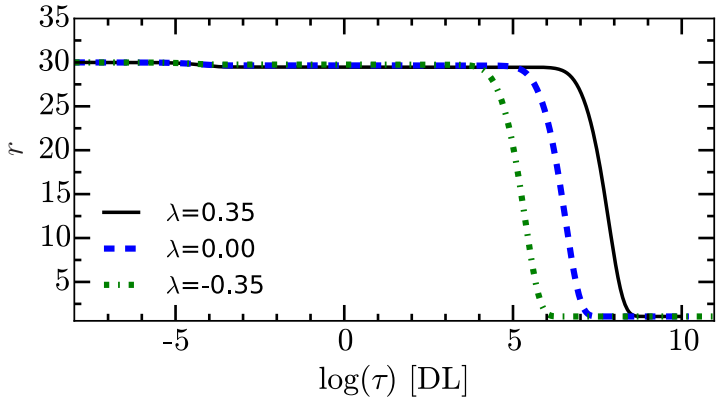

Figure 7.40: Supersaturation ratio over time at different values of λ and the static pressure of p_m = 1 MPa.

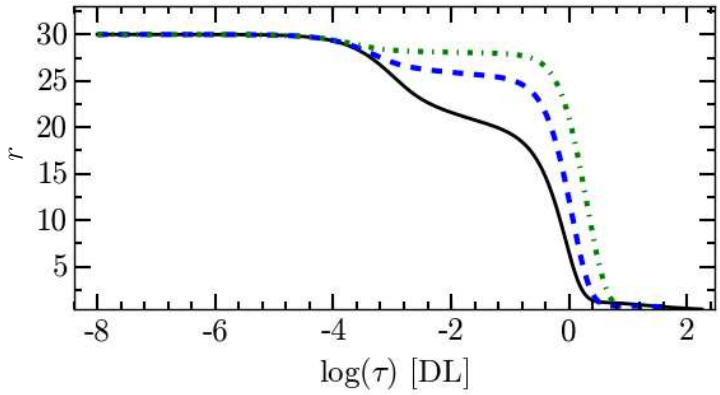

Figure 7.41: Supersaturation ratio over time at different values of λ and the static pressure of p_m = 100 MPa.The legend is the same as that of Figure 7.40.

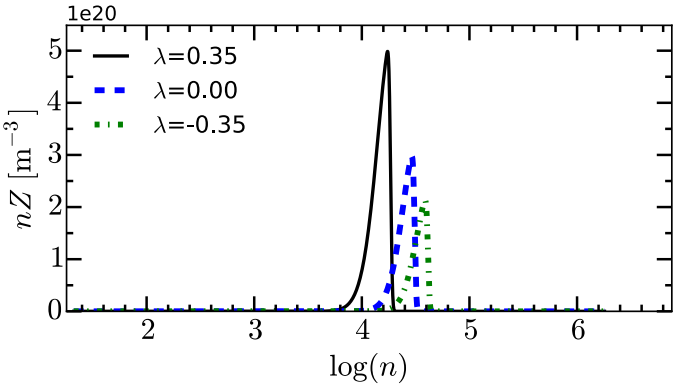

Figure 7.42: CSD at the end of the nucleation stage (log(τ) = 2) at a static pressure of 50 MPa and at different λ values.

effect of pressure on the thermodynamics and kinetics of nucleation is negligible and λ influences the kinetics through $n_\sigma{}'$ and n_n' in the first two terms of Eq. (4.40). We observe that at low pressure magnitudes, the nucleation rate increases as λ drops, whereas at a high magnitude static pressure, the inverse trend is identified (this is because of the last term in Eq. (4.40)). This change in the nucleation rate influences the CSD at different λ values. For instance, at p_m = 50 MPa and at the end of the nucleation stage, we see that the mean of the CSD is shifted towards a smaller n (Fig. 7.42). This difference becomes more noticeable at higher pressure magnitudes.

In the case of pressure fluctuations with non-zero frequency, the effect of the location of dividing surface on nucleation is more clear. Equation (4.40) shows that a non-EDS cluster can affect the kinetics of nucleation through the values of n_n, $n_\sigma{}'$ and n_n'. For the EDS cluster, $n_\sigma{}'$ and n_n' are constant and size-independent (equal to 0 and 1, respectively). However, for a non-EDS cluster these quantities are variable and size-dependent, see Fig. 7.43. This influences the pressure effect on the depletion rate and nucleation rate consequently. This can be seen in Fig. 7.44 showing the detachment frequencies of two different supercritical clusters for the simulation condition of p_m = 50 MPa, f = 2 MHz and r_0 = 30 at a pre-shock location.

For the same driving condition, Fig. 7.45 displays a variable supersaturation ratio over time for both non-EDS cases, whereas it is roughly non-oscillatory for the EDS cluster. This is particular to this combination of the supersaturation ratio and pressure magnitude as we observed a fluctuating supersaturation ratio for the case of EDS clusters either at a lower initial supersaturation ratio or a higher pressure magnitude. This is explained as follows: i) the new model 1 predicts a size-dependent pressure effect in the effective supersaturation ratio, in contrast to the EDS-based model, see Chapter 3.3, and ii) the inverse relationship between pressure and the supersaturation ratio such that the pressure effect becomes more significant at lower supersaturation ratios, see Chapter 3.

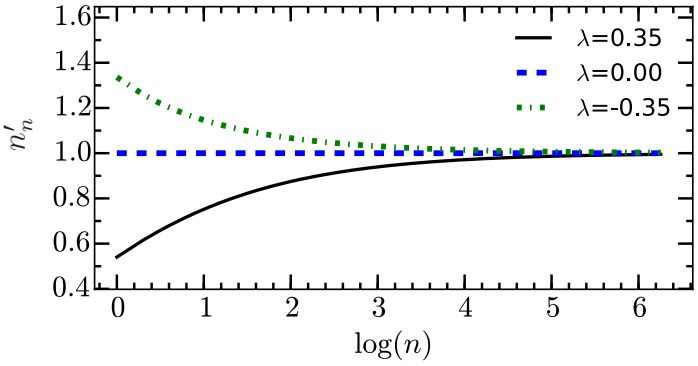

Figure 7.43: n'_n at different λ values for a range of cluster sizes.

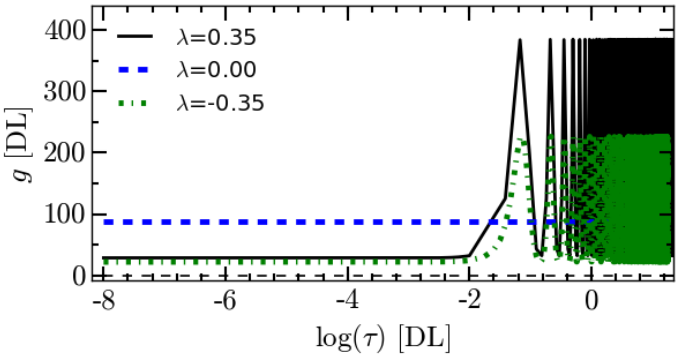

(a)

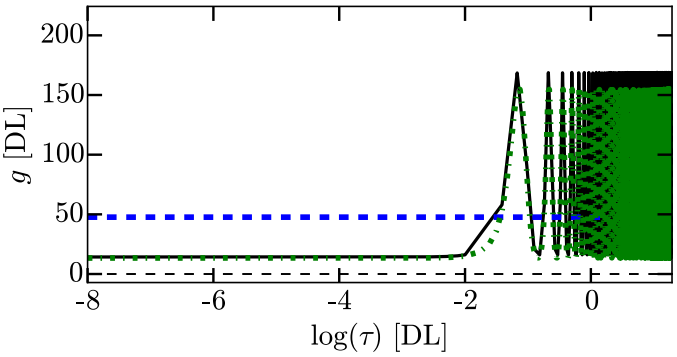

(b)

Figure 7.44: (a) Detachment frequency, Eq. (4.40), for a supercritical cluster of size n = 70 over time. Parameters of acoustic wave are f = 2 MHz and p_m = 50 MPa at a pre-shock location. (b) As in (a) but evaluated for a supercritical cluster of size $n = 10^{4.5}$.

.

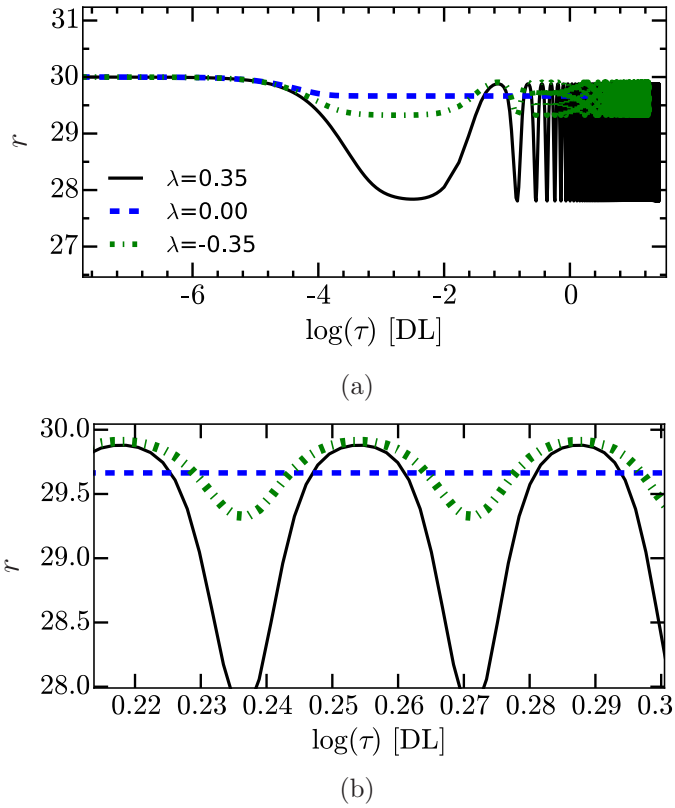

Figure 7.45: (a) Supersaturation ratio over time when the old phase is exposed to an acoustic wave, the same acoustic wave parameters as in Fig. 7.44, with different λ values. (b) magnified about $\log(\tau) = 0.25$.

We introduced the effective supersaturation ratio in Section 3.3. Moreover, contributions of pressure and the supersaturation ratio on the excess free energy are discussed and represented by Eq. (3.25). As it was discussed there, these contributions and the effective supersaturation ratio will become size-dependent if the non-EDS cluster is used. Figures 7.46 and 7.47 show r_{eff} calculated using the non-mass conserved simulation results for two different clusters, i.e. $n = 1$ and $n = 1000$ respectively, at two different locations for the excitation parameters of $p_m = 50$ MPa and $f = 1$ MHz and with $r_0 = 30$. The black solid curve shows the time-dependent r_{eff} in the location just behind the shock and the dashed blue curve displays the same quantity just after the shock. We can see that $r_{\text{eff}}(n = 1)$ is of an order of magnitude greater than $r_{\text{eff}}(n = 1000)$. This was expected as $\lim_{n\to\infty} r_{\text{eff}}(n) = r_0 \exp(\frac{k_\rho \nu \Delta p}{k_B T})$. If we zoom in around $\log(\tau) = -0.530$, we can see that the peak values of $r_{\text{eff}}(n = 1)$ are

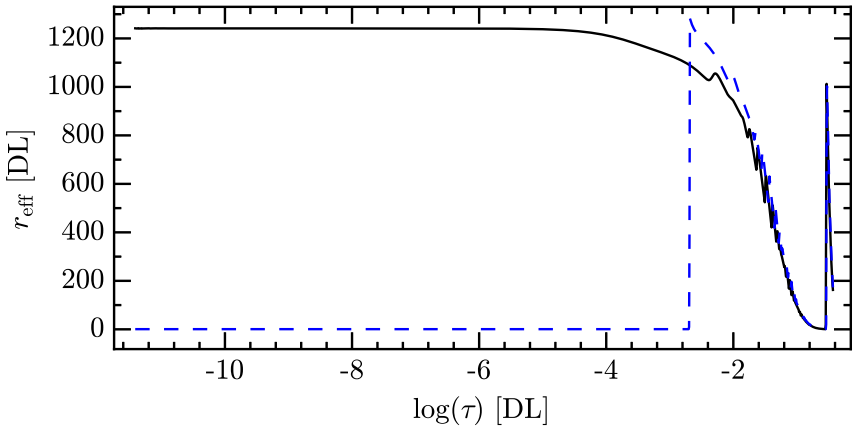

Figure 7.46: Effective supersaturation ratio calculated for a monomer over time at two locations; just before the shock $\overline{x} = 1.99$ (the black solid curve) and just after the shock $\overline{x} = 2.01$ (the blue dashed curve).

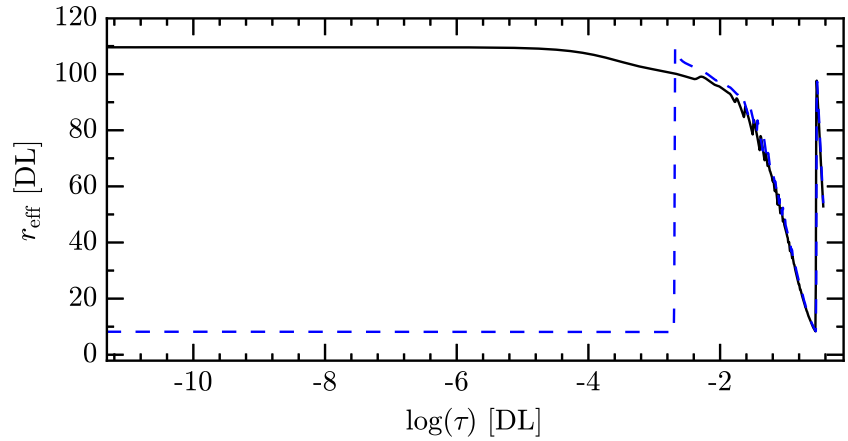

Figure 7.47: Likewise Fig. 7.46 but for a cluster of size $n = 1000$.

different by almost ten units while this difference for $n = 1000$ is very little. For a mass-conserved system, we expect the identical $r_{\text{eff}}(n = 1)$ in both locations. Thus, we may deduce that this difference is originated from mass transportation. This change is less than 0.01% of the peak value of $r_{\text{eff}}(n = 1)$ which confirms the negligible effect of mass transportation. Furthermore, for a larger cluster of $n = 1000$ this difference is even smaller. This means that the effect of mass transportation becomes more noticeable if the non-EDS cluster model is utilised.

Finally, the excess free energy of two clusters of size $n = 10$ and $n = 1000$ are calculated and depicted in Figs. 7.48 to 7.50. One can deduce the following

points from these figures: i) the excess free energy fluctuates out of phase with pressure, ii) the effect of mass transportation on $F_{\sigma,1}$ is negligible as we could not identify any noticeable difference in the extremum values at different locations, iii) $F_{\sigma,1}$ becomes a minimum behind the shock and a maximum right after the shock. Given that r_{eff} varies inversely, nucleation is highly promoted behind the shock.

In the case of the conventional form of CNT, the excess free energy reads $F^{e}_{\sigma,1} = a_0\gamma_\infty n^{2/3}$ and only varies with the size and is independent of the supersaturation ratio and pressure magnitude. The curves labeled in the legend of Fig. 7.51 display the ratio of the excess free energy of non-EDS clusters identified with $\lambda = 0.35$ calculated by Eq. (3.25) to the excess free energy of the EDS clusters ($F_{\sigma,cl}$) of the identical size. They are calculated based on the simulation results in location $\overline{x} = 1.99$ and include the effects of the pressure magnitude and mass transportation. This is the dynamic form of $F_{\sigma,r}$ which was given in Eq. (2.61) and shown here by the cyan solid curve with $r_0 = 30$. To only display the contribution of the surface tension term, the magenta dotted curve is overlaid manifesting $a_0\gamma_\infty n_n^{2/3}/F_{\sigma,cl}$. As given by Eq. (2.63), we can estimate dynamic $\gamma_{\text{eff}} = \gamma_\infty F_{\sigma,r}(p)$ by scaling these curves by γ_∞. Comparing the cyan and magenta curves with others, we can see that the contribution of mass transportation and the pressure magnitude are less important than the supersaturation ratio, but both considerably change $F_{\sigma,cl}$, especially for small clusters.

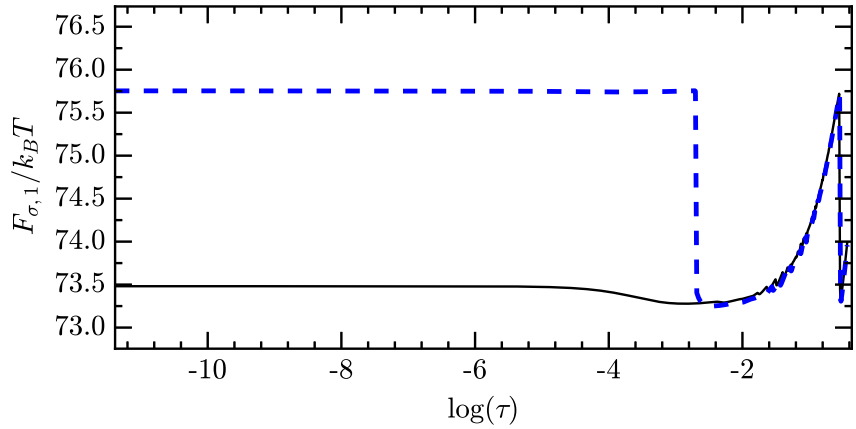

Figure 7.48: Excess free energy of a cluster of size $n = 10$ over time at two locations; just before the shock $\overline{x} = 1.99$ (the black solid curve) and just after the shock $\overline{x} = 2.01$ (the blue dashed curve). $F_{\sigma,1}$ is calculated by Eq. (3.25).

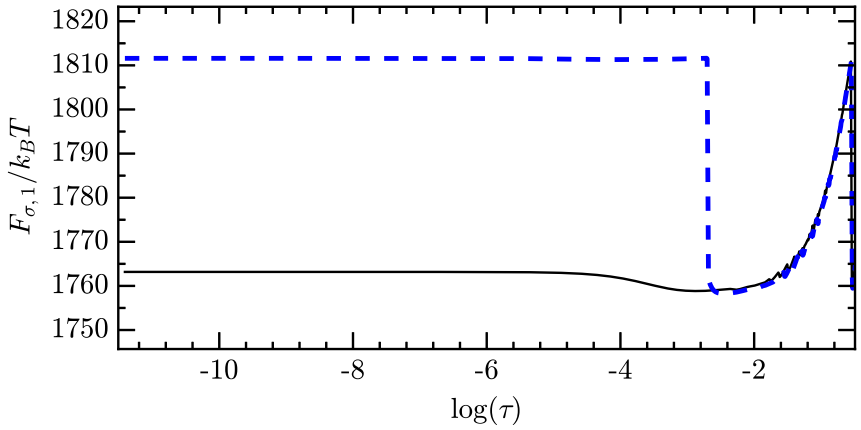

Figure 7.49: Likewise Fig. 7.48 but for a cluster of size $n = 1000$

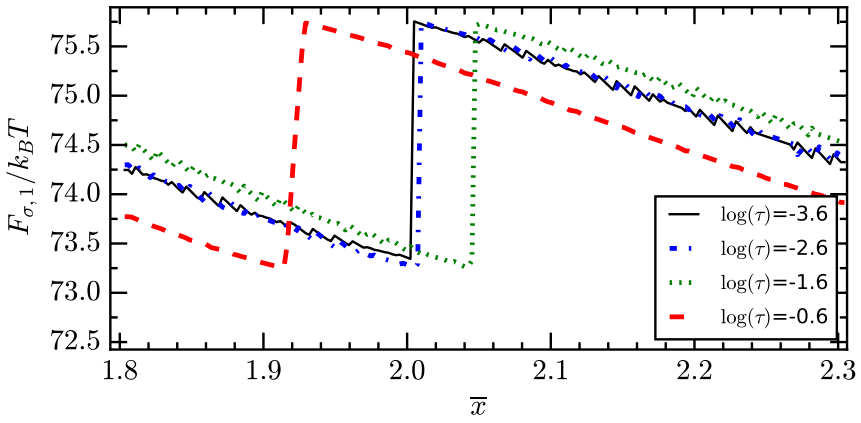

Figure 7.50: Excess free energy of a cluster of size $n = 10$ across space at different time instants.

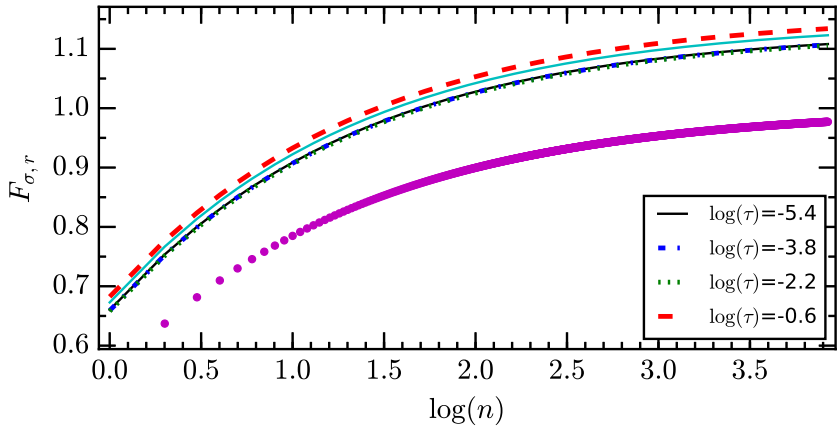

Figure 7.51: The ratio of the excess free energy for the non-EDS cluster with $\lambda = 0.35$ to the excess free energy of the EDS cluster of the same size ($F_{\sigma,cl}$), calculated at $\overline{x} = 1.99$. Curves present readings at different time instants shown in the legend. The dotted curve in magenta colour is the ratio of the contribution of the surface tension term and the cyan solid curve is $F_{\sigma,r}$ given by Eq. (2.61) with a constant supersaturation ratio, see the text for details.

7.5 Summary

We used a one-dimensional nonlinear Burgers' equation to model the acoustic field in both pre- and post-shock regions. Furthermore, a simple heat equation is solved to compute the temperature rise in the acoustic field due to absorption. The simulation results are incorporated into the full hybrid model to calculate the kinetics of crystallisation in an aqueous solution while accounting for the effect of fluctuations in the thermodynamic state of the old phase. The thermodynamic state of the old phase changes because of pressure oscillations and mass transportation. The results are summarised in the following

- the assumption of the isothermal cluster formation is justified for a system placed in the pre-shock region. This is also valid in the post-shock region if the sonication is short or pulsed.

- our new cluster model predicts a size-dependent pressure effect on the kinetics of cluster formation for the non-EDS clusters. Furthermore, the excess free energy and effective surface tension are functions of the pressure fluctuation and supersaturation ratio in addition to the cluster size.

These characteristics are in contrast to the predictions of the conventional form of CNT which is based on the EDS clusters.

- in a mass conserved system, the nucleation rate is strongly related to the pressure magnitude but not the driving frequency. However, the driving frequency influences the CSD by varying the net time in which clusters experience a high amplitude pressure field.

- in a non-mass conserved system, the driving parameters and the spatial location of the system are important and can influence the thermodynamics and kinetics of cluster formation.

- a relatively large driving pressure is required to observe the significant nucleation rate usually reported in the sonocrystallisation literature. The effect of this strong pressure field is more significant on the thermodynamics of phase transition than on mass transportation. Therefore, acoustic waves influence nucleation and growth through thermodynamic effects associated with pressure fluctuations rather than hydrodynamic effects. However, this conclusion should be tempered as mass transportation may largely vary when the boundary conditions change or the acoustic streaming is accounted for in the mass transportation equation, e.g. in the nearfield of an oscillating bubble (Louisnard et al., 2007). This highlights the importance of the profound and accurate characterisation of the system in experiments which is usually overlooked in the sonocrystallisation literature.

- the higher the molecular weight of the solute species, the more significant is the effect of mass transportation. Nevertheless, this results in a lower mobility of monomers which reduces the attachment frequency and consequently may weaken the effect of mass transportation on the kinetics of nucleation.

Although we used a simple acoustic field for numerical simulations, the model is generic and can be used to determine the thermodynamics and ki-

netics of cluster formation for the EDS or non-EDS clusters in an arbitrary acoustic field. Nonetheless, our simulations are in qualitative agreement with experimental results presented in the literature.

Chapter 8

Conclusions

The motivation throughout this thesis was to model the interaction between an acoustic field and the crystallisation process using models in the realm of continuum mechanics and thermodynamics. The thesis was divided into two parts; part one where we focused on the thermodynamics of phase transitions, and part two where we studied the kinetics of phase transitions in an acoustic field. We made original contributions in each part in line with research aims and objectives defined in Section 1.5 and these are reviewed in the following section.

8.1 Contributions to the field

We began in Chapter 1 by presenting an overview of the sonocrystallisation process, and the review of the experimental and theoretical achievements in this field. It was established that: i) sonocrystallisation is a non-stationary complex process with time varying thermodynamic states. This process has been little studied theoretically and it is required to develop fundamental studies, ii) in order to describe the thermodynamics of phase transition in acoustic fields, the model is required to be valid in the limit of small clusters, iii) the kinetics of phase transition in acoustic fields is in general unsteady. Therefore, time-dependent transition frequencies must be derived. Furthermore, the kinetic model is required to account for the effect of mass transportation created by acoustic waves.

In Chapter 2, we derived the model that can describe the thermodynamics of phase transition for small clusters based on the generic form of the Gibbs droplet model. We showed that the Gibbs droplet model can overcome some of the difficulties associated with the thermodynamics of small clusters if a non-EDS is utilised to define a cluster. For a given cluster size, moving a dividing surface modifies the size of the core new phase and its thermodynamics. Furthermore, the specification of the dividing surface influences the excess Helmholtz free energy of the interface phase, given by $F_{\sigma,1} = n_\sigma \Delta\mu + \Omega_\sigma$, and consequently the effective surface tension: see Eq. (2.63). The dividing surface is the unphysical element of the model and its corresponding surface tension is defined to make the free energy of the interface phase independent of the location of the dividing surface (Ford, 1996). Derivations are valid for any dividing surface, including the EDS and surface of tension, and their associated size-dependent surface tension $\gamma(n)$.

Computation of the excess free energy of the surface $F_{\sigma,1}$ requires the knowledge of the size of the interface phase n_σ and the surface tension. Relationships represented in Eq. (2.27) are developed to calculate the size of the core new phase and the interface phase for any location of a dividing surface relative to the conventional EDS.

Calculating $\gamma(n)$ requires a suitable model of the size-dependent surface tension but many available models often break down in the limit of small clusters. This issue becomes more significant in the case of the sonocrystallisation process: the critical cluster size (for a condensed new phase) decreases as the pressure magnitude increases. Therefore, we defined the new surface which is identified as follows: i) this surface is characterised by the size-independent surface tension γ_∞, and ii) is positioned such that we obtain a reference excess free surface energy for the clusters. This was achieved by equating γ_{eff} (obtained from Eq. (2.63) when setting $\gamma(n) = \gamma_\infty$) to the effective surface tension obtained from statistical mechanical simulations and solving for the parameter λ.

In Chapter 3 we studied the effect of variation in the thermodynamics of the old phase, i.e. pressure and temperature variation, on the thermodynamics of phase transition determined by the new non-EDS model described in the preceding chapter. We obtained Eqs. (3.7) and (3.13) to calculate the work of formation of non-critical and critical clusters under this circumstance. For an isothermal condition, this model predicts that the nucleation barrier is reduced or raised with pressure rise if the new phase is more or less dense than the old phase, respectively.

The nucleation work contour plots as a function of both the pressure magnitude and supersaturation ratio were obtained showing that an identical nucleation barrier could be surmounted with different combinations of the pressure magnitude and supersaturation ratio. This is manifested in the effective supersaturation ratio, Eq. (3.23), which accounts for both the supersaturation ratio and pressure terms. We showed that using the non-EDS cluster model predicts a size-dependent pressure effect which is stronger for smaller clusters. Moreover, in case of an acoustic wave, the nucleation work and the size of nuclei increase over half a period of the acoustic wave and decrease over the next half period.

We also derived a generic equation to estimate the non-EDS nucleus size, Eq. (3.14), which simplifies to Eqs. (3.30) and (3.32) for the non-EDS cluster identified by the new surface and the EDS cluster, respectively.

Contributions presented in these two chapters satisfy the first two research objectives defined in Section 1.5. We then incorporated this new thermodynamic model into a hybrid kinetic model constructed by combining the Szilard (or BD) equation and the FPE to determine the kinetics of phase transition in an acoustic field.

In Chapter 4 we considered the mass-conserved system and obtained transition frequencies. We showed that for a closed system and an incompressible old phase, variation in pressure and temperature of the old phase more substantially influence the detachment frequency of monomers than the attachment

frequency. We derived Eqs. (4.37) and (4.38) accounting for these effects on monomer detachment rate from a generic cluster and a cluster identified by the new surface and new model 1 , respectively. Subsequently, we evaluated the condition for quasi-stationary phase transformation in a system exposed to acoustic waves, see Eq. (4.26) for a generic system and Eqs. (4.27) and (4.30) for a closed system. It was demonstrated that this condition is satisfied only at relatively low pressure magnitudes and excitation frequencies, especially at a low supersaturation ratio. Furthermore, we showed that the Zeldovich factor is fairly pressure independent and can be approximated by its value at the reference state.

We extended the calculation of the phase transformation kinetics in Chapter 5 to account for the effect of mass transportation in an acoustic field (pressure diffusion). We formulated the evolution of cluster concentration over time in a non-mass conserved system by including mass transport in our hybrid kinetic model, see Eqs. (**??**), (5.7) and (5.10). In the limit of a dilute solution where we can reasonably assume that only monomers transport through the system, the hybrid model simplifies to Eq. (5.19) which transforms into Eqs. (5.20) and (5.21) for incompressible solutions with and without the Ostwald ripening process, respectively.

Contributions presented in Chapters 4 and 5 satisfy objectives (iii) and (iv) defined in Section 1.5. They allowed us to model the effects of acoustic waves on the aggregative and non-aggregative mechanisms of the kinetics of sonocrystallisation. The last remaining objective is the validation of the derived model.

In Chapter 6 we showed that the new model 1 with even a size-independent λ can reasonably well reproduce the excess free energy of different cluster sizes obtained from statistical mechanical simulations and successfully predict the kinetics of water droplet formation. The predicted nucleation rates of water droplets are in great agreement with experimental data.

Considering the available experimental sonocrystallisation data, we could

only evaluate our new model qualitatively. Simulations presented in Chapter 7 demonstrated that the effect of pressure field on cluster dynamics is cluster size-dependent, in contrast to the EDS clusters used in CNT. Additionally, the size of a condensed critical cluster inversely correlates to the pressure magnitude. This together with the size-dependence of n'_n may explain some sonocrystallisation experimental observations revealing the improvement in the nucleation rate for a scenario with $\rho \approx \rho_n$ (Harzali et al., 2011) while the conventional form of CNT which uses the EDS clusters is incapable of doing so. Moreover, we showed that in contrast to the binary effect of variation in the static pressure on nucleation kinetics, either enhancement or attenuation, the acoustic wave produces both effects over a cycle. This agrees with experimental observations of nucleation of solid from liquid helium subjected to a focused ultrasound field (Chavanne et al., 2001). Finally, we calculated the contribution of non-aggregative mechanism to the kinetics of sonocrystallisation, see Eq. (7.19), in different plane wave fields including travelling, standing and a weak shock. Simulations showed that this contribution depends on the magnitude and wavelength of acoustic waves, and generally tends to be negligible unless shock waves are present or a special boundary condition is imposed.

8.2 Further work

The preceding section outlined the original contributions made in this work. These contributions create extensive opportunities for future work which can be broadly classified as follows: i) model validation, ii) model extension, and iii) model simulation. They are explained in this section.

(i) **Model validation:** we validated the new model 1 against experimental data for water droplet formation. It would be beneficial to evaluate the model with other experimental data available for other fluids. Regarding the sonocrystallisation process, there is a need for well characterised (both acoustic field and crystallisation process) experiments in the absence of cavitation or around a single oscillating bubble where its dy-

namics is measured accurately. Derivations presented in this thesis are generic and can be used with any acoustic source and waveform (either direct field or the field around an oscillating bubble). Therefore, they can be used to explain such experimental data, when made available.

(ii) **Model extension:** there are possibilities for improving the model or extending the application of the model to other phase transition problems. In Chapter 5 we accounted for the effect of pressure diffusion on the kinetics of crystallisation assuming the solution is incompressible. This assumption should be amended for situations that entail compressibility, e.g. strong shock condition. In case of the strong shock, the temperature changes and the process is usually considered to be adiabatic (Duvall and Graham, 1977) instead of isothermal. Therefore the conservation of energy should be solved together with other constitutive equations too, which would lead to a more sophisticated sonocrystallisation model. This would extend the application of our model to other temperature variable processes, examples include ultrasound mediated phase transition in melts.

We developed equations to determine n_n and n_σ and to model variations in the thermodynamics of phase transformation using the non-EDS cluster model with the new surface. Derivations were simplified and implemented for the case of an incompressible new phase. An avenue for further theoretical development is to apply the notion of the non-EDS cluster model with the new surface to the case of bubble formation in an acoustic field by taking an appropriate equation of state for a gaseous new phase. This would allow application of the non-EDS cluster model to simulate bubble nucleation in an acoustic field (acoustic cavitation).

(iii) **Model simulation:** we presented sonocrystallisation simulations in a one-dimensional nonlinear plane wave field. An obvious step to extend these simulations is to consider more complex wave fields in two

or three dimensions and different boundary conditions. Different boundary conditions could tentatively influence mass transportation due to acoustic streaming (Kolb and Nyborg, 1956; Nyborg, 1958), hence the non-aggregative mechanism.

In addition, an interesting and important avenue opened by this thesis is to simulate sonocrystallisation around stable and inertially cavitating bubbles. Bubble dynamics is well developed, and there are accurate and validated mathematical models available (Leighton, 1997) which can be incorporated into our model and solve the kinetics of crystallisation spatially. These simulations would give insightful information about the interaction between cavitation and crystallisation.

Appendix A

Material properties

The physiochemical properties of a generic aqueous solution at room temperature (T = 293 K) and atmospheric pressure was used in the simulations of crystal nucleation. These properties are taken from Table 6.1 of (Kashchiev, 2000). Following this reference, we consider the new phase to be denser than the old phase with a typical value of $\Delta\nu = 10^{-28}$ m^3. This gives $k_\rho = 0.66$. All these parameters are summarised in Table A.1.

Additionally, following (Louisnard et al., 2007) we choose the average value of $\rho_{mass,2}$ = 2000 kg m^{-3} for the mass density of the solute species and calculate M_2 by $M_2 = \mathcal{N}_\mathcal{A}\nu_n\rho_{mass,2} = 0.06$ kg mol^{-1}.

For simulations including pressure variations, the reference state is considered to be at room temperature and atmospheric pressure, T_0 = 293 K and p_0 = 0.1 MPa respectively. Therefore, the values reported in this Table refer to the physicochemical properties at the reference state.

Table A.1: Solution properties at T = 293 K

Parameter	Value
ν_n [nm^3]	0.05
ν [nm^3]	0.15
ρ_n [nm^{-3}]	20.0
ρ [nm^{-3}]	6.67
k_ρ [DL]	0.66
R_0 [nm]	0.23
C_e [m^{-3}]	10^{23}
γ [mJ m^{-2}]	100
D [m^2 s^{-1}]	10^{-9}

The Burgers' and mass transportation equations are solved under isothermal condition at T = 293 K. The properties of water are given in Tables A.2 and A.3. The values and equation in Table A.2 are used to calculate the water droplet nucleation at different temperatures.

Table A.2: Water properties I

Parameter	Value
T_c [K]]	647.14 †
$M(H_2O)$ [kg mol^{-1}]	0.018015 †
$\gamma(H_2O)$ [mJ m^{-2}]	$93.6635 + 0.009133T - 0.000275T^2$ †
$\rho(H_2O)$ [g cm^{-3}]	$0.08\tanh(T-225)/46.2) + 0.741((T_c-T)/T_c)^{0.33} + 0.32$ ††
p_{ve} [Pa]	$\exp(77.34491 - 7235.42465/T - 8.2\ln T + 0.0057113T)$ ††

†Taken from Table 1 Brus et al. (Brus et al., 2009).

††Taken from Table 1 Wölk et al. (Wölk and Strey, 2001).

Table A.3: Water properties II (at T = 293 K)

Parameter	Value
β [DL]	3.5 †
η_B [Pa s]	2.4×10^{-3} ††
η [Pa s]	1.0020×10^{-3} *
c_0 [m s^{-1}]	1482.2 *
C_p [J K^{-1}]	75.377 *
κ [W m^{-1} K^{-1}]	0.598 *

†From (Hamilton and Blackstock, 1998).

††From (He et al., 2012).

*From (Lemmon et al., 2016).

Appendix B

Second-order derivative of the grand potential of the system

In Chapter 2, we determined the increment in the grand potential of the system arising from an infinitesimal variation in the system variables, see Eq. (2.42). This equation is reproduced in the following

$$\begin{aligned} d\Omega_\Sigma \;=\; & -pdV \;-\; Vdp \;-\; d\mu\,(n_n+n_\sigma) \;-\; \mu\,(dn_n+dn_\sigma) \;-\; p_n dV_n \\ & -\; V_n dp_n \;+\; \mu_n dn_n \;+\; n_n d\mu_n \;+\; \mu_\sigma dn_\sigma \;+\; n_\sigma d\mu_\sigma \;+\; A_\sigma d\gamma \\ & +\; \gamma dA_\sigma. \end{aligned} \tag{B.1}$$

Using the Gibbs-Duhem relation of $n_\sigma d\mu_\sigma = -A_\sigma d\gamma$ and $n_n d\mu_n = V_n dp_n$ and only keeping the terms which are dependent on V_n, we arrive at

$$\begin{aligned} \left.\frac{d\Omega_\Sigma}{dV_n}\right|_{T,\mu} \;=\; & -p\frac{dV}{dV_n} \;-\; \mu\frac{d}{dV_n}(n_n+n_\sigma) \;-\; p_n \\ & +\; \mu_n\frac{dn_n}{dV_n} \;+\; \mu_\sigma\frac{dn_\sigma}{dV_n} \;+\; \gamma\frac{dA_\sigma}{dV_n}, \end{aligned} \tag{B.2}$$

Given that $dV_\Sigma \;=\; dV \;+\; dV_n = 0$, we obtain $\frac{dV}{dV_n} = -1$. Differentiating this equation with respect to V_n gives

$$\left.\frac{d^2\Omega_\Sigma}{dV_n^2}\right|_{T,\mu} = -\mu\frac{d^2}{dV_n^2}\left(n_n+n_\sigma\right) + \mu_n\frac{d^2n_n}{dV_n^2} + \mu_\sigma\frac{d^2n_\sigma}{dV_n} + \gamma\frac{d^2A_\sigma}{dV_n^2}, \tag{B.3}$$

and imposing the equilibrium condition 2.46 simplifies this equation to

$$\left.\frac{d^2\Omega_\Sigma}{dV_n^2}\right|_{T,\mu} = \gamma\frac{d^2A_\sigma}{dV_n^2}. \tag{B.4}$$

Appendix C

Fokker-Planck equation with mass transportation

Equation (5.17) shows the Szilard equation in a non-mass conserved system. This equation is reproduced in the following

$$\begin{aligned}\frac{\partial}{\partial t}Z_n &= f_{n-1}(t)Z_{n-1} - g_n(t)Z_n - f_n(t)Z_n + g_{n+1}(t)Z_{n+1} \\ &\quad - Z_n \nabla\cdot\mathbf{u} - \mathbf{u}\cdot\nabla Z_n - \frac{\mathcal{N}_{\mathcal{A}}}{M_2\, n}\nabla\cdot\mathbf{j}_{[\mathrm{n}]}. \end{aligned} \tag{C.1}$$

Following Kashchiev (Kashchiev, 2000), we can derive the continuous format of this equation by writing the truncated Taylor series expansion of $f_{n-1}(t)Z_{n-1}$ and $g_{n+1}(t)Z_{n+1}$ terms about point n

$$\begin{aligned}f(n-1,t)Z(n-1,t) &= f(n,t)Z(n,t) + \frac{\partial}{\partial n}\left[f(n,t)Z(n,t)\right](n-1-n) \\ &\quad + \frac{1}{2}\frac{\partial^2}{\partial n^2}\left[f(n,t)Z(n,t)\right](n-1-n)^2, \end{aligned} \tag{C.2}$$

and

$$g(n+1,t)Z(n+1,t) = g(n,t)Z(n,t) + \frac{\partial}{\partial n}\left[g(n,t)Z(n,t)\right](n+1 - n) + \frac{1}{2}\frac{\partial^2}{\partial n^2}\left[g(n,t)Z(n,t)\right](n+1 - n)^2 . \quad \text{(C.3)}$$

Replacing these two equations into Eq. (C.1) yields

$$\frac{\partial}{\partial t}Z(n) = -\frac{\partial}{\partial n}\left((f(n,t) - g(n,t))Z(n) - \frac{1}{2}\frac{\partial\left[(f(n,t) + g(n,t))Z(n)\right]}{\partial n}\right) - Z(n)\,\nabla\cdot\mathbf{u} - \mathbf{u}\cdot\nabla Z(n) - \frac{\mathcal{N}_{\mathcal{A}}}{M_2\, n}\,(\nabla\cdot\mathbf{j}_{[n]}), \quad \text{(C.4)}$$

which employing the definitions of the dispersion and growth rates, Eq. (4.11), simplifies this equation to the following format

$$\frac{\partial}{\partial t}Z(n) = -\frac{\partial}{\partial n}\left(v(n)Z(n) - \frac{1}{2}\frac{\partial\left[d(n,t)Z(n)\right]}{\partial n}\right) - Z(n)\,\nabla\cdot\mathbf{u} - \mathbf{u}\cdot\nabla Z(n) - \frac{\mathcal{N}_{\mathcal{A}}}{M_2\, n}\,(\nabla\cdot\mathbf{j}_{[n]}). \quad \text{(C.5)}$$

This is the non-mass conserved form of the FPE.

Appendix D

Number of excess molecules

We need to determine the derivatives of n_n and n_σ with respect to n as they are required in Eq. (3.14). Using Eq. (2.27), we can write

$$n'_\sigma(n_n) = \frac{dn_\sigma}{dn} = \frac{dn_\sigma}{dn_n}\frac{dn_n}{dn} = \left[k_\rho \frac{3\lambda}{S_f}\left(\frac{2}{3}n_n^{-1/3} + \frac{1}{3}\frac{\lambda}{S_f}n_n^{-2/3}\right)\right]\frac{dn_n}{dn}, \tag{D.1}$$

furthermore

$$\frac{dn}{dn_n} = 1 + k_\rho \frac{3\lambda}{S_f}\left(\frac{2}{3}n_n^{-1/3} + \frac{1}{3}\frac{\lambda}{S_f}n_n^{-2/3}\right), \tag{D.2}$$

which gives

$$n'_n(n_n) = \frac{dn_n}{dn} = \frac{1}{1 + k_\rho \frac{3\lambda}{S_f}\left(\frac{2}{3}n_n^{-1/3} + \frac{1}{3}\frac{\lambda}{S_f}n_n^{-2/3}\right)}, \tag{D.3}$$

eventually plugging Eq. (D.3) into Eq. (D.1) gives

$$n'_\sigma(n_n) = \frac{dn_\sigma}{dn} = \frac{k_\rho \frac{3\lambda}{S_f}\left(\frac{2}{3}n_n^{-1/3} + \frac{1}{3}\frac{\lambda}{S_f}n_n^{-2/3}\right)}{1 + k_\rho \frac{3\lambda}{S_f}\left(\frac{2}{3}n_n^{-1/3} + \frac{1}{3}\frac{\lambda}{S_f}n_n^{-2/3}\right)}. \tag{D.4}$$

In the limits of very small clusters, using these equations we will have

$$\lim_{n_n \to 0} n'_\sigma \;=\; 1 \qquad , \quad \lim_{n_n \to 0} n'_n \;=\; 0, \tag{D.5}$$

and in the limits of very large clusters, we will arrive at

$$\lim_{n_n \to \infty} n'_\sigma \;=\; 0 \qquad , \quad \lim_{n_n \to \infty} n'_n \;=\; 1. \tag{D.6}$$

In order to calculate the Zeldovich factor, we need to determine the second derivative of n_n with respect to n which is given in the following

$$n''_n = \frac{d^2 n_n}{dn^2} \;=\; \frac{d}{dn}\left(\frac{dn_n}{dn}\right) \;=\; \frac{d}{dn}\left(n'_n\right) \;=\; \frac{dn'_n}{dn_n}\frac{dn_n}{dn} \;=\; \frac{dn'_n}{dn_n} n'_n, \tag{D.7}$$

and by employing Eq. (D.3) simplifies to

$$\begin{aligned} n''_n \;&=\; \frac{k_\rho \dfrac{3\lambda}{S_f} n_n^{-1}\left(\dfrac{2}{9} n_n^{-1/3} \;+\; \dfrac{2}{9}\dfrac{\lambda}{S_f} n_n^{-2/3}\right)}{\left(1 \;+\; k_\rho \dfrac{3\lambda}{S_f}\left(\dfrac{2}{3} n_n^{-1/3} \;+\; \dfrac{1}{3}\dfrac{\lambda}{S_f} n_n^{-2/3}\right)\right)^2} n'_n \\ &=\; \frac{k_\rho \dfrac{3\lambda}{S_f} n_n^{-1}\left(\dfrac{2}{9} n_n^{-1/3} \;+\; \dfrac{2}{9}\dfrac{\lambda}{S_f} n_n^{-2/3}\right)}{\left(1 \;+\; k_\rho \dfrac{3\lambda}{S_f}\left(\dfrac{2}{3} n_n^{-1/3} \;+\; \dfrac{1}{3}\dfrac{\lambda}{S_f}\; n_n^{-2/3}\right)\right)^3} \\ &=\; k_\rho \frac{2\lambda}{3S_f} n_n^{-1}\left(n_n^{-1/3} \;+\; \frac{\lambda}{S_f}\; n_n^{-2/3}\right) {n'_n}^3. \end{aligned} \tag{D.8}$$

Appendix E

Discrete form of monomer detachment frequency

In the discrete representation of the cluster formation work, Eq. (4.35) is used to determine detachment frequency. So, $\Delta\Omega_n(\ ) - \Delta\Omega_{n-1}(\ ) = \int (d\Delta\Omega_n(\ ) - d\Delta\Omega_{n-1}(\ ))$ should be determined where $(\ )$ denotes the dependency of work on all other parameters, e.g. pressure, temperature and composition, which is omitted here to avoid long relations. The two terms of the integrand are obtained with the aid of Eq. (3.5). The integrand then becomes

$$d\Delta\Omega_n(\ ) - d\Delta\Omega_{n-1}(\ ) = -[-s + s_n(n_{n,n} - n_{n,n-1}) + s_\sigma(n_{\sigma,n} - n_{\sigma,n-1})]dT - [\nu - \nu_n(n_{n,n} - n_{n,n-1})]\,dp. \tag{E.1}$$

In order to simplify this equation, we need to determine $n_{n,n} - n_{n,n-1}$ and $n_{\sigma,n} - n_{\sigma,n-1}$. Employing Eq. (2.27) gives

$$
\begin{aligned}
n &= n_{n,n} + n_{\sigma,n} = n_{n,n} + k_\rho \mathcal{G}(n_{n,n}) \\
n-1 &= n_{n,n-1} + n_{\sigma,n-1} = n_{n,n-1} + k_\rho \mathcal{G}(n_{n,n-1}),
\end{aligned}
\tag{E.2}
$$

which follows

$$
\begin{aligned}
1 &= n_{n,n} - n_{n,n-1} + n_{\sigma,n} - n_{\sigma,n-1} = \\
& n_{n,n} - n_{n,n-1} + k_\rho 3\lambda \left(n_{n,n}^{2/3} - n_{n,n-1}^{2/3} + \lambda (n_{n,n}^{1/3} - n_{n,n-1}^{1/3}) \right).
\end{aligned}
\tag{E.3}
$$

Defining the new variable $X = n_{n,n} - n_{n,n-1}$, the above equation reads

$$
\begin{aligned}
1 &= X + n_{\sigma,n} - n_{\sigma,n-1} = \\
& X + k_\rho 3\lambda \left(n_{n,n}^{2/3} - (n_{n,n} - X)^{2/3} + \lambda (n_{n,n}^{1/3} - (n_{n,n} - X)^{1/3}) \right).
\end{aligned}
\tag{E.4}
$$

Approximating the term $(n_{n,n} - X)^\beta$ by its second order truncated binomial expansion gives

$$
(n_{n,n} - X)^\beta \approx n_{n,n}^\beta - \beta n_{n,n}^{\beta-1} X. \tag{E.5}
$$

Given $\beta < 1$ this approximation introduces negligible error. Substituting this approximation in Eq. (E.4) yields

$$
1 = X + k_\rho 3\lambda X \left(\frac{2}{3} n_{n,n}^{-1/3} + \frac{\lambda}{3} n_{n,n}^{-2/3} \right), \tag{E.6}
$$

from which follows

$$X = \frac{1}{1 + k_\rho 3\lambda \left(\frac{2}{3} n_{n,n}^{-1/3} + \frac{\lambda}{3} n_{n,n}^{-2/3} \right)}. \tag{E.7}$$

This is the same as $n_n'(n_n)$ in Eqs. (D.3) and (3.14). Plugging X into Eq. (E.4) we calculate $n_{\sigma,n} - n_{\sigma,n-1}$ which reads the same as $n_\sigma'(n_n)$ in Eqs. (D.4) and (3.14). Performing the integration gives exactly the same results already achieved for the case of variation in work as a function of continuous n shown in Eq. (3.14). Considering the second order binomial truncation is applied, then all the equations derived previously to calculate detachment frequency are valid and can be used for the discrete representation of n, too.

Bibliography

Abe, H., Ogasawara, F., Saitoh, Y., Tatara, T., Kimura, S., Nomura, R., and Okuda, Y. Nucleation of crystals and superfluid droplets in ^{4}He induced by acoustic waves. *Physical Review B*, 71:214506, Jun 2005.

Abraham, F. *Homogeneous nucleation theory: the pretransition theory of vapor condensation.* Advances in Theoretical Chemistry. Academic Press, 1974.

Akhatov, I., Lindau, O., Topolnikov, A., Mettin, R., Vakhitova, N., and Lauterborn, W. Collapse and rebound of a laser-induced cavitation bubble. *Physics of Fluids*, 13(10):2805–2819, 2001.

Akulichev, V. and Bulanov, V. Crystallization nuclei in liquid in a sound field. *International Journal of Heat and Mass Transfer*, 26(2):289 – 300, 1983.

Akulichev, V. A. Acoustic cavitation in cryogenic and boiling liquids. In *Mechanics and Physics of Bubbles in Liquids*, pages 55–67. Springer, 1982.

Andreev, S., Samokhin, A., and Smurov, I. On the theory of explosive boiling of a transparent liquid on a laser-heated target. *Applied Surface Science*, 252(13):4506 – 4510, 2006.

Angélil, R., Diemand, J., Tanaka, K. K., and Tanaka, H. Properties of liquid clusters in large-scale molecular dynamics nucleation simulations. *The Journal of Chemical Physics*, 140(7), 2014. doi: 1.4865256.

Angélil, R., Diemand, J., Tanaka, K. K., and Tanaka, H. Homogeneous spc/e water nucleation in large molecular dynamics simulations. *The Journal of Chemical Physics*, 143(6), 2015.

Arakelyan, V. Effect of ultrasound on crystal growth from melt and solution. *Acta Physica Hungarica*, 61(2):185–187, 1987.

Atamanenko, T., Eskin, D., Zhang, L., and Katgerman, L. Criteria of grain refinement induced by ultrasonic melt treatment of aluminum alloys containing Zr and Ti. *Metallurgical and Materials Transactions A*, 41(8):2056–2066, 2010.

Baidakov, V. *Explosive boiling of superheated cryogenic liquids*. Wiley, 2007.

Baidakov, V., Kaverin, A., and Skripov, V. Acoustic cavitation in superheated liquids. *Akusticheskii Zhurnal*, 27:697–703, 1981.

Baidakov, V., Kaverin, A., and Boltachev, G. S. Nucleation in superheated liquid argon–krypton solutions. *The Journal of Chemical Physics*, 106(13): 5648–5657, 1997.

Baidakov, V. G. and Kaverin, A. M. Boiling-up of superheated liquid argon in an acoustic field. *Journal of Physics: Condensed Matter*, 21(46):465103, 2009.

Balibar, S. and Caupin, F. Nucleation of crystals from their liquid phase. *Comptes Rendus Physique*, 7(9):988–999, 2006.

Bird, R. B., Stewart, W. E., and Lightfoot, E. N. *Transport phenomena*. Wiley international edition. Wiley, 1960.

Blander, M. and Katz, J. L. Bubble nucleation in liquids. *AIChE Journal*, 21 (5):833–848, 1975. ISSN 1547-5905.

Brown, P. N., Byrne, G. D., and Hindmarsh, A. C. VODE: A variable-coefficient ODE solver. *SIAM Journal on Scientific and Statistical Computing*, 10(5):1038–1051, 1989.

Brus, D., Zdimal, V., and Smolik, J. Homogeneous nucleation rate measurements in supersaturated water vapor. *The Journal of Chemical Physics*, 129 (17):174501, 2008.

Brus, D., Zdimal, V., and Uchtmann, H. Homogeneous nucleation rate measurements in supersaturated water vapor II. *The Journal of Chemical Physics*, 131(7):074507, 2009.

Cahn, J. W. and Hilliard, J. E. Free energy of a nonuniform system. III. nucleation in a two-component incompressible fluid. *The Journal of Chemical Physics*, 31(3):688–699, 1959.

Castillo-Peinado, L. d. l. S. and Luque de Castro, M. D. The role of ultrasound in pharmaceutical production: sonocrystallization. *Journal of Pharmacy and Pharmacology*, 68(10):1249–1267, 2016. ISSN 2042-7158.

Chang, J. and Cooper, G. A practical difference scheme for Fokker-Planck equations. *Journal of Computational Physics*, 6(1):1–16, 1970.

Chavanne, X., Balibar, S., and Caupin, F. Acoustic crystallization and heterogeneous nucleation. *Physical Review Letters*, 86(24):5506–5509, 2001.

Chesnokov, E. N. and Krasnoperov, L. N. Complete thermodynamically consistent kinetic model of particle nucleation and growth: Numerical study of the applicability of the classical theory of homogeneous nucleation. *The Journal of Chemical Physics*, 126(14):144504, 2007. doi: 10.1063/1.2672647.

Cogné, C., Labouret, S., Peczalski, R., Louisnard, O., Baillon, F., and Espitalier, F. Theoretical model of ice nucleation induced by acoustic cavitation. part 1: pressure and temperature profiles around a single bubble. *Ultrasonics Sonochemistry*, 2015.

Cogné, C., Labouret, S., Peczalski, R., Louisnard, O., Baillon, F., and Espitalier, F. Theoretical model of ice nucleation induced by inertial acoustic cavitation. part 2: Number of ice nuclei generated by a single bubble. *Ultrasonics Sonochemistry*, 28:185 – 191, 2016. ISSN 1350-4177.

Conrad, H. Influence of an electric or magnetic field on the liquidsolid trans-

formation in materials and on the microstructure of the solid. *Materials Science and Engineering: A*, 287(2):205 – 212, 2000. ISSN 0921-5093.

de Castro, M. L. and Priego-Capote, F. Ultrasound-assisted crystallization (sonocrystallization). *Ultrasonics Sonochemistry*, 14(6):717 – 724, 2007. ISSN 1350-4177.

Dodds, J., Espitalier, F., Louisnard, O., Grossier, R., David, R., Hassoun, M., Baillon, F., Gatumel, C., and Lyczko, N. The effect of ultrasound on crystallisation precipitation processes: some examples and a new segregation model. *Particle & Particle Systems Characterization*, 24(1):18–28, 2007.

Duvall, G. E. and Graham, R. A. Phase transitions under shock-wave loading. *Reviews of Modern Physics*, 49(3):523–579, 1977. ISSN 0034-6861.

Factorovich, M. H., Molinero, V., and Scherlis, D. A. Vapor pressure of water nanodroplets. *Journal of the American Chemical Society*, 136(12):4508–4514, 2014.

Flint, E. B. and Suslick, K. S. The temperature of cavitation. *Science*, 253 (5026):1397–1399, 1991.

Ford, I. J. Imperfect vapour-gas mixtures and homogeneous nucleation. *Journal of Aerosol Science*, 23(5):447 – 455, 1992.

Ford, I. J. Thermodynamic properties of critical clusters from measurements of vapour–liquid homogeneous nucleation rates. *The Journal of Chemical Physics*, 105(18):8324–8332, 1996.

Ford, I. J. Nucleation theorems, the statistical mechanics of molecular clusters, and a revision of classical nucleation theory. *Physical Review E*, 56(5):5615, 1997.

Ford, I. J. Properties of ice clusters from an analysis of freezing nucleation. *The Journal of Physical Chemistry B*, 105(47):11649–11655, 2001.

Ford, I. J. *Statistical Physics: An Entropic Approach*. John Wiley & Sons, Ltd, 2013.

Ford, I. J. Advanced topics in statistical mechanics. 2016.

Gibbs, G. W. Collected works. Vol 1. thermodynamics. 1928.

Gracin, S., Uusi-Penttil, M., and Rasmuson, k. C. Influence of ultrasound on the nucleation of polymorphs of p-Aminobenzoic acid. *Crystal Growth & Design*, 5(5):1787–1794, 2005.

Granasy, L. Semiempirical van der Waals/Cahn-Hilliard theory: Size dependence of the Tolman's length. *The Journal of Chemical Physics*, 109(22): 9660–9663, 1998.

Groß, M. and Jaenicke, R. A kinetic model explaining the effects of hydrostatic pressure on nucleation and growth of lysozyme crystals. *Biophysical Chemistry*, 45(3):245 – 252, 1993. ISSN 0301-4622.

Guggenheim, E. A. Thermodynamics- an advanced treatment for chemists and physicists. *Amsterdam, North-Holland, 1985, 414*, 1985.

Guo, Z., Jones, A., and Li, N. The effect of ultrasound on the homogeneous nucleation of BaSO4 during reactive crystallization. *Chemical Engineering Science*, 61(5):1617–1626, 2006a.

Guo, Z., Jones, A., and Li, N. Interpretation of the ultrasonic effect on induction time during BaSO4 homogeneous nucleation by a cluster coagulation model. *Journal of Colloid and Interface Science*, 297(1):190–198, 2006b.

Hamilton, M. and Blackstock, D. *Nonlinear Acoustics*. Academic Press, 1998. ISBN 9780123218605.

Harzali, H., Baillon, F., Louisnard, O., Espitalier, F., and Mgaidi, A. Experimental study of sono-crystallisation of ZnSO4· 7H2O, and interpretation by the segregation theory. *Ultrasonics Sonochemistry*, 18(5):1097–1106, 2011.

He, X., Wei, H., Shi, J., Liu, J., Li, S., Chen, W., and Mo, X. Experimental measurement of bulk viscosity of water based on stimulated brillouin scattering. *Optics Communications*, 285(20):4120 – 4124, 2012. ISSN 0030-4018.

Helfrich, W. Elastic properties of lipid bilayers: theory and possible experiments. *Zeitschrift fur Naturforschung C*, 28(11-12):693–703, 1973.

Hem, S. L. The effect of ultrasonic vibrations on crystallization processes. *Ultrasonics*, 5(4):202–207, 1967.

Hill, T. L. Thermodynamics of small systems. *The Journal of Chemical Physics*, 36(12):3182–3197, 1962.

Hirschfelder, J. O., Curtiss, C. F., and Bird, R. B. *Molecular theory of gases and liquids*. Structure of Matter Series. Wiley, 1954. ISBN 9780471400653.

Holten, V. and van Dongen, M. E. H. Comparison between solutions of the general dynamic equation and the kinetic equation for nucleation and droplet growth. *The Journal of Chemical Physics*, 130(1):014102, 2009.

Holten, V., Labetski, D. G., and van Dongen, M. E. H. Homogeneous nucleation of water between 200 and 240 k: new wave tube data and estimation of the Tolman length. *The Journal of Chemical Physics*, 123(10):104505, 2005.

Horsch, M., Vrabec, J., and Hasse, H. Modification of the classical nucleation theory based on molecular simulation data for surface tension, critical nucleus size, and nucleation rate. *Physical Review E*, 78:011603, Jul 2008. doi: 10.1103/PhysRevE.78.011603.

Hunt, J. and Jackson, K. Nucleation of solid in an undercooled liquid by cavitation. *Journal of Applied Physics*, 37(1):254–257, 1966.

Ishiguro, R., Caupin, F., and Balibar, S. Homogeneous nucleation of crystals by acoustic waves. *EPL (Europhysics Letters)*, 75(1):91, 2007.

Johansson, F. *mpmath: a Python library for arbitrary-precision floating-point arithmetic (version 0.18)*, December 2013. `http://mpmath.org/`.

Jordens, J., Coker, N. D., Gielen, B., Gerven, T. V., and Braeken, L. Ultrasound precipitation of manganese carbonate: The effect of power and frequency on particle properties. *Ultrasonics Sonochemistry*, 26:64 – 72, 2015.

Kalikmanov, V. *Nucleation Theory*. Lecture Notes in Physics. Springer Netherlands, 2012. ISBN 9789048136438.

Kapustin, A. *The effects of ultrasound on the kinetics of crystallization*. Consultants Bureau, New York, 1963.

Kashchiev, D. Nucleation at variable supersaturation. *Surface Science*, 18(2): 293–297, 1969a.

Kashchiev, D. Solution of the non-steady state problem in nucleation kinetics. *Surface Science*, 14(1):209–220, 1969b.

Kashchiev, D. Nucleation at time dependent supersaturation. *Surface Science*, 22(2):319–324, 1970.

Kashchiev, D. On the relation between nucleation work, nucleus size, and nucleation rate. *The Journal of Chemical Physics*, 76(10):5098–5102, 1982.

Kashchiev, D. Effect of carriergas pressure on nucleation. *The Journal of Chemical Physics*, 104(21):8671–8677, 1996.

Kashchiev, D. *Nucleation*. Butterworth-Heinemann, 2000.

Kashchiev, D. Thermodynamically consistent description of the work to form a nucleus of any size. *The Journal of Chemical Physics*, 118:1837, 2003a.

Kashchiev, D. Determining the curvature dependence of surface tension. *The Journal of Chemical Physics*, 118(20):9081–9083, 2003b.

Kashchiev, D. Forms and applications of the nucleation theorem. *The Journal of Chemical Physics*, 125(1):014502, July 2006.

Kashchiev, D. and Van Rosmalen, G. Review: nucleation in solutions revisited. *Crystal Research and Technology*, 38(7-8):555–574, 2003.

Kashchiev, D. and Van Rosmalen, G. M. Effect of pressure on nucleation in bulk solutions and solutions in pores and droplets. *Journal of Colloid and Interface Science*, 169(1):214–219, 1995.

Kimura, S., Ogasawara, F., Nomura, R., and Okuda, Y. Nucleation of solid 4he by acoustic waves. *Journal of Low Temperature Physics*, 134(1):145–150, 2004.

Kinsler, L. E., Frey, A. R., Coppens, A. B., and Sanders, J. V. Fundamentals of acoustics. *Fundamentals of Acoustics, 4th Edition, by Lawrence E. Kinsler, Austin R. Frey, Alan B. Coppens, James V. Sanders, pp. 560. ISBN 0-471-84789-5. Wiley-VCH, December 1999.*, 1, 1999.

Kitayama, H., Yoshimura, Y., So, M., Sakurai, K., Yagi, H., and Goto, Y. A common mechanism underlying amyloid fibrillation and protein crystallization revealed by the effects of ultrasonication. *Biochimica et Biophysica Acta - Proteins and Proteomics*, 1834(12):2640 – 2646, 2013. ISSN 1570-9639.

Koek, Z. and Chvoj, Z. The influence of time dependence of temperature on the kinetics of nucleation. *Crystal Research and Technology*, 18(3):307–313, 1983. ISSN 1521-4079.

Kolb, J. and Nyborg, W. L. Small-Scale Acoustic Streaming in Liquids. *The Journal of the Acoustical Society of America*, 28(6):1237, 1956. ISSN 00014966.

Koop, T., Luo, B., Tsias, A., and Peter, T. Water activity as the determinant for homogeneous ice nucleation in aqueous solutions. *Nature*, 406(6796): 611–614, 2000.

Kožíšek, Z. Non-steady state homogeneous nucleation in glass-forming systems: Dimensionless kinetic equation. *Czechoslovak Journal of Physics*, 40 (6):592–604, 1990. ISSN 1572-9486.

Kozísek, Z. and Demo, P. Homogeneous nucleation at oscillating temperature. *Journal of Non-Crystalline Solids*, 152(2-3):201–206, feb 1993. ISSN 00223093.

Kozísek, Z. and Demo, P. Influence of initial conditions on homogeneous nucleation kinetics in a closed system. *The Journal of Chemical Physics*, 123(14):144502, Oct 2005.

Kožíšek, Z., Sato, K., Demo, P., and Sveshnikov, A. M. Homogeneous nucleation of droplets from supersaturated vapor in a closed system. *The Journal of Chemical Physics*, 120(14):6660–6664, 2004.

Larson, M. and Garside, J. Solute clustering in supersaturated solutions. *Chemical Engineering Science*, 41(5):1285 – 1289, 1986. ISSN 0009-2509.

Lau, G. V., Ford, I. J., Hunt, P. A., Müller, E. A., and Jackson, G. Surface thermodynamics of planar, cylindrical, and spherical vapour-liquid interfaces of water. *The Journal of Chemical Physics*, 142(11):114701, 2015a.

Lau, G. V., Hunt, P. A., Müller, E. A., Jackson, G., and Ford, I. J. Water droplet excess free energy determined by cluster mitosis using guided molecular dynamics. *The Journal of Chemical Physics*, 143:244709, 2015b.

Leighton, T. G. *The acoustic bubble*, volume 10. Academic Pr, 1997.

Lemmon, E. W., McLinden, M. O., and Friend, D. G. Thermophysical properties of fluid systems. *in NIST Chemistry WebBook, NIST Standard Reference Database Number 69, Eds. P.J. Linstrom and W.G. Mallard, National Institute of Standards and Technology, Gaithersburg MD, 20899*, 2016.

Lindinger, B., Mettin, R., Chow, R., and Lauterborn, W. Ice crystallization induced by optical breakdown. *Physical Review Letters*, 99:045701, Jul 2007.

Lorber, B., Jenner, G., and Gieg, R. Effect of high hydrostatic pressure on nucleation and growth of protein crystals. *Journal of Crystal Growth*, 158 (1):103 – 117, 1996. ISSN 0022-0248.

Louisnard, O., Gomez, F. J., and Grossier, R. Segregation of a liquid mixture by a radially oscillating bubble. *Journal of Fluid Mechanics*, 577:385–415, 2007.

Lu, H. M. and Jiang, Q. Size-dependent surface tension and Tolman's length of droplets. *Langmuir*, 21(2):779–781, 2005.

Luijten, C. C. M. and van Dongen, M. E. H. Nucleation at high pressure. I. theoretical considerations. *The Journal of Chemical Physics*, 111(18): 8524–8534, 1999.

Luijten, C. C. M., Peeters, P., and van Dongen, M. E. H. Nucleation at high pressure. II. wave tube data and analysis. *The Journal of Chemical Physics*, 111(18):8535–8544, 1999.

Malijevsky, A. and Jackson, G. A perspective on the interfacial properties of nanoscopic liquid drops. *Journal of Physics: Condensed Matter*, 24(46): 464121, 2012.

Mazhul, M. M. Cavitation phenomena and the formation of crystal nuclei. *PhD Dissertation*, 1963.

Mitome, H. An exact solution for finiteamplitude plane sound waves in a dissipative fluid. *The Journal of the Acoustical Society of America*, 86(6): 2334–2338, 1989.

Mullin, J. W. *Crystallisation*. Butterworths London, 1972.

Munir, Z. A., Anselmi-Tamburini, U., and Ohyanagi, M. The effect of electric field and pressure on the synthesis and consolidation of materials: A review of the spark plasma sintering method. *Journal of Materials Science*, 41(3): 763–777, 2006. ISSN 1573-4803.

Nakamura, K., Hosokawa, Y., and Masuhara, H. Anthracene crystallization induced by single-shot femtosecond laser irradiation: experimental evidence for the important role of bubbles. *Crystal Growth & Design*, 7(5):885–889, 2007.

Nalajala, V. S. and Moholkar, V. S. Investigations in the physical mechanism of sonocrystallization. *Ultrasonics sonochemistry*, 18(1):345–355, 2011.

Neppiras, E. and Noltingk, B. Cavitation produced by ultrasonics: theoretical conditions for the onset of cavitation. *Proceedings of the Physical Society. Section B*, 64(12):1032, 1951.

Nieminen, J. and Kaski, K. Rate-equation study of nucleation and growth of thin films. I. growth of one monolayer. *Physical Review A*, 40(4):2088, 1989.

Nii, S. and Takayanagi, S. Growth and size control in anti-solvent crystallization of glycine with high frequency ultrasound. *Ultrasonics Sonochemistry*, 21(3):1182–1186, 2014.

Nyborg, W. L. Acoustic streaming near a boundary. *The Journal of the Acoustical Society of America*, 30(4):329–339, 1958.

Ohl, C. D., Kurz, T., Geisler, R., Lindau, O., and Lauterborn, W. Bubble dynamics, shock waves and sonoluminescence. *Philosophical Transactions of the Royal Society of London. Series A: Mathematical, Physical and Engineering Sciences*, 357(1751):269–294, 1999.

Oxtoby, D. W. Homogeneous nucleation: theory and experiment. *Journal of Physics: Condensed Matter*, 4(38):7627, 1992.

Oxtoby, D. W. and Kashchiev, D. A general relation between the nucleation work and the size of the nucleus in multicomponent nucleation. *The Journal of Chemical Physics*, 100(10):7665–7671, 1994.

Oxtoby, D. W. and Laaksonen, A. Some consequences of the nucleation theorem for binary fluids. *The Journal of Chemical Physics*, 102(17):6846–6850, 1995.

Ozkan, G. and Ortoleva, P. A mesoscopic model of nucleation and ostwald ripening/stepping: Application to the silica polymorph system. *The Journal of Chemical Physics*, 112(23):10510–10525, 2000.

Platten, J. K. The soret effect: a review of recent experimental results. *Journal of Applied Mechanics*, 73(1):5–15, 2006.

Prosperetti, A. Nonlinear oscillations of gas bubbles in liquids. transient solutions and the connection between subharmonic signal and cavitation. *The Journal of the Acoustical Society of America*, 57(4):810–821, 1975.

Ratsch, C. and Venables, J. Nucleation theory and the early stages of thin film growth. *Journal of Vacuum Science & Technology A: Vacuum, Surfaces, and Films*, 21(5):S96–S109, 2003.

Ratsimba, B., Biscans, B., Delmas, H., and Jenck, J. Sonocrystallization: The end of empiricism? *KONA Powder and Particle Journal*, 17:38–48, 1999. doi: 10.14356/kona.1999010.

Reiss, H. *Methods of Thermodynamics*. Dover Publications, 1965. ISBN 978-0-486-69445-0.

Rempel, J. Y. *Insights into formation of semiconductor nanocrystals: from first principles calculations to kinetic models of nucleation and growth*. PhD thesis, Massachusetts Institute of Technology, 2008.

Revalor, E., Hammadi, Z., Astier, J.-P., Grossier, R., Garcia, E., Hoff, C., Furuta, K., Okustu, T., Morin, R., and Veesler, S. Usual and unusual crystallization from solution. *Journal of Crystal Growth*, 312(7):939 – 946, 2010.

Richards, W. T. and Loomis, A. L. The chemical effects of high frequency sound waves I. a preliminary survey. *Journal of the American Chemical Society*, 49(12):3086–3100, 1927.

Ruecroft, G., Hipkiss, D., Ly, T., Maxted, N., and Cains, P. Sonocrystallization: the use of ultrasound for improved industrial crystallization. *Organic Process Research and Development*, 9(6):923–932, 2005.

Saclier, M., Peczalski, R., and Andrieu, J. A theoretical model for ice primary nucleation induced by acoustic cavitation. *Ultrasonics Sonochemistry*, 17 (1):98–105, 2010.

Samsonov, V., Bazulev, A., and Sdobnyakov, N. Y. Rusanov's linear formula for the surface tension of small objects. In *Doklady Physical Chemistry*, volume 389, pages 83–85. Springer, 2003.

Sander, J. R., Zeiger, B. W., and Suslick, K. S. Sonocrystallization and sonofragmentation. *Ultrasonics sonochemistry*, 2014.

Schaaf, P., Senger, B., Voegel, J.-C., Bowles, R. K., and Reiss, H. Simulative determination of kinetic coefficients for nucleation rates. *The Journal of Chemical Physics*, 114(18):8091–8104, 2001. doi: 10.1063/1.1364640.

Schmelzer, J., Röpke, G., and Priezzhev, V. B. *Nucleation theory and applications*. Wiley Online Library, 2005.

Schmelzer, J. W. P. and Baidakov, V. G. Comment on Multicomponent nucleation: Thermodynamically consistent description of the nucleation work [J. Chem. Phys. 120, 3749 (2004)]. *The Journal of Chemical Physics*, 121 (3):1644–1645, 2004.

Shaw, S. and Spelt, P. Shock emission from collapsing gas bubbles. *Journal of Fluid Mechanics*, 646:363–373, 2010.

Soare, A., Dijkink, R., Pascual, M. R., Sun, C., Cains, P. W., Lohse, D., Stankiewicz, A. I., and Kramer, H. J. M. Crystal nucleation by laser-induced cavitation. *Crystal Growth & Design*, 11(6):2311–2316, 2011.

Storey, B. D. and Szeri, A. J. Water vapour, sonoluminescence and sonochemistry. *Proceedings of the Royal Society of London. Series A: Mathematical, Physical and Engineering Sciences*, 456(1999):1685–1709, 2000.

Suslick, K. S. and Flannigan, D. J. Inside a collapsing bubble: sonoluminescence and the conditions during cavitation. *Annual Review of Physical Chemistry*, 59(1):659–683, 2008.

Suslick, K. S. and Price, G. J. Application of ultrasound to materials chemistry. *Annual Review of Materials Science*, 29(1):295–326, 1999.

Talanquer, V. and Oxtoby, D. Density functional analysis of phenomenological theories of gas-liquid nucleation. *The Journal of Physical Chemistry*, 99(9): 2865–2874, 1995.

Tolman, R. C. The effect of droplet size on surface tension. *The Journal of Chemical Physics*, 17(3):333–337, 1949.

Tuulmets, A., Piiskop, S., Jrv, J., and Salmar, S. Sonication effects on non-radical reactions. a sonochemistry beyond the cavitation? *Ultrasonics Sonochemistry*, 21(3):997–1001, 2014.

van Putten, D. S. and Kalikmanov, V. I. Efficient approach to nucleation and growth dynamics: Stationary diffusion flux model. *The Journal of Chemical Physics*, 130(16):164508, 2009.

Vehkamaki, H. *Classical Nucleation Theory in Multicomponent Systems*. Springer, 2006. ISBN 9783540292135.

Venables, J., Spiller, G., and Hanbucken, M. Nucleation and growth of thin films. *Reports on Progress in Physics*, 47(4):399, 1984.

Vetter, T., Iggland, M., Ochsenbein, D. R., Hanseler, F. S., and Mazzotti, M. Modeling nucleation, growth, and Ostwald ripening in crystallization processes: A comparison between population balance and kinetic rate equation. *Crystal Growth and Design*, 13(11):4890–4905, 2013.

Virone, C., Kramer, H., Van Rosmalen, G., Stoop, A., and Bakker, T. Primary nucleation induced by ultrasonic cavitation. *Journal of Crystal Growth*, 294 (1):9–15, 2006.

Volmer, M. and Weber, M. *Zeitschrift für Physikalische Chemie*, 119:227, 1926.

Vrentas, J. and Vrentas, C. *Diffusion and Mass Transfer*. CRC Press, 2016. ISBN 9781466515697.

Ward, M. R., Rae, A., and Alexander, A. J. Nonphotochemical laser-induced crystal nucleation by an evanescent wave. *Crystal Growth & Design*, 15(9): 4600–4605, 2015.

Wedekind, J., Hyvärinen, A.-P., Brus, D., and Reguera, D. Unraveling the "pressure effect" in nucleation. *Physical Review Letters*, 101:125703, Sep 2008.

Werner, F., Beaume, G., Hobeika, A., Nascimbene, S., Herrmann, C., Caupin, F., and Balibar, S. Liquid helium up to 160 bar. *Journal of low temperature physics*, 136(1-2):93–116, 2004.

Wilhelmsen, Ø., Bedeaux, D., and Reguera, D. Communication: Tolman length and rigidity constants of water and their role in nucleation. *The Journal of Chemical Physics*, 142(17):171103, 2015.

Wohlgemuth, K., Ruether, F., and Schembecker, G. Sonocrystallization and crystallization with gassing of adipic acid. *Chemical Engineering Science*, 65(2):1016–1027, 2010.

Wölk, J. and Strey, R. Homogeneous nucleation of H2O and D2O in comparison: the isotope effect. *The Journal of Physical Chemistry B*, 105(47): 11683–11701, 2001.

Wood, R. W. and Loomis, A. L. The physical and biological effects of high frequency sound waves of great intensity. *The London, Edinburgh, and Dublin philosophical magazine and journal of science*, 4(22):417–436, 1927.

Wyslouzil, B. E. and Wölk, J. Overview: Homogeneous nucleation from the vapor phasethe experimental science. *The Journal of Chemical Physics*, 145 (21):211702, 2016.

Yano, T. Mass, momentum and total excess energy transported by a weak planen wave. *Shock Waves*, 6(6):313–322, 1996. ISSN 1432-2153.

Yano, T. and Inoue, Y. Quasisteady streaming with rarefaction effect induced by asymmetric sawtoothlike plane waves. *Physics of Fluids*, 8(9):2537–2551, 1996.

Yasuoka, K. and Matsumoto, M. Molecular dynamics of homogeneous nucleation in the vapor phase. I. lennard-jones fluid. *The Journal of Chemical Physics*, 109(19):8451–8462, 1998. doi: 10.1063/1.477509.

Yoshikawa, H. Y., Hosokawa, Y., and Masuhara, H. Explosive crystallization of urea triggered by focused femtosecond laser irradiation. *Japanese Journal of Applied Physics*, 45(1L):L23, 2006.

Yu, D., Liu, B., and Wang, B. The effect of ultrasonic waves on the nucleation of pure water and degassed water. *Ultrasonics Sonochemistry*, 19(3):459 – 463, 2012.

Ziff, R. M., McGrady, E., and Meakin, P. On the validity of Smoluchowski equation for cluster–cluster aggregation kinetics. *The Journal of Chemical Physics*, 82(11):5269–5274, 1985.

ZinkeAllmang, M., Feldman, L. C., and Grabow, M. H. Clustering on surfaces. *Surface Science Reports*, 16(8):377–463, 1992.

Zinsmeister, G. Theory of thin film condensation. part B: Solution of the simplified condensation equation. *Thin solid films*, 2(5):497–507, 1968.

Zinsmeister, G. Theory of thin film condensation part C: aggregate size distribution in island films. *Thin Solid Films*, 4(5):363–386, 1969.